

University of Nottingham

Synthesis of Metal-Polymer Nanocomposites



Tom Hasell, M.Sc. (*Hons*)

Thesis submitted for the degree of Doctor of Philosophy, May 2008

Prof. S. M. Howdle

Prof. P. D. Brown

Abstract

This thesis details the synthesis and characterisation of novel nanocomposite materials. The unifying theme of all the projects investigated, is the aim to combine metal or metal oxide nanoparticles with polymer systems. In order to investigate the structure of the materials produced, the extensive use of advanced electron microscopy techniques is essential throughout.

Chapter 1: This introductory chapter outlines key themes that are relevant to all the areas of research in this thesis. Theory, background and applications are provided for the fields of nanoparticles, polymers, and supercritical fluids.

Chapters 2, 3 and 4 each report a separate area of research. In each chapter additional theory and background is provided where appropriate, and previous literature is discussed. The aims, results and discussion of each research area are contained within the relevant chapter, as well as conclusions and future work.

Chapter 2: Supercritical CO₂ is used to impregnate optical polymer substrates with silver complexes, which are then decomposed to form nanoparticles.

Chapter 3: Metal oxide nanoparticles are used to stabilise dispersion and suspension polymerisations, providing a method of recovering nanoparticles from aqueous solutions and embedding them on the surface of polymer powders.

Chapter 4: Two alternative routes, for creating polymer microspheres surface decorated with silver nanoparticles, are compared.

Chapter 5: A detailed description of the synthetic methods, equipment, and analysis techniques used in this research is provided.

Chapter 6: A brief but overall conclusion to the research is given.

Publications

1. T. Hasell, L. Lagonigro, A. C. Peacock, S. Yoda, P. D. Brown, P. J. A. Sazio, and S. M. Howdle, *Silver Nanoparticle Impregnated Polycarbonate Substrates for Surface Enhanced Raman Spectroscopy*, *Advanced Functional Materials*, in press.
2. T. Hasell, K. J. Thurecht, R. D. W. Jones, P. D. Brown and S. M. Howdle, *Novel one pot synthesis of silver nanoparticle–polymer composites by supercritical CO₂ polymerisation in the presence of a RAFT agent*, *Chemical Communications*, 2007, 3933-3935.
3. T. Hasell, J. X. Yang, W. X. Wang, J. Li, P. D. Brown, M. Poliakoff, E. Lester and S. M. Howdle, *Preparation of polymer–nanoparticle composite beads by a nanoparticle stabilised suspension polymerisation*, *Journal of Materials Chemistry*, 2007, 17, 4382-4386.
4. J. Yang, T. Hasell, W. X. Wang, J. Li, P. D. Brown, M. Poliakoff, E. Lester and S. M. Howdle, *Preparation of hybrid polymer nanocomposite microparticles by a nanoparticle stabilised dispersion polymerisation*, *Journal of Materials Chemistry*, 2008, 18, 998-1001.
5. J Yang, T. Hasell, W. Wang, S.M. Howdle, *A Novel Synthetic Route to Metal-Polymer Nanocomposites by in situ Suspension and Bulk Polymerizations*, *European Polymer Journal* (2008), doi: 10.1016/j.eurpolymj.2008.01.044
6. T. Hasell, J. X. Yang, W. X. Wang, P. D. Brown and S. M. Howdle, *A facile synthetic route to aqueous dispersions of silver nanoparticles*, *Materials Letters*, 2007, 61, 4906-4910.

Acknowledgments

I would like to thank my supervisors, *Steve Howdle* and *Paul Brown*, for giving me the chance to study for a PhD and for all the support and encouragement over the last 3 years. I am also grateful to *Martyn Poliakoff* for his helpful advice and discussions, and to *Ed Lester* for his collaborations and enthusiasm.

A large number of people have helped me during this work, with many different techniques, collaborations and advice, and I am glad to give them credit here:

Help and advice with chemistry: *Alison Mills*, *Andy Naylor*, *Kristofer Thurecht*, *Wenxin Wang* and *Jixin Yang*.

Help with microscopy: *Keith Dinsdale*, *Mike Fey* and *Martin Roe*, always patient and ready to help me when I'd got into bother on the TEM.

Collaborators in Southampton: *Laura Lagonigro*, *Anna Peacock* and *Pier Sazio*.

I must give a special thanks to *Satoshi Yoda*, for being an excellent host and guide, and making my time in Japan so enjoyable. Also, thanks go to *Eric Beckman* for giving me the chance to work in Pittsburgh, and for his sense of humour.

This work could not have been done without the expert technical support provided by the workshop staff, especially *Martin Dellar*, *Pete Fields*, *Mark Guyler*, and *Richard Wilson*.

List of Contents

Abstract.....	1
Publications.....	2
Acknowledgments.....	3
List of Contents.....	4
Abbreviations and acronyms.....	10

Chapter 1 – Introduction

1.1 Overview.....	12
1.2 Chapter 1 - contents	13
1.3 Nanoparticles	14
1.3.1 Properties	15
1.3.1.1 Catalysis.....	18
1.3.1.2 Optics and Photonics.....	21
1.3.1.3 Medical Application of Nanoparticles.....	37
1.3.2 General Synthetic Strategies.....	41
1.3.2.2 Solution Synthesis.....	42
1.3.2.3 Chemical Vapour Deposition and Physical Vapour Deposition.....	44
1.3.2.4 Supercritical Fluid Synthesis of Nanoparticles.....	45
1.3.2.5 Stabilisation.....	45
1.4 Polymers	49
1.4.1 Definition	49
1.4.1.1 Crystallinity in Polymers	50
1.4.1.2 The Glass Transition and Melting Point.....	52
1.4.2 History and Importance.....	53
1.4.3 Metal-Polymer Nanocomposites.....	55
1.4.3.1 <i>Ex situ</i>	56
1.4.3.2 <i>In situ</i>	57
1.5 Supercritical Fluids.....	60
1.5.1 The Discovery and Development of Supercritical Fluids.....	60
1.5.2 Supercritical CO ₂	63

1.5.2.1	Polymer Processing with scCO ₂	66
1.5.2.2	Supercritical Fluids for Nanoparticle Synthesis	69
1.5.2.3	Rapid Expansion of Supercritical Solvents (RESS)	70
1.5.2.4	Hydrothermal Synthesis of Nanoparticles	71
1.5.2.5	Nanoparticles by scCO ₂ Impregnation of into Host Materials ...	73
1.6	Conclusions – Chapter 1	82
1.7	References.....	83

Chapter 2 - Supercritical impregnation of optical polymers silver nanoparticles

2.1	Hypothesis and Overview	92
2.2	Chapter 2 – Contents.....	94
2.3	Introduction.....	96
2.3.1	Aims.....	96
2.3.2	Literature review.....	98
2.3.3	Reaction scheme	112
2.3.3.1	Precursor silver complex.....	115
2.4	Choice of polymer.....	116
2.4.1	Polymer structures	116
2.4.1.1	Teflon [®] AF.....	116
2.4.1.2	PMMA	118
2.4.1.3	Polycarbonate.....	119
2.4.2	Results of polymer trials	120
2.4.2.1	Teflon [®] AF.....	120
2.4.2.2	PMMA	125
2.4.2.3	Polycarbonate.....	130
2.4.2.4	Conclusions of polymer trials	132
2.5	Effect of temperature and pressure	133
2.5.1	Temperature	133
2.5.2	Pressure.....	134
2.5.3	Influence on general method.....	136
2.6	Development of the process and equipment.....	138
2.7	Effect of precursor mass	142

2.8	Effect of H ₂ reduction time	144
2.9	Impregnation time and TEM investigation	148
2.9.1	Venting.....	149
2.9.2	UV-vis study of impregnation time	151
2.9.3	TEM Investigation	154
2.9.3.1	Problems/limitations of TEM imaging	165
2.9.3.2	Impregnation time – nanoparticle depth	168
2.9.3.3	Comparison of nanoparticle size from TEM images	171
2.10	Solubility studies.....	176
2.10.1	Complexes investigated	178
2.10.1.1	Silver complexes:.....	179
2.10.1.2	Copper complexes:.....	180
2.10.2	Results of solubility measurements	181
2.10.2.1	Silver solubility results	181
2.10.2.2	Copper solubility results	183
2.10.3	Implications for the impregnation process.....	184
2.11	Applications testing	188
2.11.1	Advantages of the substrate for SERS	188
2.11.2	Aims of these tests	189
2.11.3	Samples tested.....	190
2.11.4	Results.....	193
2.11.4.1	Reflection spectra and refractive index measurement	193
2.11.4.2	Surface Enhanced Raman Characterisation	195
2.11.4.3	Plasma etching	198
2.11.5	Conclusions of SERS testing	201
2.12	Overall conclusions and future work	202
2.13	References.....	205

Chapter 3 – The stabilisation of suspension and dispersion polymerisations by metal oxide nanoparticles

3.1	Overview.....	208
3.2	Contents	209

3.3	Introduction and aims	210
3.3.1	Preparation and nature of magnetite nanoparticle solution.....	213
3.4	Preparation of polymer-nanoparticle composite beads by a nanoparticle stabilised suspension polymerisation.....	217
3.4.1	Free radical vinyl polymerisation of MMA	221
3.4.2	Reaction procedure	225
3.4.3	Results.....	226
3.4.3.1	Scanning electron microscopy	229
3.4.3.2	Transmission electron microscopy	232
3.4.4	Other nanoparticles	237
3.4.5	Conclusions.....	240
3.5	Preparation of polymer-nanoparticle composite microparticles by a nanoparticle stabilised dispersion polymerisation	242
3.5.1	Dispersion polymerisation	243
3.5.2	Free radical vinyl polymerisation of styrene	244
3.5.3	Reaction procedure	246
3.5.4	Results.....	248
3.5.4.1	Results for 1.8 gL ⁻¹ nanoparticle concentration.....	249
3.5.4.2	SEM investigation.....	251
3.5.4.3	TEM investigation	253
3.5.4.4	Results for 40 gL ⁻¹ nanoparticle concentration.....	255
3.5.4.5	SEM investigation.....	259
3.5.4.6	TEM investigation	261
3.5.5	Conclusions.....	264
3.6	Overall conclusions and future work	265
3.7	References.....	267

Chapter 4 – Novel synthetic routes to silver nanoparticle decorated polymer microspheres

4.1	Overview.....	269
4.2	Contents	270
4.3	Introduction and aims	271

4.4	Aqueous route	273
4.4.1	Introduction.....	274
4.4.1.1	Crosslinking with DVB.....	277
4.4.1.2	Reaction procedure	278
4.4.2	Results.....	281
4.4.2.1	Silver nanoparticle solution	281
4.4.2.2	Sulfonated polystyrene synthesis and decoration with silver nanoparticles	288
4.4.3	Conclusions and future work	293
4.5	Supercritical Route.....	295
4.5.1	Introduction.....	295
4.5.1.1	Living Polymerisation.....	297
4.5.1.2	Reversible addition-fragmentation chain transfer – (RAFT)....	298
4.5.1.3	Silver nanoparticle reduction and stabilisation.....	303
4.5.1.4	Reaction procedure	305
4.5.2	Results.....	306
4.5.2.1	Nanoparticles synthesised independently	306
4.5.2.2	PMMA powder synthesised independently	307
4.5.2.3	Silver nanoparticle and PMMA combined synthesis.....	308
4.5.2.4	Concentration of Ag(hfac)COD.....	315
4.5.3	Conclusions and future work	320
4.6	Overall conclusions.....	321
4.7	References.....	322

Chapter 5 – Methods and techniques

5.1	Overview.....	325
5.2	Contents	326
5.3	Reaction methods and equipment	327
5.3.1	High Pressure Equipment	327
5.3.2	Reaction procedure for the impregnation of silver nanoparticles into polymer substrates in scCO ₂	333

5.3.3	Reaction procedure for suspension polymerisation with nanoparticles as stabiliser.....	336
5.3.4	Reaction procedure for dispersion polymerisation with nanoparticles as stabiliser	337
5.3.5	Reaction procedure for the synthesis of aqueous soluble stabilised silver nanoparticles	338
5.3.6	Reaction procedure for the dispersion polymerisation of polystyrene microparticles, their sulfonation and decoration with silver nanoparticles	340
5.3.7	Reaction procedure for the RAFT assisted synthesis of silver nanoparticle decorated PMMA microparticles in scCO ₂	342
5.4	Characterisation techniques and equipment.....	345
5.4.1	UV-Vis Spectrometry	345
5.4.2	Microtomy.....	346
5.4.3	Scanning electron microscopy (SEM)	347
5.4.4	Transmission electron microscopy (TEM)	349
5.4.5	Energy dispersive x-ray spectroscopy (EDX).....	352
5.4.6	Supercritical fluid - high pressure liquid chromatography (sc-HPLC)	354
5.4.7	Raman spectroscopy	358
5.4.8	Gel permeation chromatography (GPC)	360
5.4.9	Thermo-gravimetric analysis (TGA)	362
5.4.10	Attenuated total reflectance – Fourier transform infrared spectroscopy (ATR-FTIR).....	363
5.4.11	Inductively coupled plasma atomic emission spectroscopy (ICP-AES)	364
5.5	References.....	365

Chapter 6 - Conclusions

Abbreviations and acronyms

4-ATP - 4-aminothiophenol
AFM – Atomic force microscopy
Ag(acac) - Silver (I) acetylacetonate
Ag(hfac)COD - cyclooctadiene silver(I) hexafluoroacetylacetonate
AIBN - 2,2-azobis(isobutyronitrile)
AIST - National Institute of Advanced Industrial Science and Technology
APS - 3-(aminopropyl) triethoxysilane
BSTSP – benzylsulfanylthiocarbonyl-sulfanylpropionic acid
CODPtMe₂ - Dimethyl(cyclooctadiene) platinum(II)
Cu(acac)₂ - Copper (II) acetylacetonate
Cu(hfac)₂ – Copper (II) hexafluoroacetylacetonate
Cu(tfac)₂ – Copper (II) trifluoroacetylacetonate
Cu(tmhd)₂ – Copper (II) bis(2,2,6,6-tetramethyl-3,5-heptanedionate)
CVD - Chemical vapour deposition
DCB - 1,2-dichlorobenzene
DMF – Dimethylformamide
DNA - Deoxyribonucleic acid
DVB – Divinylbenzene
EDX - Energy dispersive x-ray analysis
E_F - Fermi energy level
E_g - Band gap
FITC - Fluorescein isothiocyanate
GPC - Gel permeation chromatography
HSA – Human serum albumin
HIV - Human immunodeficiency virus
HPLC – High pressure liquid chromatography
LC – Liquid chromatography
MEF - Metal-enhanced fluorescence
MMA - methyl methacrylate
M_n – Number average molecular weight
MRI - Magnetic resonance imaging
M_w – Weight average molecular weight
Nafion[®] - tetrafluoroethylene-perfluoro-3,6-dioxo-4-methyl-7-octenesulfonic acid copolymer

NIST - National Institute of Standards and Technology
NMR – Nuclear magnetic resonance
 P_c – Critical pressure
PDI – Polydispersity index
PDMS – polydimethylsiloxane
PMMA - Poly(methyl methacrylate)
PMP - Poly(4-methyl-1-pentene)
psi – Pounds per square inch
PTFE – Poly(tetrafluoroethene)
PTFE - Poly(tetrafluoroethylene)
PVA - poly(vinyl alcohol)
PVD - Physical vapour deposition
PVP - poly (vinyl pyrrolidone)
R6G – Rhodamine 6G
RAFT – Reversible addition fragmentation chain transfer
RESS - Rapid expansion of supercritical solvents
RNA - Ribonucleic acid
scCO₂ – Supercritical CO₂
SCF – Supercritical fluid
scWHS - Supercritical water hydrothermal synthesis
SEM – Scanning electron microscopy
SERS – Surface enhanced Raman spectroscopy
 T_c – Critical temperature
 T_E – Transverse electric
Teflon[®] AF - 2,2-bis(trifluoromethyl)-4,5-difluoro-1,3-dioxole
TEM – Transmission electron microscopy
 T_g – Glass transition temperature
TGA – Thermogravimetric analysis
THF – Tetrahydrofuran
 T_m – Melting temperature
 T_M – Transverse magnetic
UHMWPE - Ultra-high-molecular-weight polyethylene
UV-vis – Ultraviolet-visible
XRD – X-ray diffraction
 δ - Kubo gap

Chapter 1: Introduction

1.1 Overview

This introductory chapter aims to provide a foundation and background covering the main aspects that are common throughout the separate projects detailed in this thesis. These underlying themes are nanoparticles and nanocomposites, polymers, and supercritical fluids.

The idea and importance of nano-scale materials will be introduced. The theory of how and why the size of nanoparticles affects their properties will be discussed, along with potential applications. The existing general synthetic strategies for the formation of nanoparticles are outlined to provide context. Polymers will be defined and some fundamental properties explained. The history and importance of the production of polymeric materials will then be reviewed before the topic of blending nanoparticles into polymeric substrates is detailed in both *in-situ* and *ex-situ* terms. The final section aims to provide an understanding of the use and properties of supercritical fluids, especially in relation to carbon dioxide, and to show how they can be used for the processing of polymers and the introduction of nanoparticles into host materials.

As the separate projects covered in this report differ substantially in some areas, this chapter provides only the briefest of introductions to some important topics. These will be expanded in greater detail in the specific chapter they relate to.

1.2 Chapter 1 - contents

1.1	Overview	12
1.2	Chapter 1 - contents.....	13
1.3	Nanoparticles.....	14
1.3.1	Properties.....	15
1.3.1.1	Catalysis.....	18
1.3.1.2	Optics and Photonics	21
1.3.1.3	Medical Application of Nanoparticles.....	37
1.3.2	General Synthetic Strategies.....	41
1.3.2.2	Solution Synthesis	42
1.3.2.3	Chemical Vapour Deposition and Physical Vapour Deposition	44
1.3.2.4	Supercritical Fluid Synthesis of Nanoparticles	45
1.3.2.5	Stabilisation	45
1.4	Polymers	49
1.4.1	Definition.....	49
1.4.1.1	Crystallinity in Polymers.....	50
1.4.1.2	The Glass Transition and Melting Point.....	52
1.4.2	History and Importance	53
1.4.3	Metal-Polymer Nanocomposites	55
1.4.3.1	<i>Ex situ</i>	56
1.4.3.2	<i>In situ</i>	57
1.5	Supercritical Fluids.....	60
1.5.1	The Discovery and Development of Supercritical Fluids.....	60
1.5.2	Supercritical CO ₂	63
1.5.2.1	Polymer Processing with scCO ₂	66
1.5.2.2	Supercritical Fluids for Nanoparticle Synthesis	69
1.5.2.3	Rapid Expansion of Supercritical Solvents (RESS).....	70
1.5.2.4	Hydrothermal Synthesis of Nanoparticles.....	71
1.5.2.5	Nanoparticles by scCO ₂ Impregnation of into Host Materials	73
1.6	Conclusions – Chapter 1.....	82
1.7	References	83

1.3 Nanoparticles

A nanoparticle is defined by the British Standards Institute as follows:¹

nanoparticle

particle with one or more dimensions at the nanoscale

nanoscale

having one or more dimensions of the order of 100 nm or less

This is in good agreement with how the term is used in general within the scientific community, although there is some degree of ambiguity as to the upper size limit. Particles and materials with smallest domain sizes up to a micrometer and even sometimes several μm are sometimes referred to as ‘nano’, although this is becoming less common with the increasing standardization of terminology in nanoscience. Figure 1 shows the nanometer domain in the context of some common microscopic objects.

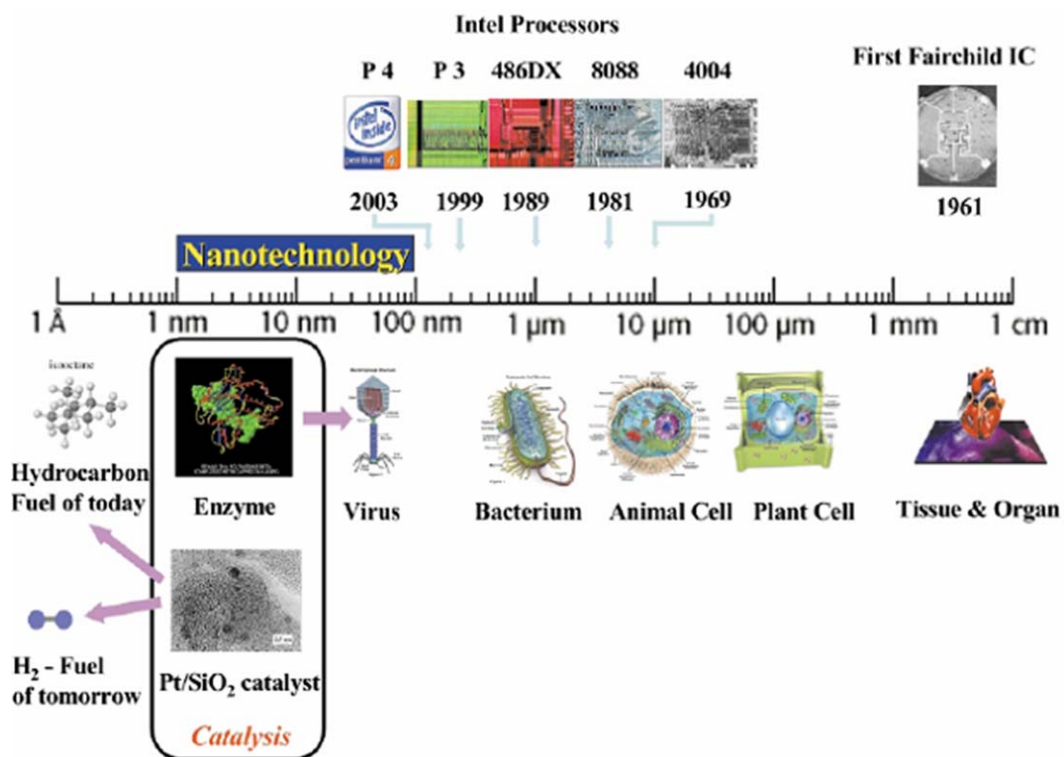


Figure 1 – The nanometer domain relative to some common architectures.²

1.3.1 Properties

Over the last three decades nanoparticles have received an increasing amount of research interest. This is due to the unique size dependent properties of nanoparticles, which are often thought of as a separate and intermediate state of matter lying between individual atoms and bulk material.³ The properties of nanoparticles arise as a consequence of the confinement of the electron wave function and of the extremely high proportion of surface atoms – both of these factors are directly dependent on the size of the nanoparticle.⁴ Indeed the possibility to control the properties, by tuning the size of the nanoparticle, has been the cause and subject of much investigation. Unlike bulk materials that have

constant physical properties regardless of mass, nanoparticles offer unique opportunities for control by varying the diameter and have manipulated electronic, magnetic and optical properties.⁵⁻⁷ These effects arise because the energy levels for small particles are not continuous, as in bulk materials, but discrete, due to confinement of the electron wavefunction. The physical properties of nanoparticles are therefore determined by the size of the particle; the relatively small physical dimension in which the wavefunction is confined (Fig. 2).

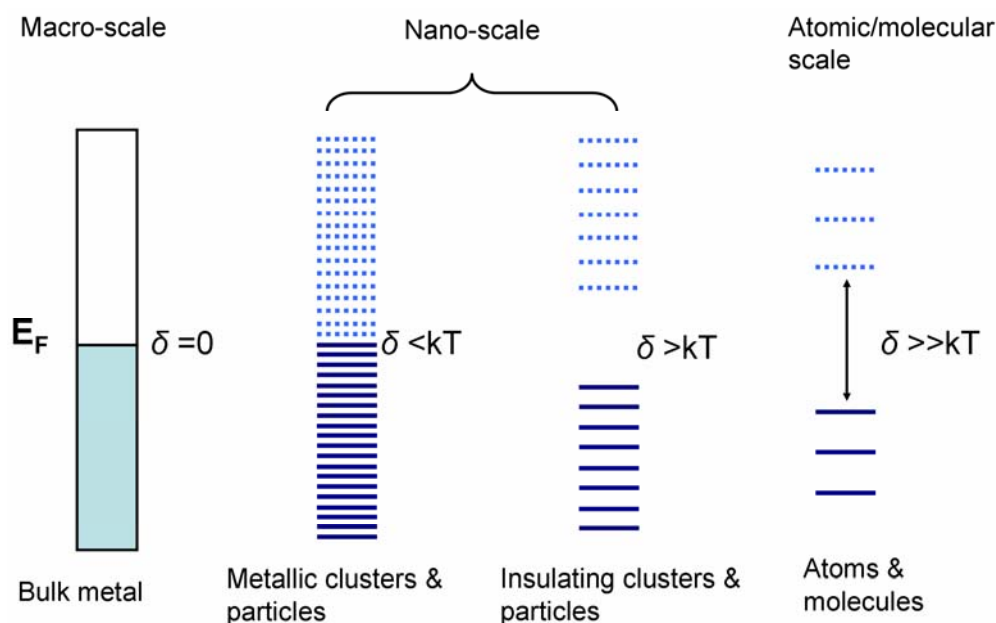


Figure 2 - The evolution of the band gap and the density of states as the number of atoms in a system increases (from right to left). E_F is the Fermi energy level of the material and δ is the Kubo gap, see below. Adapted from Roduner⁸, and the notes of Dr. Andrei Khlobystov of the University of Nottingham.

The Fermi energy level (E_F) is the highest occupied energy level of the system in its ground state (lowest energy). The band gap (E_g) of these systems is the energy gap between the highest occupied and lowest unoccupied energy states.

In these systems, from discrete atoms to bulk materials, the energy spacings are determined by the extent of the overlap between the electron orbitals of the material. Individual atoms have well known atomic orbitals. These can combine in molecules to form molecular orbitals, and further to form extended band structures, as in metals or semiconductors. The value of E_g is proportional to E_F divided by the number of delocalised electrons in the extended band structure. For a bulk metal, the number of delocalised electrons in the band structure is equal to the number of atoms in the bulk of the material. This normally results in E_g being very small, and therefore only observed at low temperature. Under normal temperature, the delocalised electrons of the metal can easily be promoted to a higher energy state, and can move freely through the structure. This gives the material its electrically conductive nature. In traditional semiconductor materials the number of delocalised electrons is significantly less than the number of atoms. This results in a higher E_g that is significant at normal temperatures. This means that in a semiconductor the electrons will not be free to move, and conduct current, without some further input of energy. Equation 1 gives the average electronic energy level spacing of successive quantum levels (known as the Kubo gap).

$$\delta = \frac{4E_F}{3n} \quad (1)$$

Equation 1: where δ is the Kubo gap, E_F is the Fermi energy level of the bulk material, and n is the total number of valence electrons in the nanoparticle

As an example, a silver nanoparticle of 3 nm diameter and approximately 1000 atoms (and therefore ~1000 valence electrons) would have a δ value of about 5-10 meV.⁴ If the thermal energy, kT , is more than the Kubo gap then the nanoparticle would be metallic in nature but if kT fell below the Kubo gap it would become non-metallic. At room temperature kT is approximately 26 meV, and therefore a 3 nm silver nanoparticle would exhibit metallic properties. However, if the size of the nanoparticle was decreased, or the temperature was lowered, the nanoparticle would show non-metallic behavior. Using this theory, and a Fermi energy for bulk silver of 5.5 eV, then silver nanoparticles should cease to be metallic when under ~280 atoms, at room temperature. Because of the Kubo gap in nanoparticles, properties such as electrical conductance and magnetic susceptibility exhibit quantum size effects. These effects have led to nanoparticles being used for many applications from catalysis⁹⁻¹⁸ to optics¹⁹⁻²⁸ and medicine.²⁹⁻³³

1.3.1.1 Catalysis

The efficiency of materials already used as catalysts would be expected to be higher for nanoparticles than other solid substrates even by conventional theory. This is simply because nanoparticles have a much larger proportion of atoms in active surface sites compared to larger objects (see Fig. 3). Nanoparticles are so close in size to atomic dimensions that an unusually high fraction of the atoms are present on the surface. It is possible to estimate this fraction by using the simple relation shown in equation 2.

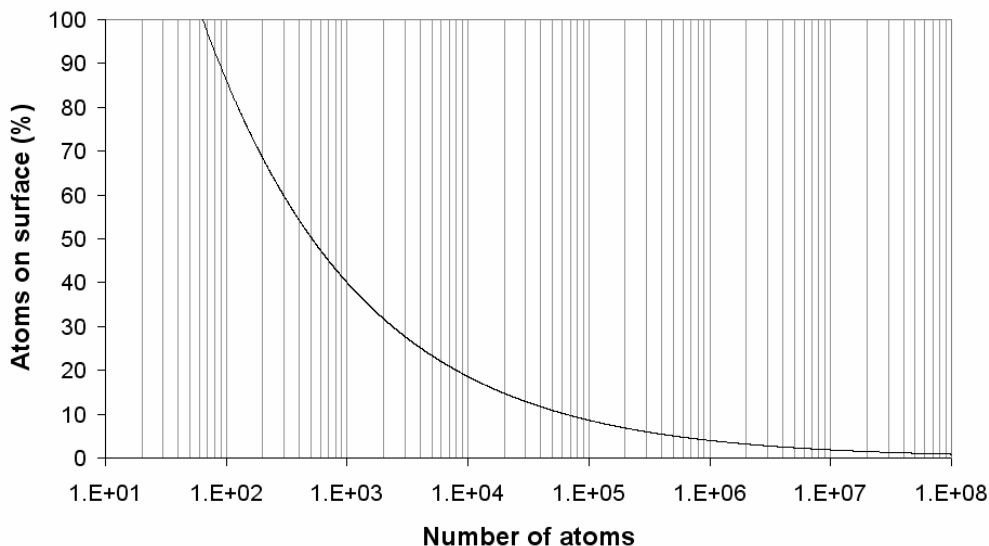


Figure 3 – A plot of the total number of atoms in a particle vs. the percentage of those atoms that are located at the surface of the particle, derived from equation 2.

$$P_s = 4N^{-1/3} \times 100 \quad (2)$$

Equation 2: where P_s is the percentage of atoms at the surface and N gives the total number of atoms in the particle³⁴

A nanoparticle with 13 atoms in closed shell configuration has 12 atoms on the surface and only one enclosed. The 3 nm silver nanoparticle we used in a previous example would contain approximately 1000 atoms.⁴ We can therefore estimate that it would have ~ 40 % of the total number of atoms on the surface. A particle 150 nm in diameter would contain approximately 10^7 atoms with less than 1 % of its atoms in surface locations. As heterogeneous catalysis occurs only at the surface of the metal being used, it is obvious to see why the use of nanoparticles is so desired to make optimum use of often expensive catalytic metals.

Aside from these simple surface/volume effects, there are changes in the reactivity of nanoparticles arising from the quantum confinement effect. This

qualitative change in the electronic structure can give rise to unusual catalytic properties in the nanoparticles that are quite different from the behaviour of the bulk material. Photoemission spectroscopy investigations have shown that the electronic structure of metal clusters smaller than approximately 5 nm is different from that of the bulk metal.¹² The small number of atoms involved in the formation of the electron bands results in a greater localization of the valence electrons, and in a smaller width of the valence band.^{35, 36} The altered electronic structure and the force towards the centre generated by the surface curvature of small metal nanoparticles gives rise to a significant contraction of the lattice compared to the bulk material.³⁷ In turn, the smaller lattice constant is responsible for a shift of the centre of the d-band to higher energies, which generally enhances the reactivity of the surface towards adsorbates.

There is also a dramatic increase in the number of edge and corner sites in the metal lattice – and these can react quite differently to the flat metal surface in terms of catalysis properties. The enhancement of the reactivity of low-coordination defect sites can be so large that their presence determines to a very large extent the catalytic activity of a material, in spite of their very low concentration.¹² Gold provides an excellent example of a material that behaves markedly differently in the form of nanoparticles. Perhaps the largest breakthrough in nanoparticle catalysis was the work done by Haruta on gold nanoparticle catalysed CO oxidation by O₂ at low temperatures.^{15, 16, 38} Gold is very popular for being chemically inert. It is indeed one of the most stable metals in the group 8 elements, and it is resistant to oxidation. The discovery by Haruta et al. that gold

nanoparticles supported on Co_3O_4 , Fe_2O_3 , or TiO_2 were highly active catalysts for CO and H_2 oxidation, NO reduction, water-gas shift reaction, CO_2 hydrogenation, and catalytic combustion of methanol was therefore a surprise, and considered important by the chemical community.¹³ Smooth surfaces of metallic gold do not adsorb CO, and this is necessary for catalysis at room temperatures.³⁹ CO is instead only adsorbed at corner, step, and edge sites, indicating that smaller metallic gold nanoparticles are preferable.⁴⁰

Nanoparticles of a large range of transition metals and metal oxides have been found to exhibit advantageous size dependent catalytic properties and are being investigated intensively.⁴¹⁻⁵⁰ The shape,⁵¹⁻⁵³ coordination and stabilization⁵⁴⁻⁶⁰ of these nanoparticles has been found to affect the catalysis and is therefore also the subject of much current research. As with many other applications of nanoparticles, catalysis often requires a suitable support/substrate for the nanoparticles. This should ideally provide a convenient means to utilize the nanoparticles, while protecting them from aggregation and allowing simple recovery. There is therefore currently much interest in finding effective methods of producing supported nanoparticle catalytic materials using substrates such as inorganic oxides; alumina,⁶¹⁻⁶⁴ silica⁶⁵⁻⁷¹ and titania,⁷²⁻⁷⁴ as well as polymers.⁷⁵⁻⁷⁸

1.3.1.2 Optics and Photonics

Nanomaterials interact with light differently from the bulk material. Materials in the nano size-range are of dimensions that are comparable to, or smaller than, the wavelength of light. If a material is of dimensions close to the

wavelength of light, and is surrounded by a substance of different refractive index, then light of appropriate wavelength will be scattered. The specific wavelength of light that is scattered is dependent on the thickness of the scattering phase. It is this effect that causes oil stretched thinly across the surface of water to produce rainbow colours. This effect has been used in optical materials known as photonic crystals, which are designed with phases of different refractive indices and specific dimensions and architectures intended to produce a desired interaction with light.⁷⁹⁻⁸¹

In the case of materials in which the separate phase is significantly smaller than the wavelength of light, this effect does not occur. Instead the two phases behave as a single material with respect to the transmitted light. Therefore, transparent materials with embedded nanoparticles may still remain transparent to light even if the material the nanoparticles are formed from is opaque or reflective. Composites, transparent materials and inorganic particles in the micrometer range, on the other hand, are often opaque. The light scattering, which is responsible for the opacity, is suppressed either by using materials with nearly matching refractive indices or by decreasing the dimensions of the filler to a range below *ca.* 50 nm.⁸² Therefore, nanocomposites with embedded nanoparticles can act as homogeneous materials with modified properties. Instead of scattering light, a merging of the refractive indices of the nanoparticles and host material takes place. Nanoparticles with a high refractive index can be dispersed in a glass or polymer to increase the effective refractive index of the medium. This approach is helpful in producing

optical waveguides where a higher refractive index leads to better beam confinement.⁸³

Nanoparticles of conducting and semiconducting materials interact directly with light through a different mechanism. It is because of this property that these nanoparticles are often added to an optical substrate to perform a desired function. Conducting metallic nanoparticles interact with light via an effect known as plasmon resonance, arising from the delocalised cloud of electrons associated with the particle. Semiconductor nanoparticles, often known as ‘Quantum dots’, interact with light according to exciton mechanisms modified by the quantum confinement effect. These will be dealt with separately. Quantum dots will only be described briefly as they are not directly relevant to this study, but are included for comparison.

Quantum Dots

The most significant electronic effect in semiconductor nanoparticles is the widening of the gap between the highest occupied electronic states (at the top of the original valence band) and the lowest unoccupied states (the bottom of the original conduction band). This occurs through quantum confinement because of the small dimensions of the particle,⁸⁴ which directly affects the optical properties of semiconductor nanoparticles as compared to the bulk material. The minimum energy needed to create an electron-hole pair in a semiconductor nanoparticle (an “exciton”) is defined by its band gap (E_g). Light with energy lower than E_g cannot be absorbed by the nanoparticle, the onset of absorption is also size dependent. As the size decreases the absorption spectra for smaller nanoparticles are shifted to

shorter wavelengths, i.e. the gap increases in size, with respect to larger nanoparticles or the bulk material.⁸⁵

Excitons in semiconductors have a finite lifetime because of recombination of the photo-excited electron-hole pair. In semiconductor nanoparticles, the energy released by this recombination is too large to be dissipated by vibrational modes. Instead it is emitted in the form of a photon of appropriate energy.³ The energy for this fluorescence is centred at a value smaller than the energy required to generate the exciton. If a narrow size distribution of quantum dots can be obtained, then a wide range of colours can be produced, even for the same semiconductor material.⁸⁶ Figure 4 shows the different colours and fluorescence spectra of a series of cadmium-selenium semiconductor nanoparticles in solution.⁸⁷

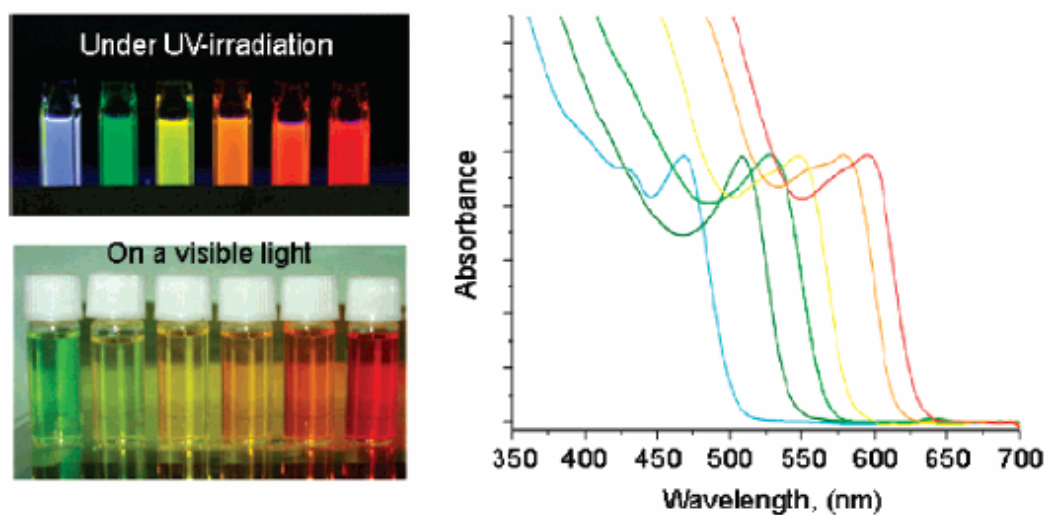


Figure 4 – A range of CdSe quantum dots in chloroform. Size was controlled by synthesis-time and temperature. Diameters (from TEM) are 2.1, 2.5, 2.7, 3.1, 3.8, and 4.2 nm from left to right.⁸⁷

Plasmons

Metallic nanoparticles can have absorption spectra with an absorption peak that looks similar to that of semiconductor nanoparticles. However, this absorption does not derive from transitions between quantized energy states, instead, in metal nanoparticles, collective modes of motion of the electron cloud can be excited.³ Under the influence of an electrical field, there is a plasmon excitation of the electrons at the particle surface. This resonance takes place at a certain frequency of incident light and results in an optical absorption.⁴ These are referred to as surface plasmon,⁸⁸⁻⁹⁰ or also as plasma resonance absorption, or localized surface plasmons.

As particle size decreases, the conduction electrons begin to interact with the boundary of the particle.⁹¹ A metal-dielectric boundary on the nanoscale produces considerable changes in the optical properties, making them size and shape dependent.⁶ When a metallic nanoparticle is irradiated by light, the electric field of the incident light induces a coherent oscillation of the conduction electrons²⁸ (see Fig 5). For nanoparticles significantly smaller than the wavelength of the light, absorption is within a narrow wavelength range, a plasmon band.

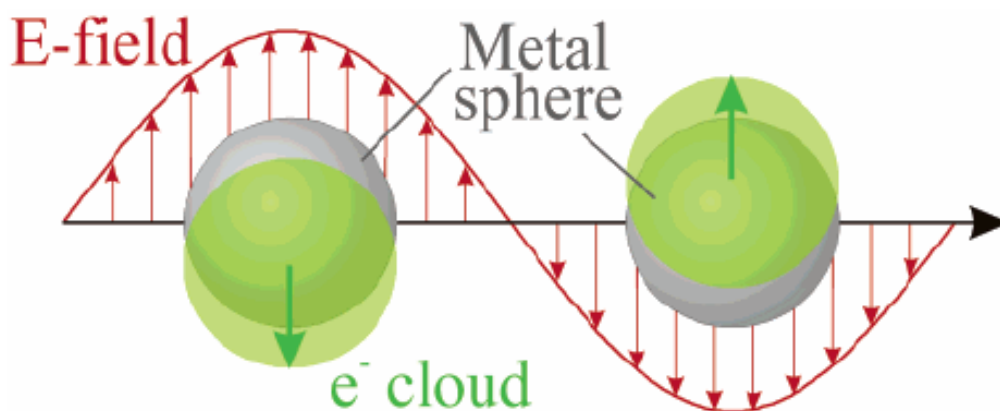


Figure 5 - Schematic of plasmon oscillation for a sphere, showing the displacement of the conduction electron charge cloud relative to the nuclei. Reproduced from Kelly *et al.*²⁸

The width, position, and intensity of the plasmon interaction displayed by nanoparticles depend on:^{4, 6, 28, 92, 93}

- The dielectric functions of the metal and the host material.
- Particle size and shape.
- The interface between the particle and the host.
- The distribution of particles within the host.

Because of the influence of these factors, a desirable amount of control over the final properties of the material is possible, provided that an equal amount of control is possible in modifying the factors themselves. Different metals produce different light-interactions and therefore colours. The extinction of light by metal nanoparticles occurs by both scattering and absorption mechanisms, but absorption is by far the dominant factor for nanoparticles of small size (<20 nm). Nanosized metal particles have long been used for colouring glass from Roman times and through the middle ages in church windows. Although this particular application

of nanoparticles may have been unintentional, small nanoparticles were often used to create glass with, ruby red Au and lemon-yellow Ag nanoparticles.⁹⁴

Today most of the use and study focuses on gold and silver nanoparticles because they exhibit the most pronounced plasmon effects, and both have absorptions in the visible spectrum. Increasing the size of the particles, or increasing the dielectric constant of the medium, causes a red shift in the plasmon absorption.⁶ However, it must be noted that the effect of nanoparticle size, though still significant, is considerably less dramatic than that observed in quantum dots. The absorption peak position in quantum dots is shifted markedly for a change in diameter of only fractions of a nanometer. For metal nanoparticles the shift in peak position is minimal for small particles (<25 nm for gold), although a broadening does take place. For larger metal particles (>25 nm for gold) the red shift of the plasmon resonance position is more significant.⁶ Figure 6 shows the effect of the diameter of gold nanoparticles on the position of the plasmon resonance absorption.⁹⁵ If the particles are distorted in shape, then the plasmon band splits into different modes corresponding to the different aspects of the electron oscillations. For example, in a nanorod-shaped metallic nanoparticle, the plasmon band splits into two bands corresponding to oscillation of the free electrons along (longitudinal) and perpendicular (transverse) to the long axis of the rod. The transverse mode resonance is close to that observed for spherical particles, but the longitudinal mode is red-shifted, dependent on the aspect ratio of the nanorod.^{6, 93} An example of this effect is displayed in figure 7, which shows the plasmon resonance absorptions of gold nanorods.

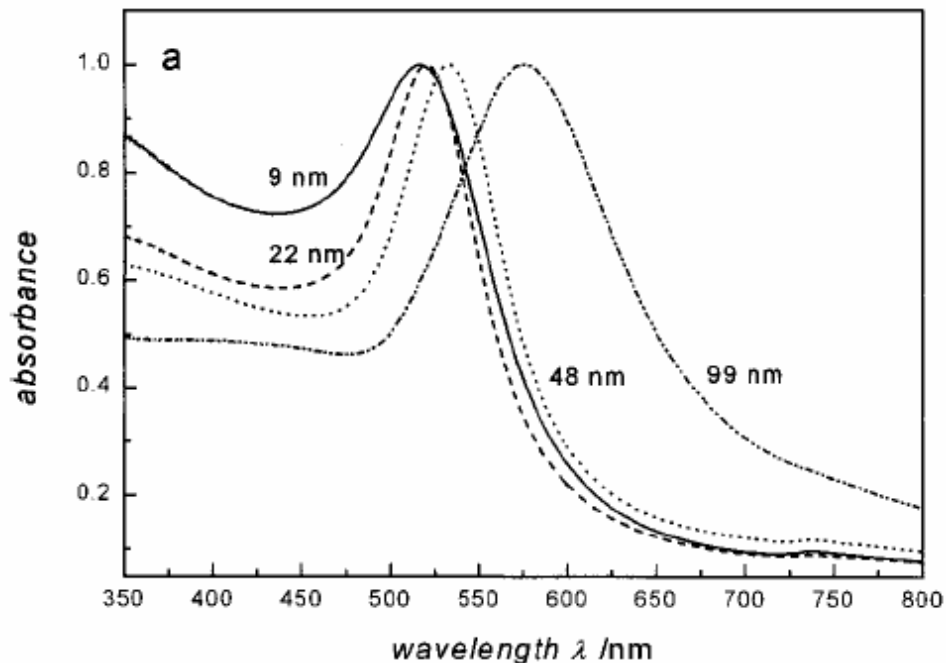


Figure 6 - The effect of particle size on the UV-vis absorption spectra of colloidal solutions of gold nanoparticles. Note the red shift as the size increases. Reproduced from Link and El-Sayed.⁹⁵

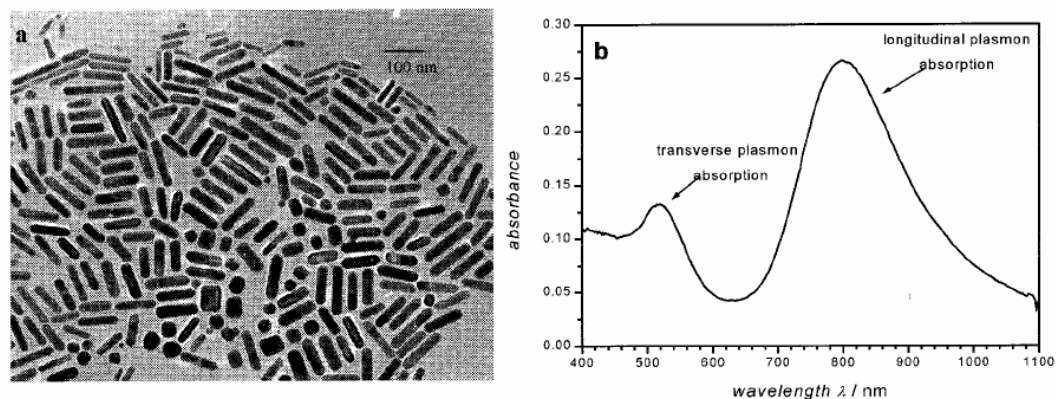


Figure 7 – a) Gold nanorods of aspect ratio 4:1. Note the 100 nm scale bar in the upper right corner. b) The plasmon resonance absorptions of these gold nanorods. Note the splitting of the plasmon band into two distinct peaks. Reproduced from Link and El-Sayed.⁹³

Metal nanoparticles of this nature, intended for use in optical or photonic applications, are often embedded into a host material such as an appropriate polymer or glass. The incorporation of metal nanoparticles into optical substrates

allows the construction of devices to utilise their advantageous properties. The host matrix not only forms the structure of the device, but also protects the nanoparticles and prevents agglomeration. There are widespread uses for these emerging materials especially in optical and photonic applications including: eye and sensor protection,⁹⁶ optical communications,⁹⁷ optical information processing,⁹⁸ Raman enhancement materials,⁶ optical switching,^{99, 100} plasmon waveguides,^{92, 101} light stable colour filters,^{102, 103} polarisers,¹⁰⁴ and modified refractive index materials.⁸²

Silver nanoparticles were singled out as the optimum choice of optically active nanoparticles for use in the research reported in this thesis. Although silver and gold nanoparticles share many similar properties and applications, suitable silver feed-stocks remain considerably more economically viable. Also silver represents the material with the most, and more general, applications. The reason for the considerable interest in the use of silver nanoparticles can best be summarised by quoting the following statement from Evanoff and Chumanov, 2005:

Of the three metals (Ag, Au, Cu) that display plasmon resonances in the visible spectrum, Ag exhibits the highest efficiency of plasmon excitation. Moreover, optical excitation of plasmon resonances in nanosized Ag particles is the most efficient mechanism by which light interacts with matter. A single Ag nanoparticle interacts with light more efficiently than a particle of the same dimension composed of any known organic or inorganic chromophore. The light-interaction cross-section for Ag can be about ten times that of the geometric cross-

*section, which indicates that the particles capture much more light than is physically incident on them. Silver is also the only material whose plasmon resonance can be tuned to any wavelength in the visible spectrum.*⁹⁴

From this statement the obvious advantages of silver, and the reason for its choice as a model nanoparticle for the novel synthesis of nanocomposite materials, is clear. Silver nanoparticles have many applications, three major opportunities of these are outlined briefly below to demonstrate how these strong plasmon interactions can be utilised.

Non-Linear Optical Limitation

Many applications of optical composites of silver or gold nanoparticles derive from their potential as optical limiters. This arises from their nonlinear susceptibility near the surface plasmon frequency with picosecond response time.¹⁰⁵ Optical limitation is the decrease in absolute transmittance of a material as incident light fluence (energy per unit area) increases. Optical limiting materials have received considerable attention as a result of a growing need for optical sensor protection. The advance of optical detection systems for applications such as signal acquisition and night vision demands the development of protective devices, such as passive optical limiters, so that highly sensitive detectors can survive undesired high-intensity signals. Also, the ever increasing use of lasers calls for more versatile and improved forms of eye protection.^{27, 100} An ideal optical limiter should display the capability of being transparent at low fluences of incident light, and opaque at high fluences.⁹⁶ It should also be capable of switching back and forth between these two states in quick response to external optical

signals. However, most materials do not possess such an unusual property, instead they often become more transparent under a strong light signal owing to the depletion of the electronic ground state. Silver nanoparticles, on the other hand, have been found to function as optical limiters by reverse saturable absorption. Although the exact mechanism is not understood, the basis must be the promotion of electrons from a weakly absorbing ground state to a more strongly absorbing excited state. It has been proposed that this behaviour is the result of photo-induced intraparticle charge separation leading to strong free carrier absorption.¹⁰⁰ While most metal nanoparticles exhibit a weak optical limitation, it has been found to be particularly strong for gold and silver.²⁷

Sun *et al*¹⁰⁰ prepared a stable suspension of silver nanoparticles and compared the optical limitation effects to similar suspensions of C₆₀ and chloroaluminium phthalocyanine, which are normally considered as benchmark materials for high performance optical limitation. The silver nanoparticles were found to be significantly more effective (Fig. 8). This study, as well as more recent research,¹⁰⁶ shows the great potential of silver nanoparticles for use in optically limiting devices, especially if they can be effectively incorporated into transparent polymer supports.¹⁰⁷

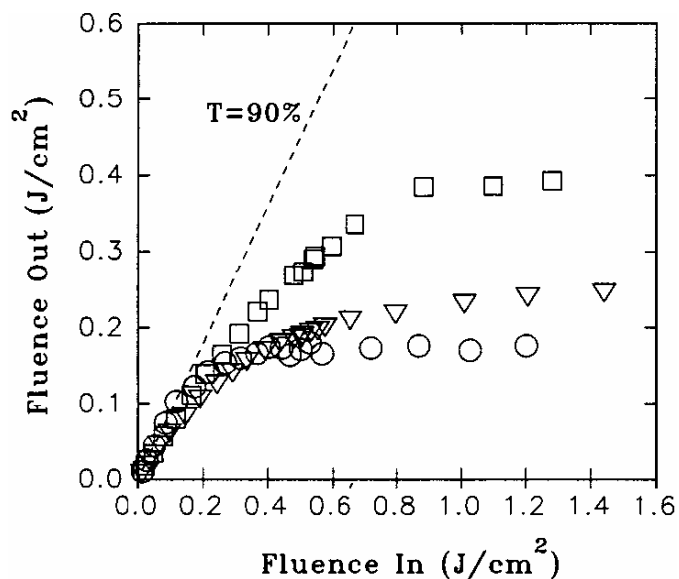


Figure 8 – Optical limiting responses of silver nanoparticles in polymer stabilised ethanol suspension (○) of 90 % linear transmittance are compared with those of C₆₀ in toluene (□) and chloroaluminium phthalocyanine in DMF (▽).¹⁰⁰

Surface Enhanced Raman Spectroscopy

The main spectroscopies employed to detect vibrations in molecules are based on the processes of infrared absorption and Raman scattering. They are widely used to provide information on chemical structures and physical forms, to identify substances from the characteristic spectral patterns (‘fingerprinting’), and to determine quantitatively or semi-quantitatively the amount of a substance in a sample. Samples can be examined in a whole range of physical states and the techniques are very wide ranging and provide solutions to a host of analytical problems. Raman scattering is less widely used than infrared absorption largely due to problems with sample degradation and fluorescence. However, recent advances in instrument technology have simplified the equipment and reduced problems substantially. These advances, together with the ability of Raman

spectroscopy to examine aqueous solutions and samples inside glass containers without any preparation, have led to a rapid growth in the application of the technique.¹⁰⁸

Raman spectroscopy is used to study vibrational, rotational, and other low-frequency modes in a system. It relies on inelastic scattering, or Raman scattering of monochromatic light, usually from a laser in the visible, near infrared, or near ultraviolet range. The laser light interacts with phonons (quantized modes of vibration) or other excitations in the system, resulting in the energy of the laser photons being shifted up or down. The shift in energy gives information about the vibrational modes in the system. Infrared spectroscopy yields similar, but complementary information. Typically, a sample is illuminated with a laser beam and light from the illuminated spot is collected with a lens and sent through a monochromator. Wavelengths close to the laser line, due to elastic Rayleigh scattering, are filtered out while the rest of the collected light is dispersed onto a detector. For a more detailed description of this technique please refer to Chapter 5.4.7.

Surface Enhanced Raman Spectroscopy (SERS) - uses silver or gold nanoparticles or a substrate containing silver or gold. The surface plasmon resonances of silver and gold are easily excited by the laser, and the resulting enhanced electric fields around the nanoparticles cause other nearby molecules to become Raman active. The result is amplification of the Raman signal, making it possible to detect very small concentrations of analytes. The essential physics which underlies the electromagnetic mechanism can be explained by referencing

the model of a metal sphere in an external electric field.¹⁰⁹ Thus, for a spherical particle whose radius is much smaller than the wavelength of light, the electric field is uniform across the particle and the electrostatic (Rayleigh) approximation is a good one. The field induced at the surface of the sphere is related to the applied, external (laser) field by equation 3:

$$E_{induced} = \{[\epsilon_1(\omega) - \epsilon_2] / [\epsilon_1(\omega) + 2\epsilon_2]\} E_{laser} \quad (3)$$

Equation 3: Where $\epsilon_1(\omega)$ is the complex frequency dependent dielectric function of the metal and ϵ_2 is the relative permittivity of the surroundings.

This function is resonant at the frequency for which $(\epsilon_1) = -2 \epsilon_2$. In other words, for frequencies where the dielectric function of the metal is close to twice the negative of the relative permittivity of the substrate, the induced field will be at a maximum. Excitation of the surface plasmon greatly increases the local field experienced by a molecule adsorbed on the surface of the particle. A very physical way to visualize this phenomenon is to consider the particle as having localized the plane wave of the light as a dipole field centred in the sphere which then decays with the dipole decay law away from the surface in all directions. The particle not only enhances the incident laser field but also the Raman scattered field. It acts as an antenna which amplifies the scattered light intensity. It is easy to see why small increases in the local field produce such large enhancements in the Raman scattering; the overall enhancement scales roughly as E^4 ! The reason that the SERS effect is so pronounced is because the field enhancement occurs twice.

Initially, the field enhancement magnifies the intensity of incident light which will excite the Raman modes of the molecule being studied, therefore increasing the signal of the Raman scattering. The Raman signal is then further magnified by the surface according to same mechanism, resulting in a greater increase in the total output signal of the experiment.

With enhancement factors of the order of 10^{14} possible, this makes SERS an extremely sensitive spectroscopic technique to the extent that applications can extend down to single molecule detection.¹¹⁰ This has created a drive to develop synthesis methods for effective metal nanoparticle based SERS materials that can be easily applied to practical analysis.

Metal Enhanced Fluorescence

Metal-enhanced fluorescence (MEF), a phenomenon where the quantum yield and photostability of weakly fluorescing species are dramatically increased, is becoming a powerful tool for the fluorescence-based applications of drug discovery, high-throughput screening, immunoassays and protein–protein detection.¹¹¹ Fluorescence has become the dominant detection/sensing technology in medical diagnostics and biotechnology. Although fluorescence is a highly sensitive technique, where single molecules can readily be detected, there is still a drive for reduced detection limits. The detection of a fluorophore is usually limited by its quantum yield, autofluorescence of the samples and/or the photostability of the fluorophores. However, there has been a recent explosion in the use of metallic nanostructures to favourably modify the spectral properties of fluorophores and to

alleviate some of these fluorophore photophysical constraints. The use of fluorophore–metal interactions has been termed radiative decay engineering, metal-enhanced fluorescence or surface-enhanced fluorescence.¹¹²

Silver nanoparticles deposited on substrates have been widely used for a variety of applications in MEF typically producing >5 fold enhancements in emission intensity, as compared to a control sample containing no silver.¹¹² Metal-enhanced fluorescence is a through space phenomenon. When fluorophores are placed within 4–10 nm of the surface of the silver nanostructures, the emission of the fluorophores is enhanced.¹¹² The increased emission intensity is a result of the metal nanoparticle increasing the local incident field on the fluorophore.

Aslan *et al*¹¹¹ reported the difference in emission from a fluorophore in the presence and absence of silver nanoparticles. A fluorophore labelled protein, fluorescein isothiocyanate – human serum albumin (FITC-HSA), was allowed to attach to the nanoparticles. The fluorescein segment was chosen to act as the fluorophore. The HSA protein was chosen for its ability to bind to silver surfaces in order to act as a spacer. The results (shown in Fig. 9) demonstrate the potential of materials like this for use in detection applications.

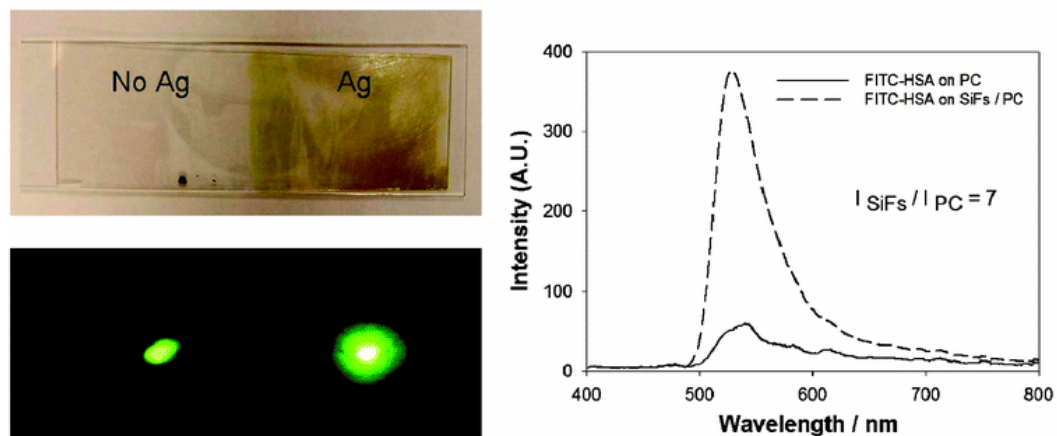


Figure 9 – Top Left: photographs of silver nanoparticle coated polycarbonate; Bottom Left: the emission of FITC-HSA on the unsilvered and silvered polycarbonate. Right: emission spectra of FITC-HSA monolayers on polycarbonate (solid line) and nanoparticle coated polycarbonate (dashed line) showing an enhanced signal.

1.3.1.3 Medical Application of Nanoparticles

Nanoparticles are being investigated for use in many varied medical applications, mostly beyond the scope of this thesis to describe. In order to provide a little insight into this field however, a few applications most relevant to the nanoparticles discussed in this report will be outlined. General near-term applications include drug delivery, improved contrast agents for imaging, fluorescence biomarkers, and chip-based nanolabs capable of monitoring and controlling individual cells. In addition, current vaccine development includes the use of nanoparticles to optimize antigen delivery to antigen-presenting cells.¹¹³ The most relevant medical applications derive from magnetic, plasmonic and antimicrobial applications of nanoparticles:

Magnetic Medical Use of Nanoparticles

Ferrous oxide is the main constituent of most magnetic particles, although metals such as cobalt and nickel are used in other fields of application. Magnetic particles are attracted to high magnetic flux density; this feature is used for drug targeting and bioseparation including cell sorting. Currently, magnetic nanoparticles are attracting attention because of their potential use as contrast agents for magnetic resonance imaging (MRI) and heating mediators for cancer thermotherapy (hyperthermia). Furthermore, a novel application of magnetic nanoparticles and magnetic force for tissue engineering, termed “magnetic force-based tissue engineering”, has been proposed, whereby magnetic nanoparticles are used to apply mechanical forces for purposes such as bone and tissue engineering.²⁹

“Quae medicamenta non sanat; ferrum sanat. Quae ferrum non sanat; ignis sanat.

Quae vero ignis non sanat; insanabilia reportari oportet” — Hippocrates.

(Those diseases which medicines do not cure, the knife cures; those which the knife cannot cure, fire cures; and those which fire cannot cure, are to be reckoned wholly incurable.)

This quote from Hippocrates (460–370 BC), who believed that most diseases could be cured by heating the patients body, suitably summarises the basic premise of magnetic nanoparticle induced hyperthermia, the use of local heating to treat cancer. Briefly, magnetic nanoparticles are brought into close contact with a tumour or cancer cells in a patient either by appropriate functionalisation of the nanoparticles, or by manually positioning the nanoparticles. Magnetic resonance

imaging can then be used to locate the nanoparticles and ensure they are in the correct position. Then finally a rapidly alternating magnetic field is used to generate heat in the nanoparticles by hysteresis loss. This heat is generated only in small and specific locations and it is able to destroy the cancer cells with minimal damage to normal healthy tissue.^{114, 115}

Plasmonic Medical use of Nanoparticles

This generally involves using silver or gold nanoparticles, chosen for their appropriate plasmonic response, non-toxicity and ease of functionalisation. The SERS Raman and MEF effects of metal nanoparticles (described above) obviously have many implications for medical use in diagnostics and detection. Another use of plasmonic nanoparticles is to specifically functionalize the surface in order to provide an interaction with a desired biological species. This can be done in order to deliver energy to the species, to trigger drug release to a specific area (by exciting the plasmon resonance), or to monitor the presence/interactions of the species by detecting changes in the plasmon resonance.^{6, 116, 117} Silver nanoparticles are now being used in this manner for the investigation of Alzheimer's disease, where they will help in screening patients for disease and possibly for studying drug interactions with target species, via detection of a pathogenic biomarker.¹¹⁸

Antimicrobial use of Silver Nanoparticles

Silver and silver salts have a long history of medical use. Silver metal has been used since ancient times to treat wounds and help preserve food. Silver salts were used extensively, especially in the form of creams and salves, as an antiseptic for the treatment of burns and wounds during the first world war. The widespread use of silver diminished significantly with the introduction of antibiotics. However, with the emergence and increase of microbial organisms resistant to multiple antibiotics, and the continuing emphasis on health-care costs, many researchers have tried to develop new, effective antimicrobial agents free of resistance and cost. Such problems and needs have led to the resurgence in the use of silver-based antiseptics that may be linked to broad-spectrum activity and far lower propensity to induce microbial resistance than antibiotics.¹¹⁹

Silver nanoparticles have been shown to have wide spectrum toxicity to both gram-positive and gram-negative bacteria, including *E-coli*.^{33, 120} They have also shown fungicidal properties and the ability to inhibit the action of viruses, including HIV,³⁰ while displaying no toxic or negative effects to human or animal cells. This has led to a host of intended antimicrobial applications of silver and silver nanoparticles, requiring the development of new synthesis routes to appropriate nanocomposite materials. Such applications include silver nanoparticle impregnated catheters,³¹ to prevent hospital infections, and silver nanoparticle impregnated water filters,³² to clean infected water and prevent disease, as well as wound dressings and silver impregnated fabrics.

1.3.2 General Synthetic Strategies

The methods of producing nanoparticles are commonly separated into two main categories, "top-down" and "bottom-up" approaches.

Top Down

The top-down method involves the systematic breakdown of a bulk material into smaller pieces using some form of grinding mechanism. This is advantageous in that it is simple to perform and avoids the use of volatile and toxic compounds often found in the bottom-up techniques. However, the quality of the nanoparticles produced by grinding is widely accepted to be poor in comparison with the material produced by modern bottom up methods. The main drawbacks include contamination problems from grinding equipment, low particle surface areas, irregular shape and size distributions and high energy requirements needed to produce relatively small particles. Aside from these disadvantages though, it must be noted that the nano-material produced from grinding still finds use, due to the simplicity of its production, in applications including catalytic, magnetic and structural purposes.¹²¹

Bottom Up

The bottom-up approach uses atomic or molecular feed-stocks as the source of the material to be chemically converted into larger nanoparticles. This has the advantage of being potentially much more controllable than the top down

approach. By controlling the chemical reactions, and the environment of the growing nanoparticle, then the size, shape and composition of the nanoparticles may all be affected. For this reason nanoparticles produced by bottom up, chemically based and designed, reactions are normally seen as being of higher quality and having greater potential for use in advanced applications. This has led to the development of a host of common bottom up strategies for the synthesis of nanoparticles.

Many of these general techniques can be adapted to be performed in gas, liquid, solid or even supercritical states, hence the applicability of bottom-up strategies to a wide range of end products. Most of the bottom up strategies require appropriate organometallic complexes or metal salts to be used as chemical precursors, which are decomposed or reduced in a controlled manner resulting in particle nucleation and growth. One of the key differences that can be used to subdivide these strategies into different categories is the method by which the precursor is decomposed or reduced. It is beyond the scope of this thesis to describe all the current and historical bottom up synthesis methods of nanoparticles, as there are a great number of variations. Instead, the most common forms of methods will be described and relevant examples given to provide a suitable overview, with specific attention being paid to silver.

1.3.2.2 Solution Synthesis

Scientific synthesis of nanoparticle solutions can be said to have started with experiments begun by Michael Faraday on gold in the mid-nineteenth

century. Deep red solutions of gold nanoparticles were produced by the reduction of chloroaurate $[\text{AuCl}_4]^-$ using phosphorus as a reducing agent. Recently these preparations were reproduced, and the diameter of the particles was shown to be $\sim 3\text{-}30\text{ nm}$.³ This is an example of chemical reduction of the metal precursor, the most common method for the generation of the nanoparticle-forming material. Other methods include thermal decomposition, and photoreduction of metal ions.

122-124

For routes in which the precursor organometallic complex or metal salt is chemically reduced, this can be accomplished using a reducing solvent such as alcohols as pioneered by Hirai and Toshima,¹²⁵ using a reducing agent dissolved or otherwise introduced into a non-reducing solvent.¹²⁶ The majority of the more straightforward approaches used for the synthesis of silver nanoparticles are based on the reduction of silver nitrate by sodium borohydride¹²⁷ or sodium citrate.¹²⁸ Hydrogen has been previously utilised as a convenient and effective reducing agent for the production of noble metal nanoparticles.¹²⁶ Indeed Evanoff and Chumanov,¹²⁹ reported a synthetic pathway to aqueous silver nanoparticles by using hydrogen acting on dissolved Ag_2O . Other, more diverse, methods of decomposing the precursor species include microwave plasma synthesis¹³⁰ (acting on AgCO_3) and electrolysis of metal salts¹³¹ (using KNO_3 and AgNO_3). In many nanoparticle synthesis routes organometallic precursors play an important role by allowing more control through tailored design,^{132, 133} i.e. by selecting appropriate ligands, the solubility and decomposition rate of the precursor can be modified.

1.3.2.3 Chemical Vapour Deposition and Physical Vapour Deposition

These methods, though consisting of many subdivisions, involve the formation of a solid from a controlled deposition of gaseous species. Both processes are commonly used, especially in the electronics industry, for coating materials with thin films, but have also been used to produce nanoparticles. Due to the nature of these processes the nanoparticles are commonly deposited onto a suitable substrate, such as an inorganic support, or with a co-deposited polymer. See section 1.4.3.2. of this chapter for more detail.⁵

Chemical vapour deposition (CVD) is a chemical process used to produce high-purity, high-performance solid materials. In a typical CVD process, the substrate is exposed to one or more volatile precursors, which react and/or decompose on the substrate surface to produce the desired deposit. Frequently, volatile by-products are also produced, which are removed by gas flow through the reaction chamber. The precursors used are volatile organometallic complexes, similar to those sometimes used in the synthesis of nanoparticles through solution methods. In CVD, precursor gases, often diluted in carrier gases, are delivered into the reaction chamber at approximately ambient temperatures. As they pass over or come into contact with a heated substrate, they react or decompose forming a solid phase which is deposited onto the substrate. Okumura *et al* used this technique to form catalytic nanoparticles of gold on inorganic substrates.¹³⁴

Physical vapour deposition (PVD) is similar, but allows the nanocomposite films to be generated more simply from the pure material/materials intended to form the nanoparticles/composite. This is achieved by thermal evaporation (by an

electron beam or resistive heating) of the starting materials to form a vapour phase. A carrier gas is then introduced to transport the evaporated metal away from the heater, towards the cool end of the reactor. As the vapour cools, nucleation occurs and liquid metal droplets form. These droplets collide, coalesce and solidify in a manner controlled by the temperature gradient, residence time and gas flow rates employed during the procedure. This is preferable to CVD as it produces no by-products. Oxygen is frequently used as a carrier gas to produce metal oxide particles.^{135, 136}

CVD and PVD coatings are usually only a few micrometers thick and are generally deposited at fairly slow rates, usually of the order of a few hundred micrometers per hour. These processes would be difficult and expensive to use on a large scale.

1.3.2.4 Supercritical Fluid Synthesis of Nanoparticles

The remaining key area of nanoparticle synthesis that must be discussed is the use of supercritical fluids. However, this is more appropriately introduced in the supercritical fluids section of this chapter after the relevant theory has been provided (see section 1.5.2.4).

1.3.2.5 Stabilisation

No matter how they may have been created, nanoparticles generally require some form of stabilisation to prevent them from coalescing, agglomerating or

aggregating – which can detrimentally affect their properties and application. Metal oxide nanoparticles are more stable, but unprotected metal nanoparticles are subject to strong attractive forces especially at short interparticle distances. The nanoparticles are attracted together by van der Waals forces and, because of their metallic lattice structure, can easily coalesce. One method of stabilising nanoparticles is simply to deposit, infuse or embed the nanoparticles into a solid substrate/host material. This matrix must, of course, be suitable for the application that the nanoparticles are intended for. However, If the nanoparticles are required for synthesis or use in solution, then other techniques must be used. The two possible routes for the stabilisation of nanoparticles in solution are electrostatic stabilisation and steric stabilisation.

Electrostatic Stabilisation

This method is often used in the more traditional routes to nanoparticle synthesis, especially for well controlled particle size distribution. Each metallic nanoparticle is surrounded by an electrical double layer, which causes repulsion between neighbouring nanoparticles. This electrical double layer forms because of the attraction to the surface of the nanoparticle of negative ions present in the solution. These negative ions are attracted to positive metal ions at the surface of the metallic lattice of the nanoparticle. This helps to stabilise and control the growth of the forming nanoparticle. The negative ions species can be by-products of the metal feedstock (the metal salt), the reducing agent, or just species present in the solution. This Coulombic repulsion between the particles caused by the

electrical double layer formed by ions adsorbed at the particle surface (e.g. sodium citrate) and the corresponding counterions is exemplified by gold sols prepared by the reduction of $[\text{AuCl}_4]^-$ with sodium citrate.¹²⁶ See Fig. 10 for a schematic representation of this process.

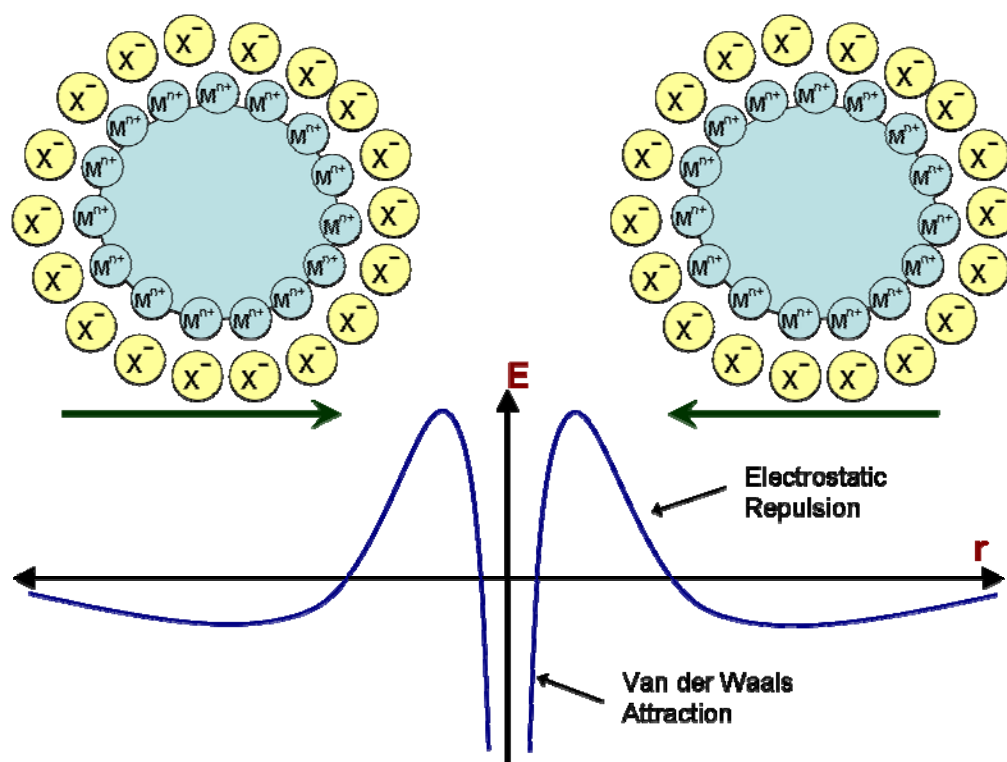


Figure 10 – Electrostatic stabilisation of metal nanoparticles. Attractive van der Waals forces are outweighed by repulsive electrostatic forces between adsorbed ions and associated counterions at moderate interparticle separation.

Steric Stabilisation

Steric stabilisation is achieved by the coordination of sterically demanding molecules such as polymers, surfactants or ligands that act as protective shields on the metallic surface. In this way, nanometallic cores are separated from each other and agglomeration is prevented¹³⁷ (see Fig. 11). This can occur because of the

electron deficient nature of the metal surface. Metal ions in the bulk of a lattice are commonly surrounded on all sides by the delocalized electrons in the structure. This leaves the metallic ions on the lattice surface, especially the curved surface of a nanoparticle, comparatively electron deficient. Therefore it is necessary for steric protecting agents to have suitable electron donating groups. These groups coordinate to the surface of the metal nanoparticle.

The main classes of protective groups are: polymers and block copolymers, usually with P, N, O and S donors (e.g. phosphanes, amines, esters/ethers, thioethers), or solvents such as tetrahydrofuran and methanol that have electron rich groups. The steric protecting agent, in order to function effectively, must not only be attracted to the nanoparticle surface, but also be adequately solvated by the dispersing fluid.

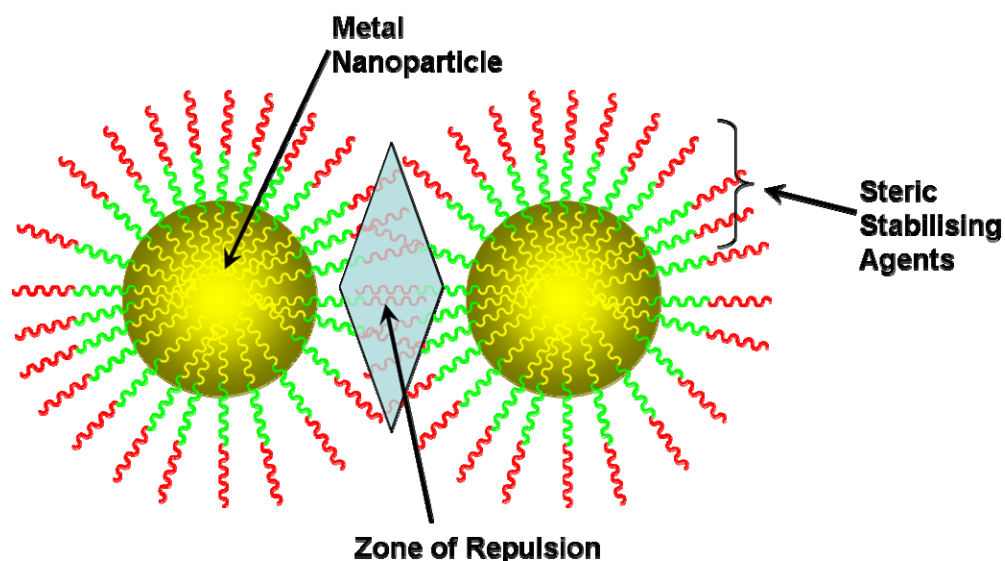


Figure 11 – Steric stabilisation of nanoparticles. Stabilising agents may be uniform or may be composed of different segments to provided separate functions, *e.g.* a nanoparticle-philic segment and a solvent-philic segment.

1.4 Polymers

1.4.1 Definition

Polymers are large molecules made up of repeating units. They are synthesised from simple monomer molecules. These monomers become linked together forming chains increasing in size from dimers and trimers to oligomers and eventually polymers with a molecular weight of at least several thousand atomic mass units or more. By changing from a monomeric to a polymeric structure, the nature of the material is greatly altered. While the monomeric substance will have been naturally liquid or even gaseous, it will become a solid or at least a viscous liquid as a polymer. This is because the polymeric chains become entangled with each other, their molecular forces of attraction to each other are greatly compounded, and the time-scale of movement of the repeating units is severely retarded.

The structure, properties and synthesis methods of the polymers that are utilized in the research detailed in this thesis will be described, where relevant, in the appropriate chapters of their use. However, it is useful to describe some general features of polymers here, such as crystallinity and glass transition, but also their history and importance as well. The production of metal nanoparticle-polymer composites will also be given a general outline in this section as it is relevant to all areas of this work. Where it is relevant in individual chapters a more detailed analysis of the previous work directly related to that chapter will be given.

1.4.1.1 Crystallinity in Polymers

The long chains that make up the structure of the polymers exist in one of two possible arrangements:

- Amorphous – chains form a randomly ordered, chaotic “mess” (like a plate of spaghetti).
- Crystalline – chains are arranged in an ordered manner (like spaghetti in a packet).

It is normal for these arrangements to co exist in the bulk of a polymer, with the proportions of each depending on the polymer in question. Most polymers are therefore described as semicrystalline (Fig. 12).

Crystallinity makes a polymer denser, more resistant to solvents and more opaque (the crystallites scatter light). The mechanical properties of a polymer are also affected by its crystallinity as well as the position of its glass transition temperature.

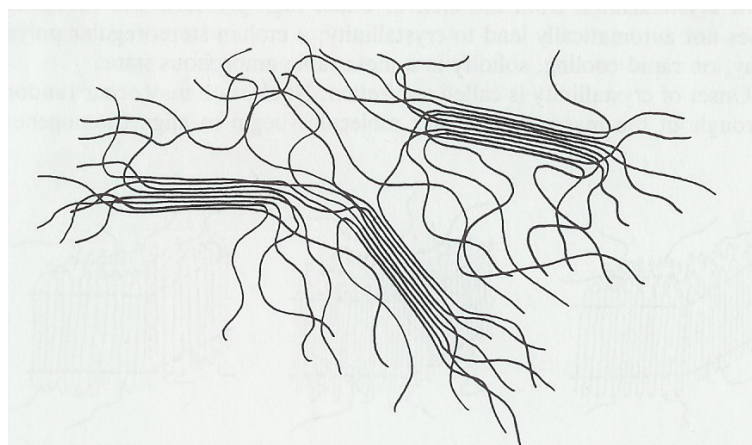


Figure 12 - Schematic of semi-crystalline polymer showing ordered crystallites separated by amorphous areas.¹³⁸

Poly(methyl methacrylate) (PMMA) provides a good example for discussing how the structure of the individual polymer chains of a polymer can determine the crystallinity of its structure. So what is it about these polymers that causes such a difference? When PMMA has an atactic structure (Fig. 13), the lack of order of the side groups prevents the chains from being able to pack together effectively, leading to a disordered, amorphous material. Isotactic PMMA, alternatively, is quite crystalline. Its ordered structure allows the polymer chains to effectively pack together into crystallites.

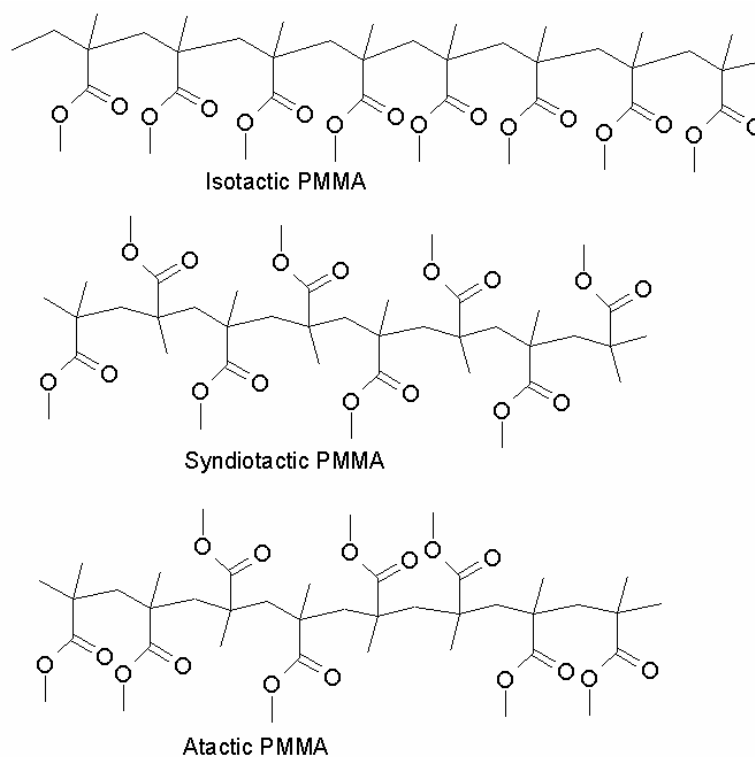


Figure 13 Possible tacticities of PMMA. Which tacticity is formed is governed by the method of polymer preparation. The free radical polymerisation mechanism commonly used allows no control over the position the side group takes, and so produces atactic PMMA.

1.4.1.2 The Glass Transition and Melting Point

The glass transition occurs at a specific temperature, T_g , that is different for each polymer. Below the glass transition temperature the polymer is hard and brittle (like glass), above it is softer and more flexible (like rubber). This glass transition is very different to melting. Melting (T_m) occurs in the crystalline part of polymers, when rigid chains in the crystals loosen, becoming a disordered liquid. The glass transition is something inherent to only the amorphous region. It is therefore normal for polymers to have both a T_g and a T_m if they possess amorphous and crystalline parts.

The position of the T_g is very important in polymer engineering and use. It governs how easy they are to process and what use they can be put to. Whether a polymer's T_g is above or below room temperature, or close to it, will affect the possible end applications of the material.

But what exactly is this transition? It is related to the amount of mobility that the polymer chains possess. Below the T_g the chains have relatively little scope for free movement, though the segments are still moving and rotating a good deal. Above the T_g the chains have gained a greater mobility, their increased thermal energy sets them moving more, creating more free volume for the polymer chains to slide past each other more easily. Because of this, if a force is applied to a polymer that is above its T_g the chains are able to move to relieve the stress, and the polymer bends. If a force is applied to a polymer that is below its T_g , the chains will be unable to move in this way, the polymer will either resist the force, or break.

1.4.2 History and Importance

Polymers have existed in natural form since the origin of living organisms, in the form of DNA, RNA, proteins and polysaccharides. These polymeric species play important roles in all plant and animal life. From the earliest recorded times, man has exploited naturally-occurring polymers as materials for providing clothing, shelter, and tools.¹³⁹ However, the origins of the polymer industry as we understand it today are far more recent, generally accepted as having begun in the early nineteenth century when important discoveries were being made concerning the modification of natural polymers.

Thomas Hancock, in 1820, discovered that natural rubber becomes more fluid, and easier to blend with additives, if it is subjected to repeated high shear forces. Later, in 1839, Charles Goodyear famously developed the process to become known as ‘vulcanisation’. This involves heating natural rubber with sulfur in order to improve its elastic properties. Cellulose nitrate was first prepared, in 1846, by Christian Schönbein and soon found application and commercial manufacture as an explosive. Later, in 1892, the ‘viscose process’ was introduced. This process consisted of dissolving and recasting cellulose to produce viscose rayon textile fibres or cellophane film.

Although the above developments marked definite advances in the semi-synthesis of materials made from natural polymers, there was still very poor understanding of the underlying structure of polymeric substances. This began to change in 1920 when Herman Staudinger published a groundbreaking paper

declaring “in high polymers many single molecules are held together by normal valency bonds. The tendency to form such compounds is observed in particular in organic chemistry because of the special nature of carbon.” Unfortunately this idea, though it did gradually win over, was met with much initial opposition. Nobel Prize winner Heinrich Wieland now humorously rebutted that “There are no organic molecules with a molecular weight greater than 5000.”¹⁴⁰ In the next few decades as this new science of macromolecules emerged, a large number of synthetic polymers went into commercial production for the first time. These polymers, which include polystyrene, poly(methyl methacrylate), nylon 6.6, polyethylene, poly(vinyl chloride), silicones, polytetrafluoroethylene, and many others, now form the backbone of the polymer industry.

Nowadays synthetic polymers have considerable commercial importance and have become an integral part of our daily lives. From the early developments to today, the breadth of polymer science has been ever increasing, and regular advances have continued to stimulate both scientific and industrial progress. The use of polymeric materials is increasing rapidly year by year in many applications as polymers are tailored to replace conventional materials such as metals, wood and natural fibres. The degree to which polymer properties can now be tailored and controlled by modification of structure, the blending of polymers, or the production of unique architectures has led to polymeric materials being designed to fill new and specific roles that no other known material could provide. It is because of this need for new functional materials that the development of new

polymeric materials is combined with the emergent field of nanotechnology via the incorporation of nanomaterials into polymers to produce novel materials.

1.4.3 Metal-Polymer Nanocomposites

The embedding of nanoscopic metals into dielectric matrices represents a solution to manipulation and stabilisation problems. For functional applications of nanoparticles, polymers are particularly interesting as an embedding phase since they may have a variety of characteristics: they can be an electrical and thermal insulator or conductor. They may have a hydrophobic or hydrophilic nature, can be mechanically hard (plastic), or soft (rubbery), and so on. Finally, polymer-embedding is the easiest and most convenient way for nanostructured metal stabilisation, handling, and application.⁴ This has fuelled investigation into the preparation of metal-polymer nanocomposites. These composites most commonly take the form of thin polymer films or powders, as this is normally the simplest structure to prepare, and also good for exploiting the desired properties. Preparation techniques can be classified as *in situ* and *ex situ* methods⁴. In the *in situ* methods the monomer is polymerised, with metal ions introduced before or after polymerisation. Then the metal ions in the polymer matrix are reduced, chemically, thermally, or by UV irradiation, to form nanoparticles. In the *ex situ* process, the metal nanoparticles are synthesised first, and their surface is organically passivated. The derivatised nanoparticles are then dispersed into a polymer solution or liquid monomer that is then polymerised. A more detailed description of some of these key techniques follows.

1.4.3.1 Ex situ

A greater overview of general nanoparticle synthesis was provided in section 1.3.2 but the methods most closely associated with ex-situ synthesis for polymer incorporation specifically, are briefly outlined here. The metal nanoparticles are prepared first, traditionally by the controlled precipitation and concurrent stabilisation of the incipient colloids. This can be done by the reduction of a metal salt dissolved in an appropriate solvent,^{4, 141-143} often containing a polymer stabiliser.^{4, 100, 137, 144} Alternatively, it can be prepared by controlled micelle, reverse micelle, or micro-emulsion reactions.^{4, 142, 145-148} The particles produced by these methods are often surface modified to prevent aggregation, either covalently by metal-thiol bonds¹⁴⁹ or by coating with a suitable polymer shell.¹⁴² These particles then need to be introduced into polymers. This is accomplished by mixing with a solution of the polymer, or monomer, which can then be spin cast *etc.* according to standard polymer processing techniques.^{4, 102} However, this method is limited by problems of dispersion. It is necessary to surface modify the particles, therefore altering their properties, in order to disperse them. Even with this step it is difficult to produce well dispersed composites, and a certain degree of aggregation remains. Also, this route is limited to compatible polymer-particle-solvent systems.

1.4.3.2 *In situ*

The *in situ* methods that have been used for the manufacture of metal nanoparticle-polymer composites consist of much more varied techniques. *In situ* methods, though often less simple and straight-forward as *ex situ*, are commonly considered to produce better quality and more controlled nanocomposite materials. An outline of the most significant methods follows.

Thermal decomposition of metal precursors added to polymers.

This represents the existing method most suited to large scale production.⁴ A number of organic precursors have been studied for this application,¹⁵⁰ but none showed completely satisfying behaviour. Recently, however, it has been discovered that homoleptic mercaptides (*i.e.* $M_x(SR)_y$) are effective in the production of metal-polymer nanocomposites.¹⁵¹ Transition metal mercaptides are covalent organic salts with a high compatibility with most hydrophobic polymers. The mercaptide is dispersed in a polymer and the polymer is then heated to 110-180 °C to decompose the mercaptide. This produces zero-valence metal or metal-sulfide nanoparticles, depending on the metal and conditions. The literature also reports similar interesting composites prepared by the inclusion of metal nitrates (*e.g.* $AgNO_3$)¹⁵²⁻¹⁵⁴ and metal salts (*e.g.* $HAuCl_4$).¹⁵⁵ In these methods organic by-products are left trapped in the polymer, and the reduction of the metal causes damage to the substrate by electron extraction. With any nanocomposites produced by this method, the precursors must be included in the

polymer *before* it is cast into a solid form. Any subsequent processing may then damage or affect the composite.

Ion implantation.

An ion beam (*e.g.* Ag⁺) of the range 30-150 keV in energy is directed at the surface of a polymer sample. As the ions enter the matrix, nuclear collisions occur, displacing atoms in the polymer matrix and breaking some of its chemical bonds. Along with this, target atoms effectively lose electrons and the implanted M⁺ ions deionise with the formation of neutral metal atoms (M⁰). It is possible in principle for metal atoms to combine with organic radicals and polymer ions. However, because of the great difference in Gibbs free energy between metal atoms and atoms of the polymer, metal-metal bonding is energetically more favourable.⁴ Though offering good control of particle size and dispersion, this method is limited to impregnating a few micrometers into the surface. Also, it can lead to the formation of carbonised shells around the metal nanoparticles. Nevertheless, it has been used for the effective synthesis of metal-polymer nanocomposite materials including PMMA-Ag nanocomposites.^{156, 157}

Chemical vapour deposition (CVD) and physical vapour deposition (PVD).

These methods were described in section 1.3.2.3 in terms of the synthesis of metal nanoparticles by deposition on existing substrates. However, they can also be effectively used for the simultaneous synthesis of metal nanoparticles and a

polymer substrate. This forms the nanoparticles inside the polymer substrate with a good deal of control on the structure of the composite produced being possible. By controlling the flows of the two feedstocks the nanocomposite can be made continuous, gradated or layered *etc.* Monomers, often in the form of ionized monomer plasma, and organometallic complexes are used together as the precursors to react and form a polymeric nanocomposite. PVD is similar, but allows the nanocomposite films to be generated more simply by thermally evaporating the pure polymer and metal intended to form the composite.

scCO₂ Impregnation into Polymers.

Supercritical fluid methods for the generation of metal nanoparticles in solid polymers by infusing precursor complexes, subsequent to their reduction, are outlined in section 1.5.2.4. The advantages of the scCO₂ method are many. It is a green process, avoiding the use of toxic and harmful solvents as well as the problems of their removal. It allows the modification of polymers which are difficult to process by normal methods. It has promising potential for effective and economical scale-up. Importantly, it allows the production of pure, non-surface-coated nanoparticles, without leaving any trapped by-products in the polymer. It would also allow pre-fabricated polymeric materials to be impregnated with nanoparticles after they had been processed into their final form, which avoids detrimental aggregation of the nanoparticles during processing.

1.5 Supercritical Fluids

1.5.1 The Discovery and Development of Supercritical Fluids

Supercritical fluids are useful because they possess both liquid-like and gas-like properties. The critical point of a substance was first discovered and defined by *Baron Charles Cagniard de la Tour* in 1822. His experiments proved the existence of supercritical fluids by heating various solvents sealed within metal cannons. By observing the changes in solvent acoustics *de la Tour* was able to identify the existence of a “new” single phase, rather than the two separate liquid and gas phases.¹⁵⁸

This initial discovery sparked subsequent investigations, and in 1869 Dr. Thomas Andrews reported the critical parameters of carbon dioxide and illustrated the phases by constructing the first supercritical phase diagram.¹⁵⁹ In 1879, at a *Royal Society* meeting, *Hannay* and *Hogarth* reported the ability of certain compressed gases to dissolve salts such as cobalt chloride, potassium iodide and potassium bromide. This was previously thought to be impossible.¹⁶⁰ In summary:

“We have the phenomenon of a solid dissolving in a gas, and when the solid is precipitated by reducing the pressure, it is brought down as a “snow” in the gas or on the glass as a “frost,” but it is always easily redissolved by the gas on increasing the pressure.”

These initial investigations lead onto further work and the eventual definition of a supercritical fluid by Darr and Poliakoff as “any substance, the temperature and pressure of which are higher than their critical values, and which has a density close to or higher than its critical density.”¹⁶¹ This is best explained with reference to a phase diagram (Fig.14). Similar to gases, SCFs possess high diffusivities, important for reaction kinetics, while also having liquid-like densities that allow them to act as effective solvents for many compounds. Small changes in pressure and temperature can be used to “tune” the density of a supercritical fluid and therefore its solvating ability, hence giving increased control of reactions.

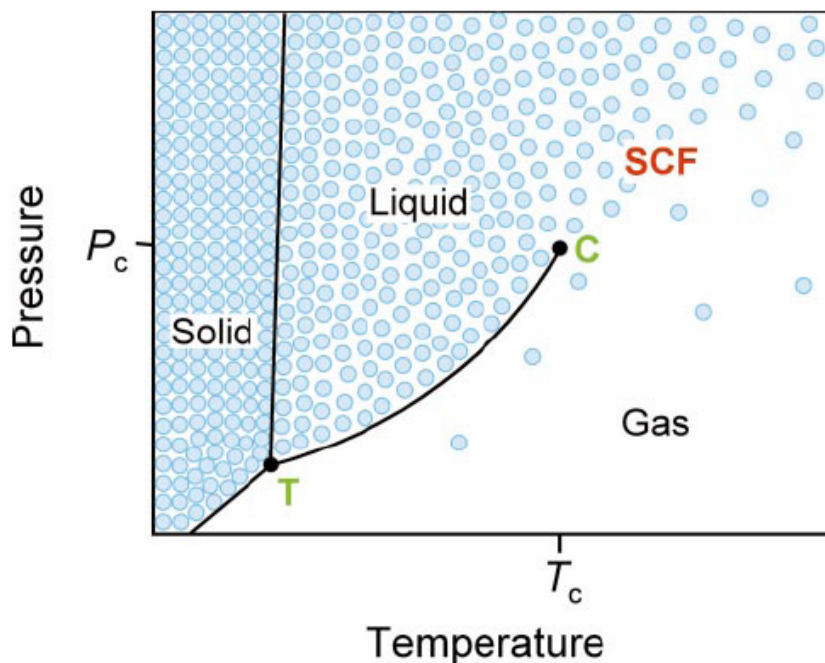


Figure 14 - Schematic pressure-temperature phase diagram for a pure component showing the supercritical fluid (SCF) region. The triple point (T) and critical point (C) are marked. The blue circles show the density variation of the substance in the different regions of the phase diagram. Note that the density varies continuously between the liquid state and the gas state, providing that the liquid-gas equilibrium line is not crossed.¹⁶²

Supercritical fluids are unique solvents with a wide range of interesting properties. They can be clean and versatile, capable of processing a wide variety of materials. An increasing drive for greener processes in chemistry and industry in the 1970's led to a move towards the wider use of SCFs as alternative reaction media, *e.g.* for extraction and separation processes.¹⁶³ This marked the need for a move away from volatile organic compounds and ozone-depleting substances such as chlorofluorocarbons, which are often used as processing solvents. Many of these traditional solvents are not only environmentally harmful but often hazardous and toxic to humans, with high costs of waste removal.

The critical temperatures and pressures of a range of common substances, along with the associated critical point density, are shown in the table below:

Table 1 – Critical parameters for selected substances.¹⁶² Critical density is given as the density the substance possesses at the conditions given.

Substance	T _c / °C	P _c / bar	ρ _c / g cm ⁻³
CH ₄	-82.5	46.4	0.16
C ₂ H ₄	10.0	51.2	0.22
C ₂ F ₆	19.9	30.6	0.62
CHF ₃	26.2	48.5	0.62
CClF ₃	28.9	38.6	0.58
CO ₂	31.1	73.8	0.47
C ₂ H ₆	32.4	48.8	0.20
SF ₆	45.6	37.2	0.73
Propylene	91.9	46.1	0.24
Propane	97.2	42.5	0.22
NH ₃	132.5	112.8	0.24
Pentane	187.1	33.7	0.23
¹ PrOH	235.4	47.6	0.27
MeOH	240.6	79.9	0.27
EtOH	243.5	63.8	0.28
¹ BuOH	275.1	43.0	0.27
Benzene	289.0	48.9	0.30
Pyridine	347.1	56.3	0.31
H ₂ O	374.2	220.5	0.32

1.5.2 Supercritical CO₂

CO₂ in particular has received much attention as a supercritical fluid, and is probably the most widely used. The choice of which supercritical fluid is used for chemical and industrial processes must be determined by a compromise of practical factors. Supercritical processes have associated costs arising from the need for high pressure equipment, and therefore solvents with more easily reached critical points will lower this cost, but this must be offset by the financial cost of the solvent, ease of handling, solvent reactivity and safety factors.

CO₂ has relatively easily accessible critical points of 31.06 °C and 1070 psi (7.38 MPa) and tuneable density, as well as a high diffusivity, making it a promising reaction medium for organic compounds.¹⁶⁴ There are of course other substances which share these properties. However, many of them have considerable disadvantages not present for scCO₂. Most of the organic solvents suitable for supercritical applications are flammable, often dangerously so. They also tend to have potentially harmful effects to health and the environment. CO₂ is non-combustible and non-toxic as well as being relatively environmentally benign. It is also easily available as it is naturally occurring as well as being the by-product of many industrial processes, such as the burning of fossil fuels for power. As a consequence of this, both high quality and low quality stock can be easily obtained, meaning that CO₂ is relatively inexpensive and financially desirable as a reaction medium. Water also shares some of these advantages of non-toxicity and availability. However, high critical parameters and corrosion problems with metal equipment impede its wider application.

As CO₂ is a gas at ambient temperatures and pressures it can be easily removed, leaving no solvent residues in the processed material.¹⁶⁵ The ease of its removal contrasts with the high energy-costs of drying for the removal of conventional solvents. In small-scale reactions the CO₂ contribution to green house effects will be negligible, but for larger scale processes CO₂ can be easily recycled back into the reaction system.

The density of scCO₂ in a range of temperatures and pressures is shown in figure 15. It is this easily tunable density, and consequently solvent strength, that allows facile control of reactions and processes.

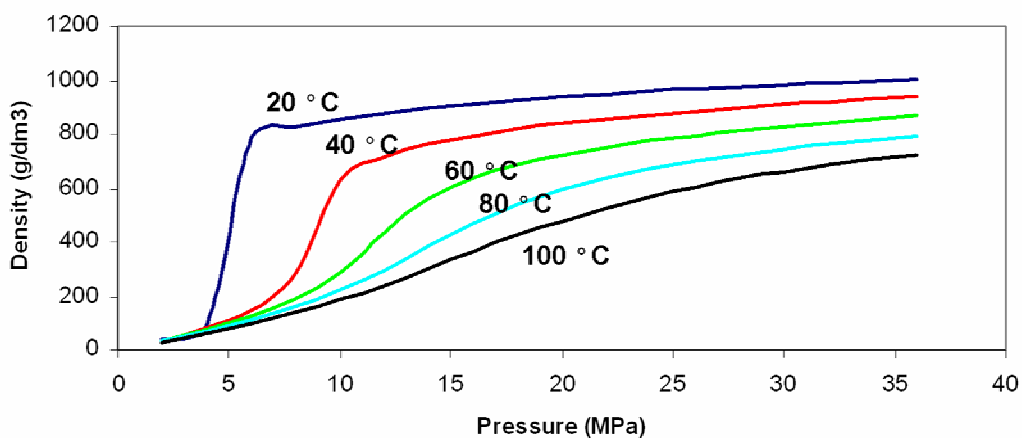


Figure 15 – The density of CO₂ as a function of pressure for a range of temperatures. Values were calculated from data taken from the NIST fluid properties database.

Many of the processes for which scCO₂ is used are aided by negligible surface tension (Fig. 16), allowing hydrophobic behaviour normally associated with liquid to substrate interactions, and other phenomena such as drying-induced substrate damage, to be avoided. This has allowed scCO₂ to be utilised as an ideal

solvent for the cleaning and processing of delicate electronic components and microdevices.¹⁶⁶

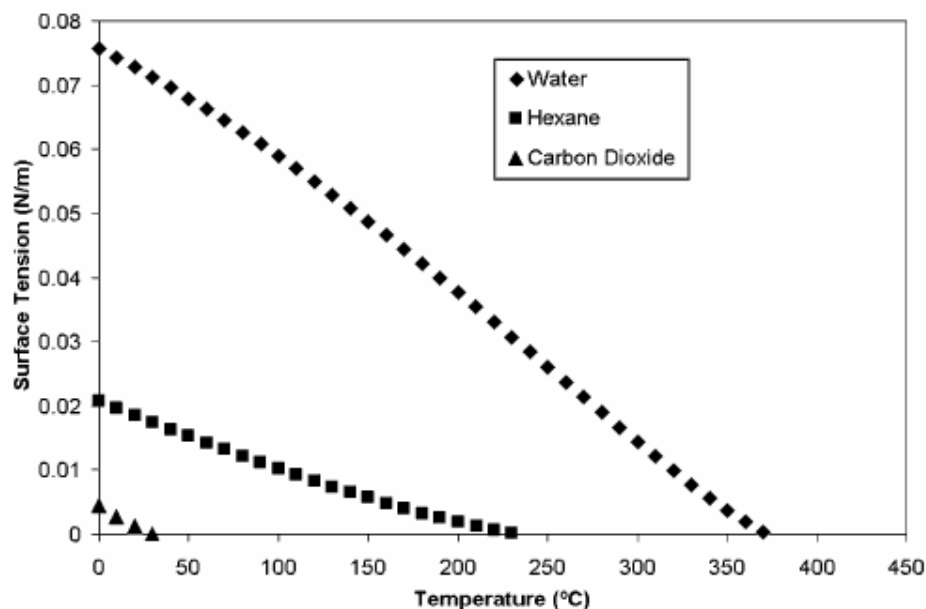


Figure 16 - Surface tension change with increasing temperature of three solvent systems. Surface tension drops to zero as the material exceeds T_c under saturated conditions. Water offers a very small window of potential operation, irrespective of corrosion concerns. Hexane possibly has some, higher temperature opportunities, while CO_2 offers zero surface tension over the whole range, making it the most attractive option.¹⁶⁶

As well as use in microelectronics, $scCO_2$ has found widespread application in other industrial processes, such as the extraction of metals or organic material. Often foodstuffs, notably caffeine from coffee, or for dry-cleaning and de-greasing.¹⁶⁷ CO_2 is also being employed in increasingly large scales for organic synthetic reactions and transformations.^{168, 169} However, two important fields most relevant to this thesis are $scCO_2$ processing and synthesis of polymers, and $scCO_2$ generation and impregnation of nanoparticles. These topics will be discussed in greater detail below.

1.5.2.1 Polymer Processing with scCO₂

The solvating ability of scCO₂ when interacting with polymers has been compared to volatile organic solvents, such as hexane. The density of scCO₂, as governed by its temperature and pressure, affects its solvent nature, which is commonly measured by dielectric constant. While a good solvent for many polar and non-polar molecules of low molecular weight (*e.g.* monomers, initiators, oligomers), scCO₂ is a poor solvent for most high molecular weight polymers.¹⁶² The solubility of polymers in scCO₂ is governed by the CO₂-polymer segment interactions, compared to the strength of the segment-segment and CO₂-CO₂ interactions, and the flexibility of the polymer chain.¹⁷⁰ As a quadrupolar molecule CO₂ does not strongly interact with non-polar groups, and hence, combined with having a lower density than most liquid solvents, is a poor solvent for many long chain polymers. Solubility in scCO₂ generally increases with the number of polar groups in the polymer.¹⁷¹ However, for very polar polymers segment-segment interactions will be too strong, therefore reducing solvation.

The factors that control polymer segment-CO₂ interactions are not yet fully understood. Fluorine-functionalised polymers have been widely investigated, as they seem to have a greater affinity for CO₂. However, this appears to be linked to carbonyl/ether groups present in the polymers, which are generally accepted to have a favourable interaction with CO₂. It is noted that poly(tetrafluoroethene) (PTFE), completely fluorinated as it is, though with no carbonyls/ethers, is no

more miscible with scCO₂ than a polyolefin. Three important features that help in making a polymer scCO₂ soluble are:

- (1) Low cohesive energy
- (2) High free volume
- (3) Groups that provide a specific interaction with scCO₂, *i.e.* F, C=O, ether *etc.*

For the polymers that are soluble, or semi-soluble, scCO₂ can be used for the extraction of low molecular weight material, as well as polymer fractionation. Polymerisation reactions have been successfully carried out in scCO₂, often with surfactants or co-solvents to aid solubility or dispersion of higher molecular weight species.^{162, 172, 173} These reactions are capable of producing particulate powders of solid polymer, easy to process and there are numerous publications in the literature where scCO₂ has been used as a solvent to facilitate clean polymer synthesis.^{162, 174-190} Much of this research has centred on the ability to develop CO₂-soluble polymer segments, to stabilise the growing polymer chain, enhance its dispersion in scCO₂ and ensure controllable, reproducible polymer preparations.

Insoluble polymers have received at least as much attention for use with scCO₂. Even though they are not soluble in scCO₂, it is still able to permeate into them, leading to some very useful effects. Even a small amount of scCO₂ absorbed into a polymer phase results in substantial and sometimes dramatic changes in the

physical properties that dictate processing. These include viscosity, permeability, interfacial tension, and glass transition temperature. By understanding the effects of CO₂ on these properties and developing techniques for incorporating CO₂ in continuous processes, a wide range of opportunities open up that impact the plastics industry.¹⁷¹ The permeation of scCO₂ into a polymer causes it to swell in volume. The CO₂ molecules, aided by their zero surface tension, permeate easily into a polymer matrix, allowing the chains a greater mobility. The CO₂ molecules act as “molecular lubricants” between the chains, giving them more free volume of movement, and therefore reducing the T_g . This also gives the polymer chains the freedom to align themselves into a more favourable order, hence increasing crystallinity.

The permeation of scCO₂ into polymers has been used for extraction, foaming and impregnation. Extraction occurs by simply removing the soluble extractant material, such as unreacted monomer, while leaving the insoluble substrate. Foaming occurs when rapid decompression forms gaseous CO₂ inside the polymer, stretching it to a foam. As for impregnation, by utilising its properties as a transport medium, molecules can be dissolved in scCO₂, impregnated into a polymer, and CO₂ can be cleanly removed afterwards (Fig. 17). Substances impregnated into polymers have included dyes, fragrances, drugs for controlled release, anti-microbial and anti-fungal agents, and metal nanoparticles.¹⁹¹ These are discussed in more detail in the following section. The impregnation technique has also led to a novel method of producing polymer blends by introducing a monomer before initiating polymerisation.

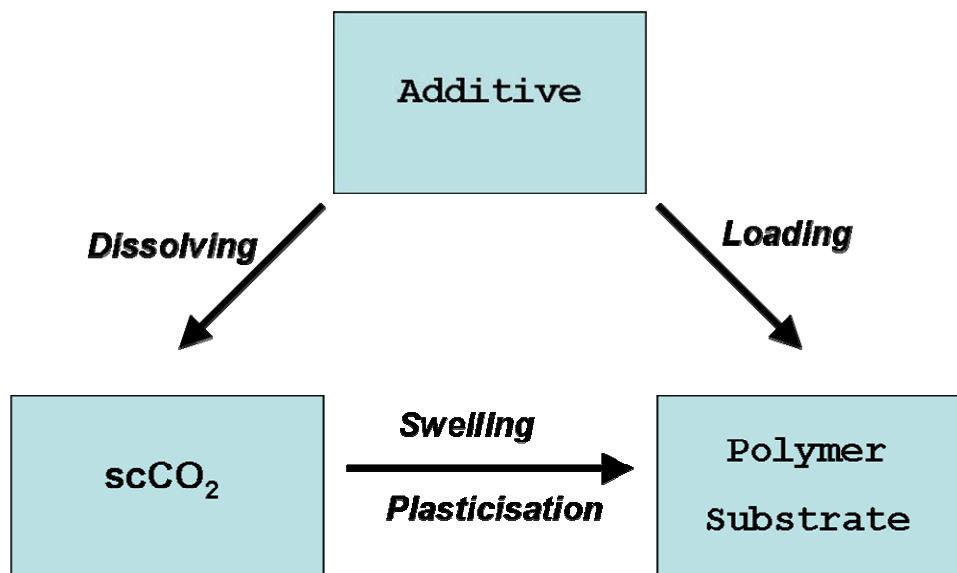


Figure 17 – Interactions between phases of scCO₂ impregnation system.

1.5.2.2 Supercritical Fluids for Nanoparticle Synthesis

Supercritical fluids, mainly scCO₂ and scH₂O, have been used in a variety of techniques for the production of inorganic nanoparticles and nanocomposite materials. The three most prominent of these techniques are:

- The rapid expansion of supercritical solvents (RESS) – using scCO₂
- Hydrothermal synthesis – using scH₂O
- Generation of nanoparticles within solid hosts by scCO₂ impregnation of precursors

All of these techniques use a soluble or semi-soluble precursor to generate the nanoparticles, such as an organometallic complex or metal salt.

1.5.2.3 Rapid Expansion of Supercritical Solvents (RESS)

In this process, a material is dissolved in a pressurized supercritical fluid and the solution is rapidly expanded to some lower pressure level which causes the solid to precipitate as fine particles. This concept has been demonstrated for a wide variety of materials including polymers, dyes, pharmaceuticals and inorganic substances.¹⁹² The dissolved solute is normally decompressed through the nozzle. This nozzle is a key component, of which two types are used, a capillary of suitable diameter (<100 μm) or laser-drilled holes of 20–60 μm diameter. A schematic representation of a typical RESS experimental apparatus is shown (Fig. 18).

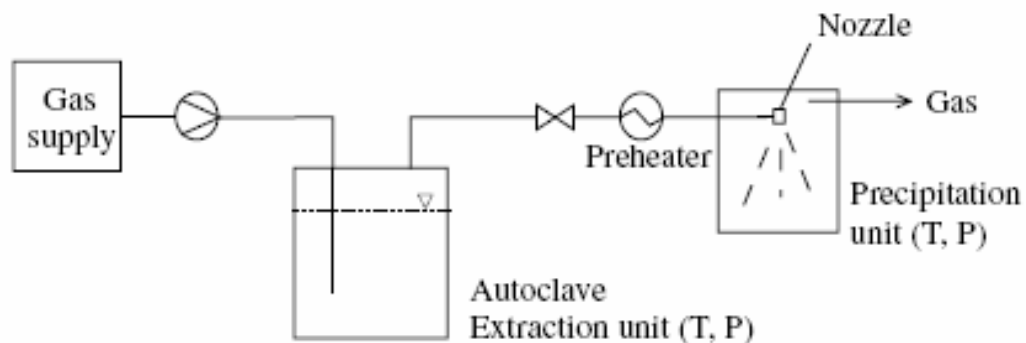


Figure 18 – Typical experimental apparatus for RESS.¹⁹²

In conventional RESS using expansion into vacuum or air, the supercritical fluid solution is transferred rapidly to sub-critical pressures. As the “solution droplets” from the rapid expansion pass through the nozzle they are extremely unstable, resulting in rapid solute precipitation. It is this rapid solute precipitation

from supercritical solution upon expansion that provides the basis for the RESS processing in particle and fibre production. The same processing conditions may be achieved by expanding into a liquid solution. Because of the high velocity of the expanding supercritical fluid solution, the conditions at the end of the expansion nozzle are little affected by the receiving medium, air or liquid. In RESS into a liquid solution, the receiving liquid solution captures the nanoscopic “solute droplets” produced in the rapid expansion, and this can often be useful in the production process. For example, in the preparation of metal sulfides such as cadmium sulfide, the nanoscopic “droplets” produced in the RESS process contain cadmium cations, which are captured by sulfide anions in the receiving liquid solution to form cadmium sulfide nanoparticles. Similarly, nanoscopic metal ion “solute droplets” produced in the RESS process may be chemically reduced in the receiving liquid solution to form metal nanoparticles. The suspension of nanoparticles thus formed can be stabilized by protective polymers.¹⁹³

This technique has been successfully used to produce nanoparticles of nickel, cobalt, iron, silver, palladium, copper, silver sulfide, cadmium sulfide, and lead sulfide from rapid expansion of scCO_2 or water in scCO_2 suspensions.¹⁹³⁻¹⁹⁸

1.5.2.4 Hydrothermal Synthesis of Nanoparticles

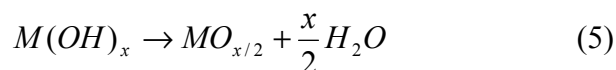
Supercritical water hydrothermal synthesis (scWHS) has received much recent attention as a possible method to produce metal oxide nanoparticles in large enough quantities, and low enough prices, to satisfy the demand from desired industrial applications. This technique is seen as advantageous as it offers a

relatively simple route which is inherently scalable and chemically much more benign than current technology. It is also a continuous process, making it particularly favourable for large scale production, especially as this means the reactor volumes can be kept low (which is helpful for high pressure processes in terms of cost and safety). As a result, scWHS has been investigated extensively by several research groups,¹⁹⁹⁻²⁰⁶ but has often been delayed towards industrial application due to problems of reliability, reproducibility and process control.

The scWHS process itself is relatively straightforward; it involves the mixing of an aqueous metal salt stream with a supercritical water stream within a continuous reactor to produce nano-size metal oxide particles. When water is heated towards its critical point ($T_c = 374\text{ °C}$, $P_c = 22.1\text{ MPa}$), it changes from a polar liquid to a fluid with a low dielectric constant and low pH. K_w , the ionic product of water, also increases, giving rise to correspondingly increased concentrations of H^+ and OH^- .²⁰⁷ These enhanced levels of OH^- were first exploited for nano-particle synthesis by Adschiri *et al.*,²⁰¹ who showed that, under these conditions, hydrolysis of the metal salts was immediately followed by a dehydration step (Equations 4 and 5).



Equation 4: Hydrolysis of metal salt by supercritical water



Equation 5: Formation of metal oxide by dehydration

The Clean Technology Research Group at the University of Nottingham has been undertaking research into the development and optimisation of the scWHS process with the objective of making the process industrially viable. This research has focussed on the production of metal oxide nanoparticles and, more recently, single-phase mixed metal oxides.^{208, 209} An important emphasis of the work performed in Nottingham has been to gain greater understanding of the factors that have caused problems of reliability, reproducibility and process control. After much practical and theoretical study of the system, the reaction apparatus was successfully modified to greatly increase the quality of nanoparticles produced. The metal oxide nanoparticles employed as stabilisers for the synthesis of polymer nanocomposites featured in chapter 3 were produced by this method and equipment. The exact synthesis method and apparatus used to produce these nanoparticles are discussed in more detail in chapter 3.3.1.

1.5.2.5 Nanoparticles by scCO₂ Impregnation of into Host Materials

Supercritical fluids have been used to deposit thin metal films onto a wide range of surfaces and to incorporate metallic particles into different inorganic and organic substrates for microelectronic, optical and catalytic applications.²¹⁰ This technique has allowed both highly dispersed and uniformly distributed metal nanoparticles, as well as agglomerated clusters of nanoparticles of wider size distribution, to be generated in host materials. These various solid substrates have included silicon wafer, metal foil, inorganic nanotubes, bulk polymers and polymer membranes, organic and inorganic porous materials. The nanoparticle

impregnation process involves dissolving an appropriate metallic precursor in an SCF (most commonly scCO_2) and then exposing the substrate to the solution. The SCF facilitates the infusion of the precursor into the host material. After incorporation of the precursor with the substrate, the metallic precursor is reduced to its metal form by a wide variety of methods resulting in films or particles. The reduction methods employed are; chemical reduction in the SCF with a reducing agent such as hydrogen and alcohols, thermal reduction in the SCF, and thermal decomposition in an inert atmosphere or chemical conversion with hydrogen or air²¹⁰ (Fig. 19).

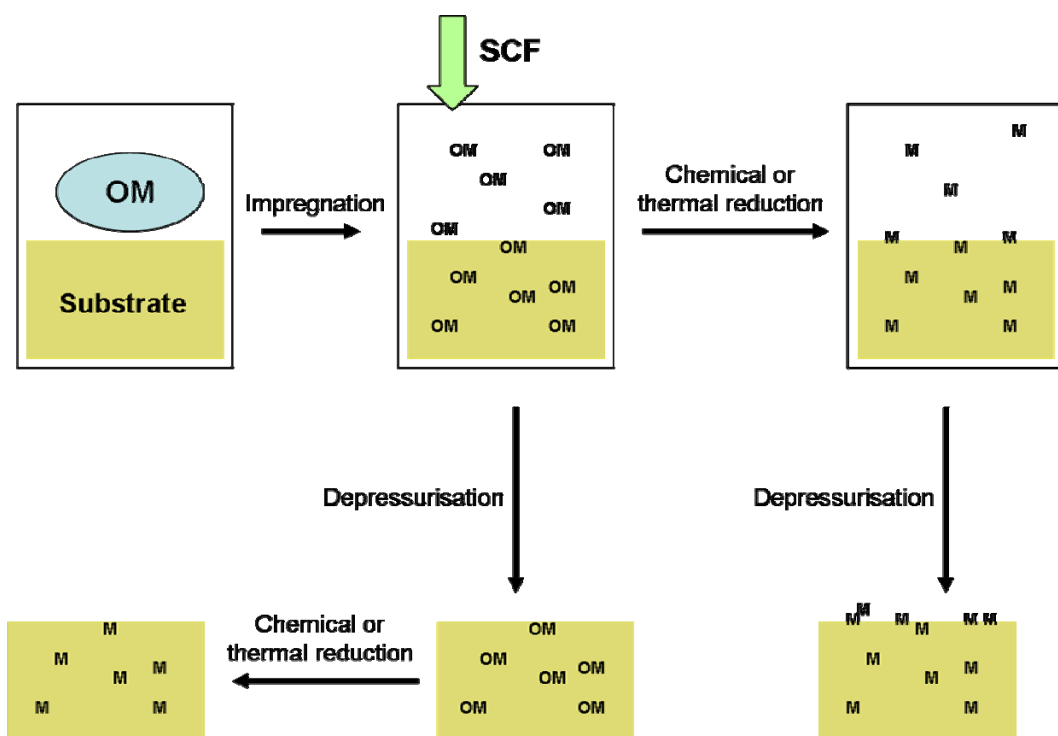


Figure 19 – Supercritical fluid mediated impregnation or deposition of nanoparticles into a substrate. OM represents a soluble organometallic precursor. Adapted from Zhang and Erkey.²¹⁰

The use of an SCF such as scCO_2 for this impregnation process is advantageous in comparison to conventional solvents for many reasons. For many

of the substrates used, a conventional solvent would be unsuitable. For high surface area substrates such as highly porous inorganics for catalysis or micro-structured materials for electronics the use of conventional solvents is not appropriate. The surface tension and viscosity of common solvents, along with poor wetting of the pores, causes very slow and often incomplete impregnation of precursor solutions into porous supports. The low surface tension of scCO₂ not only permits better penetration and wetting of pores than liquid solvent, but also avoids pore collapse which can occur on certain structures such as organic and silica aerogels with liquid solvents. This damage is caused during the drying step, as liquid solvents are removed from the substrate. Strong localised forces occur in the pores due to their small diameter in relation to the meniscus of retreating liquid. This causes cracking of the material. Even without this factor, extended heating of the substrate to remove liquid solvents can be costly and time consuming. In comparison, scCO₂ can be much more easily introduced and removed from such systems.

For polymer impregnation scCO₂ allows modification that would be difficult with conventional solvents. scCO₂ can be easily infused into polymers, without the need to dissolve the polymer and re-blend, and displays a high permeation rate in virtually all polymers. The exposure of polymers to scCO₂ results in various extents of swelling and enhanced mobility of the polymer chains, which makes it possible to incorporate metallic precursors. Moreover, the degree of polymer swelling, diffusion rates within the substrate, and the partitioning of precursors between the SCF and the swollen polymer can be controlled by density

mediated adjustments of solvent strength via changes in temperature and pressure.^{210, 211}

Regardless of the substrate used, the gas-like diffusivities of scCO₂ significantly enhance the kinetics of penetrant absorption, and no solvent residues are left after depressurisation. The average particle size and size distribution of nanoparticles is affected by the precursor reduction method used, as well as the conditions, type and amount of precursor in the system and the surface properties of the substrate.

The groundbreaking work in this field was undertaken by Watkins and McCarthy in 1995, and was the first use of a SCF for the impregnation of metal nanoparticles into a polymer substrate.²¹¹ In this case the SCF used was scCO₂ and the polymers impregnated were poly(4-methyl-1-pentene) (PMP) and poly(tetrafluoroethylene) (PTFE). The organometallic precursor used was dimethyl(cyclooctadiene)platinum(II) (CODPtMe₂), which was chosen because it was a readily available CVD precursor with good potential for scCO₂ solubility and had previously been reduced effectively with hydrogen to yield high purity platinum films.²¹² The precursor was infused into the polymers by a 4 hr impregnation time in scCO₂ at a temperature of 80 °C, and pressure of 15.5 MPa. The precursor was reduced to platinum nanoparticles in the PMP by hydrogen reduction in scCO₂, hydrogen reduction after depressurisation and by thermal decomposition in the presence of scCO₂. In PTFE the precursor was reduced by hydrogen in the presence of scCO₂. The results of these impregnation reactions

provide a useful example to discuss the effect of changes in the system, and can be observed from transmission electron micrographs of the nanocomposites (Fig. 20).

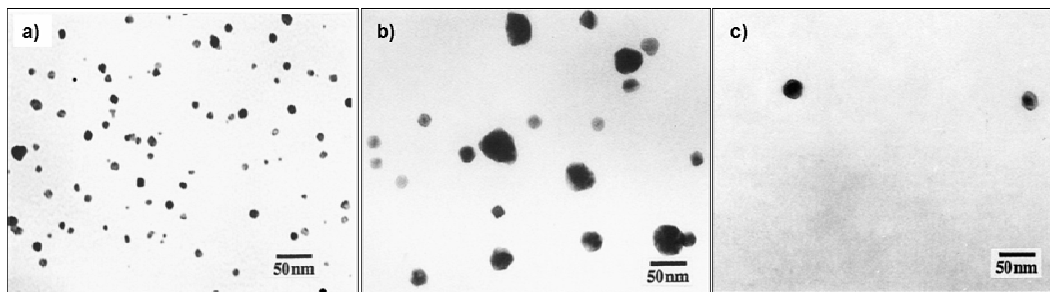


Figure 20 – a) PMP, hydrogen reduction after depressurisation. b) PMP, hydrogen reduction in the presence of scCO_2 . c) PTFE, hydrogen reduction in the presence of scCO_2 .

The comparison of figure 20a) and 20b) is useful for understanding the implications of the two alternative reduction routes shown in figure 19, *i.e.* reduction after or before depressurisation. When the precursor in PMP was reduced after depressurisation of the scCO_2 (Fig. 20a) the product appeared to be homogeneous throughout with nanoparticles of ~ 15 nm evenly distributed, apart from occasional larger clusters. When the precursor was reduced by hydrogen before venting the scCO_2 a sharp concentration gradient was seen close to the surface. The nanoparticles in the bulk of the PMP are mostly up to ~ 50 nm, but close to the surface, which had a silver sheen, a greatly increased concentration of nanoparticles was present with diameter of ~ 50 - 100 nm. This difference is caused by the effect of reducing the metal while scCO_2 is still present in the polymer. The polymer is still scCO_2 swollen and the precursor molecules are still able to diffuse freely during the reduction step. This allows the nanoparticles in the bulk to grow larger in diameter, and also caused a greater deposition of metal into the surface

layer. This is because the precursor is still able to infuse from the solvent phase into the polymer and because metal nanoparticles growing in the solvent phase will become unstable and deposit into the polymer surface. Therefore, when control of nanoparticle size and uniformity is desired, post-depressurisation reduction is preferable.

We should also compare the difference in nanocomposite structure produced depending on the change of host polymer. PTFE was impregnated with precursor which was reduced in the presence of scCO₂ (Fig. 20c) in exactly the same method as the PMP (Fig. 20b). A similar surface effect was noticed for the PTFE, compared to the PMP, in terms of there being more and larger nanoparticles at the polymer surface due to reduction occurring concurrently with impregnation. However, in the case of PTFE the nanoparticles in the bulk of the polymer were considerably fewer in number and smaller in size than those produced in PMP in the same conditions. This demonstrates that, although scCO₂ can be used to impregnate even very solvent resistant polymers such as PTFE, the degree of nanoparticle incorporation is understandably affected by the uptake of precursor and this is determined by the solubility of the precursor in each given polymer and how easily the precursor can be infused into the polymer.

This method was expanded by Watkins' group to deposit different metal nanoparticles or films, including platinum, palladium, gold, rhodium, cobalt, nickel and copper in scCO₂ by the reduction of desired precursors with hydrogen or alcohols.²¹³⁻²¹⁸ Other groups then took this new technique forward, adapting it to other substrates and metals. Ye *et al.* prepared highly dispersed nanoparticles of

palladium, rhodium and ruthenium through reduction of adsorbed metal- β -diketone precursors by hydrogen in scCO_2 .²¹⁹⁻²²² The nanoparticles were deposited onto functionalized multi-walled carbon nanotubes or SiO_2 nanotubes for catalytic applications. Preliminary experiments demonstrated that the supported Pd nanoparticles were effective catalysts for hydrogenation of olefins in carbon dioxide showing high electrocatalytic activity for oxygen reduction reaction indicative of potential fuel cell applications.

Saquin *et al.* demonstrated that metal films and highly dispersed nanoparticles could be produced simultaneously on the surface and within the matrix of porous monolithic materials by depositing platinum on carbon aerogel monoliths.²²³ Further research led by Saquin and Erkley's group continued this work to other substrates including carbon black, silica aerogel, silica, gamma-alumina, and Nafion® 112 film.²²⁴ Nafion® is a sulfonated tetrafluorethylene copolymer developed by DuPont. The porous substrates and Nafion® film were impregnated with CODPtMe_2 , which was reduced to elemental platinum by heat treatment in the presence of nitrogen gas. A comparison of nanocomposites produced under different conditions showed that both the metal contents and the particle sizes are controllable. Membrane-electrode assemblies of Nafion® membranes with incorporated palladium nanoparticles were prepared by this method and evaluated in direct methanol fuel cells. The Pd-impregnated Nafion® membranes showed reduced methanol crossover and gave higher cell performance than that of pure Nafion® membrane.

Substantial investigations into this field have been undertaken by the Howdle group at the University of Nottingham over the last few years. The method used by the Howdle group has been generally similar to that commonly used, except instead of reducing the metallic precursor at ambient pressure following SCF impregnation, chemical reduction with pure hydrogen at an elevated pressure has been used to synthesise silver nanoparticles in porous poly(styrene-divinylbenzene) beads and silica aerogels, and palladium nanoparticles in silica aerogel.^{225, 226} The palladium nanoparticles in silica aerogel supports were shown to demonstrate good catalytic activity for hydrogenation of cyclohexene in a continuous flow reactor. Similar impregnations allowed the clean synthesis of silver nanoparticles in polymer substrates for biomedical applications, and some success was demonstrated in initial applications testing.^{31, 227} More recently the group was able to extend the versatility of this technique to the synthesis of gold nanoparticles supported on silica, polyamide, polypropylene and PTFE.²²⁸ Two precursors; dimethylacetylacetonato gold(III), and its fluorinated analogue dimethylhexafluoroacetylacetonato gold(III), were compared for their effectiveness in the production of the gold nanoparticles, which have catalytic applications. Interestingly the non-fluorinated organometallic precursor was found to produce more effectively and higher loaded nanocomposite material.

Some of the most advanced polymer results are evidenced by the researches of Boggess *et al* and of Yoda *et al*. Boggess *et al*. performed the synthesis of highly reflective silver-polyimide films by impregnation of (1,5-cyclooctadiene-1,1,1,5,5,5-hexafluoroacetylacetonato)silver(I) into polyimides.²²⁹

Similarly, Yoda et al. synthesised Pt- and Pd-nanoparticle dispersed polyimide films as a precursor for the preparation of metal-doped carbon molecular sieve membranes for hydrogen separation.²³⁰ The impregnated precursors were Pt(II) acetylacetonate and Pd(II) acetylacetonate. It was found that the particle size increased with the increase of the impregnation temperature, and impregnation time. The Pd-doped carbon molecular sieve membrane was successfully prepared by carbonation of the Pd-doped film and showed good hydrogen separation performance.²³¹ Yoda *et al.* also prepared platinum/silica aerogel nanocomposites by dissolving platinum(II) acetylacetonate in scCO₂ and impregnating into the silica gel during the supercritical drying stage.²³²

These initial investigations into the use of scCO₂, though interesting and successful, only represent the beginning of what will be a considerably larger body of research that must be undertaken to bring this exciting field into full understanding and effectiveness. The early work that has been provided, however, does supply an excellent foundation for the establishment of core knowledge and the instigation of current and future study. In the words of Zhang and Erkey in their recent review: *It is clear that the SCF incorporation for synthesis of supported nanocomposites is in a very early stage of development and has great potential for creating materials with improved properties.*²¹⁰

1.6 Conclusions – Chapter 1

This introductory chapter has outlined the importance of the emergent field of nanocomposite functional materials, and has shown that the development of new routes to novel metal-polymer nanocomposites is a relevant and necessary area of study. Supercritical fluid technology has been shown to be a useful and interesting technique with many advantages over conventional solvents.

The rest of this thesis describes scCO₂ and conventional solution routes to prepare novel nanocomposite materials. The successful incorporation of different substrate materials with metal and metal oxide nano-domain species has been achieved. These new materials have been fully characterised using many different investigative techniques and these results are presented and discussed in detail.

1.7 References

1. D. Hughes, British Standards Institute, www.bsi-global.com, 2005.
2. J. Grunes, J. Zhu and G. A. Somorjai, *Chemical Communications*, 2003, 2510-2510.
3. G. Schmid, *Nanoparticles: From Theory to Applications*, Wiley, 2004.
4. L. Nicolais and G. Carotenuto, *metal-polymer nanocomposites*, Wiley, Hoboken, 2005.
5. A. Heilmann, *Polymer Films with Embedded Metal Nanoparticles*, Springer, Berlin Heidelberg New York, 2003.
6. P. N. Prasad, *Nanophotonics*, Wiley, Hoboken, New Jersey, 2004.
7. A. N. Shipway, E. Katz and I. Willner, *Chemphyschem*, 2000, **1**, 18-52.
8. E. Roduner, *Chemical Society Reviews*, 2006, **35**, 583-592.
9. S. Panigrahi, S. Basu, S. Praharaj, S. Pande, S. Jana, A. Pal, S. K. Ghosh and T. Pal, *Journal of Physical Chemistry C*, 2007, **111**, 4596-4605.
10. D. Astruc, F. Lu and J. R. Aranzaes, *Angewandte Chemie-International Edition*, 2005, **44**, 7852-7872.
11. R. Narayanan and M. A. El-Sayed, *Journal of Physical Chemistry B*, 2005, **109**, 12663-12676.
12. F. Raimondi, G. G. Scherer, R. Kotz and A. Wokaun, *Angewandte Chemie-International Edition*, 2005, **44**, 2190-2209.
13. M. C. Daniel and D. Astruc, *Chemical Reviews*, 2004, **104**, 293-346.
14. M. Moreno-Manas and R. Pleixats, *Accounts of Chemical Research*, 2003, **36**, 638-643.
15. A. Haruta, *Chemical Record*, 2003, **3**, 75-87.
16. M. Haruta, *Cattech*, 2002, **6**, 102-115.
17. M. Kralik and A. Biffis, *Journal of Molecular Catalysis a-Chemical*, 2001, **177**, 113-138.
18. R. M. Crooks, M. Q. Zhao, L. Sun, V. Chechik and L. K. Yeung, *Accounts of Chemical Research*, 2001, **34**, 181-190.
19. C. J. Murphy, T. K. San, A. M. Gole, C. J. Orendorff, J. X. Gao, L. Gou, S. E. Hunyadi and T. Li, *Journal of Physical Chemistry B*, 2005, **109**, 13857-13870.
20. W. Chen, J. Z. Zhang and A. G. Joly, *Journal of Nanoscience and Nanotechnology*, 2004, **4**, 919-947.
21. C. Voisin, N. Del Fatti, D. Christofilos and F. Vallee, *Journal of Physical Chemistry B*, 2001, **105**, 2264-2280.
22. Y. P. Sun and J. E. Riggs, *International Reviews in Physical Chemistry*, 1999, **18**, 43-90.
23. F. E. Kruis, H. Fissan and A. Peled, *Journal of Aerosol Science*, 1998, **29**, 511-535.
24. S. Bruzzone, M. Malvaldi, G. P. Arrighini and C. Guidotti, *Journal of Physical Chemistry B*, 2005, **109**, 3807-3812.
25. S. Bruzzone, G. P. Arrighini and C. Guidotti, *Materials Science & Engineering C-Biomimetic and Supramolecular Systems*, 2003, **23**, 965-970.
26. G. Carotenuto, G. La Peruta and L. Nicolais, *Sensors and Actuators B-Chemical*, 2006, **114**, 1092-1095.

27. L. Francois, M. Mostafavi, J. Belloni, J. F. Delouis, J. Delaire and P. Feneyrou, *Journal Of Physical Chemistry B*, 2000, **104**, 6133-6137.
28. K. L. Kelly, E. Coronado, L. L. Zhao and G. C. Schatz, *Journal Of Physical Chemistry B*, 2003, **107**, 668-677.
29. A. Ito, M. Shinkai, H. Honda and T. Kobayashi, *Journal of Bioscience and Bioengineering*, 2005, **100**, 1-11.
30. J. L. Elechiguerra, J. L. Burt, J. R. Morones, A. Camacho-Bragado, X. Gao, H. H. Lara and M. J. Yacaman, *Journal of Nanobiotechnology*, 2005, **3:6**, This article is available from:
<http://www.inanobiotechnology.com/content/3/1/6>.
31. F. Furno, K. S. Morley, B. Wong, B. L. Sharp, P. L. Arnold, S. M. Howdle, R. Bayston, P. D. Brown, P. D. Winship and H. J. Reid, *Journal Of Antimicrobial Chemotherapy*, 2004, **54**, 1019-1024.
32. P. Jain and T. Pradeep, *Biotechnology and Bioengineering*, 2005, **90**, 59-63.
33. J. R. Morones, J. L. Elechiguerra, A. Camacho, K. Holt, J. B. Kouri, J. T. Ramirez and M. J. Yacaman, *Nanotechnology*, 2005, **16**, 2346-2353.
34. C. N. R. Rao, P. J. Thomas and G. U. Kulkarni, *Nanocrystals: synthesis, properties and applications*, Springer, Berlin-Heidelberg-New York, 2007.
35. V. Degouveia, B. Bellamy, Y. H. Romdhane, A. Masson and M. Che, *Zeitschrift Fur Physik D-Atoms Molecules and Clusters*, 1989, **12**, 587-590.
36. A. Sandell, J. Libuda, P. Bruhwiler, S. Andersson, A. Maxwell, M. Baumer, N. Martensson and H. J. Freund, *Journal of Electron Spectroscopy and Related Phenomena*, 1995, **76**, 301-306.
37. C. R. Henry, *Surface Science Reports*, 1998, **31**, 231-325.
38. M. Haruta and M. Date, *Applied Catalysis a-General*, 2001, **222**, 427-437.
39. F. Boccuzzi, A. Chiorino, M. Manzoli, P. Lu, T. Akita, S. Ichikawa and M. Haruta, *Journal of Catalysis*, 2001, **202**, 256-267.
40. M. Mavrikakis, P. Stoltze and J. K. Norskov, *Catalysis Letters*, 2000, **64**, 101-106.
41. C. A. Stowell and B. A. Korgel, *Nano Letters*, 2005, **5**, 1203-1207.
42. R. Narayanan and M. A. El-Sayed, *Nano Letters*, 2004, **4**, 1343-1348.
43. V. Subramanian, E. E. Wolf and P. V. Kamat, *Journal of the American Chemical Society*, 2004, **126**, 4943-4950.
44. B. R. Cuenya, S. H. Baeck, T. F. Jaramillo and E. W. McFarland, *Journal of the American Chemical Society*, 2003, **125**, 12928-12934.
45. T. G. Schaaff and D. A. Blom, *Nano Letters*, 2002, **2**, 507-511.
46. T. K. Sau, A. Pal and T. Pal, *Journal of Physical Chemistry B*, 2001, **105**, 9266-9272.
47. M. Frank and M. Baumer, *Physical Chemistry Chemical Physics*, 2000, **2**, 3723-3737.
48. C. Rice, Y. Tong, E. Oldfield, A. Wieckowski, F. Hahn, F. Gloaguen, J. M. Leger and C. Lamy, *Journal of Physical Chemistry B*, 2000, **104**, 5803-5807.
49. U. Heiz, F. Vanolli, A. Sanchez and W. D. Schneider, *Journal of the American Chemical Society*, 1998, **120**, 9668-9671.
50. G. A. Somorjai, *Applied Surface Science*, 1997, **121**, 1-19.
51. Y. G. Sun and Y. N. Xia, *Science*, 2002, **298**, 2176-2179.
52. J. M. Petroski, Z. L. Wang, T. C. Green and M. A. El-Sayed, *Journal of Physical Chemistry B*, 1998, **102**, 3316-3320.

53. T. S. Ahmadi, Z. L. Wang, T. C. Green, A. Henglein and M. A. ElSayed, *Science*, 1996, **272**, 1924-1926.
54. V. Calo, A. Nacci, A. Monopoli, A. Fornaro, L. Sabbatini, N. Cioffi and N. Ditaranto, *Organometallics*, 2004, **23**, 5154-5158.
55. P. D. Cozzoli, R. Comparelli, E. Fanizza, M. L. Curri, A. Agostiano and D. Laub, *Journal of the American Chemical Society*, 2004, **126**, 3868-3879.
56. J. Prabhuram, X. Wang, C. L. Hui and I. M. Hsing, *Journal of Physical Chemistry B*, 2003, **107**, 11057-11064.
57. G. S. Fonseca, A. P. Umpierre, P. F. P. Fichtner, S. R. Teixeira and J. Dupont, *Chemistry-a European Journal*, 2003, **9**, 3263-3269.
58. D. Ishii, K. Kinbara, Y. Ishida, N. Ishii, M. Okochi, M. Yohda and T. Aida, *Nature*, 2003, **423**, 628-632.
59. S. Ozkar and R. G. Finke, *Journal of the American Chemical Society*, 2002, **124**, 5796-5810.
60. P. Braunstein, H. P. Kormann, W. Meyer-Zaika, R. Pugin and G. Schmid, *Chemistry-a European Journal*, 2000, **6**, 4637-4646.
61. R. Strobel, J. D. Grunwaldt, A. Camenzind, S. E. Pratsinis and A. Baiker, *Catalysis Letters*, 2005, **104**, 9-16.
62. L. M. Bronstein, D. M. Chernyshov, R. Karlinsey, J. W. Zwanziger, V. G. Matveeva, E. M. Sulman, G. N. Demidenko, H. P. Hentze and M. Antonietti, *Chemistry of Materials*, 2003, **15**, 2623-2631.
63. K. Okitsu, A. Yue, S. Tanabe and H. Matsumoto, *Chemistry of Materials*, 2000, **12**, 3006-3011.
64. G. Rupprechter, K. Hayek and H. Hofmeister, *Journal of Catalysis*, 1998, **173**, 409-422.
65. K. Mori, Y. Kondo, S. Morimoto and H. Yamashita, *Chemistry Letters*, 2007, **36**, 1068-1069.
66. A. Fukuoka, J. I. Kimura, T. Oshio, Y. Sakamoto and M. Ichikawa, *Journal of the American Chemical Society*, 2007, **129**, 10120-10125.
67. J. Zeng, J. Y. Lee, J. Chen, P. K. Shen and S. Song, *Fuel Cells*, 2007, **7**, 285-290.
68. R. M. Rioux, H. Song, J. D. Hoefelmeyer, P. Yang and G. A. Somorjai, *Journal of Physical Chemistry B*, 2005, **109**, 2192-2202.
69. H. Wakayama, N. Setoyama and Y. Fukushima, *Advanced Materials*, 2003, **15**, 742-745.
70. K. H. Park, S. U. Son and Y. K. Chung, *Organic Letters*, 2002, **4**, 4361-4363.
71. P. Mukherjee, C. R. Patra, A. Ghosh, R. Kumar and M. Sastry, *Chemistry of Materials*, 2002, **14**, 1678-1684.
72. L. S. Zhong, J. S. Hu, Z. M. Cui, L. J. Wan and W. G. Song, *Chemistry of Materials*, 2007, **19**, 4557-4562.
73. W. F. Yan, B. Chen, S. Mahurin, S. Dai and S. H. Overbury, *Abstracts of Papers of the American Chemical Society*, 2004, **228**, U537-U537.
74. J. A. Rodriguez, G. Liu, Z. P. Chang, T. Jirsak, J. Dvorak, J. Hrbek and A. Maiti, *Abstracts of Papers of the American Chemical Society*, 2003, **225**, U958-U958.
75. F. Ciardelli, P. Pertici, G. Vitulli, S. Giaiacopi, G. Ruggeri and A. Pucci, *Macromolecular Symposia*, 2006, **231**, 125-133.
76. C. J. Huang, F. S. Shieu, W. P. Hsieh and T. C. Chang, *Journal of Applied Polymer Science*, 2006, **100**, 1457-1464.

77. V. M. Rudoy, N. L. Sukhov, O. V. Dement'eva, E. V. Abkhalimov, O. F. Vereshchagina, M. E. Kartseva and B. G. Ershov, *Colloid Journal*, 2005, **67**, 357-362.
78. V. M. Rudoy, B. G. Ershov, N. L. Sukhov, O. V. Dement'eva, A. V. Zaitseva, A. F. Seliverstov, M. E. Kartseva and V. A. Ogarev, *Colloid Journal*, 2002, **64**, 755-758.
79. M. Notomi, *Physical Review B*, 2000, **62**, 10696-10705.
80. J. Wijnhoven and W. L. Vos, *Science*, 1998, **281**, 802-804.
81. J. D. Joannopoulos, P. R. Villeneuve and S. H. Fan, *Nature*, 1997, **386**, 143-149.
82. L. Zimmermann, M. Weibel, W. Caseri and U. W. Suter, *Journal Of Materials Research*, 1993, **8**, 1742-1748.
83. P. N. Prasad, *Current Opinion in Solid State & Materials Science*, 2004, **8**, 11-19.
84. D. J. Norris and M. G. Bawendi, *Physical Review B*, 1996, **53**, 16338-16346.
85. B. O. Dabbousi, J. RodriguezViejo, F. V. Mikulec, J. R. Heine, H. Mattoussi, R. Ober, K. F. Jensen and M. G. Bawendi, *Journal of Physical Chemistry B*, 1997, **101**, 9463-9475.
86. O. I. Micic, H. M. Cheong, H. Fu, A. Zunger, J. R. Sprague, A. Mascarenhas and A. J. Nozik, *Journal of Physical Chemistry B*, 1997, **101**, 4904-4912.
87. G. Zlateva, Z. Zhelev, R. Bakalova and I. Kanno, *Inorganic Chemistry*, 2007, **46**, 6212-6214.
88. J. H. Hodak, A. Henglein and G. V. Hartland, *Journal of Physical Chemistry B*, 2000, **104**, 9954-9965.
89. J. H. Hodak, A. Henglein and G. V. Hartland, *Pure and Applied Chemistry*, 2000, **72**, 189-197.
90. P. Mulvaney, *Langmuir*, 1996, **12**, 788-800.
91. C. F. Bohren and D. R. Huffman, *Absorption and Scattering of Light by Small Particles*, Wiley, New York, 1983.
92. N. K. Grady, N. J. Halas and P. Nordlander, *Chemical Physics Letters*, 2004, **399**, 167-171.
93. S. Link and M. A. El-Sayed, *Journal Of Physical Chemistry B*, 1999, **103**, 8410-8426.
94. D. D. Evanoff and G. Chumanov, *Chemphyschem*, 2005, **6**, 1221-1231.
95. S. Link and M. A. El-Sayed, *Journal of Physical Chemistry B*, 1999, **103**, 4212-4217.
96. S. Shi, W. Ji, S. H. Tang, J. P. Lang and X. Q. Xin, *Journal Of The American Chemical Society*, 1994, **116**, 3615-3616.
97. D. B. Yu, X. Q. Sun, J. T. Bian, Z. C. Tong and Y. T. Qian, *Physica E-Low-Dimensional Systems & Nanostructures*, 2004, **23**, 50-55.
98. S. W. Koch, N. Peyghambarian and H. M. Gibbs, *Journal Of Applied Physics*, 1988, **63**, R1-R11.
99. L. W. Tutt and T. F. Boggess, *Progress In Quantum Electronics*, 1993, **17**, 299-338.
100. Y. P. Sun, J. E. Riggs, H. W. Rollins and R. Guduru, *Journal of Physical Chemistry B*, 1999, **103**, 77-82.
101. M. L. Brongersma, J. W. Hartman and H. A. Atwater, *Physical Review B*, 2000, **62**, R16356-R16359.

102. G. Carotenuto and L. Nicolais, *Composites part B-Engineering*, 2004, **35**, 385-391.
103. A. G. de Leon, Y. Dirix, Y. Staedler, K. Feldman, G. Hahner, W. R. Caseri and P. Smith, *Applied Optics*, 2000, **39**, 4847-4851.
104. Y. Dirix, C. Darribere, W. Heffels, C. Bastiaansen, W. Caseri and P. Smith, *Applied Optics*, 1999, **38**, 6581-6586.
105. Z. X. Liu, H. H. Wang, H. Li and X. M. Wang, *Applied Physics Letters*, 1998, **72**, 1823-1825.
106. R. B. Martin, M. J. Meziani, P. Pathak, J. E. Riggs, D. E. Cook, S. Perera and Y. P. Sun, *Optical Materials*, 2007, **29**, 788-793.
107. S. Porel, N. Venkatrarn, D. N. Rao and T. P. Radhakrishnan, *Journal of Applied Physics*, 2007, **102**.
108. E. Smith and G. Dent, *Modern Raman Spectroscopy - A Practical Approach*, Wiley, Chichester, 2005.
109. A. Champion and P. Kambhampati, *Chemical Society Reviews*, 1998, **27**, 241-250.
110. K. Kneipp, Y. Wang, H. Kneipp, L. T. Perelman, I. Itzkan, R. Dasari and M. S. Feld, *Physical Review Letters*, 1997, **78**, 1667-1670.
111. K. Aslan, P. Holley and C. D. Geddes, *Journal of Materials Chemistry*, 2006, **16**, 2846-2852.
112. K. Aslan, I. Gryczynski, J. Malicka, E. Matveeva, J. R. Lakowicz and C. D. Geddes, *Current Opinion in Biotechnology*, 2005, **16**, 55-62.
113. H. Vallhov, J. Qin, S. M. Johansson, N. Ahlborg, M. A. Muhammed, A. Scheynius and S. Gabrielsson, *Nano Letters*, 2006, **6**, 1682-1686.
114. A. Jordan, R. Scholz, K. Maier-Hauff, M. Johannsen, P. Wust, J. Nadobny, H. Schirra, H. Schmidt, S. Deger, S. Loening, W. Lanksch and R. Felix, *Journal of Magnetism and Magnetic Materials*, 2001, **225**, 118-126.
115. A. Jordan, R. Scholz, P. Wust, H. Fahling and R. Felix, *Journal of Magnetism and Magnetic Materials*, 1999, **201**, 413-419.
116. A. J. Haes and R. P. Van Duyne, *Journal of the American Chemical Society*, 2002, **124**, 10596-10604.
117. M. D. Malinsky, K. L. Kelly, G. C. Schatz and R. P. Van Duyne, *Journal of Physical Chemistry B*, 2001, **105**, 2343-2350.
118. A. J. Haes, L. Chang, W. L. Klein and R. P. Van Duyne, *Journal of the American Chemical Society*, 2005, **127**, 2264-2271.
119. J. S. Kim, E. Kuk, K. N. Yu, J. H. Kim, S. J. Park, H. J. Lee, S. H. Kim, Y. K. Park, Y. H. Park, C. Y. Hwang, Y. K. Kim, Y. S. Lee, D. H. Jeong and M. H. Cho, *Nanomedicine-Nanotechnology Biology and Medicine*, 2007, **3**, 95-101.
120. I. Sondi and B. Salopek-Sondi, *Journal Of Colloid And Interface Science*, 2004, **275**, 177-182.
121. B. Wong, in *Chemistry Thesis: The Preparation of Nanocomposite Materials using Supercritical Carbon Dioxide*, University of Nottingham, Nottingham, 2005.
122. J. P. Abid, A. W. Wark, P. F. Brevet and H. H. Girault, *Chemical Communications*, 2002, 792-793.
123. H. H. Huang, X. P. Ni, G. L. Loy, C. H. Chew, K. L. Tan, F. C. Loh, J. F. Deng and G. Q. Xu, *Langmuir*, 1996, **12**, 909-912.
124. S. A. Dong and S. P. Zhou, *Materials Science and Engineering B-Solid State Materials for Advanced Technology*, 2007, **140**, 153-159.

125. H. Hirai, Y. Nakao and N. Toshima, *Journal of Macromolecular Science-Chemistry*, 1979, **A13**, 727-750.
126. H. Bonnemann and R. M. Richards, *European Journal Of Inorganic Chemistry*, 2001, 2455-2480.
127. J. A. Creighton, C. G. Blatchford and M. G. Albrecht, *Journal Of The Chemical Society-Faraday Transactions II*, 1979, **75**, 790-798.
128. P. C. Lee and D. Meisel, *Journal of Physical Chemistry*, 1982, **86**, 3391-3395.
129. D. D. Evanoff and G. Chumanov, *Journal of Physical Chemistry B*, 2004, **108**, 13948-13956.
130. J. L. H. Chau, M. K. Hsu, C. C. Hsieh and C. C. Kao, *Materials Letters*, 2005, **59**, 905-908.
131. B. S. Yin, H. Y. Ma, S. Y. Wang and S. H. Chen, *Journal of Physical Chemistry B*, 2003, **107**, 8898-8904.
132. K. Philippot and B. Chaudret, *Comptes Rendus Chimie*, 2003, **6**, 1019-1034.
133. B. Chaudret, *Comptes Rendus Physique*, 2005, **6**, 117-131.
134. M. Okumura, S. Nakamura, S. Tsubota, T. Nakamura, M. Azuma and M. Haruta, *Catalysis Letters*, 1998, **51**, 53-58.
135. K. Wegner, B. Walker, S. Tsantilis and S. E. Pratsinis, *Chemical Engineering Science*, 2002, **57**, 1753-1762.
136. V. Haas, R. Birringer, H. Gleiter and S. E. Pratsinis, *Journal of Aerosol Science*, 1997, **28**, 1443-1453.
137. M. V. Volpe, A. Longo, L. Pasquini, V. Casuscelli and G. Carotenuto, *Journal Of Materials Science Letters*, 2003, **22**, 1697-1699.
138. M. P. Stevens, *Polymer Chemistry: An Introduction*, O.U.P., New York, 1990.
139. R. J. Young and P. A. Lovell, *Introduction To Polymers*, Chapman and Hall, London, 1991.
140. G. S. Misra, *Introductory Polymer Chemistry*, Wiley Eastern Limited, New Delhi, 1993.
141. D. V. Goia, *Journal Of Materials Chemistry*, 2004, **14**, 451-458.
142. E. Hutter and J. H. Fendler, *Advanced Materials*, 2004, **16**, 1685-1706.
143. g. schmid, *clusters and colloids: from theory to applications*, VCH, Weinham, 1994.
144. N. V. Serebryakova, O. Y. Uryupina and V. I. Roldughin, *Colloid Journal*, 2005, **67**, 79-84.
145. T. S. Ahmadi, Z. L. Wang, A. Henglein and M. A. ElSayed, *Chemistry Of Materials*, 1996, **8**, 1161-&.
146. M. Ji, X. Y. Chen, C. M. Wai and J. L. Fulton, *Journal Of The American Chemical Society*, 1999, **121**, 2631-2632.
147. C. Petit, P. Lixon and M. P. Pileni, *Journal Of Physical Chemistry*, 1993, **97**, 12974-12983.
148. M. P. Pileni, *Journal Of Physical Chemistry*, 1993, **97**, 6961-6973.
149. G. Carotenuto and L. Nicolais, *Journal Of Materials Chemistry*, 2003, **13**, 1038-1041.
150. A. B. R. Mayer, *Materials Science & Engineering C-Biomimetic And Supramolecular Systems*, 1998, **6**, 155-166.
151. G. Carotenuto, B. Martorana, P. B. Perlo and L. Nicolais, *Journal Of Materials Chemistry*, 2003, **13**, 2927-2930.

152. S. Matsuda and S. Ando, *Japanese Journal Of Applied Physics Part 1- Regular Papers Short Notes & Review Papers*, 2005, **44**, 187-192.
153. S. Porel, S. Singh, S. S. Harsha, D. N. Rao and T. P. Radhakrishnan, *Chemistry Of Materials*, 2005, **17**, 9-12.
154. S. Matsuda, S. Ando and T. Sawada, *Electronics Letters*, 2001, **37**, 706-707.
155. S. Koizumi, S. Matsuda and S. Ando, *Journal Of Photopolymer Science And Technology*, 2002, **15**, 231-236.
156. A. L. Stepanov, S. N. Abdullin, V. Y. Petukhov, Y. N. Osin, R. I. Khaibullin and I. B. Khaibullin, 2000, **80**, 23-28.
157. A. L. Stepanov, S. N. Abdullin and I. B. Khaibullin, *Journal Of Non-Crystalline Solids*, 1998, **223**, 250-253.
158. T. Clifford, *Fundamentals of supercritical fluid.*, OUP, Oxford, 1999.
159. T. Andrews, *philosophical Magazine*, 1870, 150-153.
160. J. B. Hannay and J. Hogarth, *P. Roy. Soc. Lond.*, 1879, **29**, 324-326.
161. J. A. Darr and M. Poliakoff, *Chemical Reviews*, 1999, **99**, 495-541.
162. A. I. Cooper, *Journal of Materials Chemistry*, 2000, **10**, 207-234.
163. *6th International Symposium on Supercritical Fluids*, eds. M. Poliakoff, M. W. George and S. M. Howdle, Nottingham, United Kingdom, 1999.
164. J. A. Hyatt, *Journal of Organic Chemistry*, 1984, **49**, 5097-5101.
165. J. A. Behles and J. M. DeSimone, *Pure and Applied Chemistry*, 2001, **73**, 1281-1285.
166. A. O'Neil and J. J. Watkins, *Green Chemistry*, 2004, **6**, 363-368.
167. D. K. Taylor, R. Carbonell and J. M. DeSimone, *Annual Review of Energy and the Environment*, 2000, **25**, 115-146.
168. F. Furno, P. Licence, S. M. Howdle and M. Poliakoff, *Actualite Chimique*, 2003, 62-66.
169. J. R. Hyde, P. Licence, D. Carter and M. Poliakoff, *Applied Catalysis a- General*, 2001, **222**, 119-131.
170. C. F. Kirby and M. A. McHugh, *Chemical Reviews*, 1999, **99**, 565-602.
171. D. L. Tomasko, H. B. Li, D. H. Liu, X. M. Han, M. J. Wingert, L. J. Lee and K. W. Koelling, 2003, **42**, 6431-6456.
172. J. L. Kendall, D. A. Canelas, J. L. Young and J. DeSimone, *Chemical Reviews*, 1999, **99**, 543-563.
173. W. Wang, A. Naylor and S. M. Howdle, *Macromolecules*, 2003, **36**, 5424-5427.
174. T. Arita, S. Beuermann, M. Buback and P. Vana, *E-Polymers*, 2004.
175. T. Arita, S. Beuermann, M. Buback and P. Vana, *Macromolecular Materials And Engineering*, 2005, **290**, 283-293.
176. K. A. Arora, A. J. Lesser and T. J. McCarthy, *Macromolecules*, 1999, **32**, 2562-2568.
177. A. I. Cooper, C. D. Wood and A. B. Holmes, *Industrial & Engineering Chemistry Research*, 2000, **39**, 4741-4744.
178. J. M. Desimone, Z. Guan and C. S. Elsbernd, *Science*, 1992, **257**, 945-947.
179. J. M. Desimone, E. E. Maury, Y. Z. Menciloglu, J. B. McClain, T. J. Romack and J. R. Combes, *Science*, 1994, **265**, 356-359.
180. S. Villarroya, K. J. Thurecht, A. Heise and S. M. Howdle, *Chemical Communications*, 2007, 3805-3813.
181. H. Tai, V. K. Popov, K. M. Shakesheff and S. M. Howdle, *Biochemical Society Transactions*, 2007, **35**, 516-521.

182. K. J. Thurecht, A. M. Gregory, W. X. Wang and S. M. Howdle, *Macromolecules*, 2007, **40**, 2965-2967.
183. J. X. Yang, W. X. Wang, P. J. A. Sazio and S. M. Howdle, *European Polymer Journal*, 2007, **43**, 663-667.
184. S. Villarroya, J. X. Zhou, K. J. Thurecht and S. M. Howdle, *Macromolecules*, 2006, **39**, 9080-9086.
185. K. J. Thurecht, A. Heise, M. deGeus, S. Villarroya, J. X. Zhou, M. F. Wyatt and S. M. Howdle, *Macromolecules*, 2006, **39**, 7967-7972.
186. S. Villarroya, J. X. Zhou, C. J. Duxbury, A. Heise and S. M. Howdle, *Macromolecules*, 2006, **39**, 633-640.
187. D. Bratton, M. Brown and S. M. Howdle, *Journal of Polymer Science Part a-Polymer Chemistry*, 2005, **43**, 6573-6585.
188. P. Christian, M. R. Giles, R. M. T. Griffiths, D. J. Irvine, R. C. Major and S. M. Howdle, *Macromolecules*, 2000, **33**, 9222-9227.
189. M. R. Giles, J. N. Hay, S. M. Howdle and R. J. Winder, *Polymer*, 2000, **41**, 6715-6721.
190. P. Christian, S. M. Howdle and D. J. Irvine, *Macromolecules*, 2000, **33**, 237-239.
191. I. Kikic and F. Vecchione, 2003, **7**, 399-405.
192. Z. Knez and E. Weidner, *Current Opinion in Solid State & Materials Science*, 2003, **7**, 353-361.
193. Y. P. Sun, H. W. Rollins and R. Guduru, *Chemistry of Materials*, 1999, **11**, 7-+.
194. M. J. Meziani, P. Pathak, F. Beacham, L. F. Allard and Y. P. Sun, *Journal of Supercritical Fluids*, 2005, **34**, 91-97.
195. M. C. McLeod, W. F. Gale and C. B. Roberts, *Langmuir*, 2004, **20**, 7078-7082.
196. M. J. Meziani, P. Pathak, L. F. Allard and Y. P. Sun, in *Supercritical Carbon Dioxide: Separations and Processes*, 2003, pp. 309-323.
197. M. J. Meziani and Y. P. Sun, *Journal of the American Chemical Society*, 2003, **125**, 8015-8018.
198. Y. P. Sun, P. Atorngitjawat and M. J. Meziani, *Langmuir*, 2001, **17**, 5707-5710.
199. T. Adschiri, Y. Hakuta, K. Sue and K. Arai, *Journal of Nanoparticle Research*, 2001, **3**, 227-235.
200. T. Adschiri, K. Kanazawa and K. Arai, *Journal of the American Ceramic Society*, 1992, **75**, 2615-2618.
201. T. Adschiri, K. Kanazawa and K. Arai, *Journal of the American Ceramic Society*, 1992, **75**, 1019-1022.
202. F. Cansell, B. Chevalier, A. Demourgues, J. Etourneau, C. Even, Y. Garrabos, V. Pessey, S. Petit, A. Tressaud and F. Weill, *Journal of Materials Chemistry*, 1999, **9**, 67-75.
203. L. J. Cote, A. S. Teja, A. P. Wilkinson and Z. J. Zhang, *Fluid Phase Equilibria*, 2003, **210**, 307-317.
204. L. J. Cote, A. S. Teja, A. P. Wilkinson and Z. J. Zhang, *Journal of Materials Research*, 2002, **17**, 2410-2416.
205. V. Pessey, R. Garriga, F. Weill, B. Chevalier, J. Etourneau and F. Cansell, *High Pressure Research*, 2001, **20**, 289-298.
206. P. Boldrin, A. K. Hebb, A. A. Chaudhry, L. Otley, B. Thiebaut, P. Bishop and J. A. Darr, *Industrial & Engineering Chemistry Research*, 2007, **46**, 4830-4838.

207. E. Lester, P. Blood, J. Denyer, D. Giddings, B. Azzopardi and M. Poliakoff, *Journal of Supercritical Fluids*, 2006, **37**, 209-214.
208. A. Cabanas, J. A. Darr, E. Lester and M. Poliakoff, *Journal of Materials Chemistry*, 2001, **11**, 561-568.
209. A. Cabanas, J. A. Darr, E. Lester and M. Poliakoff, *Chemical Communications*, 2000, 901-902.
210. Y. Zhang and C. Erkey, *Journal of Supercritical Fluids*, 2006, **38**, 252-267.
211. J. J. Watkins and T. J. McCarthy, *Chemistry of Materials*, 1995, **7**, 1991-&.
212. R. Kumar, S. Roy, M. Rashidi and R. J. Puddephatt, *Polyhedron*, 1989, **8**, 551-553.
213. Y. F. Zong and J. J. Watkins, *Chemistry of Materials*, 2005, **17**, 560-565.
214. A. Cabanas, D. P. Long and J. J. Watkins, *Chemistry of Materials*, 2004, **16**, 2028-2033.
215. E. T. Hunde and J. J. Watkins, *Chemistry of Materials*, 2004, **16**, 498-503.
216. A. Cabanas, X. Y. Shan and J. J. Watkins, *Chemistry of Materials*, 2003, **15**, 2910-2916.
217. A. Cabanas, J. M. Blackburn and J. J. Watkins, *Microelectronic Engineering*, 2002, **64**, 53-61.
218. J. M. Blackburn, D. P. Long, A. Cabanas and J. J. Watkins, *Science*, 2001, **294**, 141-145.
219. X. R. Ye, J. B. Talbot, S. H. Jin, Y. H. Lin and C. M. Wai, *Abstracts of Papers of the American Chemical Society*, 2005, **229**, U926-U926.
220. X. R. Ye, Y. H. Lin, C. M. Wai, J. B. Talbot and S. H. Jin, *Journal of Nanoscience and Nanotechnology*, 2005, **5**, 964-969.
221. X. R. Ye, H. F. Zhang, Y. H. Lin, L. S. Wang and C. M. Wai, *Journal of Nanoscience and Nanotechnology*, 2004, **4**, 82-85.
222. X. R. Ye, Y. H. Lin, C. M. Wang, M. H. Engelhard, Y. Wang and C. M. Wai, *Journal of Materials Chemistry*, 2004, **14**, 908-913.
223. C. D. Saquing, D. Kang, M. Aindow and C. Erkey, *Microporous and Mesoporous Materials*, 2005, **80**, 11-23.
224. Y. Zhang, D. F. Kang, C. Saquing, M. Aindow and C. Erkey, *Industrial & Engineering Chemistry Research*, 2005, **44**, 4161-4164.
225. K. S. Morley, P. Licence, P. C. Marr, J. R. Hyde, P. D. Brown, R. Mokaya, Y. D. Xia and S. M. Howdle, 2004, **14**, 1212-1217.
226. K. S. Morley, P. C. Marr, P. B. Webb, A. R. Berry, F. J. Allison, G. Moldovan, P. D. Brown and S. M. Howdle, *Journal of Materials Chemistry*, 2002, **12**, 1898-1905.
227. K. S. Morley, P. B. Webb, N. V. Tokareva, A. P. Krasnov, V. K. Popov, J. Zhang, C. J. Roberts and S. M. Howdle, *European Polymer Journal*, 2007, **43**, 307-314.
228. B. Wong, S. Yoda and S. M. Howdle, *Journal of Supercritical Fluids*, 2007, **42**, 282-287.
229. R. K. Boggess, L. T. Taylor, D. M. Stoakley and A. K. StClair, *Journal of Applied Polymer Science*, 1997, **64**, 1309-1317.
230. S. Yoda, A. Hasegawa, H. Suda, Y. Uchimaru, K. Haraya, T. Tsuji and K. Otake, *Chemistry of Materials*, 2004, **16**, 2363-2368.
231. H. Suda, S. Yoda, A. Hasegawa, T. Tsuji, K. Otake and K. Haraya, *Desalination*, 2006, **193**, 211-214.
232. S. Yoda, Y. Takebayashi, T. Sugeta and K. Otake, *Journal Of Non-Crystalline Solids*, 2004, **350**, 320-325.

Chapter 2: Supercritical impregnation of optical polymers with silver nanoparticles

2.1 Hypothesis and Overview

Hypothesis

The embedding of nanoscopic metal structures into polymeric matrices represents a convenient way to stabilise a controlled dispersion of protected nanoparticles whilst taking advantage of their physical characteristics. Supercritical carbon dioxide (scCO₂) is used with the intention of producing silver nanoparticles in optically transparent polymers, creating fine scale dispersions of particles within a prefabricated polymeric component. Characterization of these nanocomposites will be performed using transmission electron microscopy (TEM) and UV-visible spectroscopy. The potential for control of the nano-structure of the products will be investigated. Also, a possible application will be tested by determining the responses in surface-enhanced Raman spectroscopy (SERS) for both 4-aminothiophenol and rhodamine 6G target molecules in the presence of the substrate. If the impregnation and response of the materials are successful, they will offer significant benefits over more conventional SERS substrates in that they should be cheap, flexible, mechanically robust and temporally stable. Post-processing the films is attempted via simple etching techniques to provide an additional degree of design control and the potential to fabricate devices with unique excitation and detection geometries for a wide range of applications.

Overview

The chapter begins by setting out the aims of this project. This is intended to provide some insight as to the intended direction of the work as well as outlining its targets. The previous literature is then discussed briefly, but in a focussed manner. This is because a general background to the fields of this work, such as nanocomposites and supercritical fluids, has already been provided in the previous chapter. Instead this more narrow-scope literature discussion attempts to sum-up all previous use of scCO₂ to produce silver-polymer nanocomposites. Then, by the use of examples, will illustrate the alternative methods of production and the applications of such materials. The introductory section of the chapter finishes with an explanation of the general reaction scheme used and the choice of precursor.

The remainder of the chapter is a discussion of the results obtained. First reported is the trial of different possible polymer substrates, and how this affected the choice of substrate to use. This is followed by an investigation of the effect of several reaction parameters, which runs parallel to the development of the system. The last two results sections describe, first, determination of the solubility of the precursor complex and associated complexes and, second, tests of the product nanocomposites for effectiveness in SERS applications. Finally, conclusions as to the effectiveness and implications of this research will be made, as well as suggestions of future work.

2.2 Chapter 2 – Contents

2.1	Hypothesis and Overview	92
2.2	Chapter 2 – Contents	94
2.3	Introduction	96
2.3.1	Aims.....	96
2.3.2	Literature review.....	98
2.3.3	Reaction scheme	112
2.3.3.1	Precursor silver complex	115
2.4	Choice of polymer	116
2.4.1	Polymer structures	116
2.4.1.1	Teflon [®] AF	116
2.4.1.2	PMMA	118
2.4.1.3	Polycarbonate	119
2.4.2	Results of polymer trials.....	120
2.4.2.1	Teflon [®] AF	120
2.4.2.2	PMMA	125
2.4.2.3	Polycarbonate	130
2.4.2.4	Conclusions of polymer trials.....	132
2.5	Effect of temperature and pressure	133
2.5.1	Temperature.....	133
2.5.2	Pressure.....	134
2.5.3	Influence on general method	136
2.6	Development of the process and equipment.....	138
2.7	Effect of precursor mass	142
2.8	Effect of H ₂ reduction time.....	144
2.9	Impregnation time and TEM investigation.....	148
2.9.1	Venting	149
2.9.2	UV-vis study of impregnation time	151
2.9.3	TEM Investigation.....	154
2.9.3.1	Problems/limitations of TEM imaging	165

2.9.3.2	Impregnation time – nanoparticle depth.....	168
2.9.3.3	Comparison of nanoparticle size from TEM images.....	171
2.10	Solubility studies	176
2.10.1	Complexes investigated.....	178
2.10.1.1	Silver complexes:	179
2.10.1.2	Copper complexes:	180
2.10.2	Results of solubility measurements	181
2.10.2.1	Silver solubility results	181
2.10.2.2	Copper solubility results	183
2.10.3	Implications for the impregnation process	184
2.11	Applications testing	188
2.11.1	Advantages of the substrate for SERS.....	188
2.11.2	Aims of these tests.....	189
2.11.3	Samples tested	190
2.11.4	Results	193
2.11.4.1	Reflection spectra and refractive index measurement.....	193
2.11.4.2	Surface Enhanced Raman Characterisation.....	195
2.11.4.3	Plasma etching.....	198
2.11.5	Conclusions of SERS testing.....	201
2.12	Overall conclusions and future work.....	202
2.13	References	205

2.3 Introduction

2.3.1 Aims

The core target of this investigation was to determine the viability of using the scCO₂ impregnation processes described in Chapter 1 for the preparation of optical quality nanocomposites based upon silver nanoparticles. This represents a particular challenge for scCO₂ processing. The key issue is to retain optical transparency, for this it is vital that the introduced nanoparticles must all be uniformly distributed and below a certain size, with no clustering or agglomeration. If this can be achieved it would mark a significant step forward in the field of scCO₂ processing.

This research is not only useful for furthering the development and versatility of the scCO₂ technique. It also represents a potentially important solution to problems associated with the manufacture of useful nanocomposite material of this nature. It is necessary to embed optically active nanoparticles into a suitable substrate for their application. The use of transparent polymeric materials allows for the fabrication of appropriate devices and components tailored for applications. However, most conventional fabrication methods for introducing metal nanoparticles into polymer cause unavoidable aggregation of the nanoparticles, disrupting their properties. scCO₂ processing provides a simple route to produce the metal nanoparticles *in situ* within prefabricated polymeric materials. This is preferable to pre-mixing nanoparticles into a polymer as it does not require surface modification of the nanoparticles and avoids the possibility of

aggregation during processing. Importantly, the polymeric materials can be impregnated with nanoparticles after they have been processed into their final form. Our process utilises scCO_2 as a solvent for an organometallic precursor molecule which provides rapid diffusion into the polymer. The precursor can then be reduced to form elemental silver nanoparticles.

In order to determine the potential of this process, it is necessary to trial different arrangements and conditions. This allows the viability and level of control to be assessed. To this end the following aspects have been involved in this work and will be described within this chapter:

- The investigation of a range of potential substrates.
- The development of the reaction process to improve reproducibility, homogeneity and quality of products.
- The investigation of the effects of reaction conditions on the products.
- Solubility studies of organometallic complexes to better understand factors affecting the impregnation process and to better design an alternative complex for future use.

In addition to these factors based upon the synthesis of a functional product, it is also a target of this work to show the potential use and application of such a product. The silver nanoparticle embedded transparent polymer substrates produced here have many potential applications. Perhaps the most relevant specifically to optical systems are the following: Non-linear optical limitation, metal enhanced fluorescence and surface enhanced Raman spectroscopy. It was

proposed to analyse the materials produced for their potential in these fields. Unfortunately it was not possible to test activity in all of these applications. However, in order to demonstrate the functional use of the material produced, it has been possible to perform investigations of the SERS activity of the products.

2.3.2 Literature review

The intention of this section is to give a brief but more detailed description of the body of work specifically regarding the formation of silver nanoparticles in polymer. Within this area attention will be paid to previous work concerning scCO₂ impregnation or optical applications.

The foundations of nanoparticle impregnation into polymers are the early works carried out by Watkins and McCarthy in 1995, detailed in Chapter 1 section 1.5.2.4. Their group undertook the first nanoparticle impregnation using this technique, initially with a platinum precursor, but then later extending the method to other metal precursors. They did not, however, extend this technique to the use of silver precursors. This was first attempted by Boggess *et al.* in 1997.¹ Boggess introduced [1,5-cyclooctadiene silver(I)-1,1,1,5,5,5-hexafluoroacetylacetonate] – abbreviated to Ag(hfac)COD, the same precursor used in this work, into polyimide films. The impregnation conditions used were as follows: Temperature of 110 °C, pressure of 5000 psi (34.5 MPa), and a reaction time of between 0.5 and 3 hours. After the scCO₂ stage the polyimide films were cured in an oven under air at 300 °C. The samples produced had a reflective mirror-like surface because of a highly surface localised impregnation of silver, most likely caused by the high

temperatures and short reaction times used. The surface is a discontinuous metallic silver layer as shown by TEM of a cross section of the polyimide (Fig. 21). The TEMs show the layer to be approximately 100 nm thick, and most of the silver in the film is part of this layer. However, there are particles of silver, most less than 20 nm in diameter, that extend several hundred nanometres into the polyimide. This demonstrated that the silver precursor, Ag(hfac)COD, could be effectively used for the scCO₂ impregnation of polymers. Unfortunately the surface coating of the polymer with a silver film is a barrier to applications that require the passing of light into the material without reflectance or scattering.

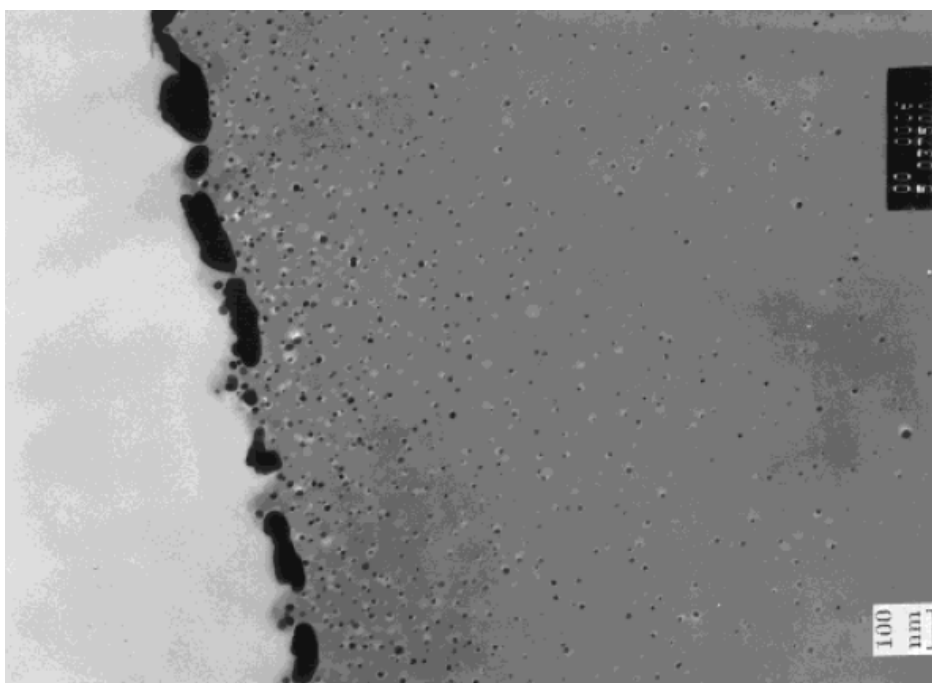
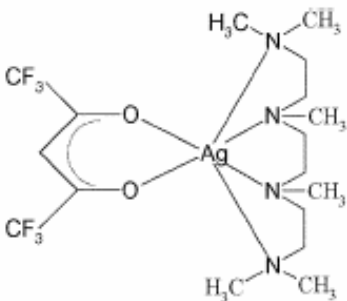
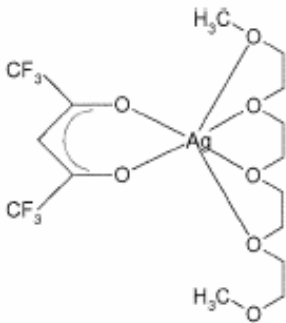


Figure 21 – Reflective silver film on polyimide surface and smaller particles deeper into the substrate.¹

The next relevant publication in this field came from Nottingham.² This paper documented the use of a further two previously undocumented and

specifically designed precursor structures (see Table 2) for the impregnation of poly(styrene divinylbenzene) beads. Impregnation was at a temperature of 40 °C and a pressure of 4000 psi (27.6 MPa) for 24 hours. The introduced precursor complex was then reduced to nanoparticles using hydrogen at 60 °C and 1000 psi (6.9 MPa) for 48 hours. Finally the substrate was cleaned with scCO₂ to remove any trapped dissociated ligands, at 4000 psi (27.6 MPa) and 40 °C for 24 hours. This lower temperature and longer impregnation time may have produced more homogeneous nanoparticles, rather than the surface metal film seen by Boggess *et al.*, although it is difficult to ascertain this for sure because the TEM imaging was performed on ground up samples rather than microtomed cross sections of the substrate (Fig. 22).

Table 2 – Precursor complexes used in the impregnation process by Morley *et al.*²

Ag(hfpd) tetraamine [A]	Ag(hfpd) tetraglyme [B]
	

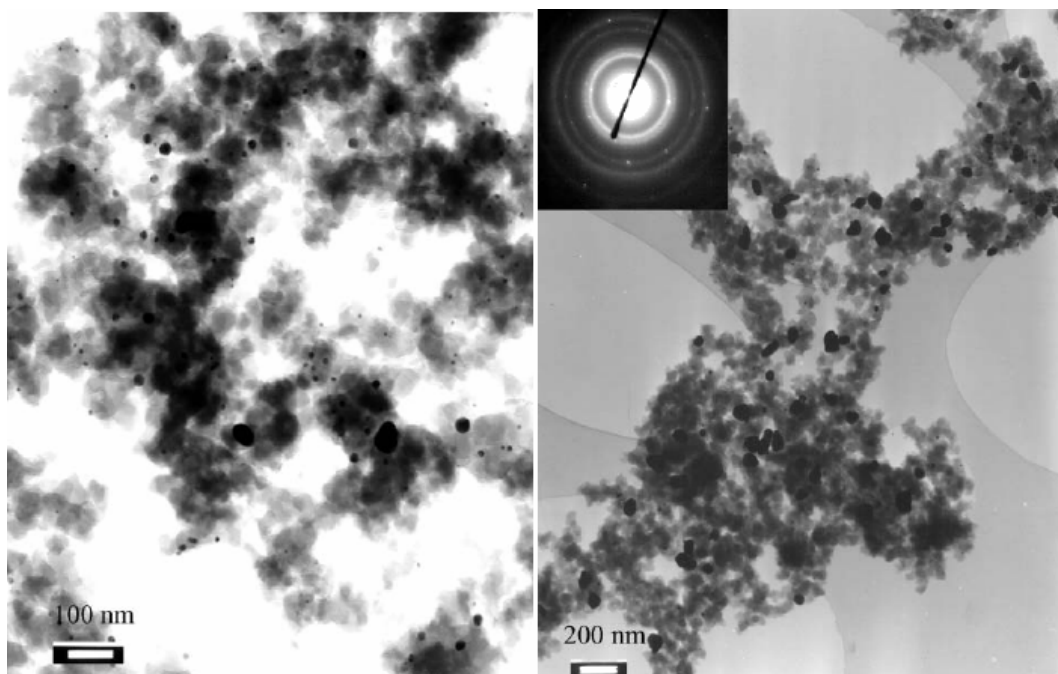


Figure 22 – TEM micrographs showing silver nanoparticles in poly(styrene divinylbenzene) prepared by grinding. Left image is impregnated with precursor A and the right image precursor B, see Table 2. From Morley *et al.*²

The development of this process by Morley *et al.* marked a step forward from the work of Boggess *et al.* especially with respect to polymer substrates, as it showed that milder conditions and hydrogen reduction could be used effectively. Later, in 2004, the same research group applied this process, under similar conditions, for the impregnation of silver nanoparticles into silicone polymeric catheter materials. This was performed in order to test the antimicrobial activity of silver nanoparticles for use in medical applications, meaning the harmful-solvent free nature of the scCO₂ process was advantageous, and shows the successful formation of silver nanoparticles as demonstrated by TEM imaging (Fig. 23).³

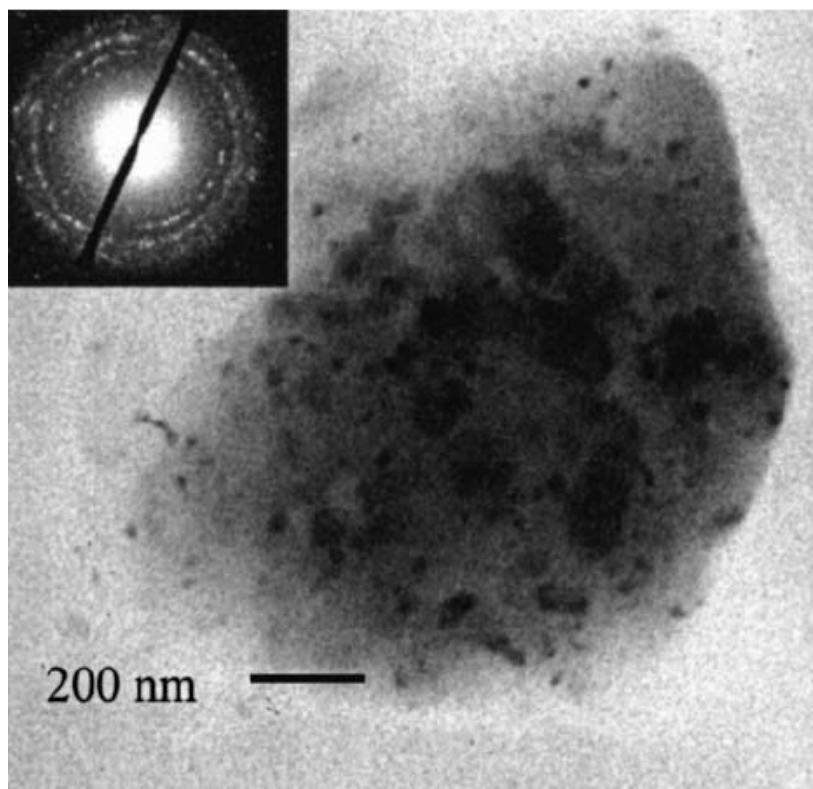


Figure 23 - TEM image of silver dispersed in silicone, from ground samples. The associated diffraction pattern (inset) has been indexed against standards to confirm that the particles are metallic silver.³

The most recent work published on the scCO_2 infusion of silver nanoparticles into polymeric substrates is again by Morley *et al.*⁴ This paper returns to the theme of biomedical application, but this time for the introduction of silver nanoparticles to ultra-high-molecular-weight polyethylene (UHMWPE). This is shown to affect the wear and tribochemical properties of the polymer substrate, which is often used in hardwearing implant materials such as artificial hips. The same silver precursor was used (identified as ‘A’ in Table 2), and under similar conditions. On removal the products were found to have a covering of metallic silver, which was removed. However this still left the polymer with a grey

metallic lustre indicating the presence of metallic silver, and a high loading. TEM confirms the presence of silver nanoparticles, as shown in Fig. 24. Again, only limited information can be drawn from the TEM imaging because the grinding method used for sample preparation. However, this paper also utilises atomic force microscopy (AFM) to compare with the TEM and to acquire a ‘bigger picture’ idea as to the location and distribution of the nanoparticles (Fig. 25). This revealed a homogeneous distribution of the nanoparticles within the bulk of the material.

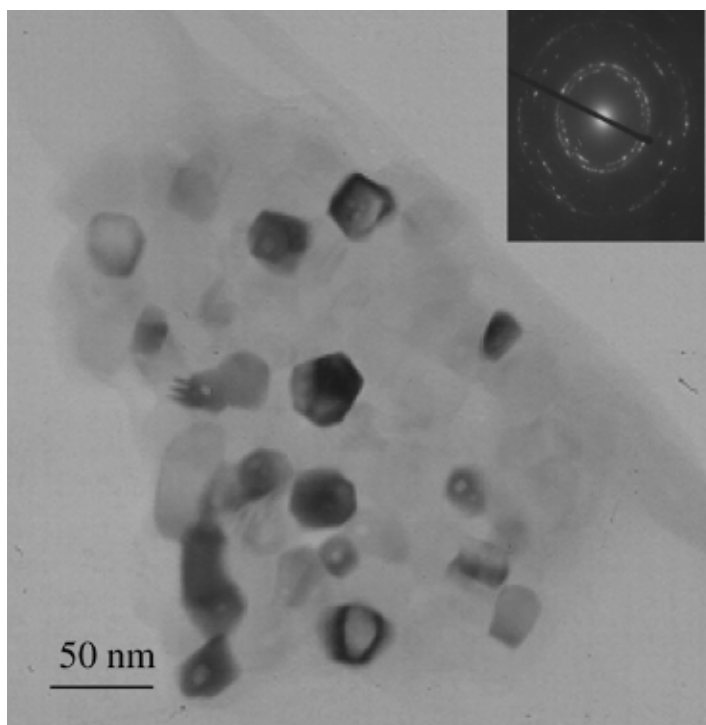


Figure 24 – TEM image showing silver nanoparticles in UHMWPE substrate.⁴

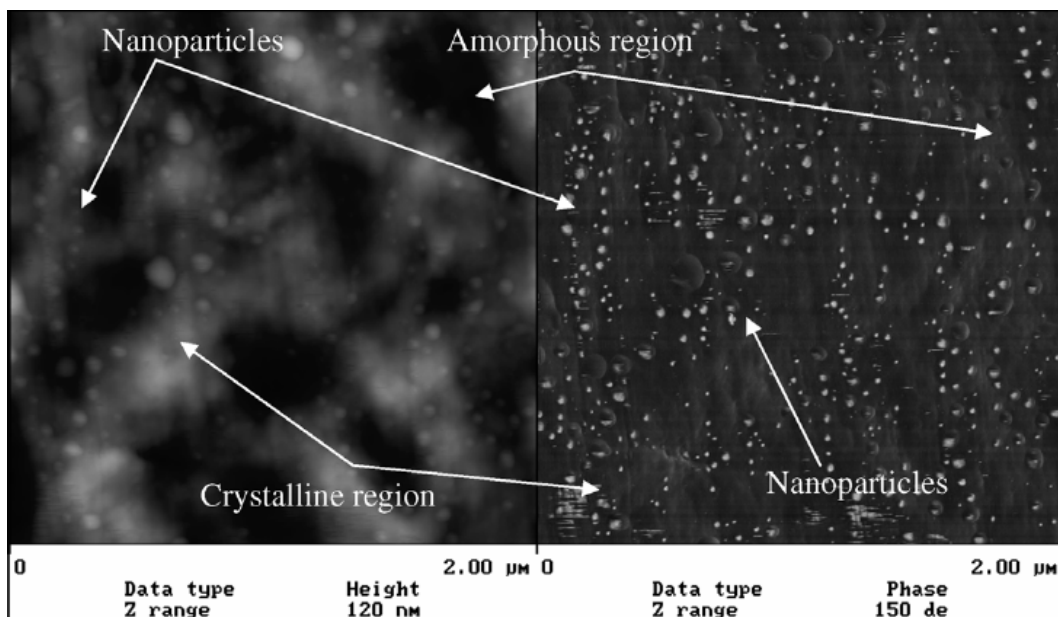


Figure 25 - 2 μm x 2 μm tapping mode AFM image, showing height (a) and phase (b) images of UHMWPE with silver nanoparticles. The images were collected from a cryomicrotomed surface and the crystalline regions of the polymer and nanoparticles can be clearly identified in both the height and phase images.⁴

The cryomicroscopy used to prepare a sample for AFM analysis is important as it allowed a cross section of the material to be observed. By this method it is possible to investigate the nanostructure in a state much more closely resembling the actual bulk of the substrate. Unfortunately the resolution of these AFM results are limited, and so only relatively large particles of silver are detected. However, it still effectively demonstrates a high loading and homogeneous distribution.

That summarises all of the most relevant publications to date concerning the scCO₂ impregnation of silver nanoparticles into polymeric substrates. Following is a brief overview of the most applicable papers on the embedding of silver nanoparticles in polymer substrates for optical applications. There has been

much interest in this topic because of the potent properties of silver nanoparticles in this field.

Porel *et al.* successfully demonstrated the synthesis of silver nanoparticle embedded polymer films and their application as non-linear optical limitation materials in 2005. Specifically, they reported the deposition of thin films of poly(vinyl alcohol) (PVA) with embedded silver nanoparticles (see Fig. 26).⁵ This was achieved by spin coating a solution of silver nitrate and PVA dissolved in water onto a sacrificial polystyrene support, which was later removed. The films were then heated to between 50 and 110 °C in order to reduce/decompose the silver nitrate and form nanoparticles. This process is assisted by the presence of the PVA, which acts as a reducing agent.

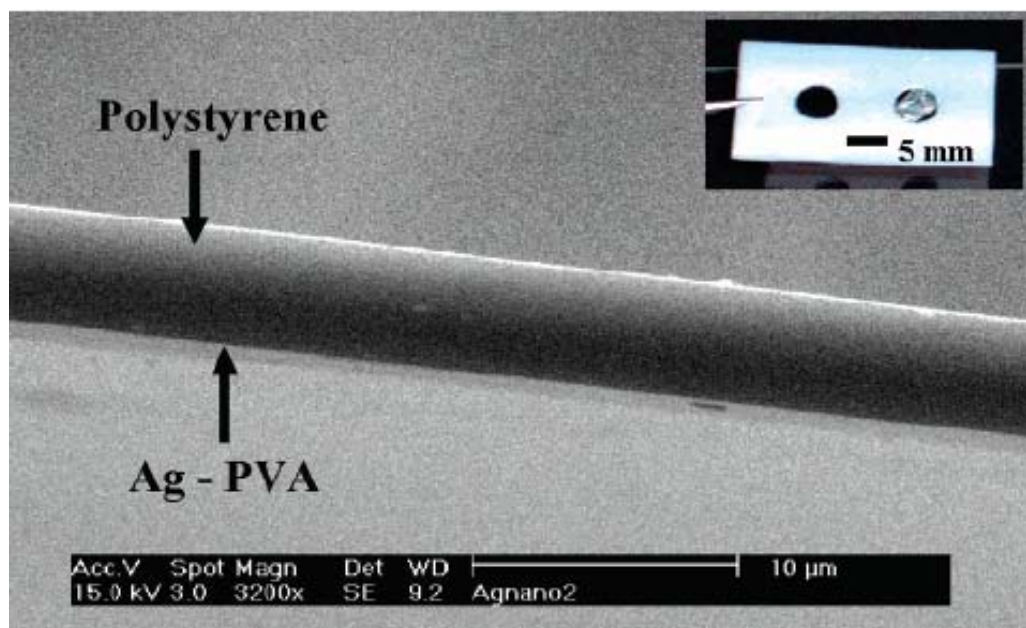


Figure 26 - SEM of the cross-sectional view of Ag-PVA/PS film. Inset shows the Ag-PVA film on a Teflon support; the empty hole shows the contrast.⁵

TEM images of the PVA film show a homogeneous distribution of silver nanoparticles. Application testing demonstrated a significant non-linear optical limitation effect (Fig. 27). These results have since been developed and investigated in more detail.⁶

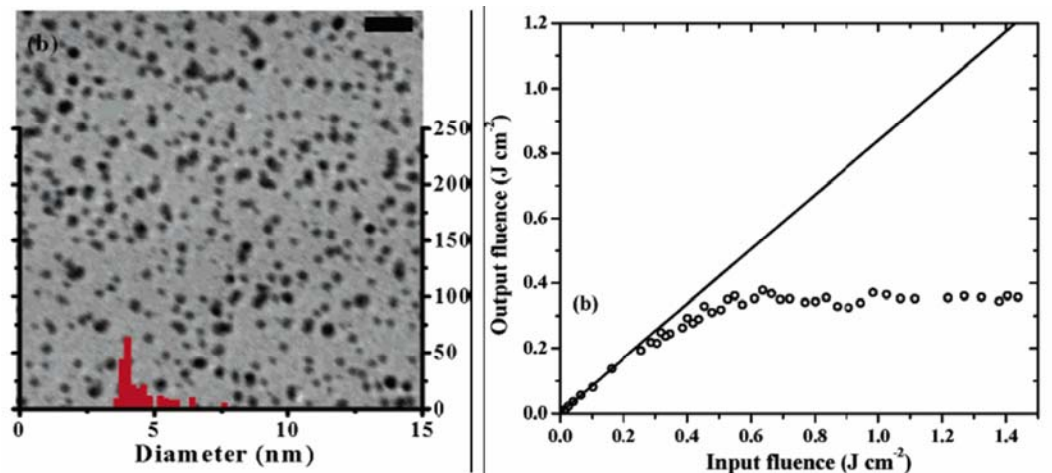


Figure 27 – Left image: Representative TEM image of silver nanoparticle embedded PVA substrate. The scale bar is 20 nm and the histogram shows the particle size distribution in the image area. Right image: Optical limiting in Ag-PVA/PS film on glass substrate (Ag/PVA 0.058), the full line represents 84% linear transmission.⁵

The most advanced work concerning polymer supported silver nanoparticles for metal enhanced fluorescence (MEF) has been completed by Aslan *et al.*^{7, 8} This group has experimented with the deposition of silver nanoparticles onto the surface of polymers, and indeed reported the first ever findings of MEF from plastic substrates. They speculate that plastic substrates for MEF will find common place, as compared to the more expensive and less versatile traditional silica based supports, and that industrial interest in utilizing

plastics is primarily driven by the fact that these materials are less expensive and easier to mass produce than silica based substrates.

The production method for the silver-polymer nanocomposites produced by Aslan *et al.* is now described. The substrate to be modified was 1 mm thick sheets of polycarbonate, chosen for its ideal properties, biocompatibility and potential for application. These were then etched in order to form hydroxylated/carboxylated surface groups using two alternative routes; UV light irradiation or base etching (see Fig. 28). In the UV-etching, the polymer was irradiated with UV-light (254 nm, 0.6 mW cm⁻²) for 2 h. This resulted in the formation of hydroxyl groups on the polycarbonate. In the base etching, the polymer was hydrolyzed in 2 M aqueous NaOH solution for 30 min at 70 °C, then rinsed with deionised water before being hydrolyzed further in acetic acid for 15 min at room temperature. This procedure resulted in the formation of a mixture of hydroxyl and carboxylic acid groups on the polymer films. The hydrolysed products from either of these routes were subsequently silanized with a 2% v/v solution of 3-(aminopropyl) triethoxysilane (APS) in denatured ethanol for 2 h, in order to introduce an amine group. The final step was then to form a film of silver nanoparticles on this surface by the reduction of aqueous silver nitrate. The exact method of this wet chemistry nanoparticle generation step is not reported clearly, but seems to be based on NaOH reduction followed by ammonia re-dissolution of the precipitate before further precipitation onto the substrate.⁹

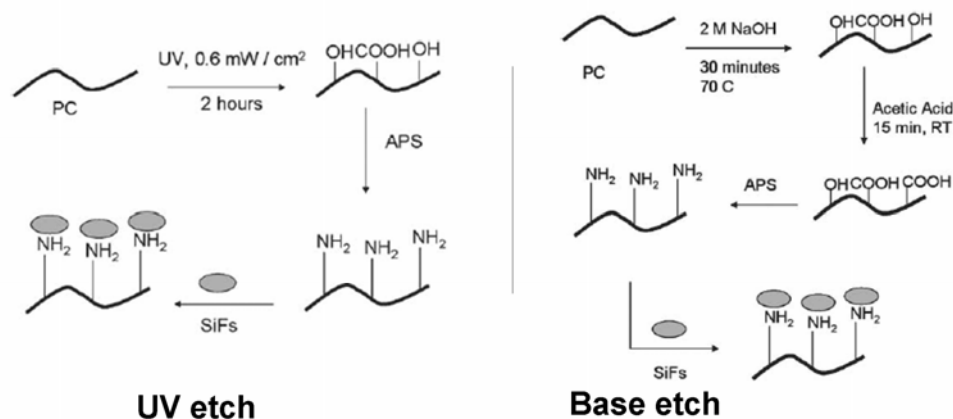


Figure 28 – Schematic of polycarbonate surface etching, by UV irradiation (left) and base treatment (right).⁸

The silver nanoparticle-polymer surfaces prepared were then tested for MEF, with significant success. These results have already been discussed as an example of MEF in Chapter 1, section 1.3.1.2. Please refer back to figure 9 of chapter 1 which displays the appearance and activity of the nanocomposite. Unfortunately there is no direct characterisation of the nano-structure by means such as TEM. However, this research demonstrates the potential of plastics in metal-enhanced fluorescence applications. The authors state that polycarbonate films are a suitable and a cheap alternative to glass for numerous metal-enhanced fluorescence applications. And also that the research is important because of its implications for the use of silver-deposited polycarbonate in microfluidic devices and other industrial sensors based on fluorescence detection with enhanced sensitivity.

An important illustration has now been given for the production and use of silver nanoparticle polymer substrates for both optical limitation and MEF. A final illustration of the use of these materials for optical applications is now described

for the field of SERS. This is provided by the work of Lu *et al.*¹⁰ Who detailed the production of a silver nanoparticle layer on the surface of a Poly (N-isopropylacrylamide) film. This is then tested for SERS activity. The production of this material is quite a complex synthesis and is only briefly described here. Silver nanoparticles are first formed in multi-step, small scale, organic solution synthesis under argon atmosphere. This involves the rapid injection of a mixture of silver nitrate, cis-9-octadecen-1-amine and 1,2-dichlorobenzene (DCB) into a hot solution of hexadecanediol and oleic acid in DCB at 182 °C. This produces silver nanoparticles capped with oleic acid and oleylamine stabilisers (Fig. 29). The hydrophobic silver nanoparticles are then formed into a Langmuir-Blodgett film on the surface of water. This film is then transferred onto a 100 µm thick film of poly(N-isopropylacrylamide). This polymer was chosen because it has a structure that swells and shrinks by switching the temperature between 20 and 40 °C. This was intended to give a method of controlling potential SERS activity by modifying the distance between nanoparticles.

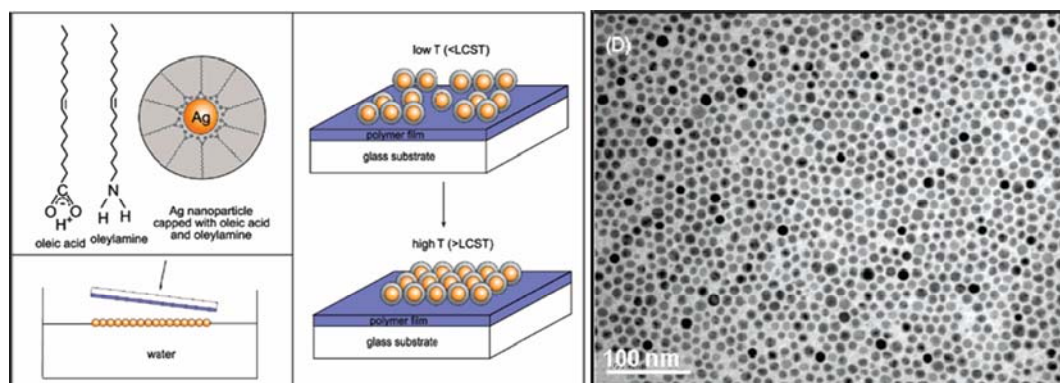


Figure 29 – Schematic showing the formation of silver-polymer nanocomposite (left), and a TEM image of the silver nanoparticle Langmuir-Blodgett film (right).¹⁰

Note that the TEM image shown is of the nanoparticles as they appear transferred to a TEM grid, and not how they appear in the polymer. Optical dark field images (not shown) indicated there is some control of nanoparticle spacing in the polymer with temperature, but also that the nanoparticles may be aggregated to some degree. The polymer must contain some water for this structure switching to occur, and after a few hours drying in air this no longer occurs. However, effective SERS enhancements were recorded from these substrates (Fig. 30). Rhodamine 6G (R6G) molecules were adsorbed on the silver nanoparticle-polymer films and SERS spectra were taken at various temperatures. The level of SERS enhancement changes with temperature because of the associated change in inter-particle spacing. This paper has shown the potential of polymeric substrates for effective SERS applications, and again this has applications for microfluidic devices and detection sensors.

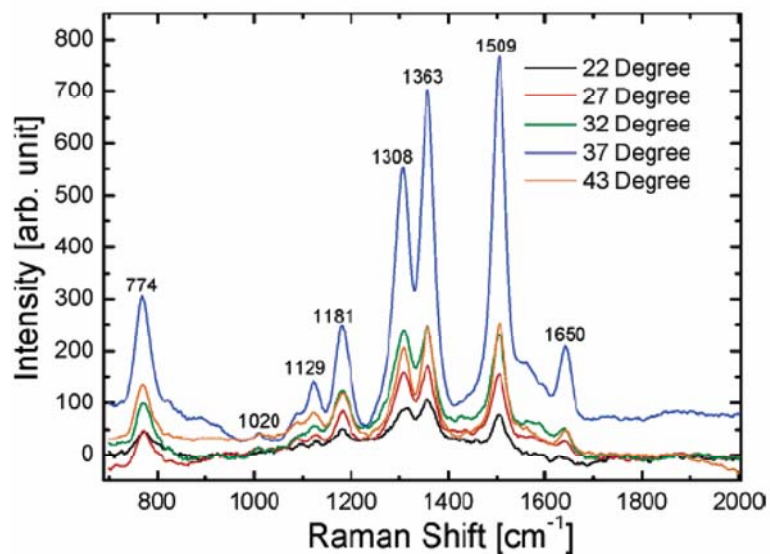


Figure 30 – SERS spectra of Rhodamine 6G (R6G) on Ag nanoparticle film at different temperatures. The R6G concentration is 10^{-5} M. The spectra are recorded using a Raman spectrophotometer (785 nm 40 mW laser excitation) and the integration time is 5 s.¹⁰

This literature review was intended to provide a foundation of the previous work in scCO₂ synthesis of silver-polymer nanocomposites, and to show, by example of non-CO₂ routes, the possible benefits to optical applications of such substrates.

2.3.3 Reaction scheme

A general reaction scheme is provided here to describe the process used. It should be noted that this does not give a comprehensive description of the exact method used for all substrates and reactions. Three alternative apparatus configurations have been used. This involved associated alterations to the reaction process described here. These changes, along with changes made to assess the effect of conditions, will be described in more detail in the relevant sections of this chapter. A technical description of the reaction apparatus and method are provided in Chapter 5.3.1 and 5.3.2 respectively.

The reaction process consists of three phases (see Fig. 31). The first phase impregnates the precursor complex into the substrate; the second decomposes the precursor and leads to the formation of nanoparticles. The third phase removes the disassociated ligands.

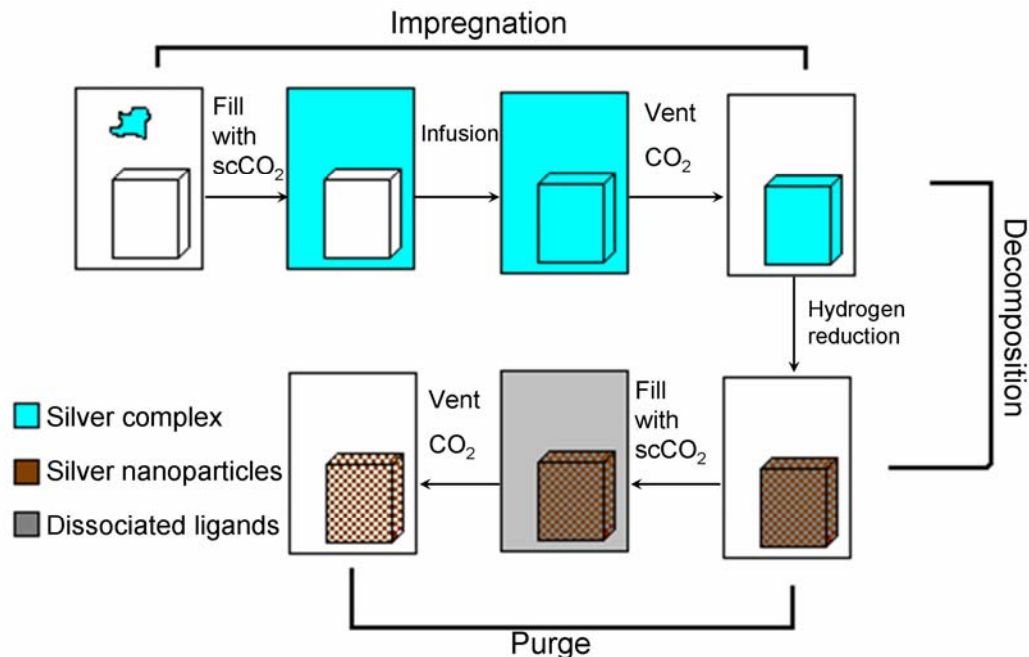


Figure 31 - Schematic of the reaction process, consisting of three phases: 1) impregnation, 2) decomposition, and 3) purging.

Impregnation - The precursor and substrate are placed in the autoclave and the equipment is assembled. CO₂ is then pumped into the autoclave to a pressure of ~800 psi (~5.5 MPa). Heating of the autoclave is then commenced. After the autoclave reaches the desired temperature it is topped up with further CO₂ to reach the required pressure (normally 1500 psi, 10.3 MPa). The standard temperature for the impregnation stage is 40 °C. This ensures supercritical conditions while minimising premature precursor decomposition. At these conditions, the precursor is dissolved in the scCO₂ and infuses into the substrate. After leaving time for this infusion to occur (normally 24 hr), the outlet tap is opened to depressurise the autoclave and vent the CO₂, leaving the precursor trapped in the substrate.

Decomposition – The autoclave is filled with H₂ to ~1000 psi (6.9 MPa) and heated to 80 °C to instigate the decomposition of the Ag(hfac)COD. This is thought to occur by a hydrogenolysis reaction resulting in Ag⁰ and free dissociated ligands. The H₂ is then vented and the autoclave allowed to cool.

Purge – The autoclave is repressurised with CO₂ to ~ 4000 psi (27.6 MPa), again at 40 °C, and the outlet tap is left slightly open. The scCO₂ is allowed to flow slowly through the autoclave for 24 hr to ensure complete extraction of the dissociated ligands. The inlet tap is then closed and the outlet tap was left open to allow complete evacuation of the CO₂ and a return to atmospheric pressure. The autoclave is then disassembled and the sample removed.

A description of the purge step is included here for completeness. Most of the products synthesised in this chapter were produced without the use of this step. Previous work in the group has demonstrated this step to be effective for the removal of ligands.^{11, 12} For this reason it was performed for some of the early work described here. However, because only a small amount of dissociated ligands are produced in the substrate, which is unlikely to affect the optical properties, it was concluded that this step was unnecessary. Therefore, for the sake of expediency, the step was omitted. If the material produced were to find application in a manner in which the dissociated ligands were problematic, then this step could of course be re-instated.

2.3.3.1 Precursor silver complex

An ideal precursor should be scCO_2 soluble, be stable under high pressure conditions, and degrade readily when required. The precursor chosen for this research, $\text{Ag}(\text{hfac})\text{COD}$ (Fig. 32), has been previously used in scCO_2 , and impregnated into polymers, and has been shown to meet these requirements.¹³ The addition of fluorinated substituents has been shown to increase solubility in scCO_2 .¹⁴ The addition of encapsulating ligands, such as a multidentate chelates, completes the coordination sphere of the metal and essentially shields the metal from the scCO_2 .¹⁵ $\text{Ag}(\text{hfac})\text{COD}$ was designed for use in CVD processes, and information on its nature and synthesis can be found in the relevant patent information.¹⁶

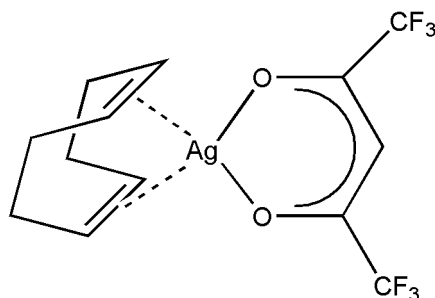


Figure 32 - (1,5-cyclooctadiene)(1,1,1,5,5,5-hexafluoroacetylacetonato) silver(I), abbreviated to $\text{Ag}(\text{hfac})\text{COD}$, the organometallic precursor complex used for the production of silver nanoparticles. Delocalisation of the electron in the β -diketonate system will occur, though this is not shown.

2.4 Choice of polymer

The first necessary part of this research was to conduct trials on a range of optical polymers in order to find a suitable material for further study. Three polymers were chosen as potential models for this process: poly(methyl methacrylate) PMMA, Polycarbonate and Teflon[®] AF. All three are wholly transparent in the visible range and have applications in visual systems, optics and photonics. The structures and properties of these polymers will be outlined first, before the results of this initial investigation. The reasons for which polymer was chosen for more in-depth investigation will then be explained.

2.4.1 Polymer structures

2.4.1.1 Teflon[®] AF

Teflon[®] AF (2,2-bis(trifluoromethyl)-4,5-difluoro-1,3-dioxole) is an amorphous fluoropolymer, recently produced by Dupont, to combine the advantages of amorphous and fluorinated polymers. For a polymer to possess high enough transparency for optical applications requires an amorphous nature. This is because the presence of any crystal phases would cause the scattering of light (see Chapter 1.4.1.1). Teflon[®] AF is similar to other amorphous polymers in optical clarity and mechanical properties. It is also comparable to fluoropolymers such as standard Teflon[®] (polytetrafluoroethylene) in its ability to withstand a wide range of temperatures, and in having excellent chemical resistance. Unlike other fluoropolymers, however, Teflon[®] AF has high gas permeability, a high

compressibility, high creep resistance, and low thermal conductivity. Teflon[®] AF polymers have the lowest dielectric constant and the lowest index of refraction of any known polymer.¹⁷ The structure of Teflon[®] AF is shown in Fig. 33. It is a copolymer made from tetrafluoroethylene (TFE) and a dioxole. TFE is the monomer used to make standard Teflon, which is opaque due to having crystalline as well as amorphous phases. The dioxole segment added to Teflon[®] AF prevents the polymer chains from packing together to form crystallites; hence the polymer becomes completely amorphous and therefore transparent.

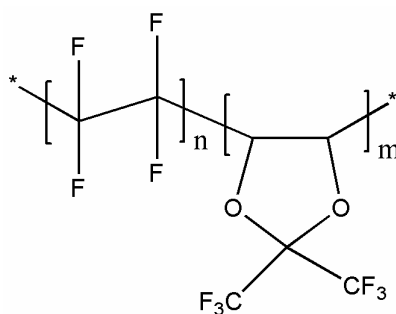


Figure 33 - The structure of Teflon[®] AF copolymer, 2,2-bis(trifluoromethyl)-4,5-difluoro-1,3-dioxole.

Two grades of the polymer are available, with different ratios of the two monomers (see Table 3). This has a pronounced effect on the glass transition temperature (T_g) of the polymer. The TFE segments in Teflon[®] AF have free rotation about the C-C bond, whereas the dioxole segments have restricted rotation due to the ring system. When the dioxole ratio in the copolymer is increased, it impedes the flexibility of the polymer chain, and therefore raises the T_g . Samples of both grades were obtained for testing, 2400 in the form of narrow tubing and 1600 in powder form, which was processed into solid discs for testing (see Chapter 5.3.2).

Table 3 – Comparison of grades.

Grade	Teflon [®] AF 1600	Teflon [®] AF 2400
Dioxole content	65 mol%	87 mol%
Glass transition temperature (T_g)	160 °C	240 °C
Refractive index at 20 °C and 589 nm	1.31	1.29
Dielectric constant at 22 °C and 100 MHz	1.93	1.90

2.4.1.2 PMMA

PMMA is a more well-established polymer in comparison to Teflon[®] AF and was amongst the earliest synthetic polymers to be developed. It has extensive and widespread applications both optically and conventionally. It is commonly used as a shatterproof alternative to glass, but also has uses such as contact lenses, visual display components and optical fibres. PMMA is a clear, strong plastic with a highly amorphous nature that gives it 92 % transmittance across the visible range and most of the infrared region. It has a refractive index between 1.49 and 1.51, a T_g at ~104 °C, and a dielectric constant of ~4.0 (at 60 Hz). See Fig. 34 for PMMA structure.

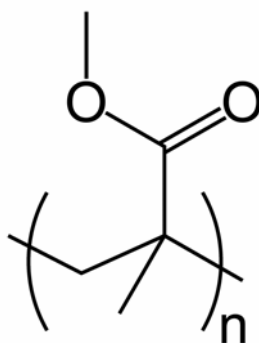


Figure 34 – The structure of PMMA.

2.4.1.3 Polycarbonate

Polycarbonate is another amorphous polymer with widespread optical applications and good mechanical properties. It has a refractive index of 1.585, density of 1.20 gcm^{-3} , T_g of $160 \text{ }^\circ\text{C}$, light transmission index of $90\% \pm 1\%$ and dielectric constant of ~ 3.2 at (60 Hz). The characteristics of polycarbonate are quite like those of PMMA, and polycarbonate is used in many similar applications to PMMA, but polycarbonate is generally stronger and more expensive. Polycarbonate is highly transparent to visible light and has better light transmission characteristics than many kinds of glass. Polycarbonate is frequently used for eyeglass lenses, bullet resistant glass, compact discs and digital versatile discs, as well as many other optical components. The most common type of polycarbonate, and the polycarbonate used in this work (Fig. 35), is produced from bisphenol A.

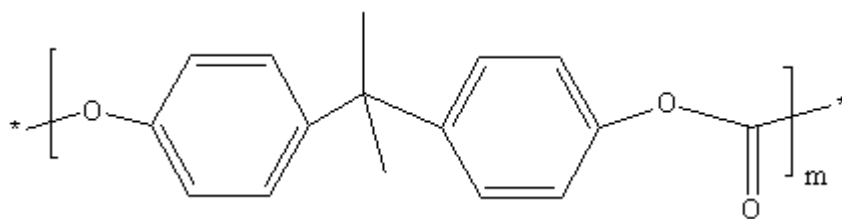


Figure 35 – The structure of the bisphenol-A polycarbonate used in this work.

2.4.2 Results of polymer trials

2.4.2.1 Teflon[®] AF

As discussed in chapter 5.3.2, the Teflon[®] AF 1600 was processed into discs prior to reaction. Though otherwise solid and transparent, a few bubbles, formed during heating to press the discs, were found to be unavoidable. Reactions were performed according to the general scheme outlined in section 2.3.3. Impregnation was at 40 °C with scCO₂ pressure varying between 2000 psi and 4000 psi in different reactions. The reduction step was performed with ~1000 psi H₂ at 80 °C. The purge step was 4000 psi scCO₂, 40 °C.



Figure 36 - Teflon[®] AF1600 samples, A to F from top left to bottom right of left hand photo. The top right photo shows a close up of a cross section strip microtomed from sample D. The bottom right photo shows a close up of sample D, showing transparency. For discussion of samples see main body of text.

Sample A (Fig. 36) shows an untreated disc. Sample B shows a disc subjected to scCO_2 reaction conditions. The extensive foaming observed was found to be unavoidable, and occurred for all Teflon[®] AF 1600 samples. Sample C was impregnated with $\text{Ag}(\text{hfac})\text{COD}$ to a theoretical maximum (nominal) loading of 2.5 wt% silver. The initial product was brown and foamed. This was reprocessed into a disc, as shown. The brown colour observed is indicative of the plasmon absorption expected for silver nanoparticles. Gravimetric analysis to determine loading was difficult. It was found that the scCO_2 treatment conditions caused a mass decrease of approximately 1-2 %, in the absence of $\text{Ag}(\text{hfac})\text{COD}$, which was taken into account. For samples C and D, with 2.5 wt% nominal loading, there was negligible mass increase. For Sample F, with 20 % nominal loading, there was a mass increase of ~2 %. Sample D, was impregnated for 24 hr, the same as sample C, but the reduction and purge steps were omitted. Instead the sample was simply re-moulded into a disc, as with sample C. This process was found to be sufficient to decompose the impregnated $\text{Ag}(\text{hfac})\text{COD}$ and cause the brown colour, i.e. nanoparticles. This presumably occurred because of thermal decomposition of the $\text{Ag}(\text{hfac})\text{COD}$. Notice the microtomed cross section from sample D (Fig. 36) showing the colour to be present throughout the disc. Sample E was impregnated in the same manner but for only 2 hr, and still took on a comparable brown colour. This suggests that the scCO_2 and $\text{Ag}(\text{hfac})\text{COD}$ permeate quickly into the polymer. Sample F was subjected to all three steps of the

reaction scheme, but left foamed. This foamed sample was cut in two and the brown colour was observed to be present evenly throughout.

Teflon[®] AF 2400 did not display the foaming problems associated with the 1600 grade. The samples shown in Fig. 37 were impregnated at 2000 psi for 2 hr with a nominal loading of 20 wt%. They clearly show the brown colour associated with silver nanoparticle plasmon resonance, while maintaining transparency. Mass increase was ~2 %. So why is the 2400 grade resistant to the foaming that is so severe in the 1600 grade? This could partly be due to the thickness of the samples, but may also be caused by plasticization effects. scCO₂ has been shown to greatly reduce the T_g of polymers. Teflon[®] AF is likely to be especially prone to these effects due to the high CO₂ affinity/solubility of its structure. This is because of the F and O groups present, as discussed in chapter 1.5.2.1. The 2400 grade, however, has a much higher T_g than the 1600 grade because of the additional number of dioxole groups restricting chain movement see section 2.4.2.1. This restricted chain movement is also likely to reduce the scCO₂ solubility of the 2400 grade compared to the 1600 grade. Experiments conducted in a view cell confirmed that under the same scCO₂ conditions the 1600 grade was visibly plasticized while the 2400 grade was not. It is this enhanced plasticization and solubility of the 1600 grade that causes it to foam, while the 2400 grade is resistant.

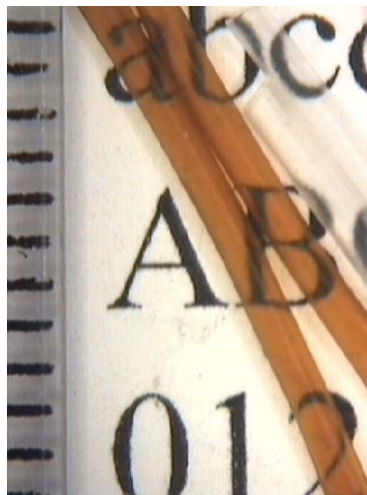


Figure 37 - Teflon[®] AF 2400. Unmodified material shown on the right, and treated material on the left. Graduations show scale in mm.

TEM investigation was performed on a microtomed cross section of sample F of the 1600 grade (see Figs. 38 and 39). Micrographs of the structure revealed silver nanoparticles to be present throughout the bulk of the sample analysed. The relatively low concentration of silver, compared to the amount of polymer present, meant diffraction patterns do not show any crystalline material. However, a selected area diffraction pattern taken of a rare local aggregation of larger particles (right image, Fig. 38) was able to show the presence of crystalline material.

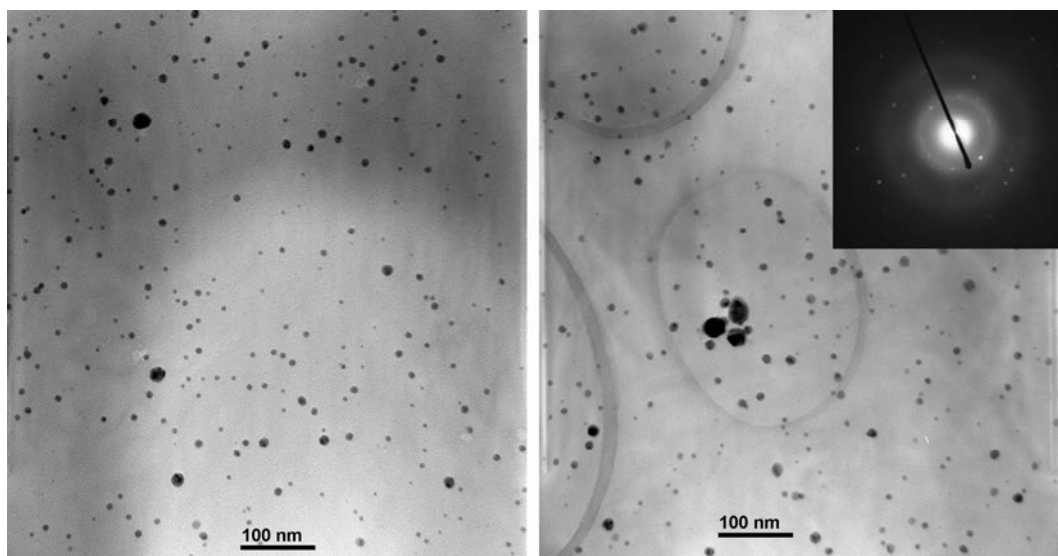


Figure 38 - TEM of Teflon[®] AF 1600 grade sample impregnated with silver nanoparticles. The image on the left is representative of the bulk of the sample. The image on the right shows an uncharacteristic agglomeration of large particles, with inset diffraction pattern showing presence of crystalline material.

Image analysis was performed to give a representative size distribution of the nanoparticles imaged in the micrographs (Fig. 39). This analysis shows the majority of the nanoparticles to be in the 2 to 10 nm size range with an average diameter of ~ 7.4 nm. This initial study has shown that while both grades have good potential for the scCO_2 impregnation of nanoparticles, the 1600 grade is unsuitable for our application because of excessive foaming.

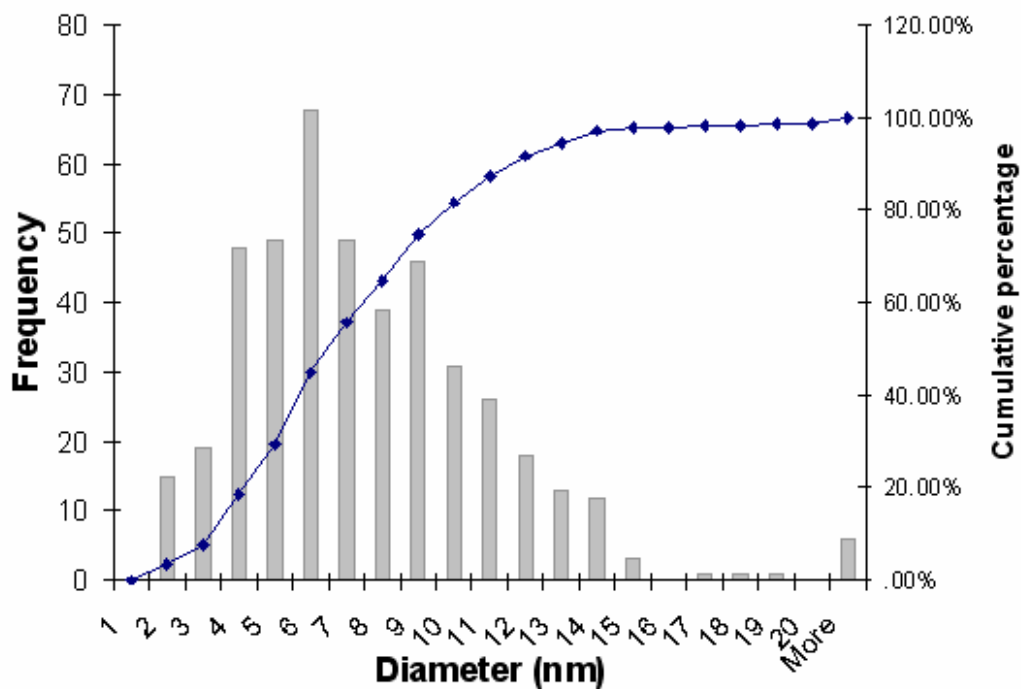


Figure 39 - Statistical size distribution of Ag particles in Teflon[®] AF 1600 sample F. Calculated from image analysis of micrographs by Andrew Madge and Hannah Edwards of *Materials Engineering Dept. University of Nottingham* using ImageJ software.

2.4.2.2 PMMA

The PMMA tested was obtained in the form of 10 mm and 6 mm. This was processed in house to form samples of 20x10x10 mm and 20x10x6 mm respectively. Many PMMA samples were impregnated, in a range of conditions. A small portion of these results are presented here to display the path taken and some of the effects observed. Foaming was again found to be a problem. Many attempts were made to reduce this foaming effect, including long venting times, nitrogen flow (see Fig. 40), and cooling prior to venting. Long venting times involved releasing the pressure slowly over a period of up to ~5 hours. Nitrogen flow

involved connecting high pressure nitrogen to the inlet before slightly opening the outlet tap, in order to replace the CO₂ in the system with nitrogen without lowering the pressure. The inlet could then be closed and the pressure allowed to decrease. In the cooling prior to venting method, the internal temperature of the autoclave is lowered by placing it in a dry-ice/acetone bath. This was intended to freeze the CO₂ into its solid form before the autoclave was opened and the CO₂ allowed to sublime. The most effective was found to be nitrogen flow, which allowed the CO₂ more time to diffuse out of the polymer without a drop in pressure, and therefore rapid expansion, causing foaming to occur. Foaming was found to occur to some extent during the CO₂ venting process, but also during the reduction step. This was thought to be because the reduction step involves heating the PMMA to higher temperatures than it experienced in the impregnation step. This causes CO₂ still left dissolved/trapped in the polymer to expand, hence causing further foaming.

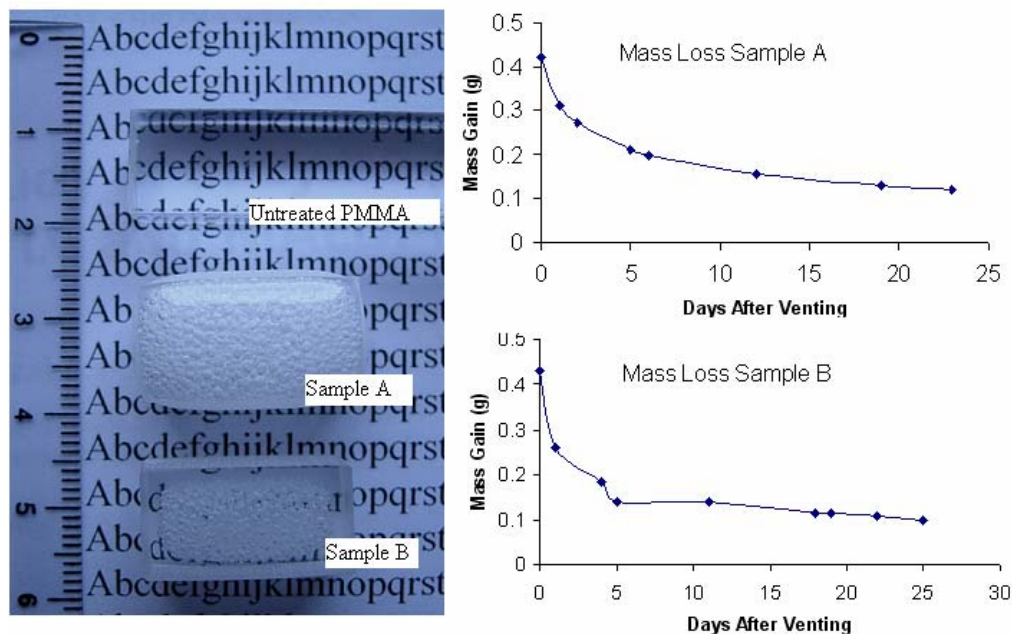


Figure 40 - Samples A and B, 10 mm PMMA blocks, were subject to standard impregnation conditions in the absence of Ag(hfac)COD. A, with a slow vent (5 hr). B, with nitrogen flow prior to venting. As well as the foaming observed, the mass of the samples was found to increase. The graphs on the right show the subsequent loss of this gained mass as the remaining CO₂ slowly diffuses out. The sharp drop in the mass of sample B just before day 5 was caused by placing the sample in a 75 °C oven. This also caused the degree of foaming to increase.

Despite the problems with foaming it was again found to be possible to impregnate the polymer with Ag(hfac)COD, which could then be reduced to silver nanoparticles inducing a brown colour (Fig. 41). As can be seen from the samples, the scCO₂ permeates into the PMMA at a faster rate than the Ag(hfac)COD. This would be expected as the Ag(hfac)COD is a much larger molecule that will experience much more resistance to diffusion in the polymer. Even for a very long impregnation, the brown colour indicative of silver nanoparticles is only present in the outer edge of the sample. So why does the Ag(hfac)COD permeate so much slower into the PMMA than it does into the Teflon[®]AF? This is because of a

number of effects. The Teflon[®] AF has more favourable interactions with the CO₂, as discussed before, leading to more swelling and greater ease of movement between the polymer chains that allows the precursor to diffuse easily into the substrate. Also the PMMA is a denser, less gas permeable polymer in comparison to the Teflon[®] AF. Finally, it is possible that the fluorinated nature of the Ag(hfac)COD increases its solubility in Teflon[®] AF, while reducing its solubility in PMMA.

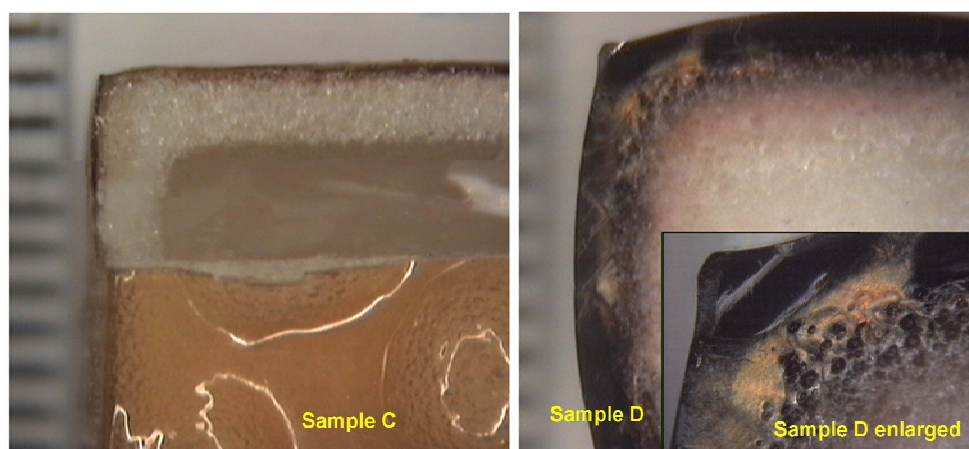


Figure 41 - Cross sections of samples C and D. Sample C was impregnated at 4000 psi, 80 °C, for only 40mins. Sample D was impregnated at 4000 psi, 80 °C, for 2 weeks. Note the difference in foaming (CO₂) and colour (silver) penetration depths.

Though it was not possible to completely avoid foaming, conditions were chosen to limit the degree of foaming. By this method it was possible to confine the foamed area to only the centre of the polymer blocks (see Fig. 42). Impregnation reactions were performed at higher temperatures (up to 80 °C) as an attempt to increase the rate of precursor diffusion into the polymer, but it was found that if the reaction was slowly cooled down to 40 °C, before the nitrogen replacement and depressurisation step, then foaming was less pronounced.

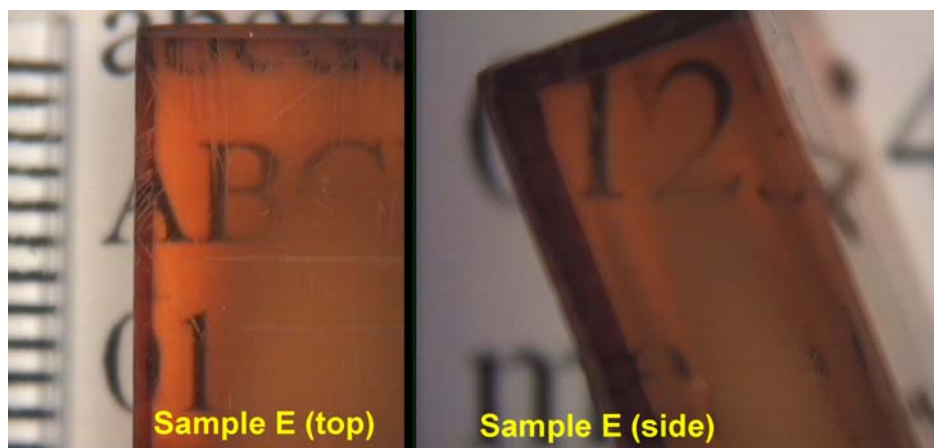


Figure 42 - Sample E, impregnated at 5000 psi for 6 days, at a maximum temperature of 75 °C. Cooled to 40 °C over 5 hr. Nitrogen flow prior to venting was used to minimise foaming.

The initial trials of PMMA and Teflon[®] AF demonstrate how the polymer composition and processing conditions can affect the silver infusion depth and degree of foaming. For PMMA the silver impregnation is limited to only the surface layer, and foaming occurs more severely towards the centre of the polymer, as it is more difficult for the trapped CO₂ to escape from this region. Therefore, an obvious possibility of avoiding the problems associated with polymer foaming would be the use of much thinner polymer substrate samples, from which the CO₂ could easily diffuse out without causing foaming to occur. This was an important factor in the decision to trial polycarbonate strips. Polycarbonate was chosen because it is a similar polymer to PMMA; though, amorphous and transparent, with many close applications and properties. However, we were able to obtain polycarbonate samples in much thinner sheets than PMMA, 0.8 mm and later 0.5 mm. Polycarbonate is often used in preference to PMMA at these dimensions because its superior physical properties make it

more resistant to fracture. It was intended that these dimensions would allow completely transparent un-foamed samples to be produced.

2.4.2.3 Polycarbonate

0.8 mm polycarbonate sheets were cut to a size of 10x20 mm and tested (Fig. 43). It was shown that they could withstand the conditions of the scCO₂ impregnation step and maintain transparency. The reduced width of the sheets allowed four separate samples to be placed in the autoclave in each reaction. Whether nitrogen flow was used or not seems less important at this thickness, but temperature is obviously a factor (Fig. 43). For most impregnation reactions attempted it was found that foaming could normally be avoided if impregnation was performed at 40 °C and if the same temperature was maintained during a vent step of ~3 to 5 minutes with no need for a nitrogen step. It is likely that at this width, the dissolved CO₂ is able to diffuse to the surface of the polymer and escape without causing foaming. However, if a higher temperature of 80 °C is used then the polymer is plasticized, and therefore more easily foamed by expanding CO₂ during depressurisation.

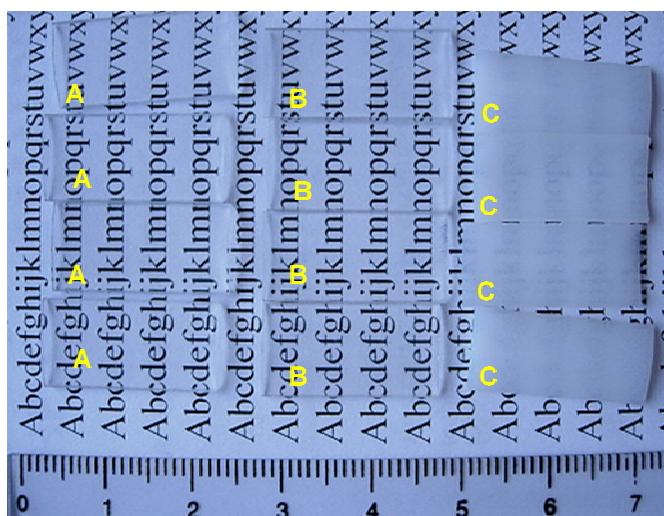


Figure 43 - 0.8 mm polycarbonate strips treated with scCO₂ conditions. A) 40 °C, 24hr, no N₂ flow. B) 40 °C, 24 hr, N₂ flow. C) 80 °C, 24 hr, N₂ flow. Note that the N₂ flow appears to be unnecessary at 40 °C.

When Ag(hfac)COD was introduced, a brown colour was produced in the polymer substrates, indicative of silver nanoparticles. Although the polycarbonate strips became coloured, their transparency was maintained (Fig. 44a). However, when the polycarbonate samples were cross sectioned it could be observed that the nanoparticle infusion was again limited in depth to close to the surface (Fig. 44b). UV-visible spectroscopy shows the plasmon resonance (see Fig. 44c).

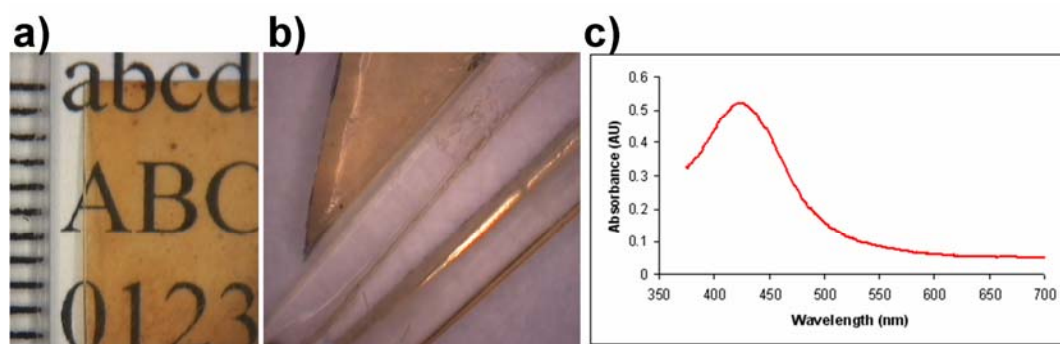


Figure 44 – Polycarbonate impregnated with silver nanoparticles, showing transparency and colour (a), depth limit in cross section showing a sample that has been cut into segments, from above and looking through (b), and plasmon resonance absorption (c).

2.4.2.4 Conclusions of polymer trials

The results suggest all three of the polymers tested were successfully impregnated with silver nanoparticles. Teflon[®] AF showed mixed results for optical applications as the 1600 grade was found to be too prone to foaming to be used effectively. However, the 2400 grade has good potential for impregnation in this manner. Unfortunately, as the Teflon[®] AF 2400 material was still in a relatively new stage of production, it was not possible to procure a sufficient amount of sample to perform more extensive investigation. Therefore the use of a more established optical polymer, with widespread current application and better availability was considered preferable. To this end both PMMA and polycarbonate were assessed. Both polymers showed similar behaviour, with depth limited but successful nanoparticle impregnation coupled with problems of foaming. However, polycarbonate represented the most viable substrate for further investigation because it was only for thin sheets of polycarbonate that foaming could be completely avoided, maintaining transparency at the same time as introducing nanoparticles. Polycarbonate was therefore chosen as the model substrate for all of the further investigation in this research.

2.5 Effect of temperature and pressure

At this stage of the research the general method was seen to be working, with transparent polycarbonate strips impregnated with nanoparticles being produced. The next step was therefore to investigate what conditions were most suitable for performing this process. The first factors to be investigated were the effect of temperature and pressure on the impregnation step. In this section the effects of temperature and pressure are discussed by visual analysis of the samples produced. For clarity only a few samples are displayed and reported here, but many more were prepared in similar conditions and all showed the same general trends.

2.5.1 Temperature

Samples shown in Fig. 45 display the effect of impregnation temperature on the resulting nanocomposite produced. Higher temperature causes a darker colour in the samples, due to higher absorption of silver. The polycarbonate is more plasticized at higher temperature and the diffusion rates of the scCO₂ and precursor will also be higher. However, higher temperatures also lead to more pronounced foaming effects, causing opacity. Foaming occurs if the impregnation and venting are performed at 60 °C. Note that the colour could be easily removed from the 20 °C sample (but not from the other samples) by simply rubbing with paper. This demonstrates the importance of supercritical conditions for successful impregnation. At 20 °C the CO₂ was in a liquid state capable of acting as a solvent for the precursor and so able to deposit it on the surface of the polycarbonate.

When the temperature is increased to 40 °C the CO₂ is well into the supercritical region. This causes the swelling of the polymer and allows the infusion of the precursor deeper into the polycarbonate.

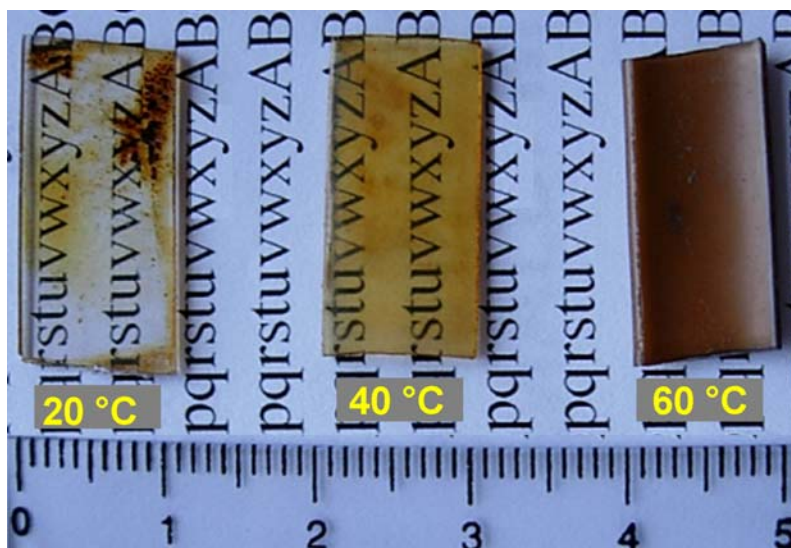


Figure 45 – Photograph depicting the colouration and transparency of 0.8 mm thick polycarbonate strips produced in a range of impregnation temperatures. Impregnations were all 24 hr, 4000 psi, 10 wt% nominal precursor loading.

2.5.2 Pressure

The effect of impregnation pressure can be seen from the samples displayed in Fig. 46. A series of reactions were performed at two different impregnation pressures, three at 4000 psi and three at 3000 psi. Unfortunately at this stage in research the equipment was not optimised (see the next section), and it was normal for some pressure to be lost over the course of the impregnation because of slow leaks from the autoclave. If the degree of colouration is observed for the samples

shown and compared to the impregnation pressure it can be seen that lower pressure results in higher silver loading. This at first seems counter-intuitive, more pressure should lead to more scCO_2 , and therefore $\text{Ag}(\text{hfac})\text{COD}$, being forced into the polymer. However, partitioning effects also need to be taken into account. These are determined by the relation between the solubility of the precursor in the scCO_2 phase and the solubility of the precursor in the scCO_2 swollen polymer phase. At higher pressures the CO_2 has higher solvating power (because of higher density). This causes the $\text{Ag}(\text{hfac})\text{COD}$ to preferentially partition into the scCO_2 outside of the polymer. Alternatively, at lower pressures scCO_2 is less dense and has a lower solvating power for the silver complex, causing the relative proportion of silver complex that infuses into the polymer during the impregnation to increase. Therefore the partitioning of the silver complex into the polycarbonate at the lower pressure is likely to be favoured compared to the high pressure impregnation, leading to greater precursor concentration in the polycarbonate during the impregnation step, and hence a higher final loading of silver. This is consistent with previous studies of the partitioning of solutes from scCO_2 into polymer phases, by Kazarian *et al.*¹⁸⁻²⁰

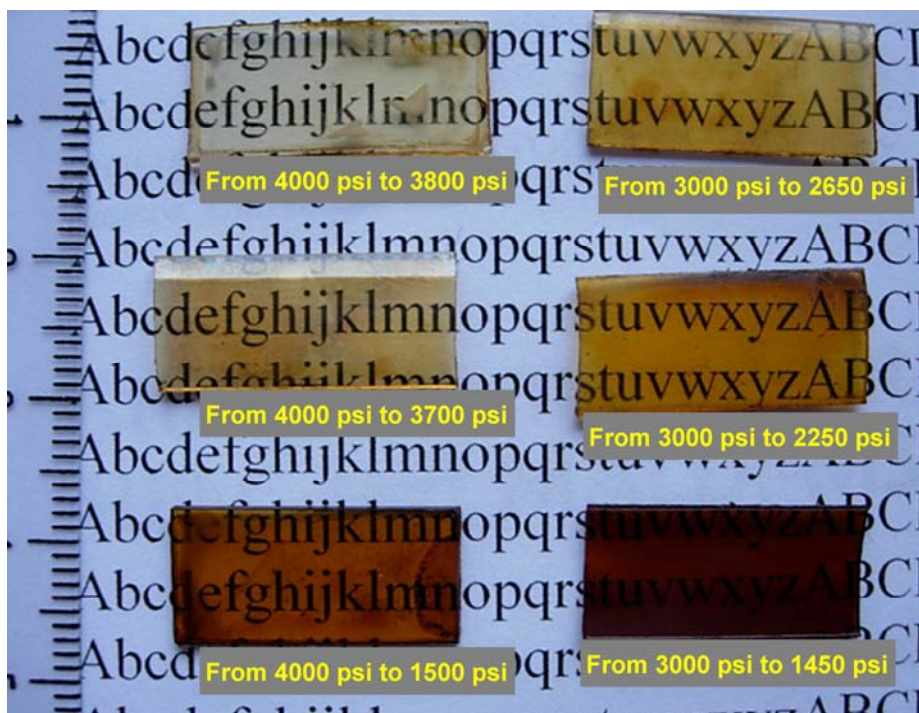


Figure 46 – Photograph showing the colouration and transparency of 0.8 mm thick polycarbonate strips. The effect of impregnation pressure on silver loading can be observed. Pressures are given as the starting pressure and the pressure remaining after the 24 hr reaction time, due to slow leaks. Impregnations were all 24 hr, 40 °C, 10 wt% nominal precursor loading.

2.5.3 Influence on general method

The results of these temperature and pressure tests determined the conditions chosen as standard for the rest of the reactions performed in this work. The optimum temperature for model impregnation reactions was set at 40 °C. This is sufficiently beyond the critical temperature of CO₂ to ensure a supercritical state even allowing for some temperature fluctuations within the autoclave. This temperature is low enough to avoid the problems associated with foaming that occur at higher temperatures. Lower pressure is superior in terms of nanoparticle

impregnation, but the impregnation reaction should occur in the supercritical state of CO₂ to be successful. In gaseous conditions the precursor is not soluble, and in liquid conditions the diffusivity is much lower, less suitable for impregnation. For this reason a pressure just over the critical pressure of 1070 psi would seem most suitable. However, because of the tendency of the autoclaves to lose some pressure during reactions, a pressure of 2000 psi was chosen in order to allow for some possible decrease in pressure during the reaction. At later stages, when more reliable apparatus decreased the frequency and severity of pressure loss, this standard pressure was lowered to 1500 psi for the impregnation step.

2.6 Development of the process and equipment

During the temperature and pressure trials the impregnation process consisted of placing 4 polycarbonate strips into a *Thar cell* autoclave for each reaction (described in Chapter 5.3.1). However, the nanocomposite products were found to be inhomogeneous. Lighter and darker areas could clearly be seen on each individual polycarbonate strip, and also the strips often differed with respect to each other in terms of colouration and degree of foaming. As well as being undesirable in terms of applications, this made comparative analysis by UV-vis or TEM difficult. Therefore it was necessary to improve this homogeneity before further research was undertaken. This was accomplished by re-design of the reaction vessel as summarised in table 4.

Table 4 - Summary of modifications in autoclave design.

Autoclave version	Description	Volume	Stirred?	Polycarbonate location
Mk I	Thar cell	10 ml	No	Static, bottom of cell
Mk II	Nottingham type	60 ml	Yes	Static, bottom of cell
Mk III	Nottingham type	60 ml	Yes	Dynamic, stirrer/holder

A full description of the three autoclave types is given in chapter 5.3.1. The differences between the autoclaves are outlined here more briefly, along with the implications these differences have for the uniformity of the products. The original *Thar cell* type autoclave is a 10 ml volume tubular vessel, commercially available and simple to use. However, drawbacks of this equipment are the repeated

tendency to lose pressure over the course of a reaction, and the lack of any stirring or agitating mechanism to encourage efficient mixing of the scCO₂. This leads to a non-uniform impregnation environment for the polycarbonate strips. It is known that scCO₂ has strongly temperature dependent properties.²¹ The CO₂ in the vessel is heated via the steel walls of the reactor, causing a temperature gradient and convection effects. Areas with different scCO₂ temperature will cause regions differing in density and therefore solvent strength, leading to concentration inhomogeneities in the system.

The situation was improved by using a stirred 60 ml autoclave, which produced polycarbonate strips of a much more uniform colouration. Checking reproducibility and homogeneity of this effect is possible with UV-vis spectroscopy (Fig. 47). By taking UV-vis spectra, four nanocomposite strips produced in a single reaction can be compared. If all four strips give very similar plasmon peaks then the impregnation process can be considered homogeneous. If the UV-vis spectra of the four strips in the same reaction differ greatly this suggests inhomogeneity in the nanocomposite products. In simple terms the intensity of the plasmon peaks corresponds to the concentration of nanoparticles in the sample and the position of the peak relates to the size of the nanoparticles, with an increase in nanoparticle size causing a red-shift of the plasmon peak.

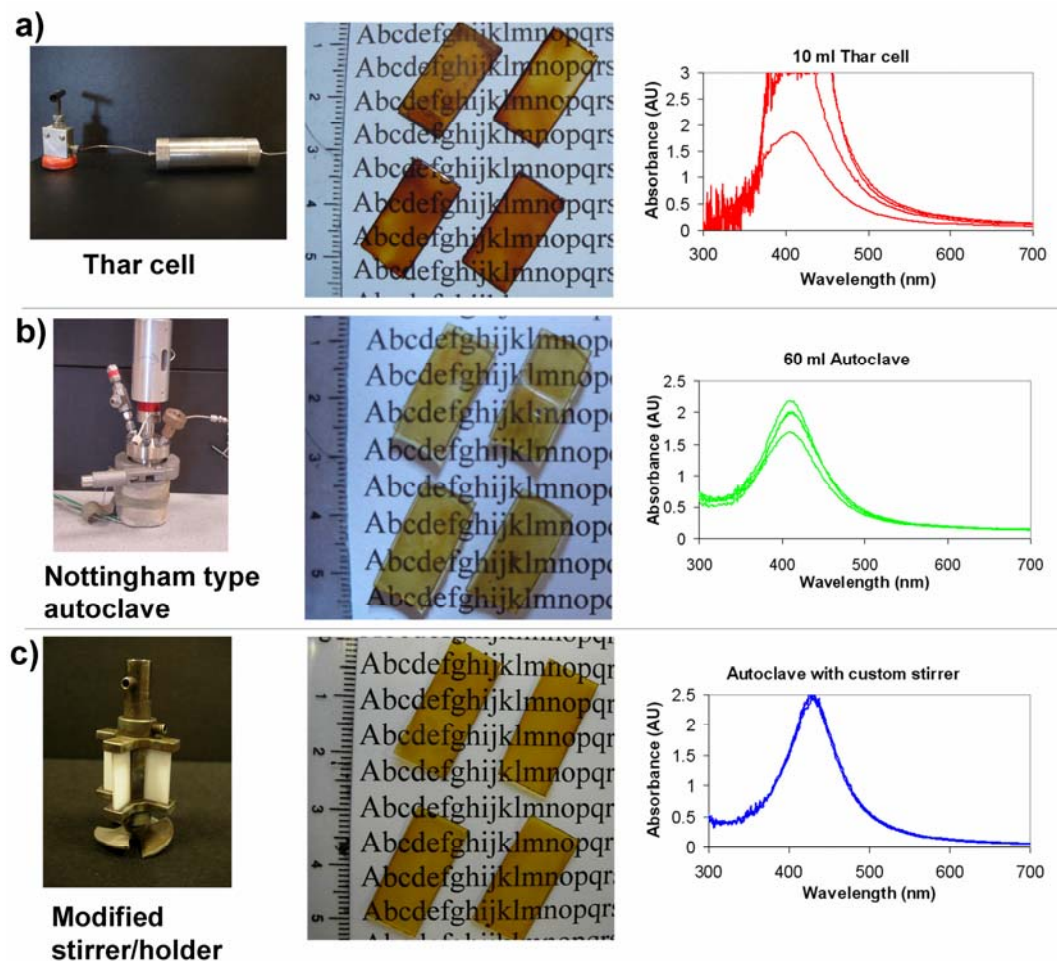


Figure 47 – The evolution of the equipment in order to improve homogeneity. Photographs of the equipment are shown on the left. The four samples produced in a single batch are shown in the centre column adjacent to the appropriate equipment. UV-vis spectra (right hand column) allow more accurate comparison of homogeneity.

The four UV-vis spectra observed for the reaction performed in the *Thar cell* (Fig. 47a) show a large discrepancy in plasmon intensity, indicating inhomogeneous loading. This is caused by a non-uniform impregnation environment. When the reaction is transferred to the larger volume Nottingham type autoclave, complete with stirring, the homogeneity can be seen to improve as evidenced by the narrower range of plasmon spectra (Fig. 47b). However, there is

still a noticeable difference between the plasmon peaks. This can be explained by the location of the polycarbonate strips in the reaction. Two strips were placed laying flat side-by-side on the floor of the autoclave, with another two strips laying flat and side-by-side on top of the first pair. This unsymmetrical environment, either in terms of scCO₂ flow around them or temperature profile, is the likely cause of the difference in the resulting plasmon spectra. This problem was solved in the MkIII autoclave by attaching the polycarbonate strips to the sides of the stirrer bar. This provides a symmetric environment for all four polycarbonate strips, keeps them away from the walls of the autoclave, and ensures they are all in a dynamic scCO₂ environment. This gives very closely comparable plasmon spectra (Fig. 47c) indicating improved homogeneity of nanoparticle loading. The nanocomposites produced in this matter are visibly uniform in colour and are transparent.

This modification of the autoclave design and sample position in order to improve homogeneity represents a significant step forward in this research. Good homogeneity is desirable if the material is to find application. Also, the achievement of uniform products within each reaction allows UV-vis spectroscopy to be used as a useful investigative tool in the comparison reactions with different conditions. All further samples and results reported in this chapter were obtained by use of a MkIII autoclave system.

2.7 Effect of precursor mass

In order to investigate the effect of the amount of precursor used in the impregnation step, a series of reactions were performed on 0.5 mm thick polycarbonate strips. The achievement of uniform and reproducible samples allows the use of UV-vis spectroscopy to effectively analyse the nature of the nanocomposites. With this technique the comparison of variable reaction conditions on the products of many reactions becomes possible without having to rely on time consuming TEM. The largest possible path length is the width of the samples, 500 μm . However, it is believed the silver nanoparticles are not impregnated throughout the sample, and therefore the actual path length will be less. The amount of organometallic precursor loaded into the autoclave in the impregnation step was altered in steps of 25 mg from 50 mg to 200 mg. This range spans the point at which plasmon absorption becomes significantly detectable to the point at which absorption is saturated in the UV-vis detector (Fig. 48). In comparison to the mass of polycarbonate used, this range corresponds to ~2.5 to 10.5 wt% silver, or to a concentration in the vessel of 1.97 mmolL^{-1} to 7.88 mmolL^{-1} . The intensity of the plasmon peak increases in proportion to the mass of precursor used, indicating an increase in the concentration of nanoparticles produced in the polycarbonate. This occurs because when more precursor is present in the autoclave there is an increased partitioning of precursor into the polycarbonate. This effect can be used to control the nanoparticle loading and therefore optical properties of the resulting nanocomposites.

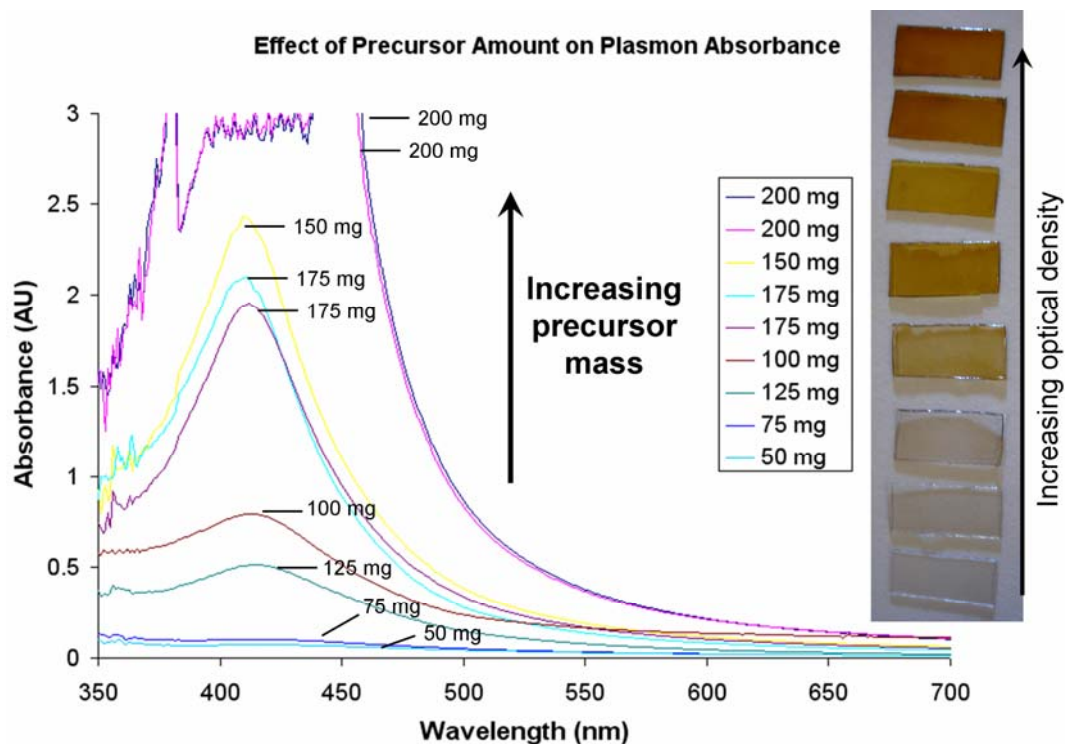


Figure 48 – The effect of the precursor mass used in the impregnation step on the plasmon absorbance of the products. The general trend is an increase although there are some discrepancies. The legend lists the results in order of highest to lowest plasmon absorbance at peak maximum.

The results displayed in figure 48 are each an average of the four plasmon spectra taken from a given reaction. The impregnation reactions were performed for 24 hr at 1500 psi and 40 °C. As can be seen, although the general trend is an increase in plasmon absorbance, there are some discrepancies, i.e. the peak for 125 mg occurs below that of 100 mg, and the peak for 150 mg is higher than the two experiments performed with 175 mg precursor mass. This is not surprising however, and only demonstrates that the effect of a 25 mg step increase is relatively small in comparison to reproducibility effects.

2.8 Effect of H₂ reduction time

The standard reaction conditions were initially set as 80 °C, 1000 psi H₂ and 24 hr. The temperature is raised in order to increase the rate of the reduction. Temperatures above 80 °C were avoided because of possible damage to the polymer, and because the use of high temperatures with compressed hydrogen is undesirable for safety reasons. Elevated pressure was used to ensure excess hydrogen and to encourage infusion; 1000 psi was the highest pressure that could be conveniently obtained from the hydrogen cylinders used. Previous research in the group had set a long reduction time of 24 hr in order to ensure the reduction process would be complete. In order to elucidate and optimise this step, the exact reduction time necessary to fully generate the nanoparticles was investigated.

After the completion of an impregnation step, UV-vis spectra of all four polycarbonate strips were taken. The strips were then placed back into the autoclave and subjected to hydrogen reduction for a measured period of time, before the hydrogen was vented and UV-vis spectra were re-taken. Figure 49 shows four spectra taken before and during a reduction at the standard conditions after a 150 mg impregnation (1500 psi, 40 °C, 24 hr). The results suggest that a plasmon peak maximum absorbance is reached between ~0.5 and 1 hr, but because the plasmon peaks are saturated this is not conclusive. This reinforces the assumption that 24 hr is an excess reduction time and allows the advantageous adoption of shorter reductions times. However, the fast reduction rate and saturated absorption make it difficult to plot an effective profile from these results. In order to investigate this step more clearly another reaction was performed with

a lower load of precursor during the impregnation (100 mg) and a lower temperature of 60 °C (Fig. 50).

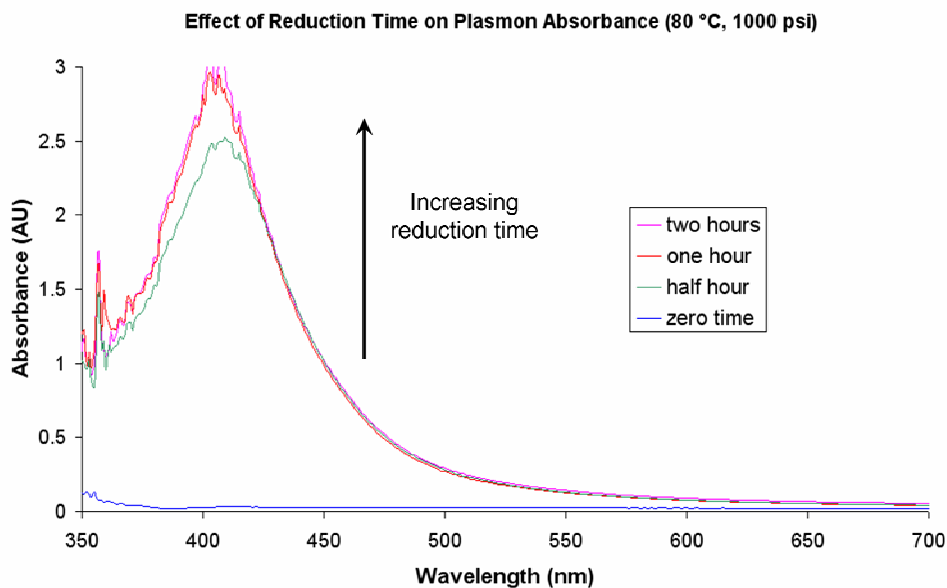


Figure 49 – Plasmon absorbance spectra a of polycarbonate strips as a function of reduction time. The reduction reaction was 80 °C and 1000 psi.

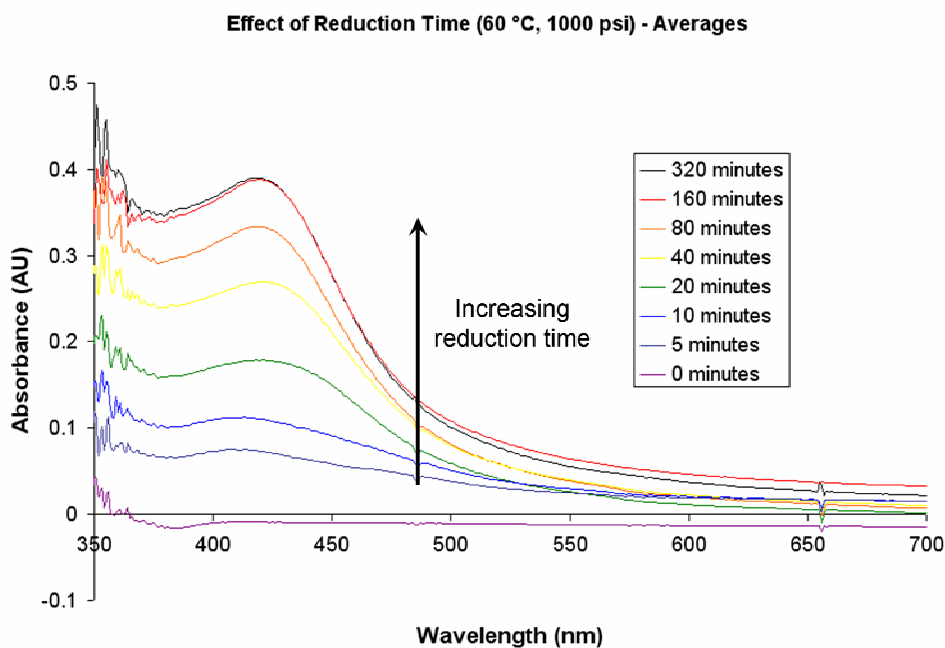


Figure 50 - Plasmon absorbance spectra of polycarbonate strips as a function of reduction time. The reduction reaction was 60 °C and 1000 psi.

From the development of the spectra in Fig. 50 it can be seen that the plasmon peaks increase in size as a function of reduction time. The peaks increase in intensity and broaden in width. This indicates the growth of the nanoparticles during the reduction step, both in size and in number. It is difficult to comment on the concentration of nanoparticles from plasmon data as the intensity is not just dependent on the number of nanoparticles but also on the size of the nanoparticles. It is useful, however, to consider the maximum intensity with respect to time as a function of the amount of silver converted from the precursor to metal nanoparticles. By plotting this as a graph (Fig. 51, left) it can be seen that the rate of conversion is initially high but decreases as the feedstock is depleted before reaching a plateau when all the available silver has been converted.

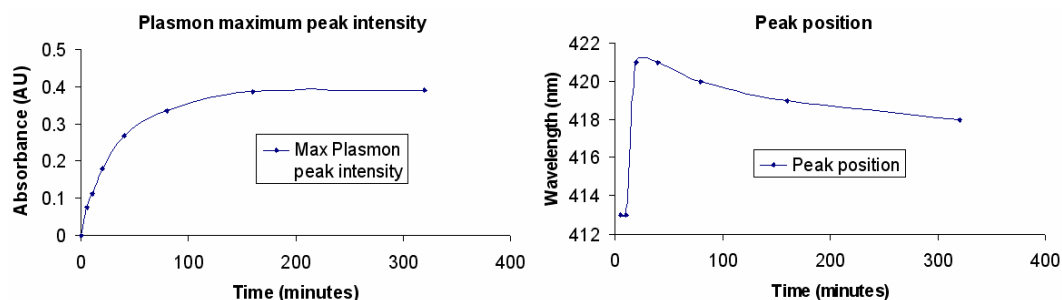


Figure 51 – Plasmon peak intensity and position as a function of reduction time (shown left and right respectively).

The peak position can also be used to give information on the nanoparticle size, but this must be done with caution. The peak position, breadth and shape will depend on an average of the plasmon spectra of all the nanoparticles detected across a range of sizes. The relative contribution of nanoparticle sizes will depend

on the number of nanoparticles of that size. The position of the peak maximum is plotted as a function of reduction time (Fig. 51, right). The peak position is at the shortest wavelength at the earliest time of detection. This corresponds to a smaller nanoparticle size, as would be expected for the initial time when the nanoparticles are beginning to nucleate and grow. After this, the peak position shifts quickly to the right corresponding to a fast growth of nanoparticle size. Again this is as would be expected from the growth of the originally nucleated nanoparticles. What is more surprising is that the peak position then moves slightly back to lower wavelengths, i.e. a smaller average nanoparticle size. Clearly the particles cannot shrink, the effect arises from the masking of the peaks of larger nanoparticles by the formation of many smaller nanoparticles. It is possible that the larger nanoparticles that are formed sooner in the reduction correspond to a region of the polycarbonate closer to the surface. This could be expected to have a higher concentration of precursor, leading to larger nanoparticles, and would be reduced sooner because this region is more accessible to the hydrogen and heat of the reaction. The area deeper into the polycarbonate that is reduced later in the reaction, as hydrogen infuses further, may correspond to the formation of smaller nanoparticles responsible for shifting the peak back to lower wavelength. This size-distribution of nanoparticles is one of the issues to be addressed by the use of TEM, reported later.

2.9 Impregnation time and TEM investigation

The effect of impregnation time was found to be the most difficult factor to study. The impregnation of nanoparticles into the polycarbonate is known to be depth limited (section 2.4.2.3.). Therefore it should be expected that for longer reaction times the precursor complex would diffuse further into the polycarbonate leading to a higher loading of silver. The intention of the design of the reaction is to introduce the precursor in the impregnation step, and to reduce it separately in the reduction step. Unfortunately, these steps do not occur ideally. The 40 °C temperature necessary for the impregnation step will cause some degree of slow decomposition of the precursor complex. This effect will be magnified by the increased pressure and the catalytic nature of the heated stainless steel walls of the reactor towards decomposition. This means that the impregnation step can be considered to be 'ideal' (i.e. no decomposition) only for short impregnation times. As the impregnation times become long with respect to the (unknown) decomposition rate of the precursor under these conditions then the impregnation will cease to be ideal. The resultant decomposition of some amount of the precursor will result in a lower silver loading than expected.

Another challenge in studying the effect of impregnation time on the reaction is the poor reproducibility often found for supercritical reactions such as this. Under impregnation conditions both the temperature and pressure are close to the critical points (1500 psi and 40 °C reaction conditions compared to P_c and T_c of 1070 psi and 31.1 °C). Therefore even small fluctuations in temperature or pressure can cause large changes in CO₂ density and hence precursor solubility. It

is common for the temperature of the reaction to fluctuate ~2 degrees during the reaction, and also for the temperature to overshoot during the initial filling and heating of the autoclave. Also, small leaks of CO₂ from the autoclave cause a loss of pressure. If the loss of pressure is large the reaction is aborted, but unfortunately for small losses of pressure (~100 psi) the reactions needed to be accepted for the sake of expediency.

2.9.1 Venting

When considering the impregnation step it is useful for us now to discuss the venting process that is the final part of this reaction step in more detail. This is likely to have an effect on the silver loading, and the degree of control of this process also has implications for reproducibility. As the pressure is reduced during the venting process, the solubility of the precursor complex in the scCO₂ will decrease. This causes the precursor to ‘fall out’ of the CO₂, precipitating/depositing onto the floor and walls of the autoclave and into the surface of the polymer. The intention was to investigate silver infusion during the main part of the impregnation, and therefore it was desirable to keep any precursor infused during venting to a minimum.

In order to do this the CO₂ was vented in a short time (~3 mins). The method of venting the CO₂ is by the manual partial opening of the needle valve of the outlet tap. During the venting process some partial blockage of the valve can occur, requiring the valve to be opened further to restore the intended venting rate. It is also possible for these blockages to clear, requiring the valve to be partially

closed again. These blockages can occur either from precipitated precursor, or from the formation of solid CO₂, which freezes as 'dry ice' because of adiabatic expansion at the outlet tap. As the pressure decreases, the valve must be opened further to allow the venting of CO₂ to continue at a suitable rate. The unpredictable and manual nature of this process causes discrepancies in the venting of different reactions. This is another reason why it is preferable to keep the venting as brief as possible, in order to minimise these discrepancies.

An obvious choice would seem to be to open the valve fully to allow the fastest possible venting time in each reaction (as opposed to the ~3 minute time used). However, this was attempted but was found to cause foaming of the substrate. This was thought to result from a rapid drop in CO₂ temperature, and therefore pressure. In order for the strips not to become foamed it is necessary for the CO₂, under the influence of pressure difference, to diffuse to the surface of the polymer and escape. As either the temperature or the pressure decrease, then the CO₂ will drop below supercritical conditions becoming either gas or gas and liquid. If this occurs too quickly then the CO₂ that is still dissolved in the polymer will crash out and expand to form bubbles. The adiabatic expansion of the CO₂ during fast venting causes a dramatic cooling effect inside the autoclave. This was noticed to cause foaming of the polycarbonate, especially if the temperature dropped below ~32-35 °C. Therefore, during the venting step a system was adopted to attempt to vent the CO₂ as quickly and smoothly as possible while maintaining a temperature of between 35 and 40 °C inside the autoclave. This resulted in the standard ~3 min venting time.

2.9.2 UV-vis study of impregnation time

Visible inspection of the reaction products, combined with UV-vis spectroscopy where appropriate, was the simplest method to begin analysis of impregnation time. Initial work using optical microscopy on sectioned samples had shown that the nanoparticle impregnation was limited to the surface layer for a 24 hr impregnation. In order to determine if a longer reaction could provide higher silver loading, an impregnation reaction lasting a full week was performed. This could then be compared to a 24 hr impregnation under the same conditions. The surprising result was a lower plasmon absorbance for the full week impregnation reaction (see Fig. 52). The week long impregnation reaction was repeated in case of anomaly, but a similar result was obtained the second time. This suggests that the effect of unwanted precursor decomposition is significant on these timescales. It is believed that for the one week impregnation a high level of precursor decomposition outside the polycarbonate may cause some precursor to re-partition back out of the polycarbonate into the CO₂ phase.

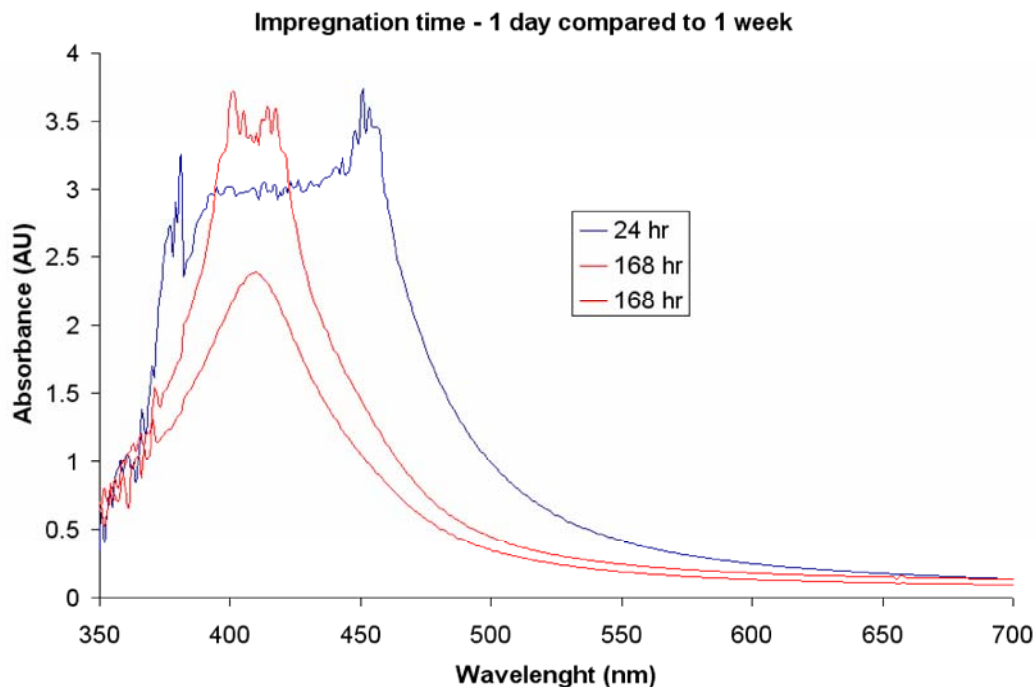


Figure 52 – Plasmon absorbance of samples impregnated for 1 day (blue) and one week (red). Impregnations were at 40 °C, 200 mg precursor, and ~2000 psi. Absorbance spectra are shown as averages of four polycarbonate strips each.

In order to investigate further, a wider range of samples was prepared from 1 hr to 48 hr, in order to perform UV-vis and TEM. At this stage of the research the supply of precursor material changed in nature. The precursor that had been purchased previously was a dull brown in colour. The newer material purchased was an off-white powder. The newer material was found to be of higher purity (it is possible the older supply was partially decomposed) and consistently produced a higher silver loading than was expected from previous results. The range of products of different impregnation times were all found to be saturated in UV-vis spectroscopy. Although this prevents comparison by UV-vis, the high loading is beneficial for comparison by TEM imaging. Photographic comparison of the

products (Fig. 53) shows little difference in colour. Some samples have been sectioned in order to perform characterisation techniques such as TEM.

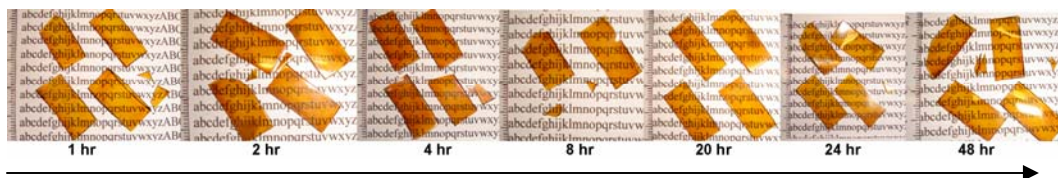


Figure 53 – Photograph of samples impregnated for various times at 40 °C, 1500 psi, and 150 mg precursor.

Another set of samples were produced using a lower precursor mass of 50 mg. This gave a lower silver loading leading mostly to unsaturated UV-vis spectra, allowing comparison (Fig. 54). However, reproducibility in terms of plasmon absorbance was found to be poor. For this reason samples were produced only at two impregnation durations, 2hr and 24 hr. This allowed the level of reproducibility to be observed, and helped prevent error in the comparison of the two times, by averaging several reactions (Fig. 54 inset). As can be seen, the effect of impregnation time on plasmon absorption for these timescales is small compared to the level of irreproducibility. If the difference in average plasmon absorption is seen as significant then it suggests a decrease in nanoparticle loading with time, possibly due to precursor decomposition. However, it must be remembered that the degree of plasmon absorption only gives indirect information about the nature of the nanocomposite. The plasmon bands observed may be dominated by surface deposits or the presence of larger uncharacteristic particles. It is possible that for longer impregnation times there is a deeper impregnation of nanoparticles, but that the concentration or nanoparticle size is lower. In order to

investigate the structure more directly, TEM investigation must be used. Suggestions of how the poor reproducibility may be improved, and how the unwanted decomposition of precursor might be reduced, are discussed in future work (section 12 of this chapter).

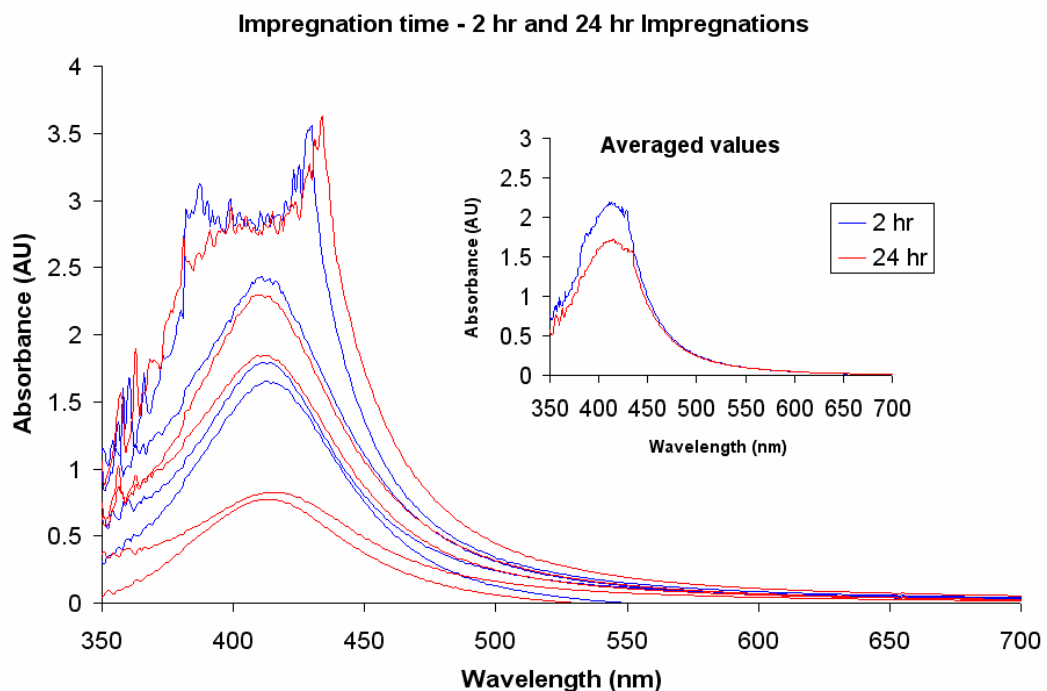


Figure 54 – Plasmon absorbance of samples impregnated for 2hr and 24 hr in order to compare the effect of impregnation time and reproducibility. Reactions were 40 °C and 1500 psi. A lower precursor mass of 50 mg was used to prevent saturation.

2.9.3 TEM Investigation

TEM imaging was performed on cross sections of a silver-polycarbonate nanocomposite strip produced in a 24 hr impregnation. This allowed the size and distribution of nanoparticles to be observed (Fig. 55a). This imaging revealed a

band of nanoparticle impregnated polycarbonate running along the outermost edge of the cross section. This nanoparticle band is of a uniform thickness of $\sim 6.5 \mu\text{m}$ and uniform in composition along the length of the sample. The silver particles are $\sim 10 \text{ nm}$ or less in diameter, roughly spherical, and of relatively uniform size and distribution on a local scale. The nanoparticles are present up to the surface of the polymer, but at the limit of furthest infusion a very definite boundary is evident, after which the nanoparticles cease abruptly. Discrete nanoparticles can be observed at the outermost surface of the polycarbonate, with no sign of metallic film formation (Fig. 55b). The nanoparticle size is relatively even throughout the depth of the sample, becoming significantly smaller only towards the boundary of furthest impregnation (Fig. 55c).

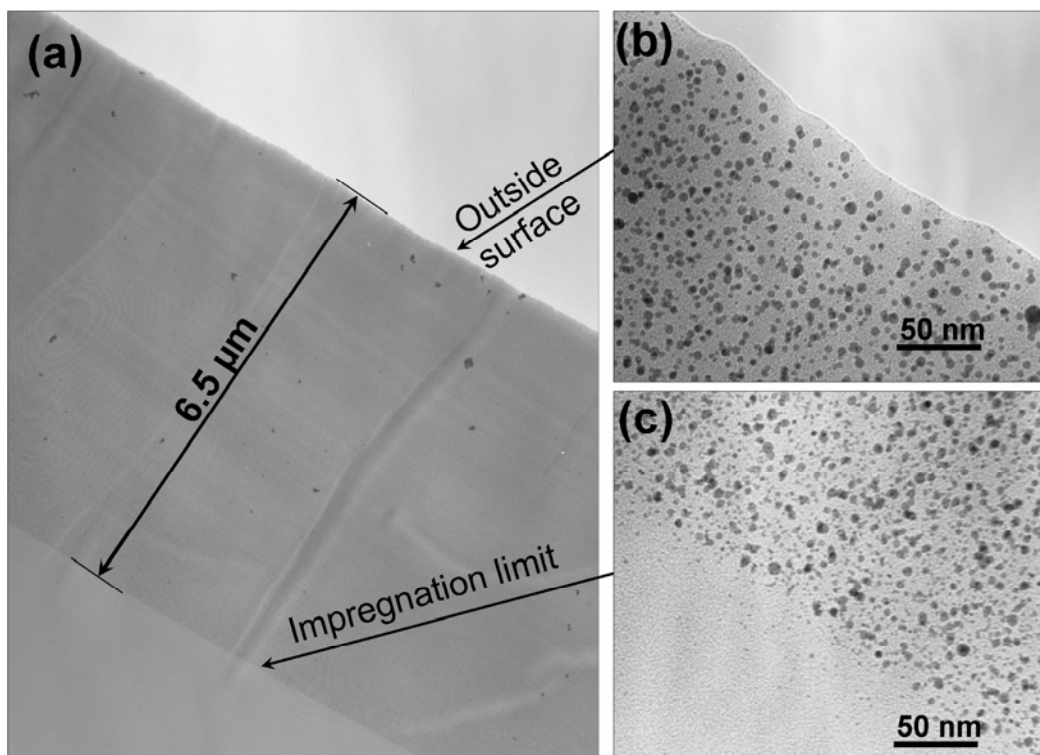


Figure 55 – Sample A: Bright field TEM micrographs of a sample produced at 1500 psi, 40 °C for 24 hr impregnation time of 200 mg precursor. (a) The surface located band of silver nanoparticles in a cross section of the polycarbonate substrate. (b) A magnified section showing nanoparticles at the outside edge of the polymer. (c) A magnified section showing nanoparticles at the limit of furthest impregnation of the nanoparticles.

The size range of the nanoparticles was assessed more fully by constructing a size distribution histogram for nanoparticles in the near surface region. The diameters of 500 nanoparticles, as observed in the TEM images, were measured accurately to provide this data (Fig. 56). The diameters were determined by manually measuring each nanoparticle, on high-magnification prints, using Vernier callipers. It can be seen that the distribution is unimodal, and from the data the mean average diameter is found to be 4.1 nm.

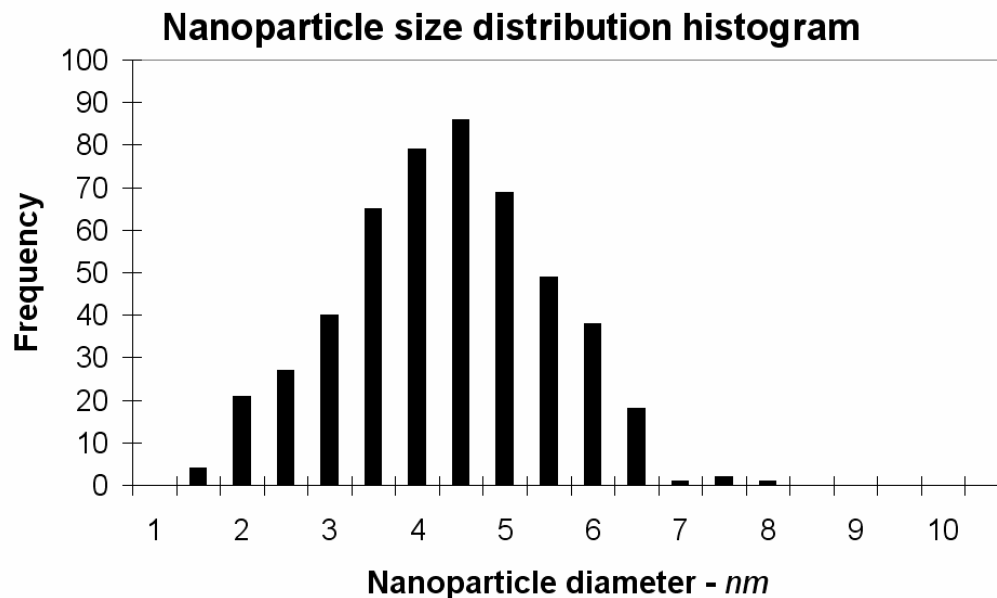


Figure 56 - Histogram showing the distribution of nanoparticle diameters as taken from 500 nanoparticles observed in TEM images of the near surface region of sample A.

Energy dispersive X-ray analysis (EDX) spectra taken within the nanoparticle band, and beyond it, confirm the presence and absence of silver, respectively (Fig. 57a and 57b). The peak observed for silicon is likely to be caused by silicon containing oils being removed from the sealing O-ring of the autoclave and impregnated into the polycarbonate by the action of the $scCO_2$. The depth limited incorporation of nanoparticles confirms incomplete infusion of the organometallic precursor during the 24 hr impregnation step. The only other possibility is that the depth limit is caused by the limit of furthest infusion of H_2 during the reduction step. If this were the case, however, then the EDX spectra would be expected to show silver still to be present further into the polycarbonate even if still as un-decomposed precursor. A selected area diffraction pattern taken in the area containing silver nanoparticles shows the expected spacing for metallic

silver (Fig 57c). The diffraction pattern is weak because of the large masking effect of the amorphous polycarbonate present. The ring pattern observed is characteristic of many small crystallites being present (see Chapter 5.4.4).

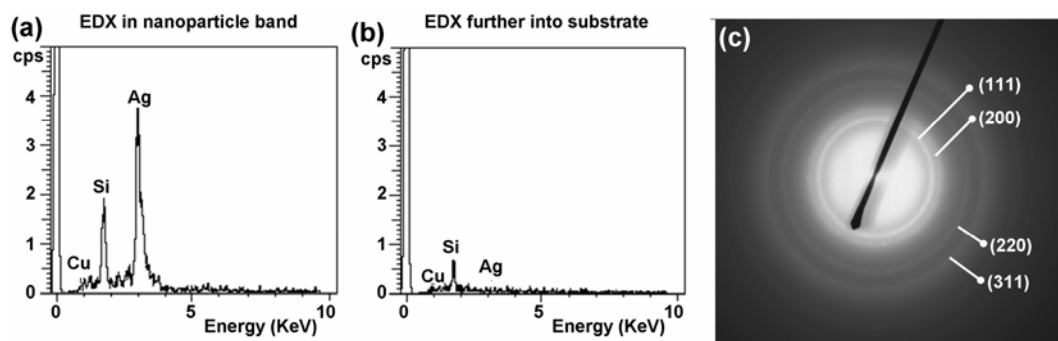


Figure 57 - (a) EDX spectrum taken inside the nanoparticle region. (b) EDX spectrum further into the polymer, past the limit of impregnation. (c) Selected area electron diffraction from the nanoparticle region.

Over the course of this work many TEM imaging investigations have been attempted. Not all were successful. The development of the method of how the samples were prepared for TEM imaging was found to be of vital importance. An improvement of the quality of equipment available, as well as technical skills, allowed satisfactory images to be obtained. This process began with the samples being cross sectioned using stainless steel blades fitted to a conventional microtome. This was replaced by the use of an ultra-microtome, capable of much finer precision, coupled with the use of glass and then finally diamond blades (see Chapter 5.4.2). Samples have been successfully imaged for precursor mass of 150 – 200 mg. Lower silver loadings were not found to be able to produce conclusive imaging in TEM. A collection of TEM images taken of a representative selection of samples is shown over the next few pages. The figures are all shown in the

same format as figure 55; the left micrograph depicts the depth limit of the nanoparticle band, and the upper and lower micrographs on the right hand side show the surface and limit of nanoparticle infusion respectively. The results of these TEM investigations, especially with respect to impregnation time and some limitations of this data, are discussed after the figures. A list of the conditions used for each of the samples is given in table 5, after the TEM images are shown.

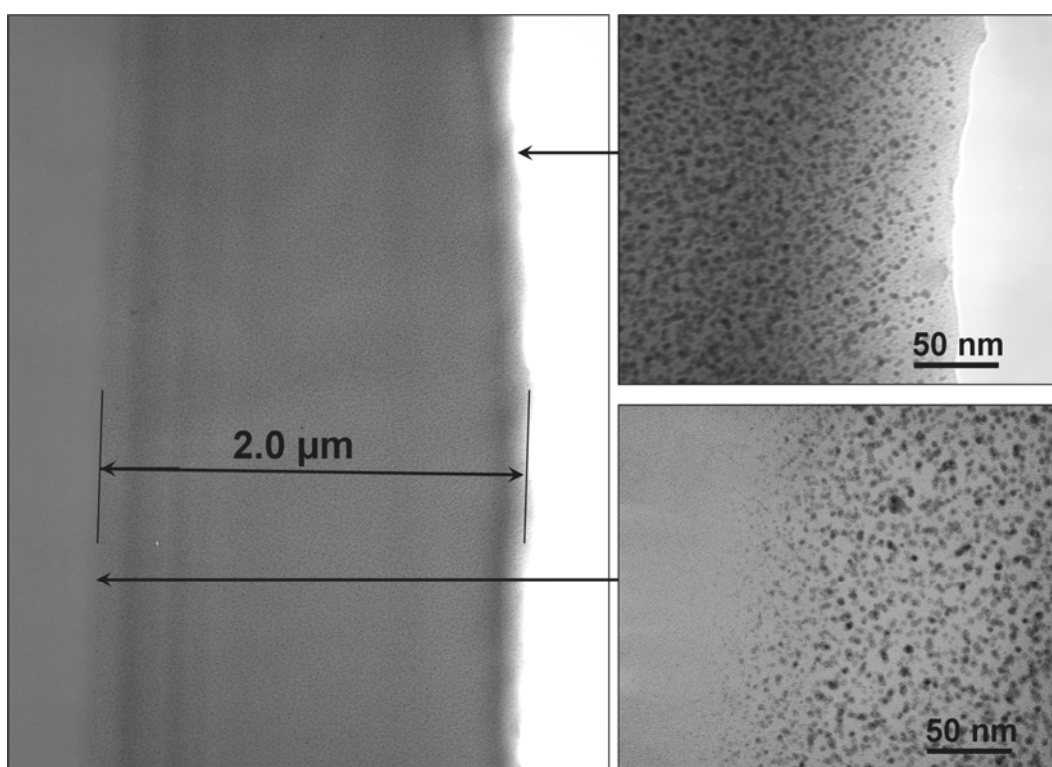


Figure 58 – Sample B: 1 hr impregnation of 150 mg precursor. A uniform band of nanoparticles, ~2.0 μm wide, runs along to the surface of the sample.

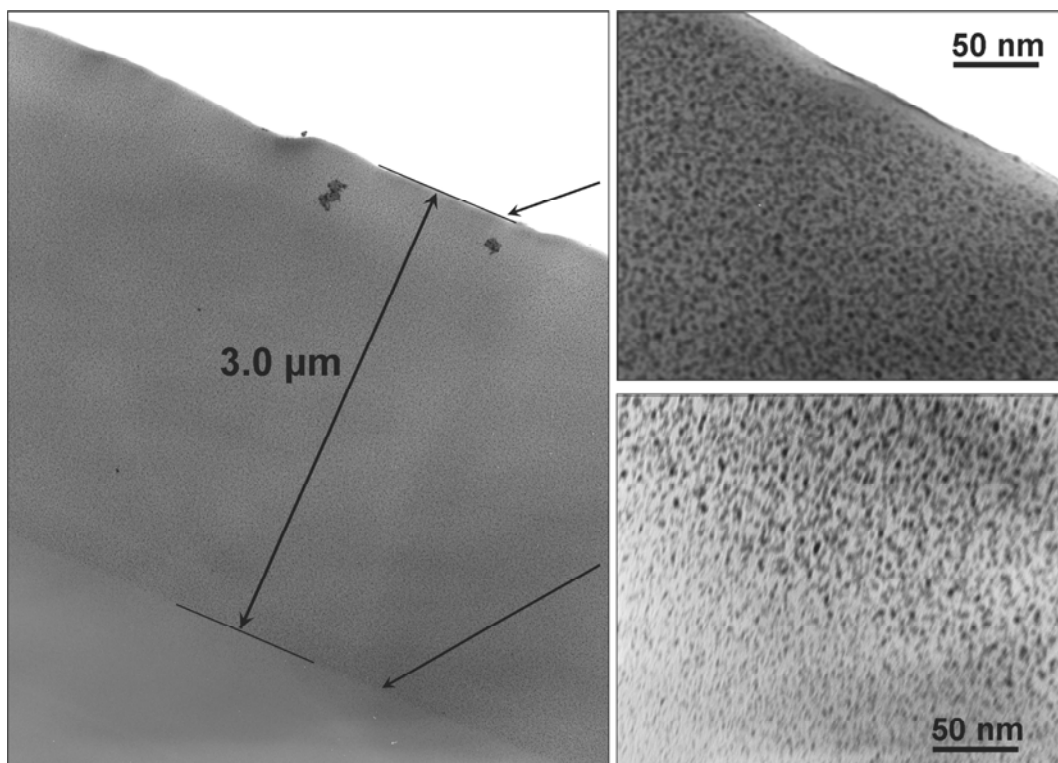


Figure 59 – **Sample C:** 2 hr impregnation of 150 mg precursor. A uniform band of nanoparticles, $\sim 3.0 \mu\text{m}$ wide, runs along to the surface of the sample.

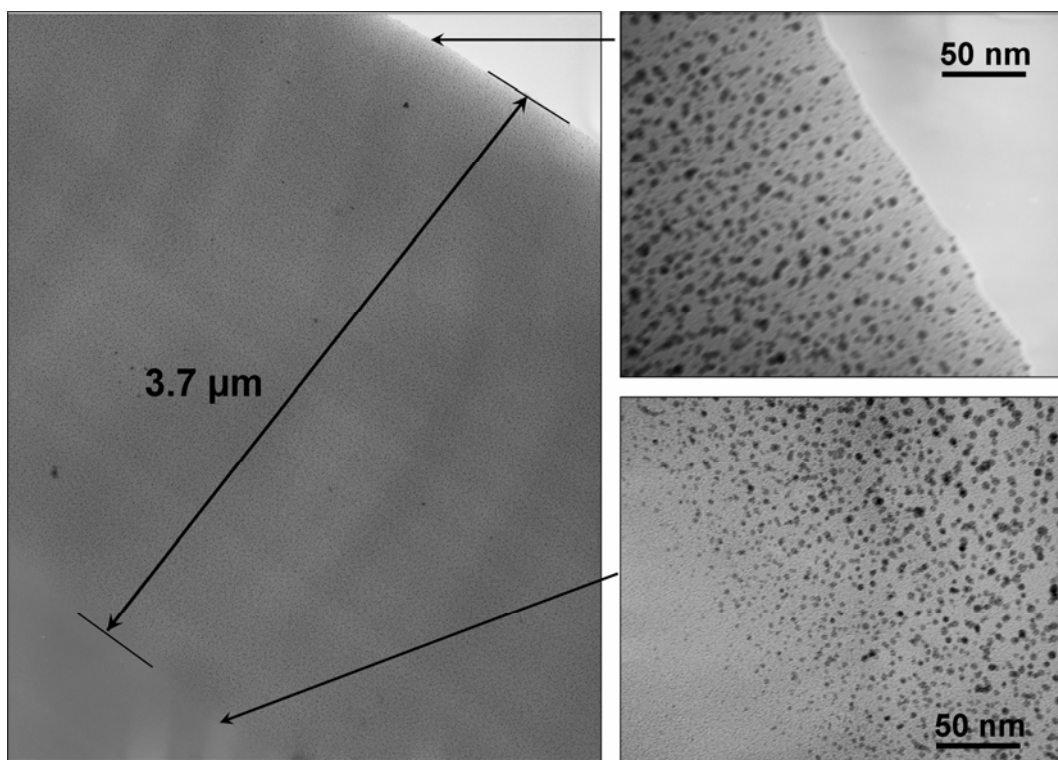


Figure 60 – **Sample D:** 4 hr impregnation of 150 mg precursor. A uniform band of nanoparticles, $\sim 3.7 \mu\text{m}$ wide, runs along to the surface of the sample.

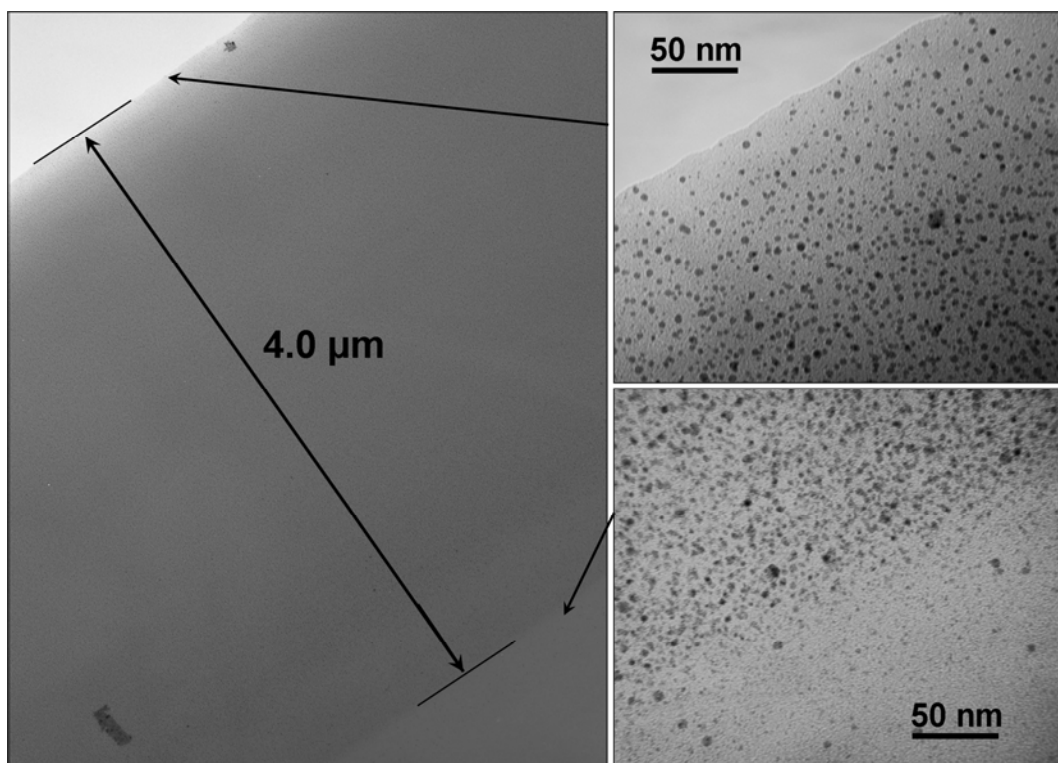


Figure 61 – Sample E: 8 hr impregnation of 150 mg precursor. A uniform band of nanoparticles, ~4.0 μm wide, runs along to the surface of the sample.

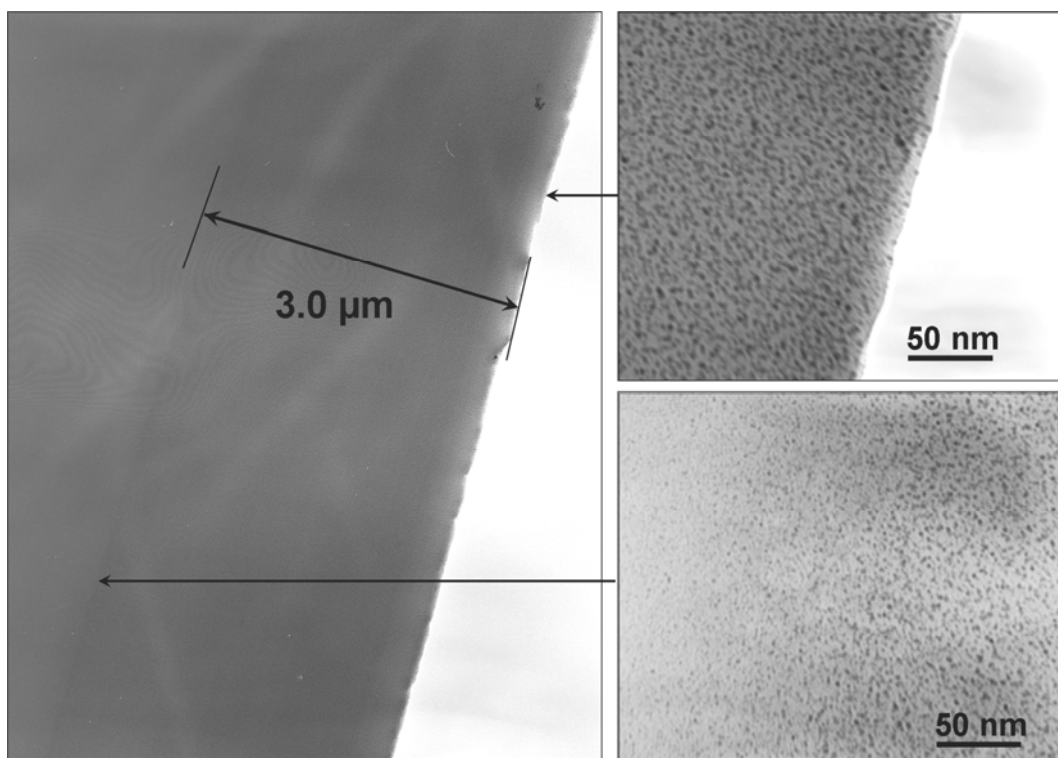


Figure 62 – Sample F: 24 hr impregnation of 150 mg precursor. A uniform band of nanoparticles, ~3.0 μm wide, runs along to the surface of the sample.

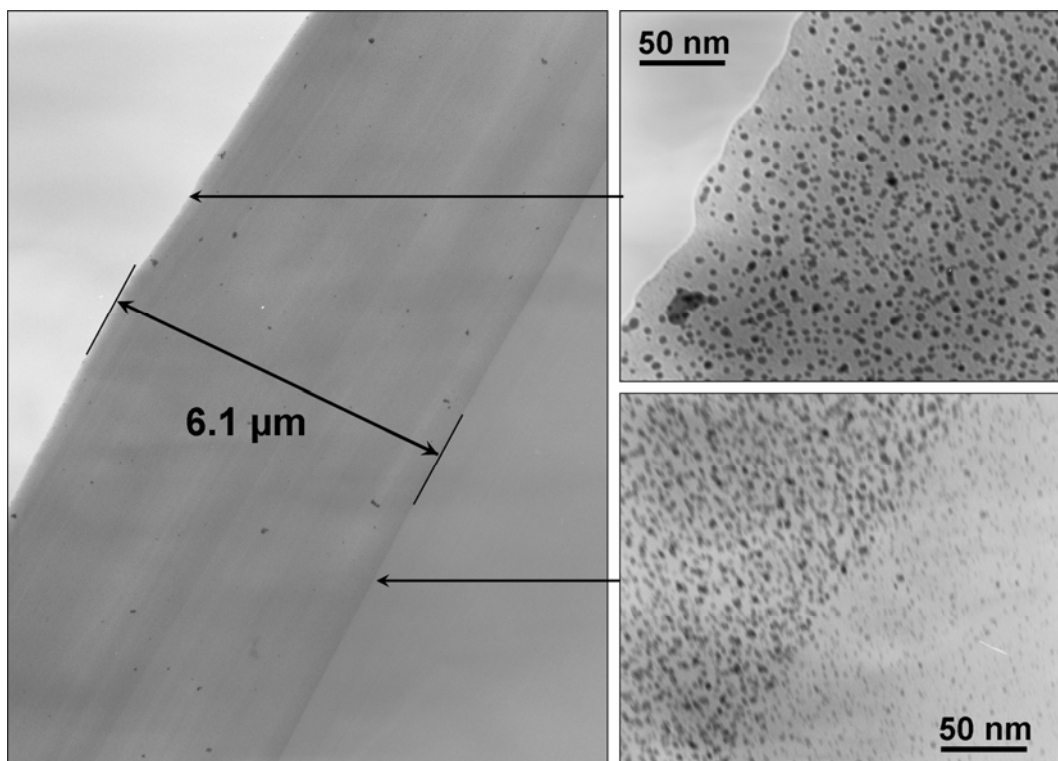


Figure 63 – Sample G: 24 hr impregnation of 200 mg precursor. A uniform band of nanoparticles, ~6.1 μm wide, runs along to the surface of the sample.

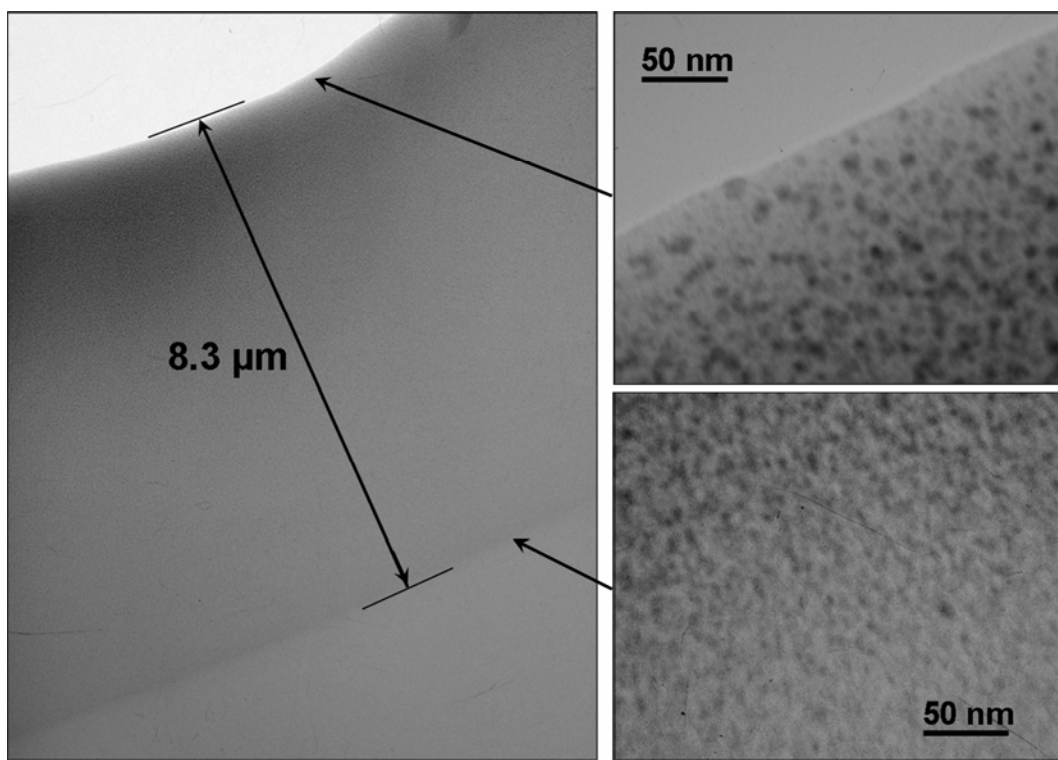


Figure 64 – Sample H: 24 hr impregnation of 200 mg precursor. A uniform band of nanoparticles, ~8.3 μm wide, runs along to the surface of the sample.

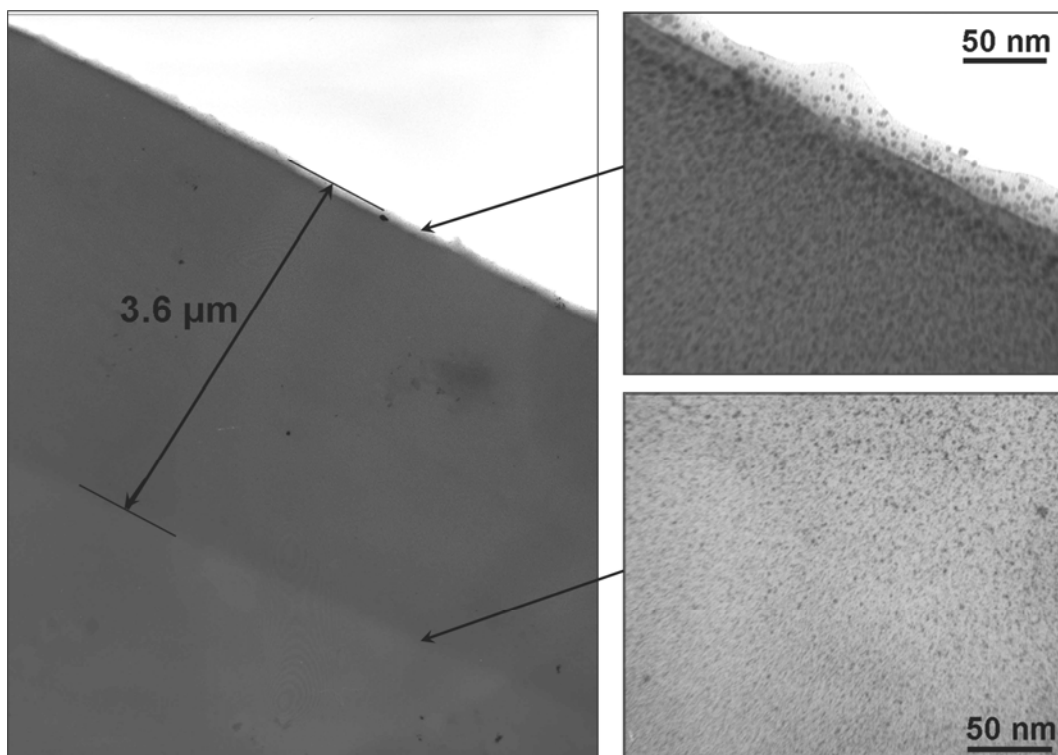


Figure 65 – Sample H: Repeat imaging, showing a thinner band of nanoparticles, 3.6 μm, than the previous TEM session.

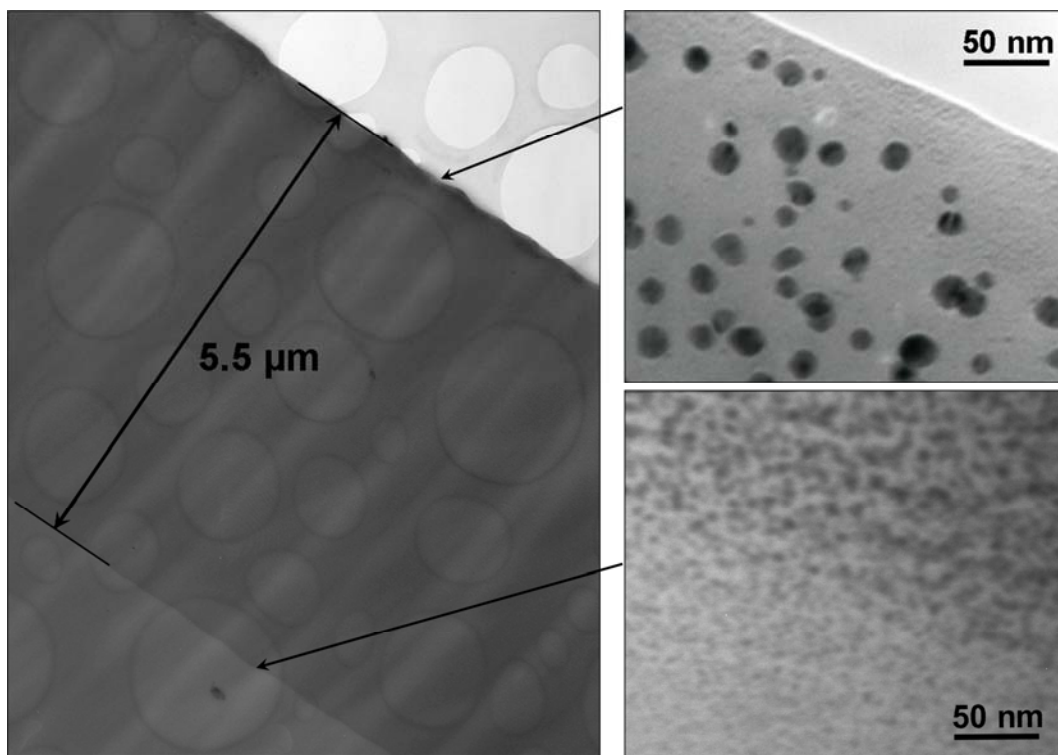


Figure 66 – Sample I: 24 hr impregnation of 200 mg precursor, reduced separately using a 10 ml Thar cell. The sample is supported by a holey carbon film. The nanoparticle band is 5.5 μm wide.

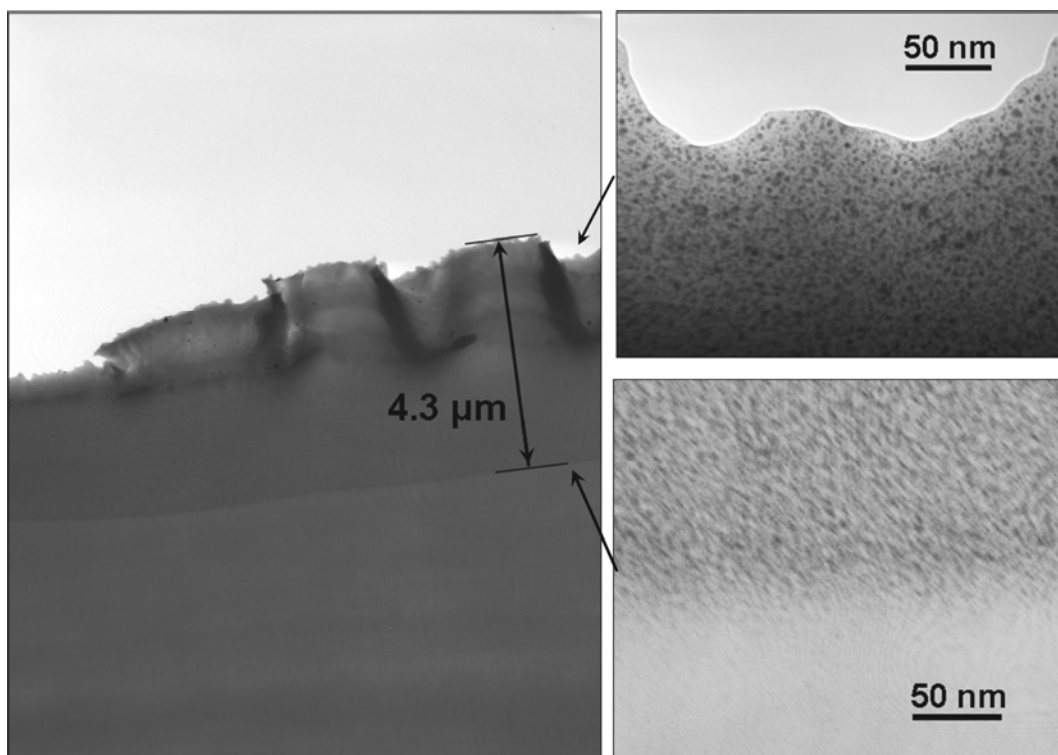


Figure 67 – Sample J: 48 hr impregnation of 150 mg precursor. An uneven, wrinkled, and possibly torn band of nanoparticles is seen running along the surface of the polycarbonate. The band is 4.3 μm at the widest section imaged.

Table 5 – The reaction conditions and nanoparticle band width, from TEM, of samples A to K. Sample K is discussed separately, in section 2.11.3.

Sample	Impregnation conditions				Reduction conditions	NP band width
	Temperature	Pressure	Time	Precursor		
A	40 °C	10.3 Mpa	24 hr	200 mg	80 °C, 1000 psi, 3 hr	5.5 μm
B	40 °C	10.3 Mpa	1 hr	150 mg	80 °C, 1000 psi, 3 hr	2.0 μm
C	40 °C	10.3 Mpa	2 hr	150 mg	80 °C, 1000 psi, 3 hr	3.0 μm
D	40 °C	10.3 Mpa	4 hr	150 mg	80 °C, 1000 psi, 3 hr	3.7 μm
E	40 °C	10.3 Mpa	8 hr	150 mg	80 °C, 1000 psi, 3 hr	4.0 μm
F	40 °C	10.3 Mpa	24 hr	150 mg	80 °C, 1000 psi, 3 hr	3.0 μm
G	40 °C	10.3 Mpa	24 hr	200 mg	80 °C, 1000 psi, 3 hr	6.1 μm
H	40 °C	10.3 Mpa	24 hr	200 mg *	80 °C, 1000 psi, 3 hr	8.3 μm , and 3.6 μm
I	40 °C	10.3 Mpa	24 hr	200 mg *	80 °C, 1000 psi, 3 hr ^F	5.5 μm
J	40 °C	10.3 Mpa	48 hr	150 mg	80 °C, 1000 psi, 3 hr	4.3 μm uneven band
K	40 °C	9.0 Mpa	24 hr	200 mg	80 °C, 1000 psi, 3 hr	no discernible limit

* these reactions were performed using the older, less effective, batch of precursor.

^F this reduction reaction was performed in a Thar cell instead of the MkIII autoclave

2.9.3.1 Problems/limitations of TEM imaging

The TEM images acquired provide important information on the nano-scale structure of the material produced. However, when working with TEM images it is necessary to note the possible complications that may cloud clear interpretation of this information. TEM images can often be misused, especially if they are considered as ‘magic pictures’ that are a direct and accurate representation of the bulk of the material. This can often happen when there is a knowledge gap between the researchers that produce the material and those that image the material, with images being given back to researchers with little communication. In order to correctly interpret the TEM information it is useful to consider the method by which it was acquired and how the sample was prepared, and to recognize and acknowledge any possible faults.

As has been reported, the samples shown here were cross sectioned to provide a thin slice for TEM imaging. The cross section was taken perpendicular to the plane of the polycarbonate sheet, in such a way that the edge being analysed would be part of one of the two large flat surfaces. Care was taken to provide as perpendicular a cross section as could be accomplished. If this was achieved then the nanoparticle depth bands in the images will show accurately the direct depth of the nanoparticles. However, it should be noted that if the cross section was anything less than a true perfectly perpendicular cut, then the TEM images will give an overestimation of the true depth of the nanoparticle band. This is one possible inaccuracy.

Another possible problem is the interaction of the electron beam of the TEM with the non-conducting polymer substrate. The charging of the polymer by the electron beam can cause warping and bending effects. Careful operation of the beam, and discretion when acquiring images can minimise this effect. Any areas that appeared damaged were avoided where possible when taking images. However, some unavoidable effects can still be observed in some of the images. Warping of the polycarbonate by the action of the electron beam occurred in the larger image of sample H (Fig. 64). The poor quality furthest nanoparticle infusion image in sample J (Fig. 67) is a result of unpreventable ‘drift’ of the polymer during exposure.

The nature of the cross section of polymer cut from the substrate and deposited on the TEM grid is also important to the structure of the image observed. Ideally the cut cross section will be whole and undamaged. Unfortunately, because of imperfections in the edge of the microtome blade and because of the fragility of the sections, this was not always possible. Often during TEM characterisation it could be observed that the polymer had separated into smaller ‘ribbons’ along the direction of cutting. Of course, as long as the polymer is not separated in part of the nanoparticle band this should not affect the correct imaging of the sample. However, for some samples it was not possible to find totally undamaged segments, as shown in the larger image of sample J (Fig. 67). As can be seen, the polymer edge has become wrinkled in the right of the image, but has become totally separated on the left. This is less significant in this image because it can be easily observed and therefore taken into account, but it must be

noted that it is a possibility that in other images a portion of the nanoparticle band may have been lost. This would give an under-representation of the depth of nanoparticle infusion. Figure 64 and Figure 65 both show the results of separate TEM investigations of sample H, the first performed in Japan, the second performed in Nottingham with similar equipment. The second investigation shows a nanoparticle depth less than half that of the first. If the outside edge of the polymer is observed in both figures it can be seen that the edge appears more smooth and even in the first figure. The second figure, showing shallower depth, appears more ragged. Also, in the second image the very edge can be seen to be noticeably lighter, and therefore thinner, than the bulk of the material. This may indicate one of two possibilities, either the edge of the polymer may have been ripped away, or the edge of the polymer may have become folded over. This folding could have occurred either during deposition of the polymer to the TEM grid, or under the influence of the electron beam during imaging. Of course it is also possible that both investigations give an accurate representation of different areas of the polymer, and that on a larger scale there are some inhomogeneities in nanoparticle depth.

It is for these reasons that although TEM is a vital tool to observe the nanostructure of these samples, it must be remembered that these results are fallible and care should be taken in their interpretation. However, despite possible discrepancies, some definite trends and similarities can be noted that allow conclusions to be drawn.

2.9.3.2 Impregnation time – nanoparticle depth

From the TEM images of the nanoparticle impregnated bands of samples B – E (Figs. 58 - 61), impregnated for 1 – 8 hr, the depth of the nanoparticles increases with impregnation time (Fig. 68). This effect is less clear when comparing, on the same graph, the samples produced at 24 hr and 48 hr. There is poor reproducibility of the depth of the samples impregnated for 24 hr, and the 48 hr impregnated sample is a shallower depth than would be expected. The poor reproducibility of the several samples impregnated for 24 hr may be caused by inconsistencies in the reactions themselves or by one of the faults of TEM discussed. If the average of the 24 hr impregnations is considered, and if the 48 hr impregnation is seen as significant, then the observable trend is as follows: there is an initial fast increase in nanoparticle depth with impregnation time which becomes less pronounced, or possibly absent, for longer times of impregnation. If the result for 48 hr is seen as anomalous then there is potentially a continuous increase in nanoparticle depth with time. If the 48 hr result is seen as valid this would suggest that the nanoparticle depth ceases to increase a significant amount after $\sim 5 \mu\text{m}$. Let us assume for the moment that there is a definite decrease or even lack of further nanoparticle infusion after an initial fast infusion rate. What theoretic mechanism could cause this effect? Two possibilities are discussed: 1) Slow precursor infusion, 2) CO_2 saturation limited infusion.

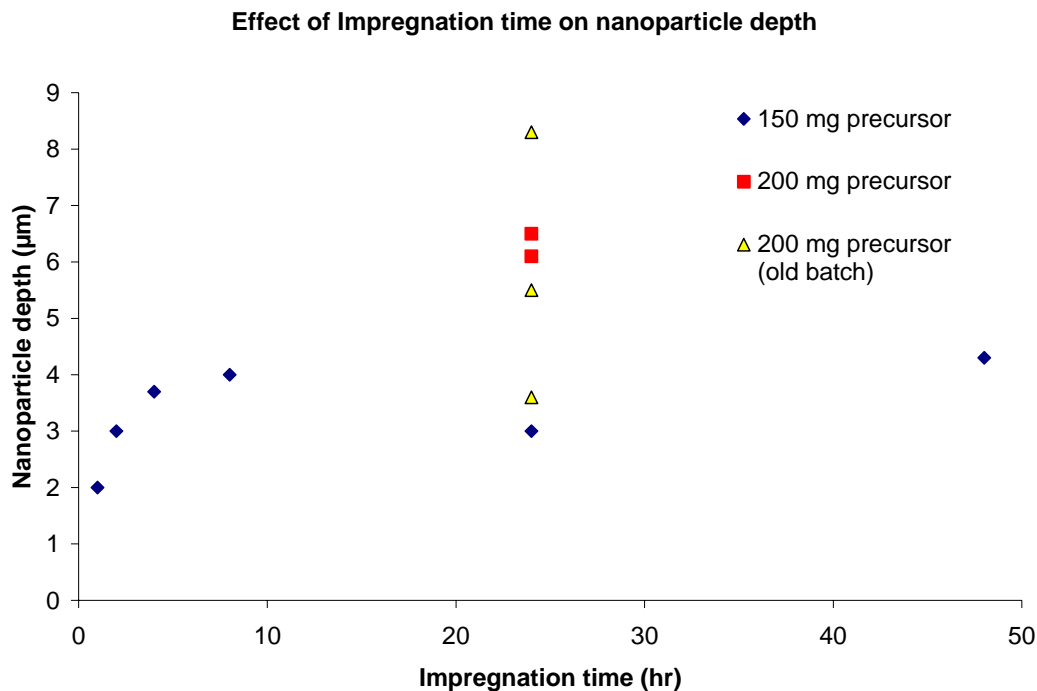


Figure 68 – Nanoparticle depth as a function of impregnation time. Depth is shown as observed by TEM imaging. All samples were produced under identical conditions except for discrepancies in precursor mass and quality, which are depicted by the legend.

Slow precursor infusion

There is a slow infusion of the precursor into the polycarbonate because of the size and steric hindrance of the precursor complex passing between the closely packed polymer chains of the polycarbonate. The rate of this infusion is fastest at the beginning of the reaction when there is the largest difference between the concentration of precursor in scCO_2 and the concentration of precursor in the polymer. Over the course of the reaction the concentrations in the two phases become more even as the precursor partitions into the polymer. At the same time as this process there is a gradual decrease in the concentration of the precursor in the scCO_2 phase because of decomposition on the walls of the autoclave. This

resultant decrease in the driving force for precursor infusion into the polycarbonate results in a slowing down or cessation of the rate increase of nanoparticle depth with time.

CO₂ saturation limited infusion

It is possible that there is very poor partitioning of precursor into the polycarbonate during the main duration of the impregnation step. This could be caused by poor compatibility between the non-fluorinated substrate and the fluorinated precursor, the later of which would be expected to be highly soluble in the scCO₂ phase. If this is the case then only a negligible amount of precursor may infuse into the polycarbonate over most of the impregnation time, and the significant step may instead be during the venting process. As the scCO₂ is vented, and the pressure rapidly drops, the solubility of the precursor in the scCO₂ phase will drastically decrease. This will force the precursor rapidly into the polycarbonate substrate. The initial increase in nanoparticle depth as a function of impregnation time would therefore be dependent on the duration of time it takes to fully saturate the polymer substrate with scCO₂, rather than for the infusion of precursor. After this initial increase the nanoparticle depth would be expected to level out with time, or even to decrease slightly because of the decrease in precursor concentration by decomposition.

In actuality it is more probable that both of these factors have some influence, the more critical question being to what degree each affects the

mechanism. From the discussed limitations of these results it is impossible to determine this for certain. However, previous *in-situ* studies of polymer impregnation suggest that slow precursor infusion is likely to be the dominant effect.²² In order to ascertain the degree of both of these effects and to fully understand the mechanism and control of nanoparticle depth with time it is necessary to perform further work. This should require the investigation of modified and repeatable venting rates to determine the importance and influence of this step. It is also important to perform longer duration impregnation reactions, but to do this accurately the decomposition of precursor must be minimised. It would also be useful to investigate the effect of different precursor designs and solubilities on this process to influence the relative partitioning. The adoption of a suitably scCO₂ soluble non-fluorinated precursor would mark a significant step forward in this process. Recent research on the replacement of fluorinated surfactants, for CO₂, with hydrocarbon surfactants suggests that, with appropriate functionalisation, this may also be possible for metal precursors.²³

2.9.3.3 Comparison of nanoparticle size from TEM images

Within each sample, the size of the nanoparticles is relatively consistent throughout the nanoparticle band, both in parallel and perpendicular to the direction of the band, and is in the 2 – 10 nm range. The exception to this is sample I (Fig. 66) which is discussed separately later. The uniformity of the nanoparticles along the length of the band suggests a homogeneous impregnation environment. The uniformity of nanoparticle size perpendicular to the nanoparticle

band, with nanoparticles becoming noticeably smaller only close to the limit of impregnation, suggests a relatively uniform concentration of precursor occurred across this band during impregnation. This is supported by EDX evidence taken as part of the TEM characterisation performed in Japan on sample H. EDX spectra were taken at five specific locations across the strip: at the surface, at the centre of the nanoparticle band, immediately before the limit of nanoparticle impregnation, immediately past the limit of nanoparticle impregnation, and further past the limit of nanoparticle impregnation. Figure 69 shows the EDX spectra overlaid onto the TEM image at the appropriate depths. The relative detection levels at the locations show that the amount of silver is consistent across the bulk of the nanoparticle band but decreases rapidly at the impregnation limit.

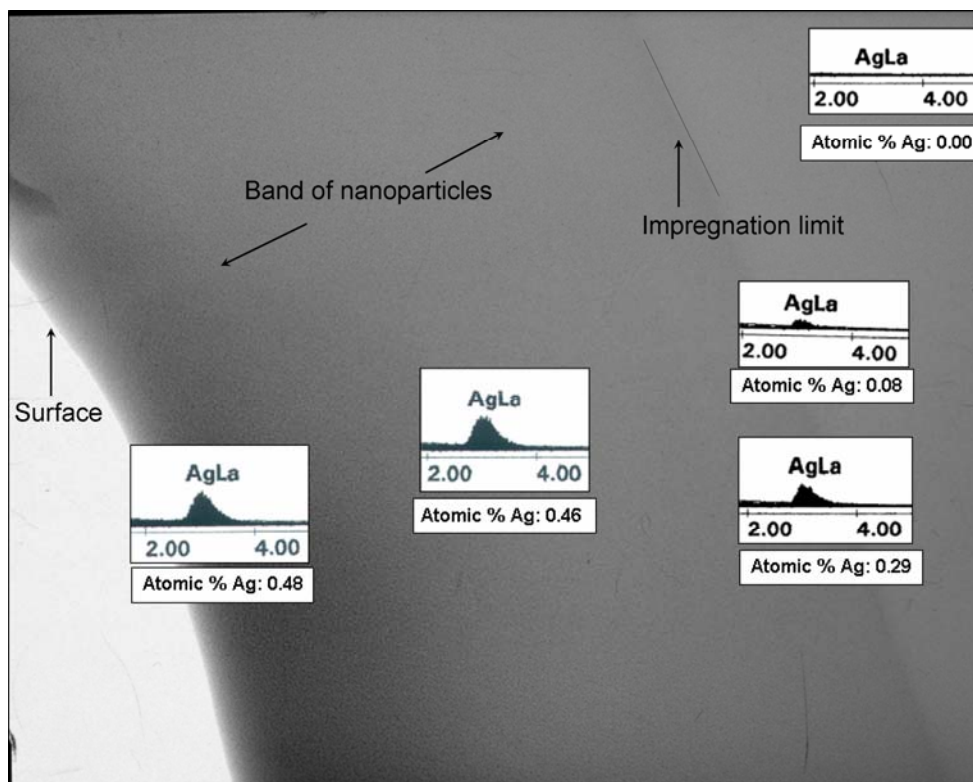


Figure 69 – EDX spectra taken at the approximate depth locations show, on sample H. The atomic % should be considered only in a relative sense and not as an exact value.

The size distribution of nanoparticles between one sample and another is not uniform. Some of the samples are seen to contain mainly smaller nanoparticles generally closer to the lower end of the 2-10 nm range. Other samples contain larger nanoparticles generally closer to the upper end of the 2-10 nm range. It is significant to note that the two impregnation reactions performed with 200 mg of good quality precursor are those with larger nanoparticle size (samples A and G, Figs. 55 and 63). The samples produced with 150 mg of precursor, or with 200 mg of the partially decomposed older precursor, are those with smaller nanoparticles.

This would be expected theoretically as the size of nanoparticles produced may be expected to depend on the concentration of precursor in the polycarbonate.

The exception to these trends is sample I (Fig. 66), which has significantly larger nanoparticles at the surface of the polymer. These nanoparticles decrease more continuously in size between the surface and the limit of impregnation (Fig. 70).

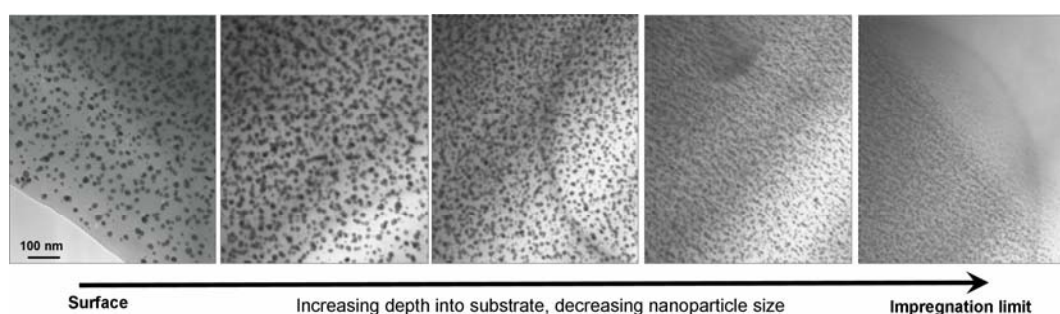


Figure 70 – TEM micrographs of the nanoparticles in sample I. The size of the nanoparticles decreases with their depth into the substrate.

Although the impregnation conditions of sample I were comparable to the other samples, the reduction step was performed differently. Rather than reducing the substrate with hydrogen in the same autoclave in which it was impregnated, as normal, sample I was transferred to a separate 10 ml Thar cell for reduction. This adaptation was intended to allow for the production of more samples, as impregnation steps and reductions steps could then be performed separately in the 60 ml autoclave and 10 ml Thar cell respectively. However, after only a few reactions this was abandoned because it was feared that precipitated precursor from impregnation reactions may deposit in the pipes of the autoclave, and thus

avoid being effectively removed through cleaning. This would then interfere with the next impregnation to be performed. If both steps are performed in the same autoclave this cannot occur because all of the precursor will be reduced by the hydrogen.

The reduction of sample I in the Thar cell caused the polymer substrate to be subjected to a different thermal environment compared to reduction in the autoclave. In the Thar cell the polycarbonate strips must be positioned much closer to the heated metal walls of the reactor than they are held away from in the 60 ml autoclave. Also, in the Thar cell the heating rate is controlled by a thermocouple external to the reactor, as opposed to the internal thermocouple used in the 60 ml autoclave. Factors such as this, and the difference in volume, no doubt lead to a different rate of temperature increase and heat exchange between the hydrogen and the polymer. This is the likely reason for the discrepancy between the size and depth profile of the nanoparticle in this sample compared to the samples reduced in the 60 ml autoclave. It can be observed from figure 70 that although the nanoparticles are larger towards the surface, they are also less dense in number than they are deeper in the substrate. This suggests that the impregnation may still have produced a uniform precursor concentration across the band, but that the reduction conditions may have caused the silver to form into fewer, larger nanoparticles or more plentiful, smaller nanoparticles depending on depth. Although this effect was not investigated further, it suggests that it may be possible to provide some degree of control of the nanoparticle size by manipulating the reduction conditions.

2.10 Solubility studies

The supercritical impregnation reactions performed in this investigation have revealed two key effects that it is useful to reiterate at this point.

- Impregnation reactions of the precursor complex infusing into polymer, at supercritical conditions, are more effective at lower pressure because of partitioning effects.
- The precursor complex infuses deeper and more easily into Teflon[®] AF, a fluorinated polymer, than it does to either PMMA or polycarbonate, both non-fluorinated polymers.

How the precursor partitions into the polymer during impregnation is dependent on precursor solubility in both the scCO₂ and the scCO₂-swollen-polymer. Solubility measurements of the silver precursor, and related complexes, in scCO₂ were performed over a range of pressures. It was hoped this would provide information on the state of the system in order to confirm the hypothesis as to partitioning and to suggest ways in which the process could be improved.

If the silver precursor has a significantly high solubility in scCO₂, which decreases appreciably at the lower pressures used, then this would help to confirm the partitioning effects thought to explain the higher silver loading observed at lower pressure. Therefore an alternative precursor should be chosen/designed that has a more suitable solubility in scCO₂. To this end alternative structures were investigated in order to understand the factors governing the relationship between ligand design and solubility.

The silver precursor that has been used so far is itself a fluorinated complex. It is likely that this may be a factor in the poor partitioning of the precursor into non-fluorinated polymers. Therefore the move to a non-fluorinated precursor of suitable solubility is a target. The original precursor was chosen by our research group specifically because it was believed that its fluorinated structure would enhance the solubility, as has been shown in the literature.²⁴⁻²⁷

These solubility measurements were performed by the author under the supervision of our collaborator Dr. Satoshi Yoda in Tsukuba, Japan. Dr. Yoda is part of the Nanofluidic Process Group which is based in the Nanotechnology Research Institute of the National Institute of Advanced Industrial Science and Technology (AIST). He has considerable experience of nanomaterial synthesis with scCO₂ and the dissolving/decomposing properties of precursors.^{12, 28-32}

Noble metal complexes soluble in scCO₂ have now become important for the fabrication of nano-functional materials such as electronic devices and metal-polymer composites.^{33, 34} The solubility of these complexes in scCO₂ is useful information for the design of the materials and monitoring of the fabrication process. However the solubility data of these complexes is limited, probably because classical solubility measurement (by extraction and gravimetry / quantitative analysis) requires long time experiments and significant amounts of expensive analyte compounds. Hansen and Bruno,³⁵ and later Ashraf-Khorassani *et al.*,²⁷ developed a useful method for solubility measurements using direct injection of scCO₂ solution into LC eluent. This technique has been replicated and developed by Yoda and colleagues and is used here for the evaluation of the

solubility of a range of metal complexes applicable to the scCO₂ impregnation process described in this work.

A brief outline of the process for solubility measurement is given here. For a more detailed description see Chapter 5.4.6. In a typical solubility measurement a metal complex is packed into the sample column dispersed with glass beads. The sample column is part of a high pressure CO₂ system that is enclosed in a heating unit to keep the system at the chosen temperature (40 °C for the studies described here). CO₂ is then flowed slowly through the system driven by a liquid CO₂ pump and vented via a back pressure regulator. Pressure control is achieved by the back pressure regulator and flow rate is controlled by the pump rate. After equilibrium solubility is reached, 2 µl of the scCO₂ solution is injected into the HPLC eluent via a sample loop. The eluent phase can then pass through the LC column as normal before the analyte sample is detected by UV-vis spectroscopy. Solubility was then derived from the analytical curve of the samples from LC, volume of the sample loop, and scCO₂ density.

2.10.1 Complexes investigated

Initially a range of only silver complexes were chosen for analysis. It was hoped to ascertain the solubility of the complex already used and to compare this to some other potential complexes. Also it was intended to study the effect of ligand fluorination, and whether a suitable solubility could be reached without the need for fluorination. Unfortunately, the results of many of the silver complexes tested proved inconclusive. This was caused by a poor suitability of the UV-vis

spectra and by insufficient separation by the LC column. Many of the complexes only contained spectral features at ~200-250 nm, which were at the limit of detection and impaired by noise caused by the injection of CO₂. In order to overcome these obstacles a similar range of copper complexes was chosen as a model system for silver. The more easily detectible UV-vis spectra of the copper complexes allowed the same factors to be studied.

2.10.1.1 Silver complexes:

The following complexes were tested:

1. Silver (I) acetylacetonate – Ag(acac)
2. Silver (I) cyclooctadiene hexafluoroacetylacetonate – Ag(hfac)COD
3. Silver (I) trifluoroacetate
4. Silver (I) pentafluorobutyrate
5. Silver (I) heptafluorobutyrate
6. Silver (I) dimethyl heptafluorooctanedionate

The structures of these complexes are shown in figure 71. Only the Ag(acac) and Ag(hfac)COD were found to be suitable for analysis.

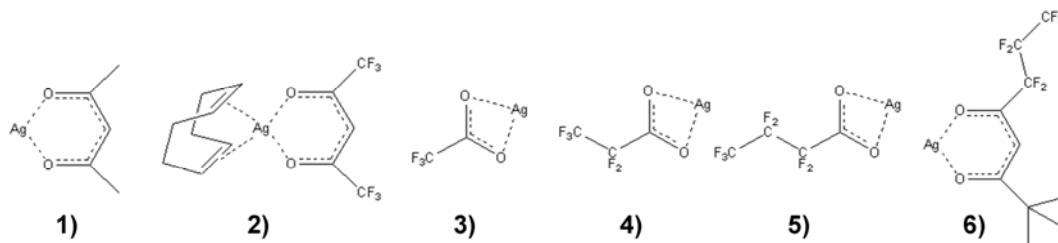


Figure 71 – 1) Silver (I) acetylacetonate, 2) Silver (I) cyclooctadiene hexafluoroacetylacetonate, 3) Silver (I) trifluoroacetate, 4) Silver (I) pentafluorobutyrate, 5) Silver (I) heptafluorobutyrate, 6) Silver (I) dimethyl heptafluorooctanedionate.

2.10.1.2 Copper complexes:

The following copper complexes were tested:

1. Copper (II) acetylacetonate – $\text{Cu}(\text{acac})_2$
2. Copper (II) trifluoroacetylacetonate – $\text{Cu}(\text{tfac})_2$
3. Copper (II) hexafluoroacetylacetonate – $\text{Cu}(\text{hfac})_2$
4. Copper (II) bis(2,2,6,6-tetramethyl-3,5-heptanedionate) – $\text{Cu}(\text{tmhd})_2$

The copper complexes all have a suitable UV-vis absorption at ~ 300 nm and acceptable interaction with the HPLC column. The solubility of each of these complexes was measured successfully. Structures are shown in figure 72.

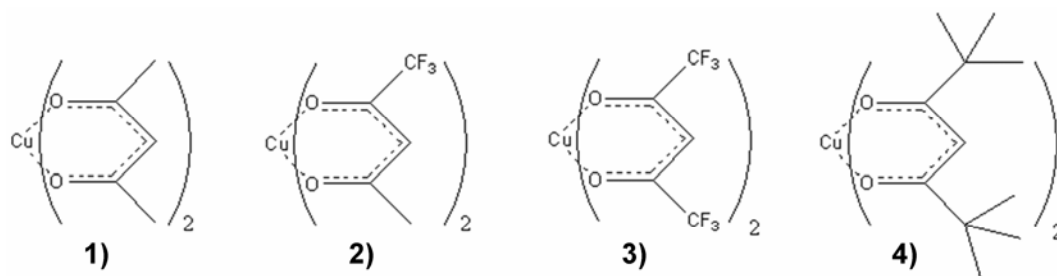


Figure 72 – 1) Copper (II) acetylacetonate, 2) Copper (II) trifluoroacetylacetonate, 3) Copper (II) hexafluoroacetylacetonate, 4) Copper (II) bis(2,2,6,6-tetramethyl-3,5-heptanedionate).

2.10.2 Results of solubility measurements

2.10.2.1 Silver solubility results

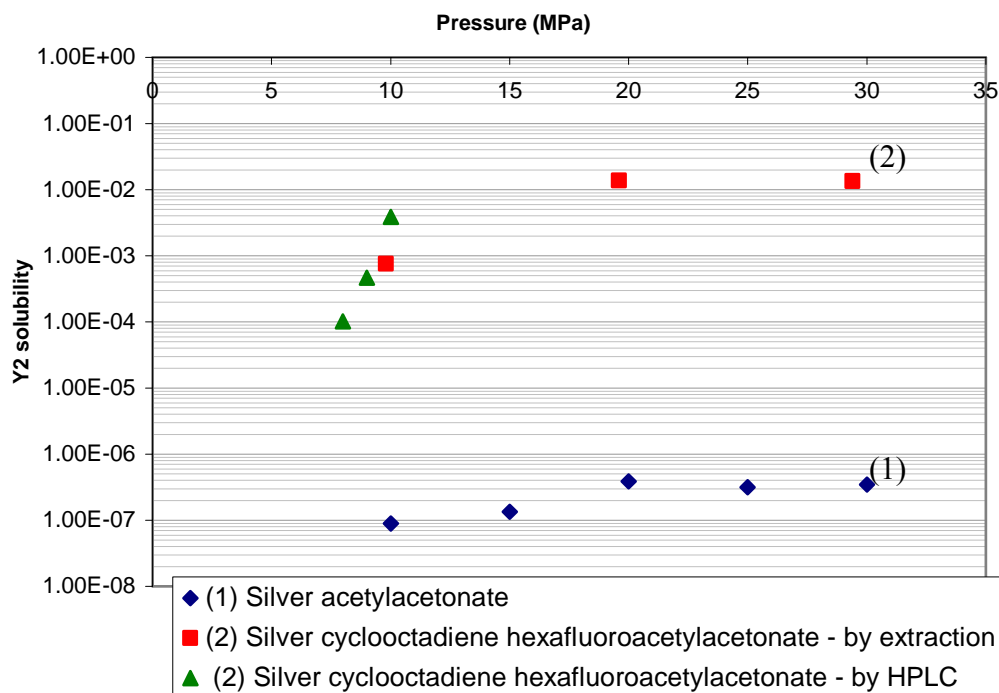


Figure 73 – scCO_2 solubility of silver complexes as a function of pressure. The series are labelled with the appropriate number corresponding to the structures listed in Fig. 51.

The solubility is given as moles of complex per mole of CO_2 (Fig. 73). Results for $\text{Ag}(\text{hfac})\text{COD}$ were provided by combining HPLC data with earlier studies performed by Yoda using a gravimetric extraction rather than LC process. The solubility of $\text{Ag}(\text{hfac})\text{COD}$ was found to be extremely high, which caused difficulty in taking the measurements because of depletion of the material below equilibrium levels. This problem was particularly pronounced at higher pressures, where solubility is higher. It was for this reason that extraction data were

substituted. However, it should be noted there is good agreement between the results.

During impregnation trials in Nottingham the precursor complex Ag(acac) was found to be unsuccessful, with no trace of silver being infused into the polymer. Presumably this is because Ag(acac) had insufficient solubility in scCO₂ for effective transport to the polymer. This low solubility is confirmed by the measurements shown here. The solubility of Ag(hfac)COD can be seen to be much higher. In fact at the pressure used for most of the experiments performed at Nottingham the solubility of Ag(hfac)COD is four orders of magnitude higher than Ag(acac). It is because Ag(hfac)COD was expected to have this high solubility that it was chosen, in order to have good solubility for silver transport to the polymer. However, impregnation results in Nottingham showed a greater degree of impregnation at lower pressures, suggesting the high solubility inhibited partitioning. These results show the solubility is in fact significantly less at the lowest impregnation pressure used compared to the highest. The lowest impregnation pressures used in Nottingham were ~1300 psi (9 MPa) and the highest were ~4000 psi (28 MPa). The solubility measurements show Ag(hfac)COD is ~ 28 times more soluble at high pressure than low pressure. Although this is not such a surprising result it does reinforce the partitioning hypothesis explaining the results found during impregnation reactions.

2.10.2.2 Copper solubility results

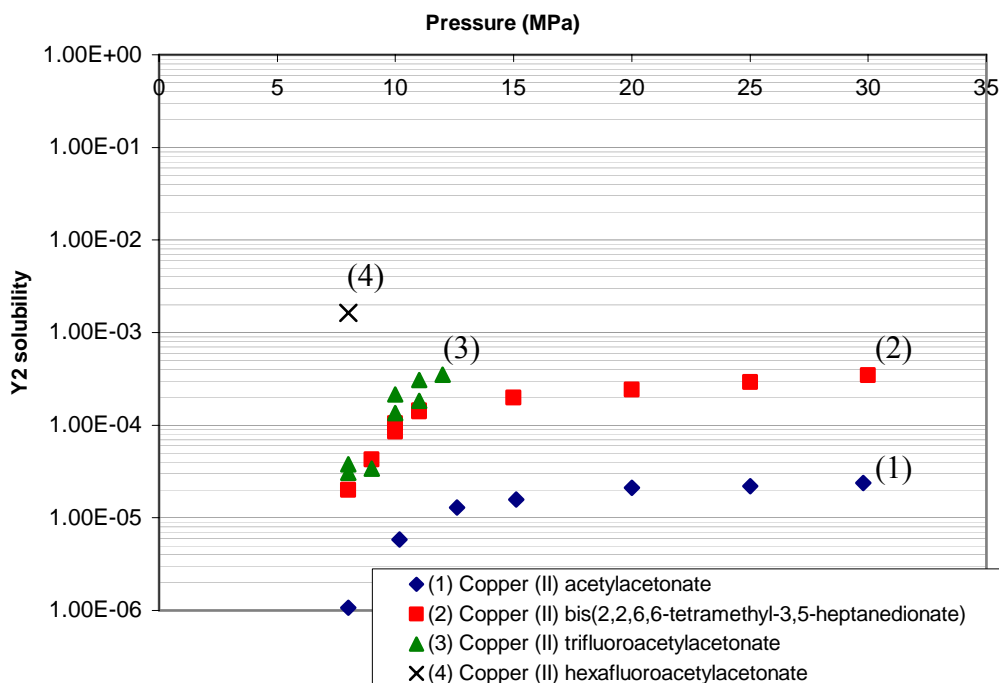


Figure 74 - scCO₂ solubility of copper complexes as a function of pressure. The series are labelled with the appropriate number corresponding to the structures listed in Fig. 72.

The solubilities of the copper complexes are more closely grouped than the silver complexes (Fig. 74). However, there is still a difference in solubility of over 3 orders of magnitude when comparing the least and most soluble complex. For Cu(acac)₂ and Cu(tmhd)₂ the solubility was recorded over the full range of pressures intended. Unfortunately problems of sample depletion again made it difficult to obtain data for the more soluble complexes, especially at higher pressure. For this reason some recordings were omitted for Cu(tfac)₂ and Cu(hfac)₂, but the trends can be assumed to follow those shown for the less soluble complexes.

The strong effect of fluorination to increase solubility can be easily observed from the measurements taken of these copper complexes. $\text{Cu}(\text{acac})_2$, $\text{Cu}(\text{tfac})_2$ and $\text{Cu}(\text{hfac})_2$ are non-fluorinated, partially fluorinated and fully fluorinated analogues of the same complex respectively. The solubility jumps markedly higher for each increase in fluorination. This is as would be predicted from the theory and literature. It is interesting to compare this increase in fluorination to the effect of increasing the steric ‘fingers’ of the complex without fluorination. This was investigated by substituting the fluorine groups of the original complex with methyl groups in order to provide greater interaction with CO_2 than a H group would. The solubility data show that this increase in branching of the complex is roughly equivalent to half fluorinating the complex, in terms of solubility. However, metal ions may be solubilized via binding them to an organic ligand which results in the formation of a neutral stable metal complex.

2.10.3 Implications for the impregnation process

It is known that cationic metal ions are not soluble in pure CO_2 due to weak interactions between the positively charged metal ion and the non-polar CO_2 .³⁶ It is seen from the literature, as has been seen here, that fluorous ligands generally enhance the solubility of the complex compared with the corresponding non-fluorous species. It is also known that alkyl groups and long-chain alkyls in the ligands lead to a higher solubility of the complex, whereas aryl groups generally lower the solubility.³⁷ This again is supported by the results presented here in

terms of a comparison of $\text{Cu}(\text{acac})_2$ to $\text{Cu}(\text{tmhd})_2$. A comprehensive explanation for the effect of the fluorination on solubility is yet to be provided. However it has been suggested that the bulky and highly electronegative fluorine substitution around the central metal ion of a metal complex solute reduces the cohesive energy by reducing the van der Waals attraction and intermolecular hydrogen bonding of the solute.³⁸

Impregnation experiments with $\text{Ag}(\text{hfac})\text{COD}$ showed a higher infusion at lower pressure, and hence lower solubility. This indicates that the use of a less scCO_2 soluble complex would be beneficial in future work. The specific desired ideal solubility level is not yet known, but must be between that of $\text{Ag}(\text{acac})$ and $\text{Ag}(\text{hfac})\text{COD}$. In future work alternative complexes should be tested in order to find a suitable position in this range, compromising between high solubility for transport and lower solubility for partitioning. If a non-fluorinated complex could be found that possessed a suitable solubility then it is reasonable to assume it would partition and infuse into the polycarbonate more easily.

In the design of a new complex for use in future work it is useful to draw from the structures of $\text{Ag}(\text{hfac})\text{COD}$ and $\text{Ag}(\text{acac})$ as models as the desired solubility is between that of these complexes. Diketonate ligands have been shown to be effective for CO_2 solubility,³⁷ but it is likely that $\text{Ag}(\text{acac})$ is inhibited in solubility by insufficient shielding of the metal centre. The electron deficient metal centre will interact poorly with CO_2 , therefore when it is more protected from the CO_2 the solubility increases. This effect is one reason that $\text{Ag}(\text{hfac})\text{COD}$ has a higher solubility than $\text{Ag}(\text{acac})$. The COD, as well as providing some favourable

interaction itself with the CO₂, helps to shield the metal centre from the CO₂. The other factor that increases the solubility of Ag(hfac)COD over that of Ag(acac) is of course the fluorination of the diketonate group. It is therefore reasonable to assume therefore that if a non-fluorinated analogue, i.e. Ag(acac)COD, could be found or synthesised then this may provide the desired solubility level (see Fig. 75, (1)). Such a complex would possess a higher solubility than Ag(acac) because of the presence of the cyclooctadiene group shielding the metal, but a lower solubility than Ag(hfac)COD because of the lack of fluorination. However, we must consider the possibility that this structure modification may reduce the solubility too much, causing failure of the impregnation process. If this occurs then lessons can be drawn from the investigations of the copper complexes. The silver complex could be given a more branched structure, as with Cu(tmhd)₂, to give a silver (I) cyclooctadiene 2,2,6,6-tetramethyl-3,5-heptanedionate structure, Ag(tmhd)COD (see Fig. 75, (2)). This would be expected to have a higher solubility than Ag(acac)COD, but should definitely be a second choice for potential silver complex. This is because although the lack of fluorination may cause more preferential partitioning, the added steric hindrance may inhibit diffusion between the polymer chains, hence slowing infusion into the polymer.

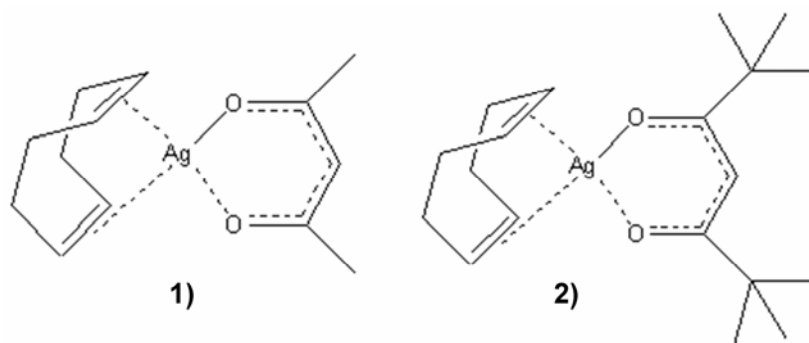


Figure 75 – Potential future silver precursor complexes. 1) Silver (I) cyclooctadiene acetylacetonate. 2) Silver (I) cyclooctadiene 2,2,6,6-tetramethyl-3,5-heptanedionate.

These two suggested complexes will hopefully offer a ‘best of both worlds’ approach for any future work using this technique. The solubility should be ideal for high silver transport to the polymer, but with better partitioning aided by a non-fluorinated structure. The solubility of the complexes themselves need not be at an exact value, only in an appropriate range, as the ability of pressure to control solubility has been demonstrated.

2.11 Applications testing

The potential of silver nanoparticle impregnated polycarbonate substrates for surface enhanced Raman spectroscopy was investigated. This was undertaken in collaboration with the Optoelectronics Research Centre of the University of Southampton, involving the work of L. Lagonigro, Dr. A. C. Peacock and Prof. P. J. A. Sazio.

2.11.1 Advantages of the substrate for SERS

These metal-polymer composites allow for the construction of optical-plasmonic devices that could exploit the mechanical robustness and flexibility of the polymers whilst providing protection of the particles from the surrounding environment to yield a high degree of temporal stability. Silver nanoparticles are known to have superior plasmonic properties, ideal as SERS substrates, but are predisposed to oxidation. Although there has been some progress in developing methods to coat silver SERS substrates to improve their temporal stability, this often requires complicated multiple processing with the resulting SERS response being highly sensitive to the affinity of the target molecule to the coating material and the layer thickness.³⁹ The materials reported in this work have some advantages over other more conventionally prepared SERS substrates. The use of polymer substrate as opposed to more conventional silica, as well as having practical advantages, also represents a lower cost alternative. This is advantageous for the production of low cost disposable materials for applications in which it is

unsuitable to re-use the 'testing strip', be it for concerns over hygiene or contamination etc. Alternatively, in the production of high cost complex devices, this preparation route has other advantages. Many of the applications of such a material will involve the fabrication of microfluidic devices, lab-on-a-chip systems, or other such intricate architectures. The scCO₂ impregnation process means it would be possible to process the polycarbonate into the desired structure, possibly even incorporated into its location in the device, before the silver nanoparticles were introduced. This would avoid any detrimental effects of processing on the nanoparticles or nanoparticle distribution. The embedding of the nanoparticles in the bulk of the polymer will protect the nanoparticles – making the SERS materials easily storable over time with no loss of activity. Also, as the nanoparticles extend below the surface, it may be possible to remove a layer of the material in order to regenerate/renew the substrate to extend its use. Finally, if material could be removed from the surface of the substrate in a controlled manner, then this would allow the simple production of waveguides from this material.

2.11.2 Aims of these tests

The intentions of the characterisations performed on these samples can be summarised as follows:

- **Structural Characterisation:** In order to give relevance to the SERS measurements, and in order to understand their cause, it was necessary to determine the nano-structure of the material tested. This was accomplished

by the complementary use of TEM, reflectance UV-visible spectroscopy, and refractive index measurement.

- Measurement of the SERS effect. This is performed to determine the effectiveness, if any, of the samples for use in this technique. This is tested with respect to two separate analyte systems, and the temporal stability of the samples is also noted.
- Plasma etching: this is attempted, in association with additional SERS, to determine if it would be possible to etch the samples for the production of waveguides or to refresh the surface. This also allows the comparison of the degree of SERS observed from different sample depths.

2.11.3 Samples tested

A number of polycarbonate-silver samples were provided to Southampton for analysis. The most effective were found to be the more highly loaded samples. Therefore a number of samples were produced, in the manner thought in Nottingham, to be capable of providing the highest loading without any loss of quality in the samples. The conditions for these samples were as follows: 24 hour impregnation of 200 mg precursor at 1500 psi (10.3 MPa) and 40 °C, then reduced in 1000 psi (7.0 MPa) of hydrogen at 80 °C for 3 hours. As well as the samples produced in these conditions, another set of samples were prepared in the same manner except at a lower pressure of 1300 psi (9.0 MPa). This was done to satisfy a request from Southampton, which was for samples produced with a higher silver content than the others, even if at lower quality, in order for comparison. It was for

this reason that a lower pressure was used in the synthesis. According to the theory we have discussed and developed so far, this should cause more silver to partition into the polycarbonate during impregnation. However, normally in synthesis, a pressure of 1500 psi (10.3 MPa) had been used as it was noted that lower pressures tended to cause a slight ‘clouding’ or mottling effect on the nanocomposites produced, and this could be a symptom of a loss of optical homogeneity.

The effect of impregnation pressure can be seen by comparing sample A (10.3 MPa) with a second sample K produced at a lower pressure (9.0 MPa). TEM results of sample A have already been introduced as part of section 9.3, but these are repeated here for ease of comparison. The second sample is therefore designated as sample K following on from the lettering of samples in section 9.3, so as to avoid any possible confusion. TEM micrographs of the cross-sections of the two samples (Fig. 76) show that in both cases there is a locally uniform distribution of embedded nanoparticles, but that substrate A has a defined film thickness of $\sim 6.5 \mu\text{m}$ whilst the particles in substrate K penetrate much deeper, with no definite boundary of furthest infusion being observed.

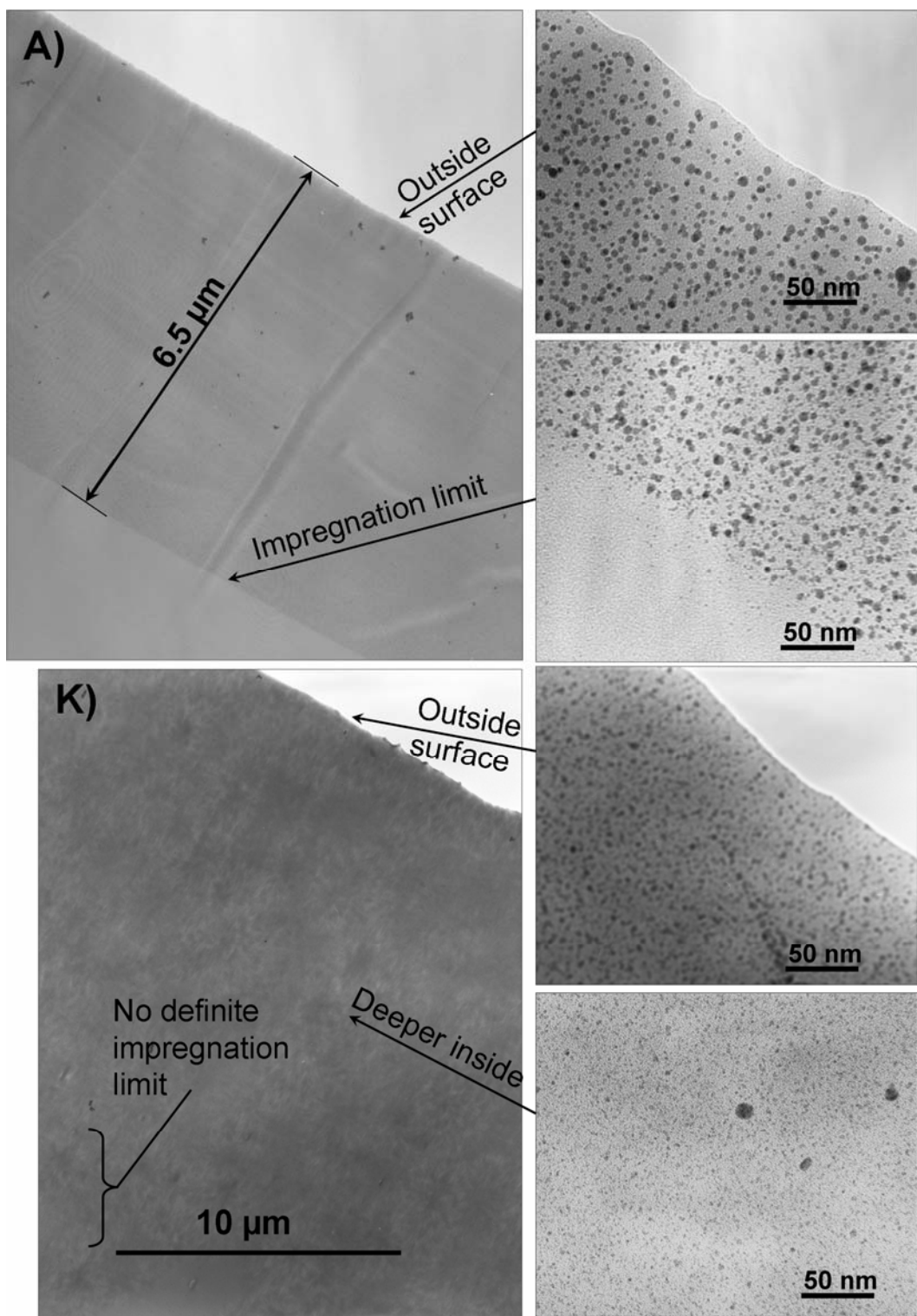


Figure 76 - Bright field TEM micrographs of comparing sample A to sample K, produced at 10.3 MPa and 9.0 MPa respectively.

At the lower pressure it is well known that scCO₂ is less dense and has a lower solvating power for the silver complex. At the higher pressure the precursor solubility is 5×10^{-3} mol mol⁻¹ and at the lower pressure it is 4×10^{-4} mol mol⁻¹, in terms of moles of complex per mole of CO₂ (see solubility studies, section 10). The relative proportion of silver complex that infuses into the polymer during the impregnation step depends on the ratio of solubility in the scCO₂ compared to solubility in the polymer. Therefore the partitioning of the silver complex into the polycarbonate at the lower pressure is likely to be favoured, leading to deeper impregnation of nanoparticles compared to the high pressure impregnation. However, at lower pressure and scCO₂ density the system may be less homogeneous and this could also contribute to the loss of the definite nanoparticle limit.

2.11.4 Results

2.11.4.1 Reflection spectra and refractive index measurement

The reflection spectra of the two samples taken using a UV-vis spectrometer are plotted (Fig. 77a). The positions of the main absorption dips are close to the predicted extinction peak of ~ 410 nm for a distribution of particles with diameters < 10 nm in a dielectric host with a refractive index of the pure polycarbonate ($n = 1.585$), as calculated using Mie scattering theory. We attribute the observed blue shift in the dip minima (from the ideal 410 nm) to an exaggerated contribution from the metal particles at the surface, which are partially exposed to air. The cause of the slight difference in the peak position of the spectra of the two

substrates is unclear. It would seem to suggest that the nanoparticles of sample K were of a larger size than of sample A, but this is not what is observed in the TEM images. The appearance of a second absorption dip in substrate A at ~ 510 nm is likely to arise due to contributions from interactions between neighbouring particles, which is known to shift the plasmon resonance out to longer wavelengths,⁴⁰ indicating an increased silver density in substrate A. To investigate this, the refractive index of the nanoparticle composites were measured using a prism coupling technique.⁴¹ In this technique a 633 nm He-Ne source is launched onto the surface of our substrate, at varying angles of incidence and the reflected light is collected with a photodetector. Figure 77b plots the collected transverse electric (TE) polarised spectra for both substrates A and K (solid curves) as functions of the effective refractive index, related to the incident angle θ_0 via: $n_{\text{eff}} = n_{\text{prism}} \sin \theta_0$.

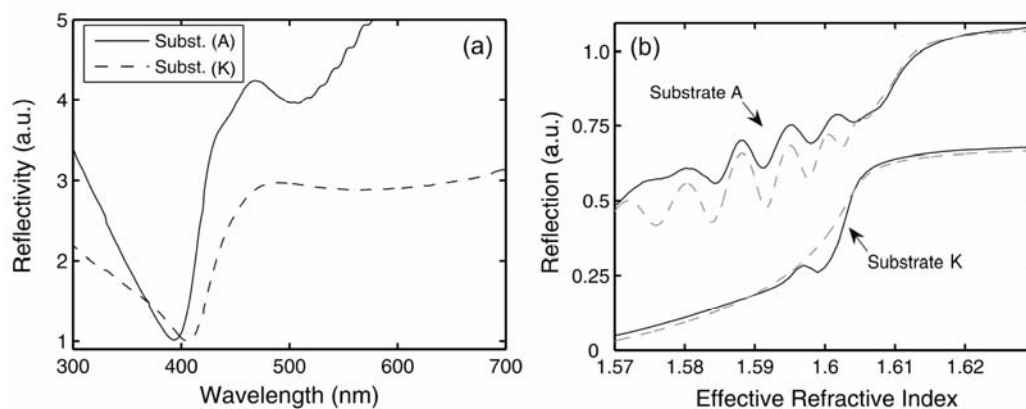


Figure 77 - (a) Reflectivity spectra of the two polycarbonate substrates. (b) TE reflection spectra for varying incident angles, plotted as a function of the effective refractive index, obtained from the prism coupling measurements (solid curves) together with the calculations for a multilayer film (dashed curves).

The refractive index of the composite film is found from the angle at which the reflection intensity starts to drop off and corresponds to the point where the light starts to couple into the thin film, with the decreasing intensity being due to the absorption of the silver nanoparticles. The oscillations in substrate A are due to interference effects in the multilayer film, thus providing information about the film thickness, and their absence in substrate K is due to the lack of definite silver film thickness, where we attribute the single absorption dip to scattering losses. To obtain the most accurate values for the film parameters the curves were fitted using a multilayer reflection calculation for both the TE and TM (transverse magnetic curves not shown) polarisation spectra (dashed curves). From this we obtained the refractive indices of: $n = 1.611 \pm 0.003$ for substrate A and $n = 1.602 \pm 0.005$ for substrate B, and a film thickness of $\sim 7 \mu\text{m}$ for substrate A, in good agreement with the TEM measurement. The higher average index obtained for substrate A over that of substrate K confirms the higher particle density in A compared with K and further evidence to this is provided via close examination of the TEM images in Fig. 76.

2.11.4.2 Surface Enhanced Raman Characterisation

To test the metal-polymer substrates for SERS activity we first considered 4-aminothiophenol (4-ATP) as a target molecule because it has very distinct Raman features and it is known to form an ordered self-assembled monolayer on coinage-metal surfaces. The samples were treated by drop casting a 0.5 mM

solution of 4-ATP in ethanol and allowing the solvent to evaporate. Significantly, polycarbonate is only moderately resistant to ethanol so that we expect the solution to slightly permeate the substrates and thus access more of the silver nanoparticles. The measured SERS spectra for the two substrates are shown (Fig. 78a) together with a control spectrum taken on an undoped (silver-free) polycarbonate sample treated with 4-ATP in the same manner. The peaks in the control sample simply correspond to the Raman spectrum of the polycarbonate whilst those of the silver nanoparticle loaded sample clearly show strong features of the main vibrational modes of the target molecule, as assigned in the reported literature.⁴² Comparing the SERS signals from the two metal composites, the stronger SERS signal obtained from substrate A is as we would expect from the higher nanoparticle density and also in part to the presence of the second plasmon resonance at ~ 510 nm, which is closer to the laser excitation wavelength. Since the SERS active metal nanoparticles are partially embedded in the substrate, calculation of a precise enhancement factor is difficult. However, from the TEM micrograph of substrate A we have estimated an upper bound on the exposed silver to be 30 % of the surface area. Thus, comparing the SERS response to that of a bulk 4-ATP Raman signal, and assuming a monolayer coverage with a packing density of 8×10^{14} molecules/cm²,⁴³ the resulting enhancement factor is estimated to be of order greater than 10^7 ,⁴⁴ which compares favourably to enhancements reported elsewhere in the literature.

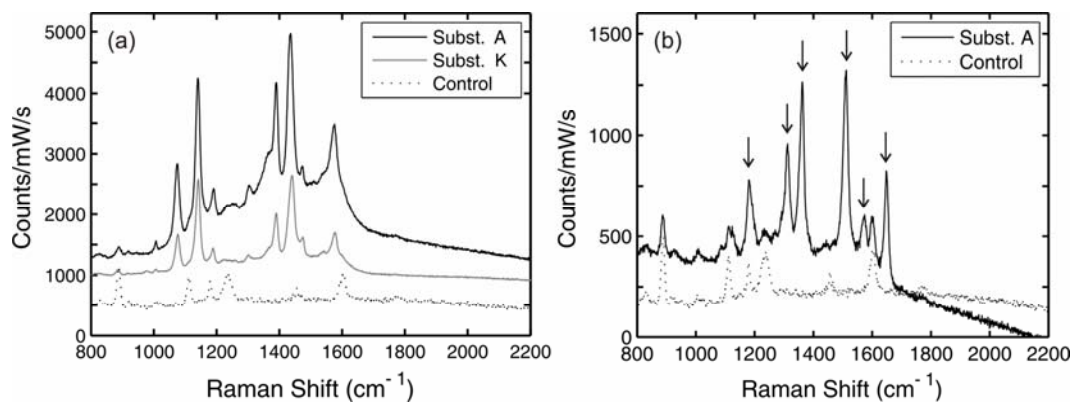


Figure 78 - (a) SERS spectra of 4-ATP on the two metal-polycarbonate substrates (A and K) and (b) SERS spectrum of R6G taken on substrate A, where the arrows indicate the vibrational peaks of the dye. Both figures are plotted together with a control spectrum taken on undoped polycarbonate and the spectra are offset for clarity.

Motivated by the potential biocompatibility offered by our plasmonically active polycarbonate substrates, with inherent advantages for the detection of biological pathogens in their native aqueous environment by exploiting SERS as a whole-organism fingerprinting technique,^{45, 46} the SERS activity of substrate A has also been investigated using a water soluble target molecule, Rhodamine 6G (R6G). This is a useful biological analogue as the dye is dissolved in an aqueous solution that does not permeate the polycarbonate. The SERS spectrum of a 2 mM R6G solution drop cast on substrate A is shown in Fig. 78b. In this figure six vibrational bands of R6G can be clearly identified, as indicated by the arrows,⁴⁷ with the remaining peaks being the underlying polycarbonate modes. The much weaker SERS signal obtained using this dye can be attributed to weaker bonding of the R6G molecules to the Ag metal, the more passive nature of the water solvent so that only the pre-exposed particles contribute to the response, as well as

the larger size of the R6G molecules and their tendency to attach to surfaces in a random orientation.⁴⁸

As previously mentioned, if these samples are to find wide use in routine SERS analysis then temporal stability of the substrates is of vital importance. The fact that the metal nanoparticles are embedded in the polycarbonate means that the substrates have an extremely long shelf life and to date we have successfully measured SERS responses from substrates stored in air which are over a year old. However, what is more surprising is the temporal stability of the substrates after use. Indeed, we have demonstrated that our samples still yield comparable SERS measurements up to one month after treatment with a 4-ATP solution. Such long lifetimes are likely to be a result of the small percentage of silver that is exposed to the atmosphere and thus we expect that in this instance the bulk of the response is coming from Raman probe molecules which have penetrated down to attach to the more deeply embedded particles. This ability to check measurements over time scales of weeks is a significant advantage.

2.11.4.3 Plasma etching

The ability to post-process the metal-polymer films is of considerable interest not only as it allows access to deeper areas of the deposition, where the particle distribution may differ, but also as a means to introduce an additional level of structural design to the substrates and, for example, to fabricate optical waveguides. SERS substrates that incorporate waveguiding geometries into the

devices are advantageous as the enhanced propagation lengths average over many plasmon-analyte interactions thus offering increased sensitivity and reproducibility of the measured response. To etch the metal impregnated films we use an oxygen plasma etching technique as typically employed for the processing of pure polycarbonate substrates.⁴⁹ As a simple mask, we placed a cover-slip over half of the substrate before loading it in an Oxford Instruments Plasma Technology RIE80plus Reactive ion etcher. The chamber was then evacuated to 5×10^{-6} torr before 5 sccm of oxygen and 5 sccm of argon were flowed into the chamber under a controlled pressure of 50 mtorr. After 20 mins of etching the sample was removed and it was noted that the exposed half of the substrate was now darker and cloudier than the untreated side. Transparency of the etched side was improved on washing with ethanol to remove some of the roughness in the surface layer. The resulting substrate was then analyzed using a stylus profiler (KLA Tencor P16) which revealed an etched step of $\sim 2 \mu\text{m}$ with a surface roughness of $< 50 \text{ nm}$ (Fig. 79a).

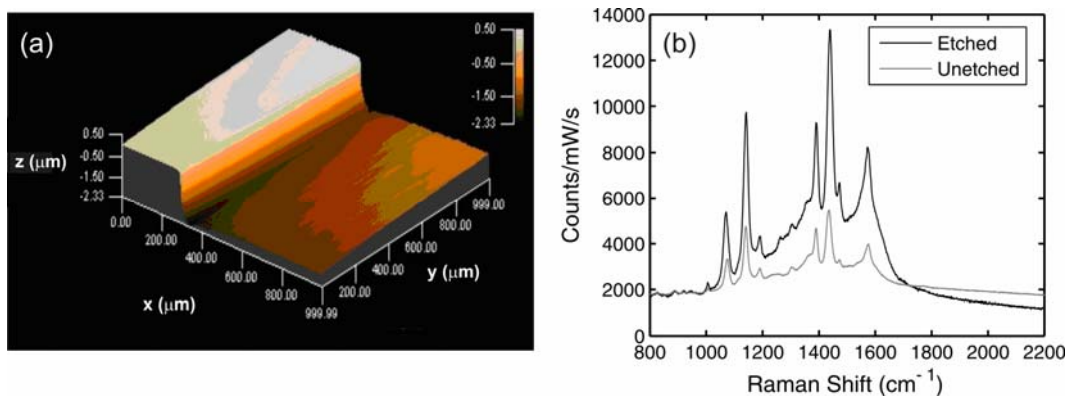


Figure 79 - (a) 3D profile image of the etched metal-polycarbonate substrate. (b) SERS spectra of 4-ATP on both the etched and unetched regions of the substrate in (a).

To test the SERS activity of the etched region we repeated the earlier Raman measurements using 4-ATP as the target molecule. The sample used in the etching process was fabricated using the same parameters as substrate A above and showed a similar SERS response to that in Fig. 78a. Fig. 79b shows the measured SERS spectra on both the etched and the unetched regions of the sample. Despite fears that the etch process may oxidize the metal nanoparticles, clearly this is not the case and in fact we obtain a signal which is $> 2\times$ stronger than the unetched region. This additional enhancement could be attributed to an increase in the density of the nanoparticles going deeper into the film (as confirmed from the TEM micrographs) and importantly this also results in an improvement in the reproducibility of the SERS measurements across the etched region.

2.11.5 Conclusions of SERS testing

The silver impregnated polycarbonate films have been demonstrated as unique substrates for routine SERS analysis. These substrates offer a number of significant benefits over more conventional SERS substrates in that they are cheap, flexible, mechanically robust and temporally stable so that they can be stored for long lengths of time, easily handled and discarded after use to avoid cross contamination. Post-processing of the films via simple etching techniques has been demonstrated without compromising the SERS capabilities thus providing the opportunity to introduce additional structural features into the substrates such as optical waveguides. The robustness of the substrates and the bio-compatibility of the polycarbonate host opens up significant new possibilities for the next generation of plasmonic devices and sensors and in particular biological or *in vivo* monitoring.⁵⁰

2.12 Overall conclusions and future work

Conclusions:

The main aim of this work was to demonstrate the possibility of using scCO₂ techniques for the formation of an optical quality polymer-metal nanocomposite. This has been successfully achieved. It has been shown that scCO₂ is a viable technique to produce uniform and transparent plasmonic nanocomposites. The impregnation process shows good potential for control of both depth and size/concentration of the nanoparticles by modification of time and pressure variables. The process itself has been significantly improved by the development of the high pressure equipment and system. As a result of this development, the method presented here is ideally suited for the production of optical and photonic materials as it does not require surface modification of the nanoparticles and avoids aggregation of the nanoparticles in the polymer. The products have been demonstrated as excellent SERS enhancement materials, which could find application in many emergent optical devices and systems.

Future work:

In future work it would be prudent to also test these materials for activity in other potential applications, such as non-linear optical limitation or metal enhanced fluorescence. Also in future work, if this impregnation system is to find further use, it is important to further improve the method and equipment. Important aspects that must be tackled are the development of the precursor, the

modification of the apparatus to prevent premature precursor decomposition, and the improvement of reproducibility.

It has been shown from the solubility studies that the precursor used is unlikely to be the optimum choice for this system, and potentially superior complexes have been suggested. These should be trialled in an attempt to improve partitioning, increase impregnation possibilities, and to increase understanding of the effect of precursor design.

The partial decomposition of the precursor complex, during impregnation, represents a problem that must be overcome especially if longer/deeper impregnations are to be performed in future. This problem could be significantly decreased if the catalytic effect of the heated steel walls of the autoclave towards precursor decomposition could be minimized. This may be possible by the coating of the steel by a more inert substance. Also, this would be beneficial in general as it would prevent reaction with/ corrosion of the steel by other reactants that may be used. A good possibility for this would be the coating of the steel with a thin layer of enamel. This should at least be investigated.

The most significant contribution to irreproducibility of the products is likely to be the manually controlled nature of the venting process. If this impregnation method is to be developed for future use then it is important that this is corrected. This could be best achieved by the introduction of a controllable back pressure regulator to the system. By the use of this, the venting step could be performed accurately and repeatably. One potential problem that may occur is that the back pressure regulator is likely to become blocked by the solid precursor as it

precipitates out of the scCO₂. This could be avoided by introducing an additional high pressure vessel between the impregnation autoclave and the back pressure regulator. This could be used as a collection vessel for the precursor, similar to a cold trap. It would be filled to the same pressure as the impregnation vessel, but at a temperature lower than the critical point of scCO₂. Then a tap between the collection autoclave and the impregnation autoclave would be opened. The CO₂ would then be released from the back pressure regulator, with the dissolved precursor flowing through from the impregnation autoclave to the collection autoclave where it would be deposited.

2.13 References

1. R. K. Boggess, L. T. Taylor, D. M. Stoakley and A. K. StClair, *Journal of Applied Polymer Science*, 1997, **64**, 1309-1317.
2. K. S. Morley, P. C. Marr, P. B. Webb, A. R. Berry, F. J. Allison, G. Moldovan, P. D. Brown and S. M. Howdle, *Journal of Materials Chemistry*, 2002, **12**, 1898-1905.
3. F. Furno, K. S. Morley, B. Wong, B. L. Sharp, P. L. Arnold, S. M. Howdle, R. Bayston, P. D. Brown, P. D. Winship and H. J. Reid, *Journal Of Antimicrobial Chemotherapy*, 2004, **54**, 1019-1024.
4. K. S. Morley, P. B. Webb, N. V. Tokareva, A. P. Krasnov, V. K. Popov, J. Zhang, C. J. Roberts and S. M. Howdle, *European Polymer Journal*, 2007, **43**, 307-314.
5. S. Porel, S. Singh, S. S. Harsha, D. N. Rao and T. P. Radhakrishnan, *Chemistry of Materials*, 2005, **17**, 9-12.
6. S. Porel, N. Venkatram, D. N. Rao and T. P. Radhakrishnan, *Journal of Nanoscience and Nanotechnology*, 2007, **7**, 1887-1892.
7. K. Aslan, I. Gryczynski, J. Malicka, E. Matveeva, J. R. Lakowicz and C. D. Geddes, *Current Opinion in Biotechnology*, 2005, **16**, 55-62.
8. K. Aslan, P. Holley and C. D. Geddes, *Journal of Materials Chemistry*, 2006, **16**, 2846-2852.
9. J. R. Lakowicz, Y. B. Shen, S. D'Auria, J. Malicka, J. Y. Fang, Z. Gryczynski and I. Gryczynski, *Analytical Biochemistry*, 2002, **301**, 261-277.
10. Y. Lu, G. L. Liu and L. P. Lee, *Nano Letters*, 2005, **5**, 5-9.
11. B. Wong, in *Chemistry Thesis: The Preparation of Nanocomposite Materials using Supercritical Carbon Dioxide*, University of Nottingham, Nottingham, 2005.
12. B. Wong, S. Yoda and S. M. Howdle, *Journal of Supercritical Fluids*, 2007, **42**, 282-287.
13. J. Rosolovsky, R. K. Boggess, A. F. Rubira, L. T. Taylor, D. M. Stoakley and A. K. StClair, *Journal of Materials Research*, 1997, **12**, 3127-3133.
14. J. A. Darr and M. Poliakoff, *Chemical Reviews*, 1999, **99**, 495-541.
15. K. Morley, in *Chemistry*, University of Nottingham, Nottingham, 2003.
16. J. T. Welch, S. C. Ngo and K. K. Banger, Univ New York State Res Found (Uyny), United States.
17. *Technical information published by dupont*, 2005.
18. T. T. Ngo, *Journal of Supercritical Fluids*, 2003, **27**, 215-221.
19. S. G. Kazarian, *Journal of Supercritical Fluids*, 1998, **13**, 107-112.
20. B. L. West, *Journal of Applied Polymer Science*, 1998, **69**, 911-919.
21. X. Y. Shan, D. P. Schmidt and J. J. Watkins, *Journal of Supercritical Fluids*, 2007, **40**, 84-92.
22. S. M. Howdle, *Journal of Polymer Science Part B-Polymer Physics*, 1994, **32**, 541-549.
23. J. Eastoe, S. Gold and D. C. Steytler, *Australian Journal of Chemistry*, 2007, **60**, 630-632.

24. N. G. Smart, T. Carleson, T. Kast, A. A. Clifford, M. D. Burford and C. M. Wai, *Talanta*, 1997, **44**, 137-150.
25. C. M. Wai and B. Waller, *Industrial & Engineering Chemistry Research*, 2000, **39**, 4837-4841.
26. C. M. Wai and S. F. Wang, *Journal of Chromatography A*, 1997, **785**, 369-383.
27. M. AshrafKhorassani, M. T. Combs and L. T. Taylor, *Talanta*, 1997, **44**, 755-763.
28. S. Yoda, A. Hasegawa, H. Suda, Y. Uchimaru, K. Haraya, T. Tsuji and K. Otake, *Chemistry of Materials*, 2004, **16**, 2363-2368.
29. S. Yoda, Y. Nagashima, A. Endo, T. Miyata, H. Yanagishita, K. Otake and T. Tsuchiya, *Advanced Materials*, 2005, **17**, 367-+.
30. S. Yoda, K. Ohtake, Y. Takebayashi, T. Sugeta, T. Sako and T. Sato, *Journal of Sol-Gel Science and Technology*, 2000, **19**, 719-723.
31. S. Yoda, Y. Sakurai, A. Endo, T. Miyata, H. Yanagishita, K. Otake and T. Tsuchiya, *Journal of Materials Chemistry*, 2004, **14**, 2763-2767.
32. S. Yoda, Y. Takebayashi, T. Sugeta and K. Otake, *Journal Of Non-Crystalline Solids*, 2004, **350**, 320-325.
33. A. O'Neil and J. J. Watkins, *Chemistry of Materials*, 2007, **19**, 5460-5466.
34. J. M. Blackburn, D. P. Long, A. Cabanas and J. J. Watkins, *Science*, 2001, **294**, 141-145.
35. B. N. Hansen and T. J. Bruno, *Journal of Supercritical Fluids*, 1993, **6**, 229-232.
36. M. AshrafKhorassani, M. T. Combs and L. T. Taylor, *Journal of Chromatography A*, 1997, **774**, 37-49.
37. O. Aschenbrenner, S. Kemper, N. Dahmen, K. Schaber and E. Dinjus, *Journal of Supercritical Fluids*, 2007, **41**, 179-186.
38. A. F. Lagalante, B. N. Hansen, T. J. Bruno and R. E. Sievers, *Inorganic Chemistry*, 1995, **34**, 5781-5785.
39. X. Y. Zhang, J. Zhao, A. V. Whitney, J. W. Elam and R. P. Van Duyne, *Journal of the American Chemical Society*, 2006, **128**, 10304-10309.
40. E. Hao and G. C. Schatz, *Journal of Chemical Physics*, 2004, **120**, 357-366.
41. T. Sharda, T. Soga and T. Jimbo, *Journal of Applied Physics*, 2003, **93**, 101-105.
42. M. Osawa, N. Matsuda, K. Yoshii and I. Uchida, *Journal of Physical Chemistry*, 1994, **98**, 12702-12707.
43. R. C. Thomas, L. Sun, R. M. Crooks and A. J. Ricco, *Langmuir*, 1991, **7**, 620-622.
44. Z. H. Zhu, T. Zhu and Z. F. Liu, *Nanotechnology*, 2004, **15**, 357-364.
45. R. M. Jarvis and R. Goodacre, *Analytical Chemistry*, 2004, **76**, 40-47.
46. F. Yan, M. B. Wabuye, G. D. Griffin, A. A. Vass and T. Vo-Dinh, *Ieee Sensors Journal*, 2005, **5**, 665-670.
47. H. Chen, Y. L. Wang, S. J. Dong and E. K. Wang, *Spectrochimica Acta Part a-Molecular and Biomolecular Spectroscopy*, 2006, **64**, 343-348.

48. H. Watanabe, N. Hayazawa, Y. Inouye and S. Kawata, *Journal of Physical Chemistry B*, 2005, **109**, 5012-5020.
49. J. W. Kang, J. S. Kim and J. J. Kim, *Japanese Journal of Applied Physics Part 1-Regular Papers Short Notes & Review Papers*, 2001, **40**, 3215-3219.
50. S. M. Moghimi, K. D. Pavey and A. C. Hunter, *Febs Letters*, 2003, **547**, 177-182.

Chapter 3: The stabilisation of suspension and dispersion polymerisations by metal oxide nanoparticles

3.1 Overview

This chapter describes how aqueous metal oxide nanoparticles are tested as stabilisers for biphasic polymerisation reactions. If successful, this would provide both a useful way to recover nanoparticles from solution, and also a method to locate them on the surface of a support material. The chapter begins by summarising the aims of this research, as well as introducing the general theory and previous work. The nature, and synthesis method, of the nanoparticle solutions that are used is then described. The rest of the chapter is split into two main sections according to the form of polymerisation reaction, suspension or dispersion. These reactions occur according to different mechanisms, and it is therefore more appropriate to look at each in turn. Suspension polymerisation is tackled first. The theory and mechanism is explained, before the results are reported and discussed. The same format is then repeated for dispersion polymerisation. A final section summarises the work, providing conclusions and suggesting the directions future investigations should take.

3.2 Contents

3.1	Overview	208
3.2	Contents	209
3.3	Introduction and aims	210
3.3.1	Preparation and nature of magnetite nanoparticle solution	213
3.4	Preparation of polymer-nanoparticle composite beads by a nanoparticle stabilised suspension polymerisation.....	217
3.4.1	Free radical vinyl polymerisation of MMA.....	221
3.4.2	Reaction procedure	225
3.4.3	Results	226
3.4.3.1	Scanning electron microscopy.....	229
3.4.3.2	Transmission electron microscopy	232
3.4.4	Other nanoparticles.....	237
3.4.5	Conclusions	240
3.5	Preparation of polymer-nanoparticle composite microparticles by a nanoparticle stabilised dispersion polymerisation.....	242
3.5.1	Dispersion polymerisation.....	243
3.5.2	Free radical vinyl polymerisation of styrene	244
3.5.3	Reaction procedure	246
3.5.4	Results	248
3.5.4.1	Results for 1.8 gL ⁻¹ nanoparticle concentration.....	249
3.5.4.2	SEM investigation	251
3.5.4.3	TEM investigation.....	253
3.5.4.4	Results for 40 gL ⁻¹ nanoparticle concentration.....	255
3.5.4.5	SEM investigation	259
3.5.4.6	TEM investigation	261
3.5.5	Conclusions	264
3.6	Overall conclusions and future work.....	265
3.7	References	267

3.3 Introduction and aims

One significant problem with the synthesis of nanoparticles is their collection. This was found to be a challenge by Lester *et. al.*¹⁻⁴ who have developed a method of synthesising metal and metal-oxide nanoparticles in a continuous manner in supercritical water. This allows for the low cost production of large quantities of particles in aqueous solution. The development of commercially viable and affordable nano-material has lead to the formation of a spin out company.⁵ The key difficulty encountered by this group was that on the removal of the water from the nanoparticle solutions, the nanoparticles had an irreversible tendency to aggregate, impeding application. I became involved when I was approached for assistance in the collection of these nanoparticles from solution. The request from Lester *et. al.* was whether a method could be found to remove the nanoparticles from this aqueous solution and incorporate them into polymer, to better provide for their use. As has been explained in Chapter 1, the embedding of inorganic nanoparticles into dielectric matrices represents a solution to manipulation and stabilisation problems. Polymer-embedding represents the simplest way to protect nanoparticles and take advantage of their physical characteristics, providing a means of stabilisation, handling, and application, or essentially in this case, formulation for use.

Alternative methods for the formation of such nanoparticle-polymer hybrids were discussed in chapter 1.4.3. There now follows a discussion of some of the problems associated with these traditional methods. Often during *in situ* methods, by-products from the formation of the nanoparticles from chemical precursors are produced in the resulting polymer. In *ex situ* processes,

the dispersion process requires surface modification of the particles, which alters their properties.⁶⁻⁹ Other routes utilise the incorporation of inorganic nanoparticles as part of the polymerisation step itself. An important attraction of the inclusion of nanoparticles during polymer formation, is the avoidance of extra reaction steps and hence simple production and scale-up.¹⁰⁻¹³ However, there are two major drawbacks limiting the practical application of such nanocomposites. The nanoparticles will be incorporated inside the polymer beads rather than on their surface. Moreover after the polymerisation, the stabiliser, which covers the surface of the polymer beads, may inhibit the performance of the nanoparticles or severely reduce the effectiveness of the particles.

The interface between two immiscible liquids is an ideal site for the self-assembly of nanoparticles.¹⁴ Several recent papers show that suspended or dispersed nanometre-sized objects tend to assemble at a liquid-liquid interface in a biphasic system, which rapidly approaches an equilibrium.^{15, 16} Consequently, a monolayer of nanoparticles can be formed and the high interfacial energy of the biphasic system can be reduced because of the adsorption of functional moieties to the nanoparticle surfaces. At the same time, the nanoparticles may generate a certain level of stabilising activity to the small dispersed droplets which have a substantially greater interfacial area than a planar interface. After the interfacial assembly, the small droplets are actually covered by a monolayer of the nanoparticles. Emulsions formed in such a way are often referred to as 'Pickering emulsions', named after Percival Spencer Umfreville Pickering who in 1907 discovered the phenomenon that emulsions

can be stabilised by small particles instead of emulsifiers.¹⁷ These emulsions have attracted attention as an alternative to conventional stabilisers.^{16, 18-20}

It has been reported that organic surfactant-free emulsion polymerisations can be successfully carried out using this solid-stabilised Pickering emulsion technique.²¹⁻²³ Voorn and co-workers showed a stabilisation effect from nano-sized organically modified clay platelets in emulsion polymerisation of methyl methacrylate (MMA).²⁴ Furthermore, the stabilisation of an alcoholic dispersion polymerisation by nanoparticles has been recently reported by Schmid *et. al.*, by the use of commercially available silica nanoparticles of narrow size dispersion.²⁵⁻²⁷

This chapter reports the result of attempts to use nanoparticles produced by Lester *et. al.* as stabilising agents for dispersion and suspension polymerisations. If successful, this would represent a definite advance in this emergent field of nanoparticle stabilised polymerisation. Nanoparticle stabilised suspension polymerisation has not yet been reported. Reports of nanoparticle stabilised dispersion polymerisation are limited, only involving silica particles. The adaptation of this technique to more functionally relevant metal and metal oxide nanoparticles would support this previous work as well as enabling future applications. The targets of this project were not only to improve the theory of nanoparticle stabilised polymerisation, but also the practical aim of recovering the aqueous nanoparticles. This method of 'harvesting' the nanoparticles from solution and embedding them into a substrate has two important advantages: 1) Because the nanoparticles function as the stabiliser, the nanoparticles should become located on the surface of the polymer, which is the optimum position for most applications. 2) The nature of the nanoparticle stabilised

polymerisation means that no conventional surfactants/stabilisers need to be used. This is important because these additives could coat the surface of the nanoparticles and inhibit their function. There are also no by-products produced in the process, and no unwanted contaminants are left in the polymer.

The dispersion polymerisation of styrene and suspension polymerisation of MMA, performed with nanoparticles as stabilisers, will be discussed in two separate sections of this chapter. Both reactions focus on the use of magnetite nanoparticles as a model for nanoparticle stabilisation in general. The supercritical fluid reactor used by Lester et. al. has been successful at producing a range of metal and metal oxide nanoparticles, and has the potential to produce many others.¹ The magnetite nanoparticles were chosen as they were readily available in large supply, but other nanoparticles were also tested to ensure the transferability of the technique. These included cobalt oxide and hematite. The preparation of the magnetite nanoparticles, as well as their characterisation, is described briefly in the following section.

3.3.1 Preparation and nature of magnetite nanoparticle solution

The aqueous nanoparticle solution used in this work was produced by continuous supercritical water hydrothermal synthesis (scWHS), which has been recently used to produce nanoparticulate metal oxides.^{1, 3} As water is heated towards its critical temperature and pressure ($T_c = 374\text{ }^\circ\text{C}$, $P_c = 221\text{ bar}$), it changes from a polar liquid to a fluid with a low dielectric constant and low pH. The self-dissociation constant of water also increases up to $300\text{ }^\circ\text{C}$, giving rise to correspondingly increased concentrations of H^+ and OH^- .²⁸ The lower dielectric constant in scH₂O induces supersaturation and precipitation of small

particles of metal hydroxides, which then undergo rapid dehydration. When used with an appropriate metal salt precursor this technique can therefore be used to produce metal oxide nanoparticles in aqueous solution in a continuous reaction.

In the nanoparticle synthesis process in general, water is pumped through a pre-heating coil and heated to the desired temperature. It is then brought into contact with a concurrently flowing solution of metal salt at room temperature. The flow rates of the two solutions are carefully controlled by the liquid pumps. The pressure is maintained at the desired level by a back pressure regulator. After the mixing point the mixture is passed through a water cooler and products collected as aqueous suspensions.

The specifics of the magnetite synthesis are provided briefly here. The preparation of an Fe₃O₄ nanoparticle aqueous solution was achieved by hydrolysis of ammonium iron (III) citrate in supercritical H₂O. Fresh salt solution (0.02 M, 10 ml/min flow rate, 25 °C, 240 bar) was mixed with supercritical water (20 ml/min flow rate, 415 °C, 240 bar) in a patented nozzle reactor (volume of 4 ml).² The mixture was then cooled down to room temperature by water cooler. The magnetite particles were concentrated after settling. No capping agents or stabilisers were used.

Characterisation of these nanoparticles was performed by TEM imaging of the nanoparticles after deposition from solution onto carbon coated TEM grids. From this imaging it can be seen that the nanoparticles are ~10-20 nm in size, with a relatively narrow, though in no way monodisperse, size range (Fig. 80).

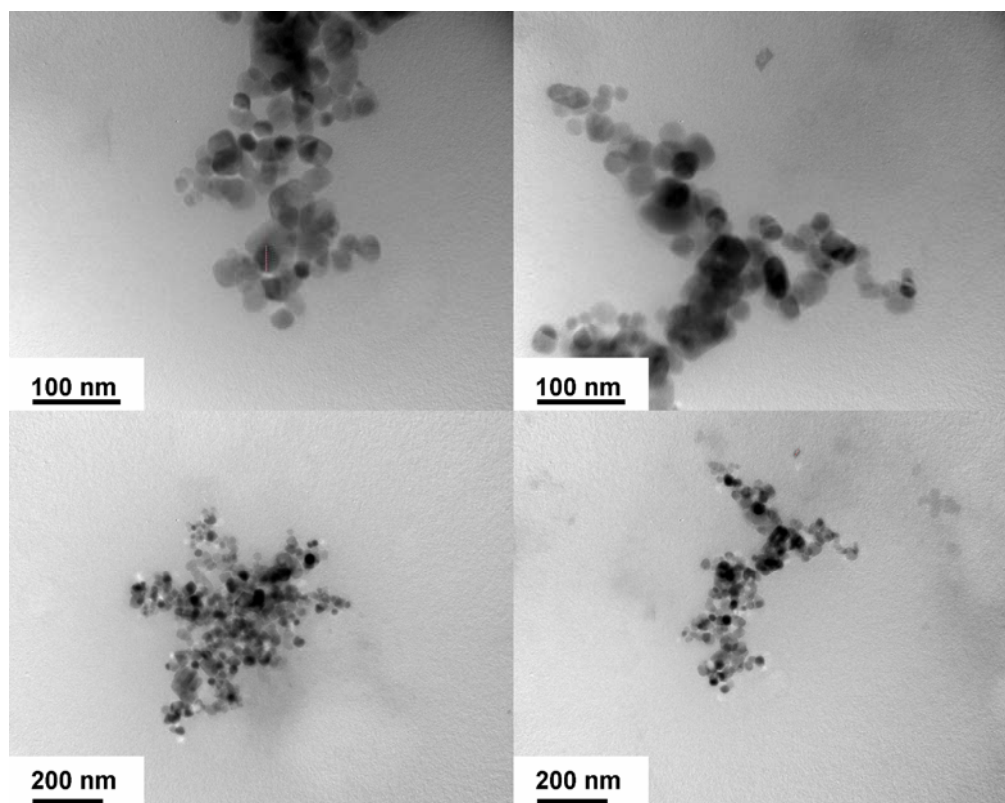


Figure 80 – TEM imaging of magnetite nanoparticles produced by hydrothermal synthesis.

In order to ascertain the composition of the nanoparticles, X-ray powder diffraction (XRD) investigation was performed. The suspension of nanoparticles was allowed to settle for 12 hours and approximately 80 % of excess water was decanted. The remaining solution was frozen by liquid nitrogen and put in a freeze-dryer at a temperature of $-50\text{ }^{\circ}\text{C}$ to get powder. The powder was characterized by Phillips EXPERT 1830 diffractometer with $\text{Cu K}\alpha$ radiation (2θ 0.02 degree/s from $20\text{-}80^{\circ}$) The obtained diffraction data (Fig. 81) were compared with the Joint Committee on Powder Diffraction Standards - International Centre for Diffraction Data [07-0322]. This determined the nanoparticles were composed of magnetite, Fe_3O_4 , by comparison with known spectra.

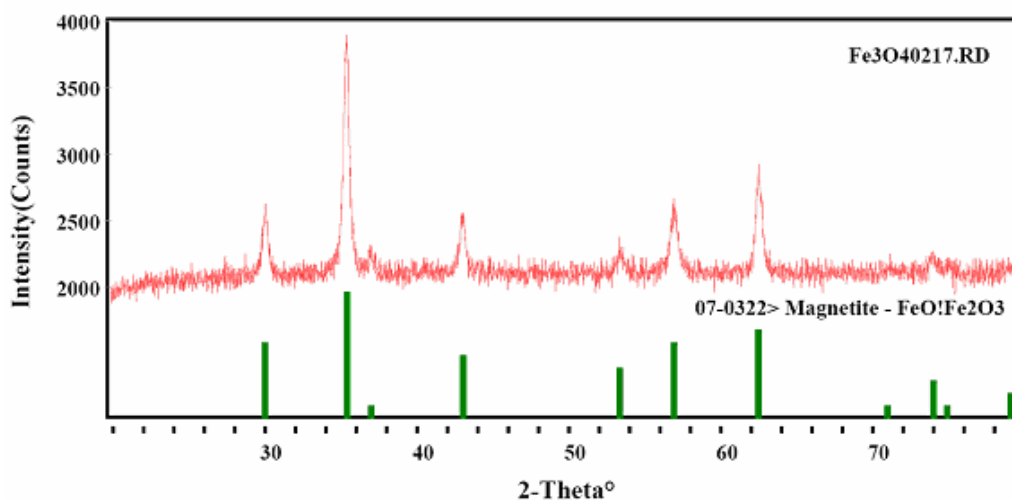


Figure 81 – XRD of magnetite nanoparticle powder, showing the obtained spectrum (above) in comparison to reference data for bulk magnetite.

For the main peak, the XRD estimated size is 22 nm based on the Scherrer equation. The Scherrer equation is derived from the Bragg equation, and allows particle size to be determined from the full-width-at-half-maximum of XRD peaks (see equation 6). This estimation of nanoparticle size is in agreement with the size of ~10-20 nm observed from TEM imaging, especially when it is considered that the Scherrer equation is often known to give an over-estimation of size for nanoparticles.²⁹

$$T = \frac{0.9\lambda}{B \cos\theta} \quad (6)$$

Equation 6 - Where T = thickness of crystal, 0.9 = an expected shape factor, λ = wavelength, B = full width at half maximum in radians and θ = Bragg angle.

3.4 Preparation of polymer-nanoparticle composite beads by a nanoparticle stabilised suspension polymerisation

Hypothesis

A novel strategy based on nanoparticle stabilised suspension polymerisation is attempted for the preparation of hybrid nanocomposites in the absence of any conventional stabiliser. By using this in-situ polymerisation technique, functional nanoparticles are immobilised onto the surface of polymer beads to significantly modify their properties. Magnetite, Fe_3O_4 , nanoparticles are used as stabiliser for the suspension polymerisation of MMA in water. The intention is to synthesise magnetic magnetite-PMMA nanocomposite polymer particles. The experimental results aim to show magnetite nanoparticles uniformly distributed on the surface of spherical polymer beads.

Suspension polymerisation is well established and usually requires suitable surfactants/stabilisers to hinder coalescence or break-up of monomer droplets. For suspension polymerisations, the common stabilisers are water-soluble organic polymers such as PVA or water-insoluble inorganic salts, such as MgCO_3 . However, to the best of our knowledge, there are no previous reports on the application of inorganic nanoparticles as surfactants/stabilisers for suspension polymerisations. The general method of suspension polymerisations will now be described, in the context of other general forms of polymerisation. This comparison is intended to show the differences and advantages of these different forms of polymerisation in order to show why suspension

polymerisations are often found to be useful systems of material synthesis. Bulk, solution, suspension and emulsion polymerisations are defined and compared. Dispersion polymerisations will be dealt with in the second half of this chapter, in section 3.5.

Bulk Polymerisation

Bulk addition polymerisation is the most basic and straightforward of the polymerisation processes, but it is not always suitable for commercial synthesis. A bulk addition polymerisation is a homogeneous system with an organic initiator, in other words, it is a one phase system with no additional solvent. At the beginning of the reaction it is the monomer, or monomers, that form the liquid phase in which the reaction occurs. The viscosity of the monomer/polymer phase increases over the course of the reaction while the concentration of monomer decreases continuously as it is converted into polymer. As the viscosity increases, the diffusion rate of the polymer chains decreases, which leads to a reduction in the rate of termination. This can lead to auto-acceleration and a runaway polymerisation with lack of control over polymer chain-length. The heat of polymerisation can also overheat the reaction and cause safety concerns.

Solution Polymerisation

These systems are defined by the use of an appropriate solvent system for the monomer phase. The main advantage of this diluent, be it either water or an organic solvent, is to aid with efficient heat transfer and control, which overcomes the problems associated with bulk polymerisation. For solution

polymerisations, there are two possibilities. Either the monomer is soluble and the polymer is soluble, which is homogeneous polymerisation, or the monomer is soluble and the polymer is insoluble, which is precipitation polymerisation. The main disadvantage associated with homogeneous solution polymerisation is the necessity to remove the solvent from the final polymer. This normally requires further time and cost in the production process, by heating/vacuum distillation. Precipitation based solution polymerisations result in filterable products so polymer separation is easier. However, control of polydispersity and morphology of precipitation systems is poor, unless agitation and/or stabilising agents are used to keep the precipitated polymer dispersed in the reaction system (this is known as 'dispersion polymerisation', discussed later - section 3.5.1).

Suspension Polymerisation

This is also sometimes called pearl polymerisation, bead polymerisation or granular polymerisation. It requires mechanical agitation to suspend the monomer or mixture of monomers in a liquid phase such as water, with the aid of stabilising agents. The continuous liquid phase must be one in which the monomer is immiscible. Polymerisation is then triggered by initiators soluble in the monomer droplets, which are kept suspended by continuous agitation. Essentially this is similar to carrying out bulk polymerisation reactions in the insoluble droplets of monomer phase. The water phase then becomes the heat transfer medium. Unlike for bulk polymerisations, the viscosity of the heat transfer agent does not change over the reaction because the continuous water phase is not affected by the growing polymer chains. The monomer droplets are

small in size, so more rapid reaction rates can be used, compared to bulk polymerisation, without overheating the monomer. This is because the heat generated is easily transferred away by the water phase. The advantages therefore are better heat control of the reaction, and much simpler separation of the products than for homogeneous solution polymerisation. The polymer granules produced can be simply filtered out. A disadvantage is that it can be relatively difficult to control the size of the polymer beads produced. Emulsion polymerisations are able to obtain a narrower size distribution with more control.

Emulsion Polymerisation

An emulsion polymerisation comprises a continuous liquid phase and a separate and immiscible monomer phase. This monomer phase is maintained in small droplets by the use of an emulsifier. The emulsifier acts as a surfactant to maintain the stability of the droplets, which form as micelles. By this route the concentration of the emulsifier can be used to control the size of the droplets. The initiator used to instigate polymerisation is commonly soluble in the continuous phase, which is normally aqueous. This differs from a suspension polymerisation as follows. A suspension polymerisation requires constant mechanical agitation to maintain the suspension of the droplets. In an emulsion polymerisation, after initial mixing by agitation, the stability of the droplets is maintained purely by the emulsifiers/surfactants, with no necessity for further agitation. Emulsion polymerisations normally produce much smaller beads of polymer than suspension polymerisations. Emulsion products range from tens of nanometres to a few micrometres, while suspension products range from tens of

micrometers to a millimetre. A disadvantage of emulsion polymerisations is the large concentration of emulsifiers needed that contaminate the polymer. The end product of these reactions is often a stable latex, an aqueous emulsion of polymer that is difficult to isolate from water.

The polymerisation reactions reported in this section use a suspension method, stabilised by magnetite nanoparticles. The monomer being stabilised in this way is MMA. The initiator used is 2,2'-azobis(isobutyronitrile) (AIBN). The reaction mechanism occurs by simple free radical vinyl polymerisation, discussed below.

3.4.1 Free radical vinyl polymerisation of MMA

The overall process of the reaction is depicted simplistically (Fig. 82). The monomer, MMA, adds to the growing polymer chains forming PMMA. The initiator, AIBN, acts to start the reaction by the generation of free radicals. This occurs by thermal decomposition, whereby a nitrogen molecule is eliminated from the AIBN to generate two 2-cyanoprop-2-yl radicals (Fig. 83).

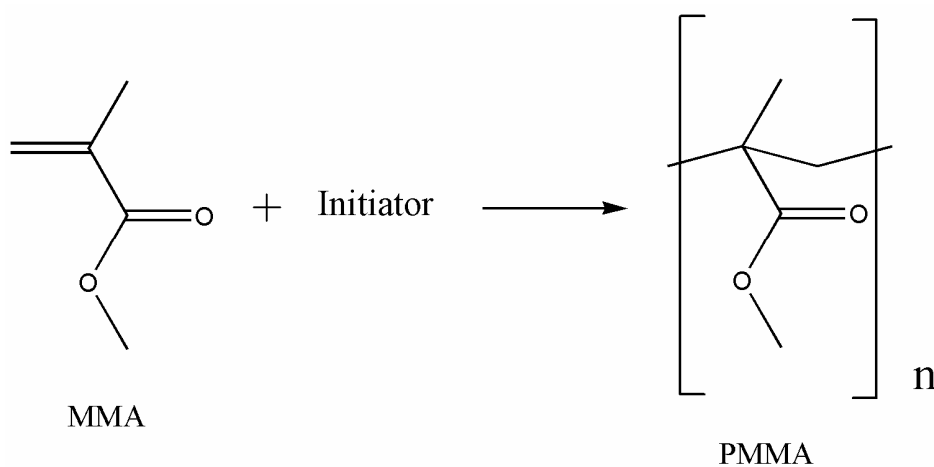


Figure 82 – Overall product of the free radical vinyl polymerisation of MMA to form PMMA.

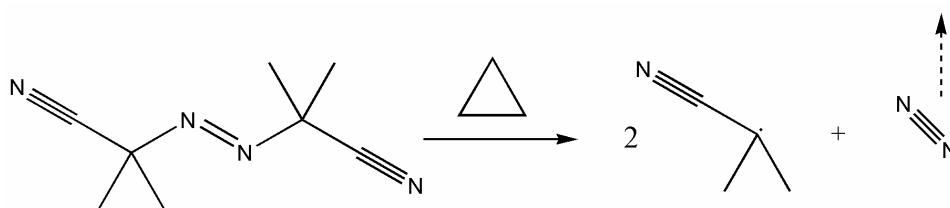


Figure 83 – Thermal decomposition reaction of AIBN. Nitrogen is eliminated from the AIBN to generate two radical moieties.

The first step in the polymerisation is the *initiation step*. The initiator radicals that are generated from the initiator go on to attack the MMA, which generates new species composed of monomer-initiator radicals (Fig. 84). In the *propagation step*, this new radical species goes on to attack the double bond of another MMA, each time forming a new radical species and the growing polymer chain (Fig. 85).

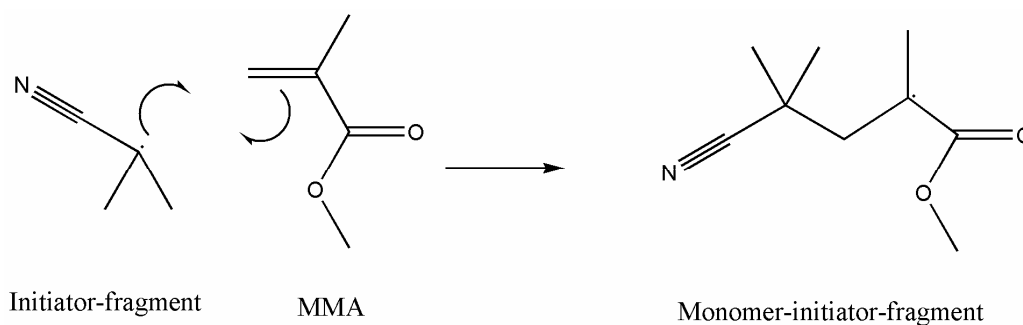


Figure 84 – *Initiation step* in the free radical vinyl polymerisation of MMA by AIBN.

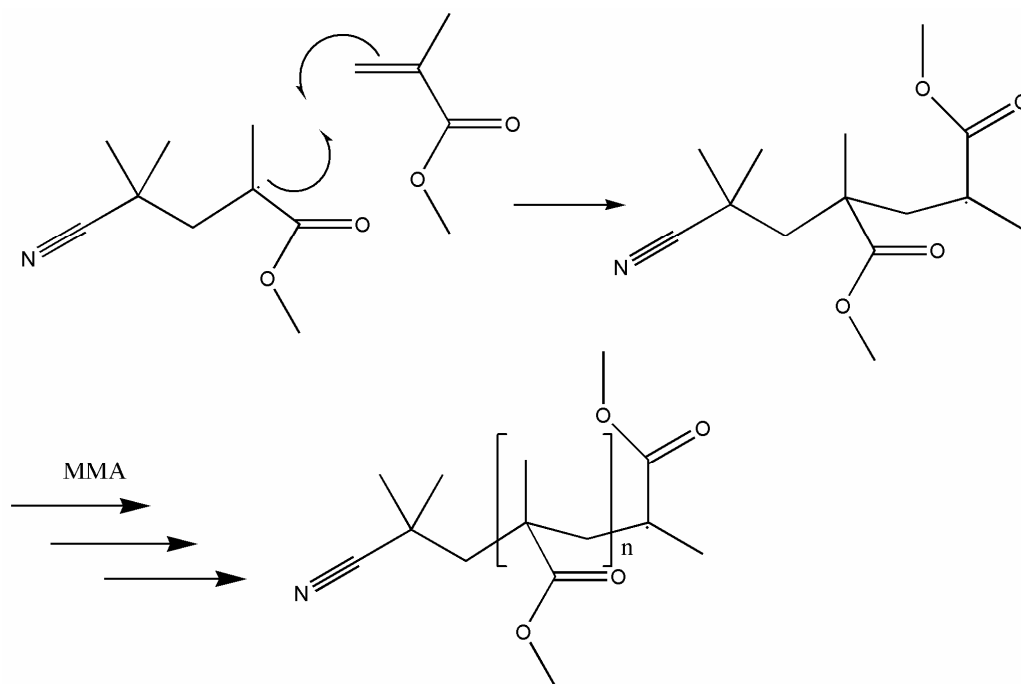


Figure 85 – *Propagation step* in the free radical vinyl polymerisation of MMA to form PMMA. The new monomer-initiator radical then goes on to react with other monomers forming oligomer and eventually polymer radicals

The propagation will continue until a *termination step* occurs. Termination can occur by combination or disproportionation. In combination two radicals form a direct head to head linkage, leading to a chain with initiator-fragment segments at either end (Fig. 86). Disproportionation involves transfer of hydrogen from one chain end to another, producing two, non-radical, polymer chains with initiator segments at one end only (Fig. 87). Both processes occur for PMMA radicals, but disproportionation predominates above 60 °C.³⁰

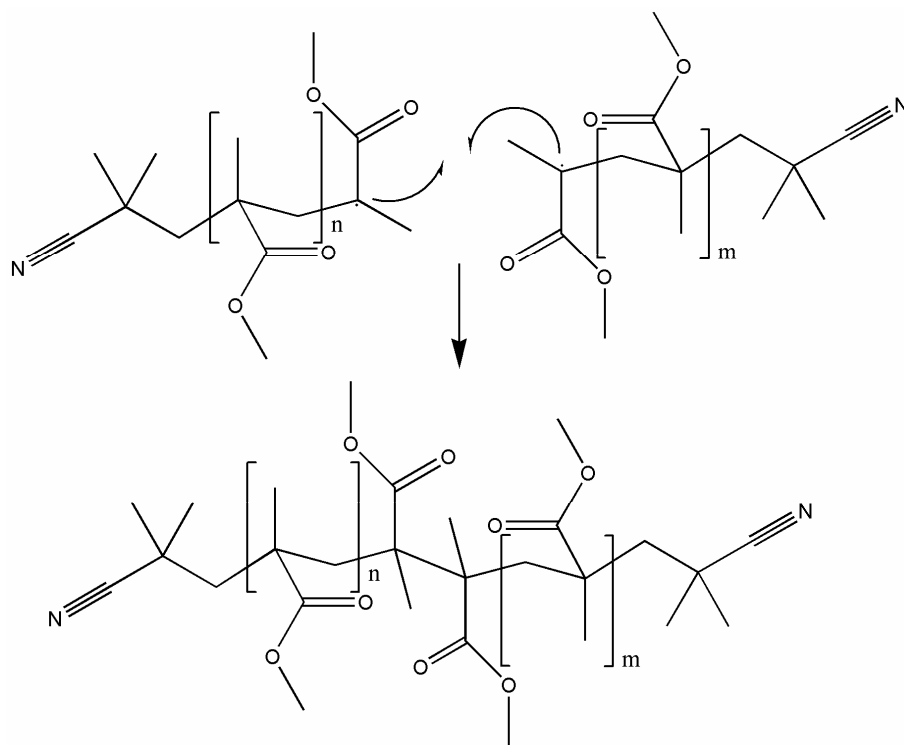


Figure 86 – Termination step, by recombination, in the free radical polymerisation of MMA. Two radical species combine to form a stable polymer with an initiator fragment at each end.

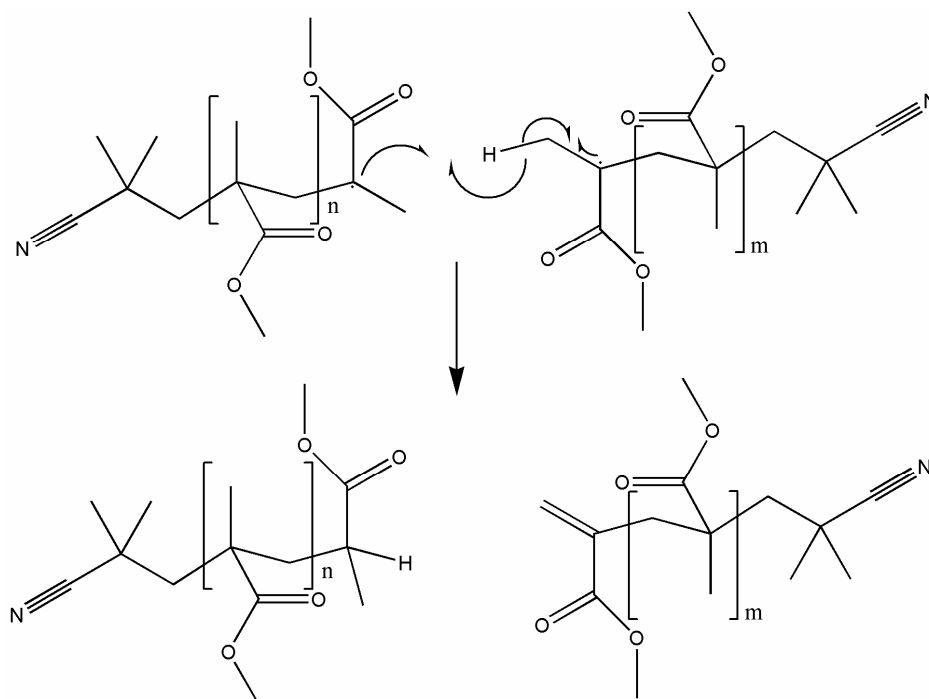


Figure 87 – Termination step, by disproportionation, in the free radical polymerisation of MMA. Only the hydrogen atom that is transferred in the reaction is displayed.

3.4.2 Reaction procedure

The procedure used for a typical polymerisation reaction is outlined here. For a more technical description see Chapter 5.3.3. In a standard polymerisation experiment, AIBN initiator was dissolved in MMA monomer and then combined with an aqueous nanoparticle solution. The resulting biphasic solution was stirred and brought up to temperature. The agitation and temperature were then maintained for the duration of the reaction. After sufficient time for the completion of the reaction, the heating was removed and the reaction was allowed to cool before being filtered to remove the solid polymer beads.

We will demonstrate that an aqueous dispersion of nanoparticles can be used as the continuous phase, where monomer and initiator are suspended, and the nanoparticles act as an effective stabiliser. A schematic representation of the nanoparticle-stabilised suspension polymerisation is shown (Fig. 88). At the early stage, the magnetite nanoparticles assemble at the MMA/water interface and thereafter provide a strong stabilising effect on the polymerisation. The high stabilisation efficiency from the nanoparticles ensures a successful suspension polymerisation with high yield and controlled morphology.

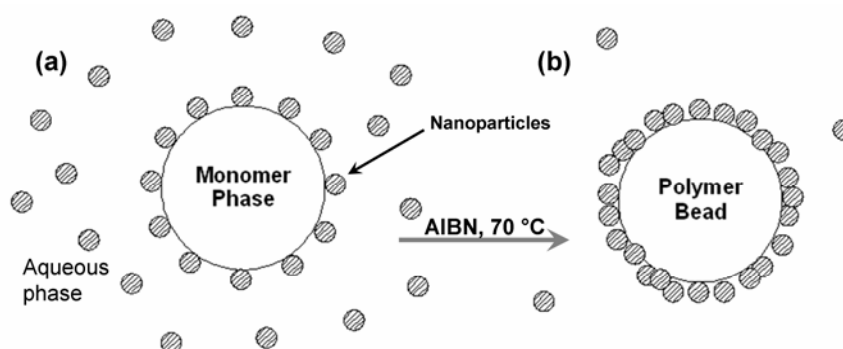


Figure 88 - Mechanism of nanoparticle stabilised suspension polymerisation of MMA with AIBN as the initiator. a) The nanoparticles assemble at the MMA/water interface, stabilizing the droplets. b) Over the course of the polymerisation more nanoparticles collect at this surface.

3.5 Results

Observations for standard suspension polymerisation reactions were taken to compare the effectiveness of reactions with no stabiliser, magnetite nanoparticle stabilisers and PVA stabilisers. PVA is a commonly used stabiliser for MMA suspension polymerisations. The product from the suspension polymerisation with magnetite nanoparticles is a dark free-flowing powder which consists of spherical particles (Fig. 89). The individual PMMA beads are mostly transparent with a few occasional black spots on some of the surfaces, which are probably due to the local aggregation of magnetite nanoparticles. The average size of the polymer beads is around 400 μm . The interesting magnetic properties of these magnetite-PMMA nanocomposites has been demonstrated (Fig. 1a) by their attraction to a magnetic stirrer bar. This clearly demonstrates that these nanocomposites are natural carriers for the nanoparticles and these retain their characteristics to provide opportunities for practical applications.

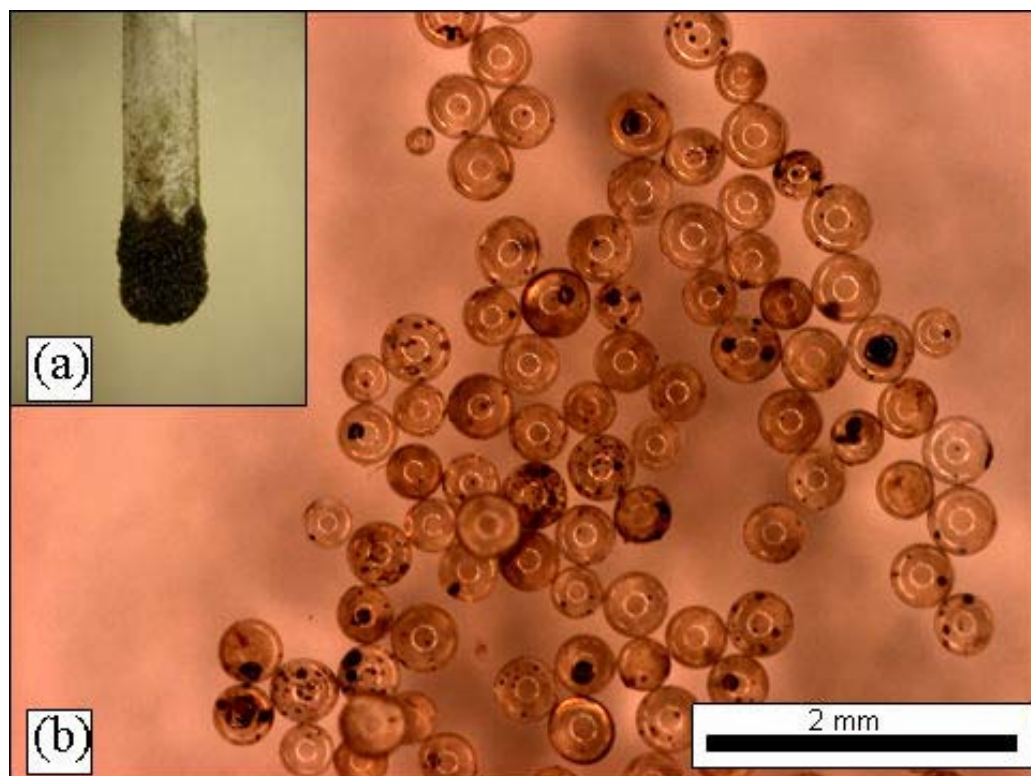


Figure 89 - Digital photographs of the magnetite-PMMA nanocomposite: (a) the magnetic property of the product is demonstrated by attracting a cluster of polymer beads to a magnetic stirring bar. (b) Optical microscope image showing magnified particles. Scale bar = 2 mm.

The polymeric product of the magnetite stabilized polymerizations was compared with the control systems by use of gel permeation chromatography (GPC). GPC is a method of ascertaining the molecular weight, and therefore chain length, of polymer systems (see Chapter 5.4.8). Table-6 shows the polymerisation results from the same monomer system under the same conditions with PVA as the stabiliser or in the absence of any stabiliser. The PVA stabilised PMMA product is also a fine powder with molecular mass very close to that of the PMMA nanocomposite discussed above. The control experiment of MMA polymerisation without any stabiliser led to the formation of an amorphous gel with much lower molecular mass.

Table 6 – Products from MMA suspension polymerizations with different stabilisers. M_n gives the number average molecular mass and PDI gives the polydispersity of this result.

Stabiliser	M_n	PDI	Morphology
Magnetite nanoparticles	169,200	2.96	Polymer beads
PVA	157,800	2.73	Polymer beads
None	113,700	3.21	Gel

The concentration of magnetite nanoparticles in the aqueous phase used for the successful reactions was 900 mgL^{-1} . At lower concentrations of nanoparticles the polymerisation was not stabilised effectively, either ending in a single agglomerated mass, or enlarged and distorted beads. The concentration of nanoparticles was increased until the suspension could be successfully stabilised. Therefore this concentration is likely to be close to the minimum needed for successful stabilisation. Under these conditions the majority of the nanoparticles should have been harvested from the aqueous phase and embedded into the polymer. Thermogravimetric analysis (TGA) of the polymer was performed to assess the loading of magnetite (see Chapter 5.4.9 for details). The results showed that magnetite accounted for less than one percent of the nanocomposite product by mass. Although this seems low, it is in agreement with calculations from the ratio of the reactants, which predicts maximum inclusion of magnetite should give 0.36 wt% in the product. This confirms the extraordinary stabilisation efficiency of the nanoparticles for the suspension polymerisation. The aqueous by-product solution is almost colourless, supporting the belief that almost all of the nanoparticles have been incorporated into the polymer. This observation is confirmed by elemental analysis, which was performed by means of inductively coupled plasma atomic emission

spectroscopy of the remaining aqueous solution (see Chapter 5.4.11). This showed only a trace presence of iron. The level of iron detected in the remaining water is 0.076 mgL^{-1} , corresponding to 0.105 mgL^{-1} of magnetite and contrasting to the level in the original solution of $\sim 900 \text{ mgL}^{-1}$. This indicates there is only $\sim 0.012 \%$ of the iron, and therefore nanoparticles, remaining in the solution after the polymer capture. This demonstrates a high nanoparticle capturing efficiency ideal for harvesting nanoparticles from aqueous solution.

3.5.1.1 Scanning electron microscopy

The polymer beads produced were examined by scanning electron microscopy (SEM) (see Chapter 5.4.3 for a description of SEM and details of the preparation method). This technique does not have high enough resolution to directly observe the nanoparticles. However, it is a useful method to observe the polymer beads in more detail than can be obtained from optical microscopy. From the images it can be observed that the beads are almost perfectly smooth and spherical in structure (Fig. 90). It should also be noted that no visible clumps or aggregations of nanoparticles were detected on the surface of the beads (Fig. 91). This suggests that the nanoparticle layer is relatively even.

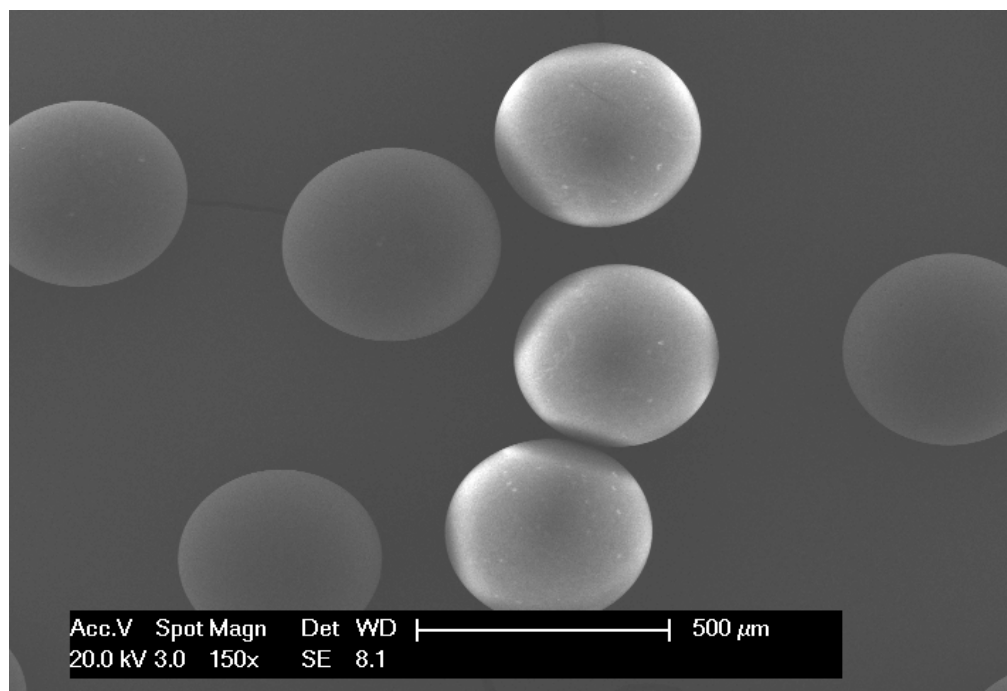


Figure 90 – Secondary electron mode SEM image showing the general morphology of the PMMA beads.

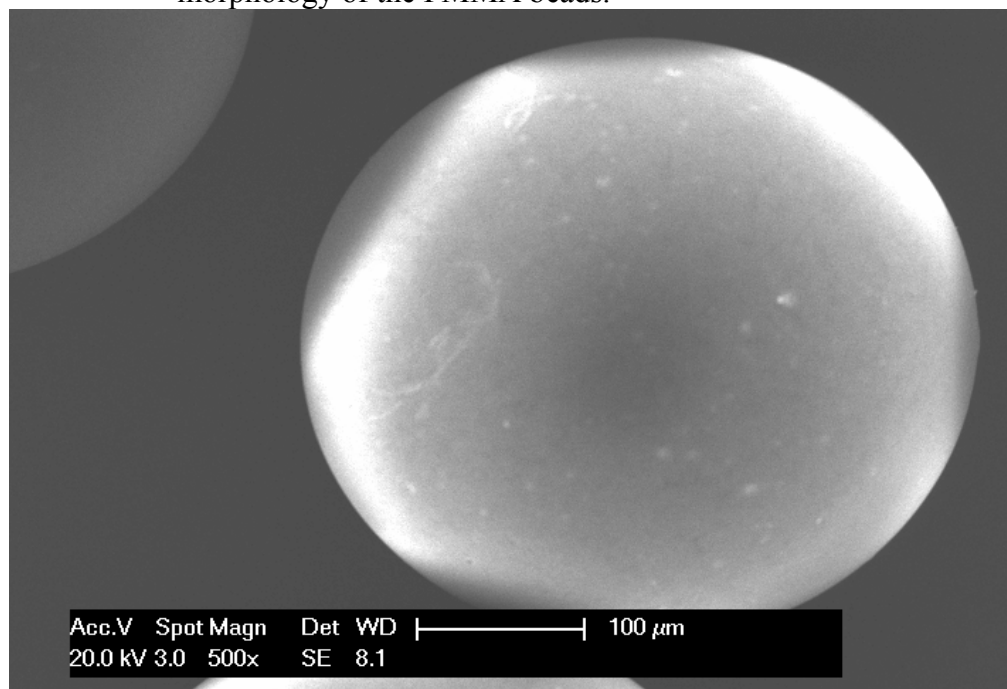


Figure 91 – Secondary electron mode SEM image showing a PMMA bead at higher magnification to allow surface observation.

Most images were taken in secondary electron mode, to best observe the topology. By comparing this to backscattered electron mode it should be possible to observe any local high concentration of magnetite. Backscattered

electrons may be used to detect contrast between areas with different chemical compositions, especially when the average atomic number of the various regions is different, since the brightness of the image tends to increase with the atomic number. Two SEM images of the same area, in secondary electron and backscattered electron modes, are shown side by side (Fig. 92). No apparently brighter or darker spots are detected. Also the polymer beads are not especially brighter than the carbon support tab they are on. This indicates that the nanoparticle layer must be both even and relatively thin, so as not to cause bright spots or an increase in the brightness of the polymer beads over their surroundings.

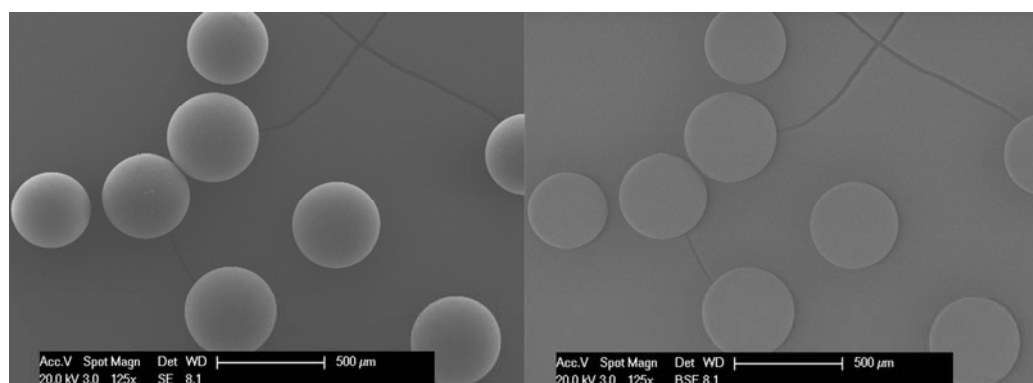


Figure 92 – Left, secondary electron mode SEM image of a group of PMMA beads. Right, backscattered electron mode SEM image of the same group of particles.

According to the theory discussed so far, and supported by the elemental analysis data, the magnetite nanoparticles should be present in the polymer beads. However, the SEM images themselves cannot confirm this hypothesis. In order to prove that magnetite was indeed present in the polymer beads observed in the SEM images, energy dispersive X-ray analysis (EDX) was performed. This involves using characteristic X-rays produced *in-situ* during SEM imaging

to determine which elements are present in the area under observation. X-rays emitted by electron interaction with the polymer beads produced spectra indicating the presence of iron (Fig.93). Other elements detected were carbon, oxygen and gold. The gold is from the thin gold coating layer deposited during sample preparation for SEM to prevent charging. The carbon is from the PMMA polymer. Oxygen is expected to be present both as part of the PMMA and also the magnetite.

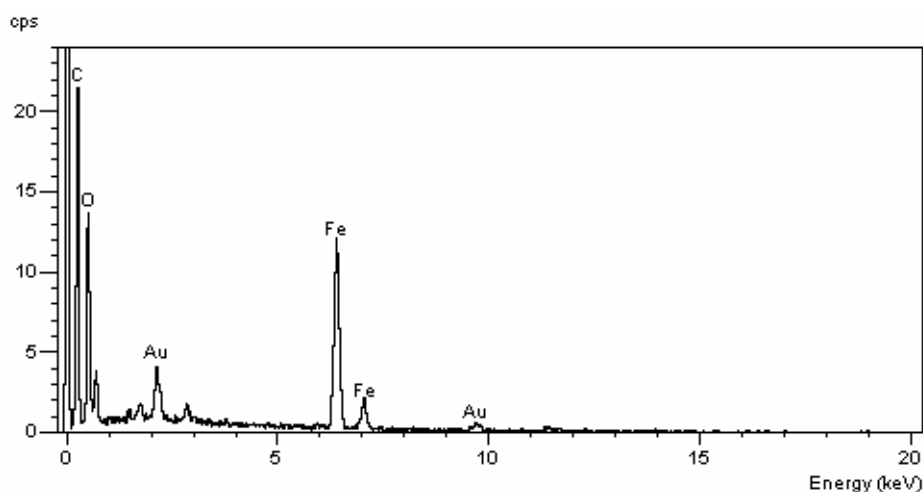


Figure 93 – EDX spectra from the polymer beads observed in SEM. Elements detected are carbon, oxygen, gold and iron.

3.5.1.2 Transmission electron microscopy

The SEM imaging is able to demonstrate the morphology of the polymer beads and the presence of magnetite. However, in order to satisfactorily characterize this material there is one last factor that it is important to investigate. This is the nano-structure and composition of the beads. It must be determined whether the magnetite is still in the form of nanoparticles and where in the polymer bead they are located. Theory and SEM data support that the

nanoparticles should be in a thin layer across the surface of the polymer, but this must be confirmed. Unfortunately a significant challenge must first be overcome in order to image the polymer nanocomposites in TEM. During TEM imaging the electron beam must pass through the sample being imaged. Therefore, the sample to be imaged cannot be much thicker than ~ 100 nm to acquire good quality images. For polymeric samples above ~ 1 μm in thickness, no imaging at all can be performed. The polymer beads that must be characterized are in the range of ~ 400 μm , obviously precluding them from imaging in this form.

In order to make it possible to image the nanocomposite beads, the samples were specially prepared for TEM. This involved embedding the polymer beads in a solid resin support, before microtoming this into ~ 100 nm sections (see Chap 5.4.4). This allows cross sections of the polymer beads to be investigated in the TEM. Unfortunately there are two further problems with this method. The first is a problem of scale. As the polymer beads can be as large as hundreds of μm in diameter, it is impossible to view any more than a small segment of the cross section in the TEM. The second problem is one of contrast. The density and structure of the PMMA that comprises the beads is very similar to that of the epoxy resin that they are embedded in. This means that in the TEM imaging it is almost impossible to tell the difference between the polymer inside the beads and the polymer outside the beads. Fortunately it is easy to image the nanoparticles, and these can provide information as to the structure of the beads.

TEM imaging of embedded polymer in such a fashion revealed rings or curved bands of nanoparticles (Fig. 94). These nanoparticles are from the surface of the polymer beads. They appear in curved or crescent formations in

the TEM images following the curve of the polymer bead surface. The individual nanoparticles can still be seen to be discrete and unchanged in comparison to their original structure. From this we can conclude that the polymerisation process does not affect the nanoparticles in terms of damage or coalescence.

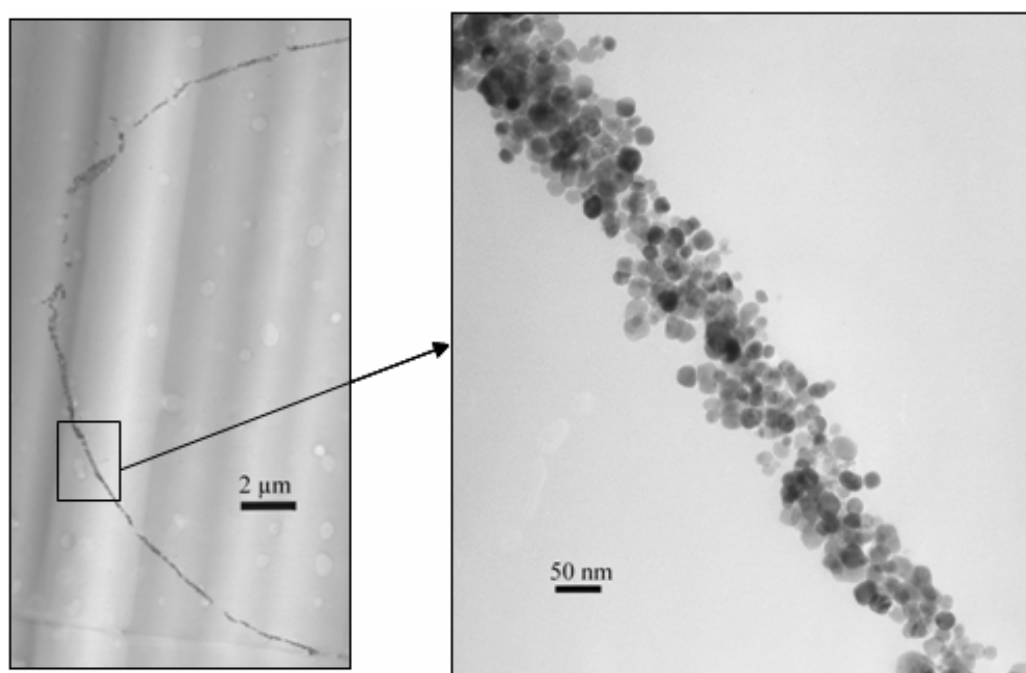


Figure 94 – Bright field TEM imaging revealing a curved band of nanoparticles from the surface of a polymer bead. In the magnified image it can be seen that the nanoparticles are still intact and unaffected. Small holes can be seen in the polymer and embedding resin caused by the effect of the electron beam.

The image shown (Fig. 94) is representative of the type of structure found in the TEM imaging of this material in general. It was not possible to acquire a single image of such a large curve for the full circumference, because of problems with the TEM process. However, other segments of other large curves were imaged (Fig. 95), as well as smaller rings in full (Fig. 96). It should be noted that the majority of the material observed during TEM was in the form of

larger curves. The smaller complete spheres were only occasionally observed and are less representative. However, several pictures were taken out of interest, and because of the greater ease of capturing these complete structures. There are several possible origins of the smaller nanoparticle rings. It is possible they are smaller discrete spheres of polymer that are stabilised by the nanoparticles, though such smaller beads were not observed in SEM. A more likely explanation is that they are either inclusions in the beads, or simply a cross section of the very edge of a larger polymer bead. Inclusions inside larger beads could be explained by small stabilised spheres being consumed by larger droplets of polymer during the early stages of polymerisation. This would also explain the dark spots that can be seen in the polymer beads in optical microscopy (Fig. 89b).

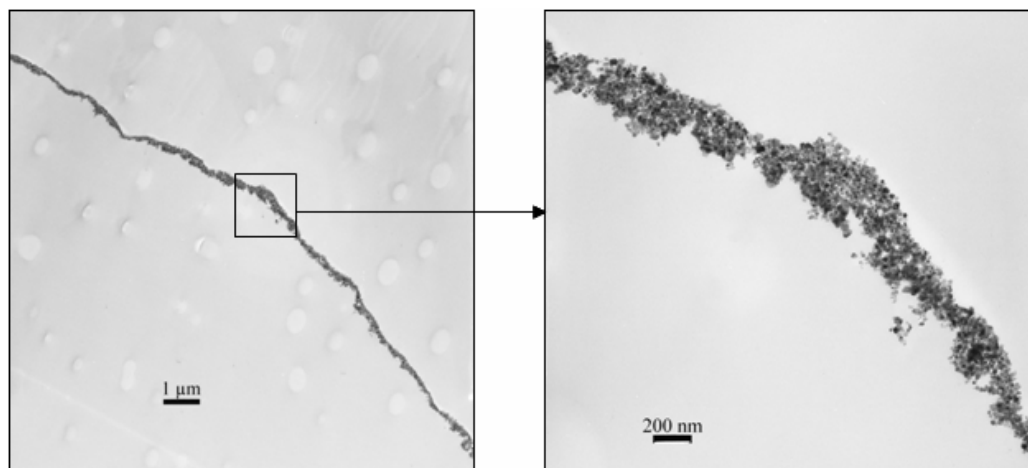


Figure 95 – Bright field imaging of a crescent of nanoparticles from the surface of a polymer sphere. Small holes can be seen in the polymer and embedding resin caused by the effect of the electron beam.

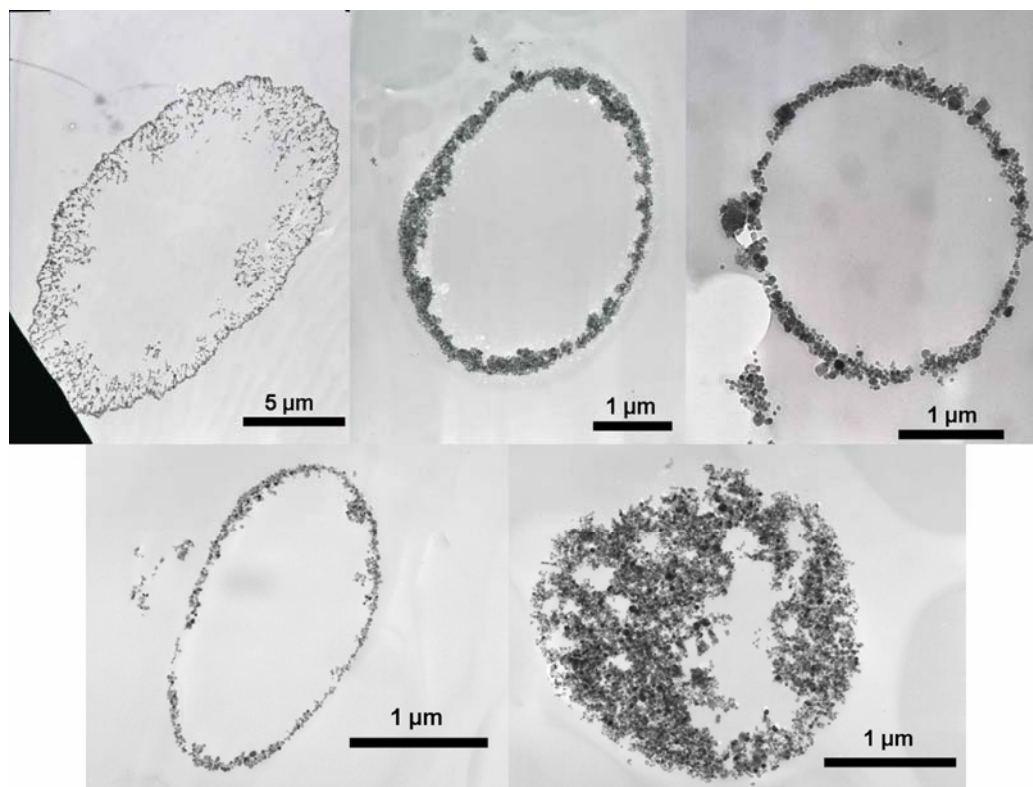


Figure 96 – Bright field TEM image collage of 5 rings of nanoparticles. The origin of these smaller sized circles is discussed in the text.

These images clearly demonstrate that magnetite nanoparticles have acted as a stabiliser and are located on the surface of the PMMA spheres. This provides further evidence that at the start of the polymerisation process, the nanoparticles assemble at the liquid-liquid interface between water and MMA monomer, and then act as an effective stabiliser for the polymerisation. The size of nanoparticles is still very uniform, between 10-20 nm, and despite a few occasional aggregations, there is no change in the nanoparticles compared to their initial size in aqueous solution by TEM analysis.

3.5.2 Other nanoparticles

A few brief experiments were performed with other nanoparticles. The intention of this was to show that this method is transferable to other systems. Detailed study of these systems was not intended, only to show viability. Two alternative nanoparticle solutions were used, haematite (Fe_2O_3) and cobalt oxide (Co_2O_3) (3.0 gL^{-1} concentration). This was the concentration readily available, though it should be noted this is a higher concentration than the concentration used for magnetite, (0.9 gL^{-1}). Suspension polymerisations completed with these nanoparticles were found to be successful, though with a poor morphology. Digital photographs (Fig. 97) show the colour of the polymer powders, indicating the presence of the respective nanoparticles in the polymer. Some of the beads are a distorted shape.

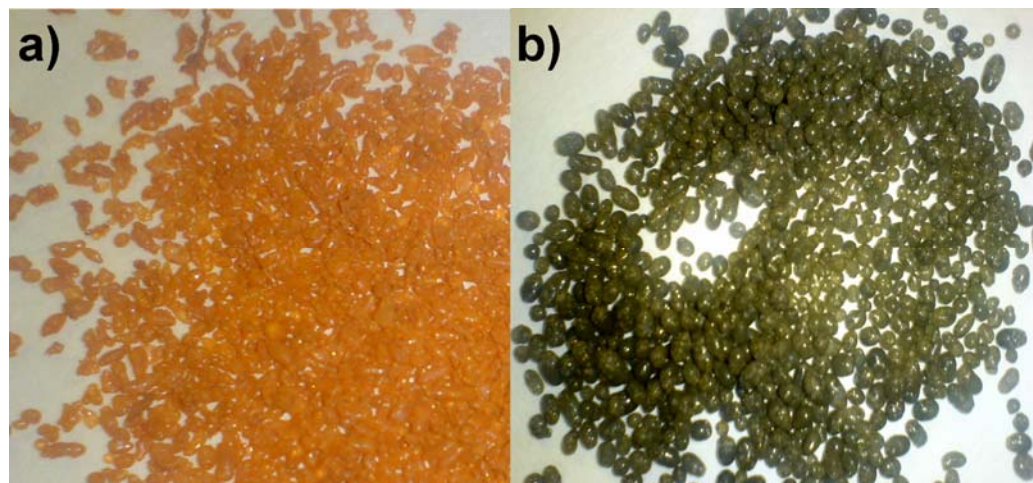


Figure 97 – Digital photographs of nanoparticle stabilized polymer powders. a) haematite nanoparticles, b) cobalt oxide nanoparticles.

SEM imaging of these polymer beads shows a roughly spherical shape, often with some distortion, and a normally smooth surface (Fig. 98). However, unlike for the magnetite products, some areas of excess nanoparticles can be

observed. These areas of clusters of nanoparticles show up as brighter areas on the SEM images, because of increased contrast in back scattered electron mode. These areas of nanoparticles also cause the surfaces of the beads to appear uneven, and create malformed aggregated masses. It is suggested that these areas of excess nanoparticles occur in these systems because of the increased concentration of nanoparticles.

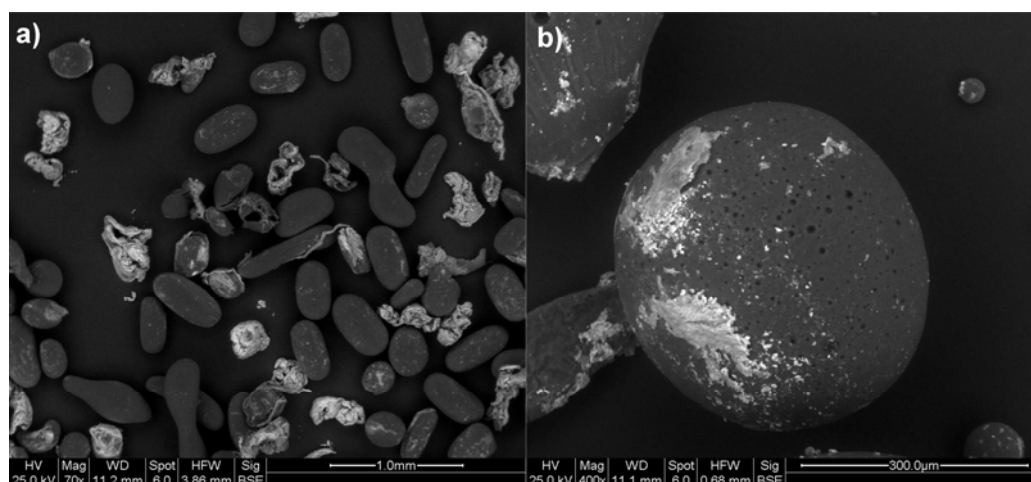


Figure 98 – Back scattered electron SEM imaging of nanoparticle polymer composites. a) haematite stabilized polymer, scale bar shows 1 mm. b) cobalt oxide stabilized polymer, scale bar shows 300 μm.

TEM imaging of these nanocomposite products confirms the presence of nanoparticles. Using this method it was possible to see lines of nanoparticles, presumably that were stabilizing the surface of the beads (Fig. 99). It was also possible to observe areas of higher nanoparticle concentration, presumably the clustered areas outside the surface of the polymer (Fig. 100). Where the occurrence of large amounts of nanoparticles is observed in TEM, at a higher amount than would be necessary to stabilize the interface, it is clear that the extra nanoparticles locate on the outside of the curve. The inner side of the curves seen have a much more defined limit of nanoparticles, from their

location at the interface. The outer sides of the curves have a more disordered distribution of nanoparticles, and even some shapes that look like smaller discretely stabilized shapes.

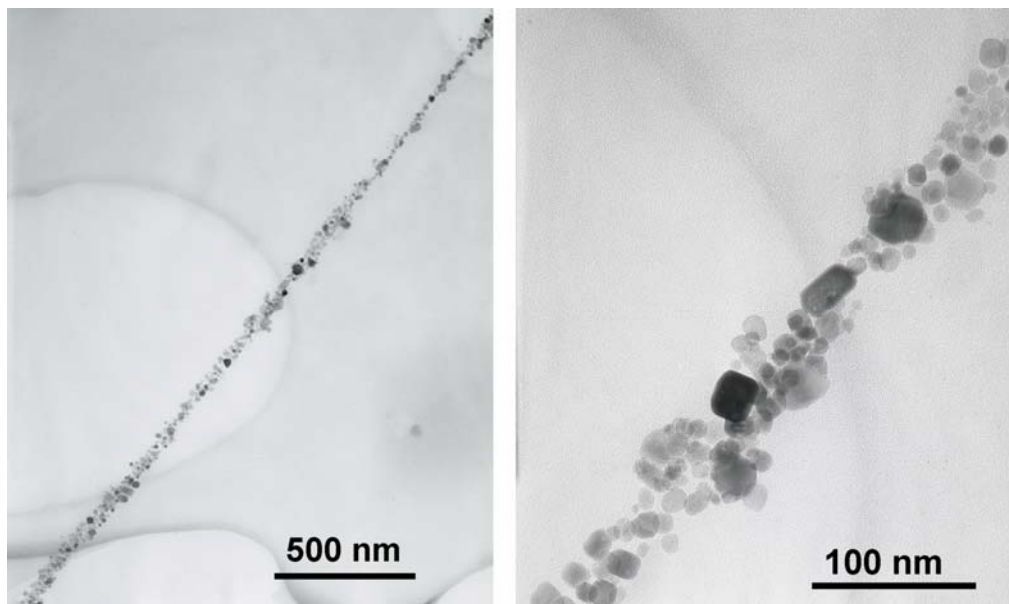


Figure 99 – Bright field TEM imaging of cobalt oxide nanoparticles from a microtomed cross section of the polymer nanocomposite. The ordered line of nanoparticles is from the stabilised surface of a polymer bead.

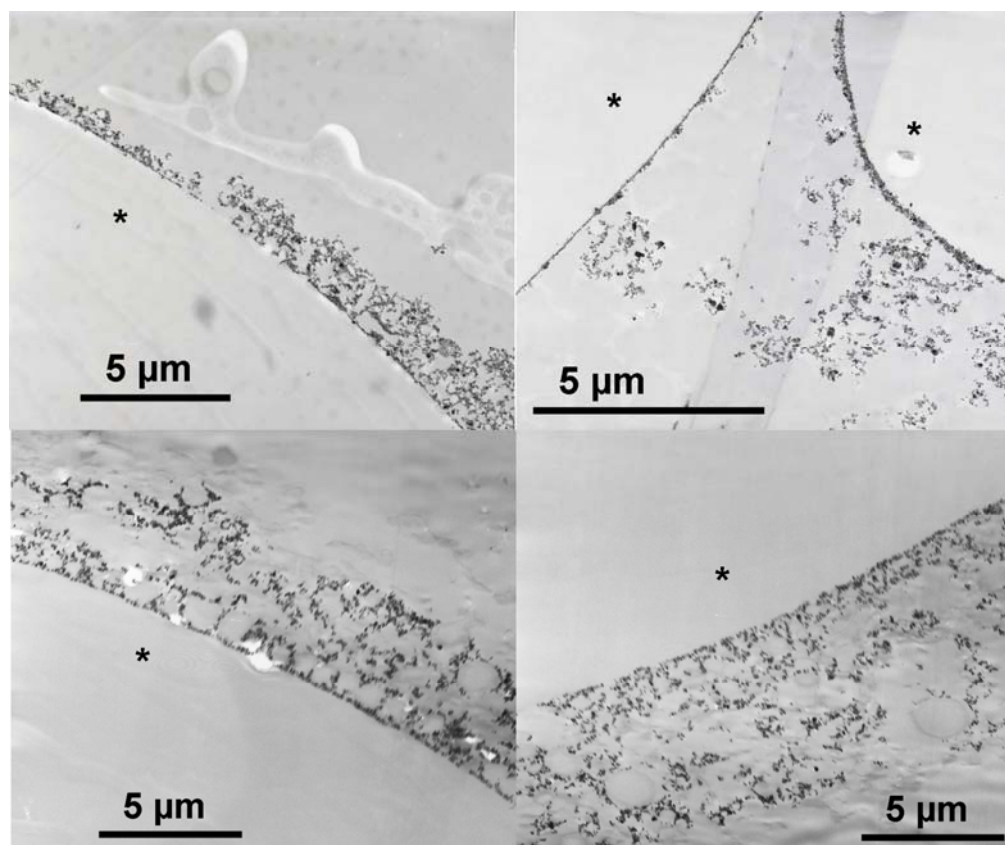


Figure 100 – Bright field TEM images of haematite stabilised polymer beads. Notice both the clear surface of the beads, stabilized by nanoparticles, and the presence of excess nanoparticles outside of these boundaries. The inner sides of the curves, and therefore the insides of the polymer beads, are marked with an asterix (*).

It is clear from these trials of other nanoparticle systems that the technique should be effectively transferable. However, it is also clear that future work would be necessary in order to optimise the method for better control of product structure and quality.

3.5.3 Conclusions

A novel suspension polymerisation based on nanoparticle stabilisation has been successfully carried out in water in the absence of any other conventional stabiliser. Magnetic magnetite-PMMA nanocomposite polymer particles have

been synthesised via this *in-situ* polymerisation technique. The special magnetic property of the polymer nanocomposites is of great interest and has potential uses for either catalytic or other practical purposes (such as magnetic recovery, post use). We have demonstrated both the harvesting, and the capturing upon the surface of polymer beads, of nanoparticles from aqueous dispersion. The applicability of this technique has been shown to be transferable to other nanoparticle systems. Moreover the unique magnetic properties of the magnetite nanoparticles are retained by the composite material produced. This *in-situ* polymerisation method using functional nanoparticles as stabiliser will open up a new route to preparation of a wide range of polymer nanocomposites.

3.6 Preparation of polymer-nanoparticle composite microparticles by a nanoparticle stabilised dispersion polymerisation

Hypothesis

Proposed is a strategy for the preparation of polystyrene nanocomposites by metal-oxide nanoparticle stabilised dispersion polymerisation, in the absence of any other conventional stabiliser. The products should be spherical polymer microparticles decorated with nanoparticles on their surface. This process, with magnetite nanoparticles, aims to demonstrate the formation of products with a strong magnetic property. By using this in-situ polymerisation technique, not only can nanoparticles in the aqueous solution be harvested, but this also represents a new route to polymer composites. Thus, functional nanoparticles can be immobilised onto the surface of the polymer beads to significantly modify their properties.

This dispersion polymerisation with magnetite nanoparticles as stabilisers functions in much the same way as the suspension polymerisation of PMMA. Again the magnetite nanoparticles are acting as the sole stabilizing agent, and they become located at the surface of the forming polymer powder. Therefore, this method shares the same aims and advantages as those described for suspension polymerisation. The use of conventional stabilisers is avoided, which prevents the possibility of such chemical agents coating the nanoparticles and inhibiting their activity. It is a useful route to harvest nanoparticles from

aqueous solution and embed them in a useful polymeric substrate, in which they occupy the surface. However, there are some significant differences between the dispersion polymerisation described here and the suspension route described previously. Most importantly, from a practical sense, this dispersion route should produce significantly smaller polymer spheres, and allow different polymeric systems to be used. This is why it is important to test if such a system can be successful. The resulting polymer beads should be of a few μm in diameter. This is two orders of magnitude lower than those normally produced by suspension polymerisation, and so represents a useful complementary technique. Dispersion polymerizations, as a general physical system, will be explained, followed by a description of the mechanism of radical styrene polymerisation. After a brief outline of the reaction setup, the results and characterization of products will be reported and discussed.

3.6.1 Dispersion polymerisation

Dispersion polymerisations are a form of precipitation polymerisation in which the continuous phase is chosen to be a good solvent for the monomer, initiator and stabiliser, but not for the resulting polymer. They are similar to emulsion or suspension polymerisations, in that they result in a biphasic system that must be stabilised. However, the important factor that separates dispersion polymerisation is that, unlike suspension or emulsion, it begins as a single phase system. In an emulsion polymerisation, the monomer must be poorly soluble in the continuous phase, and so able to form into micelles by the function of a surfactant. Likewise in suspension polymerisation, the monomer is poorly soluble, and is formed into droplets by the agitation and the use of stabilising

agents. In dispersion polymerisation the monomer begins the reaction dissolved in the continuous phase. However, as the reaction proceeds and the polymer chains grow in length, the solubility of the polymer will decrease. Once the polymer reaches a critical molecular weight, polymer chains collide to nucleate particles, which precipitate. At this point the stabiliser is absorbed or coordinated onto the surface of the particles, providing a protective barrier which helps to solubilise the particles and prevents coalescence. Polymerisation can proceed by the absorption of monomer into the polymer from the continuous phase. Conversion can therefore continue until all monomer is consumed.

Heat transfer is simple because the viscosity of the continuous phase is not significantly changed over the reaction because it is not affected by the precipitated polymer. Product recovery is normally straightforward because the solid polymer powder can be easily filtered out. The size distribution and control of the polymer granules produced is less precise than for emulsion polymerisation. The size of the resulting polymer beads will be influenced by both the concentration and nature of the surfactant/stabilising agent, and the method of agitation.

3.6.2 Free radical vinyl polymerisation of styrene

This will only be discussed in outline, as it is essentially the same mechanism as that already shown for MMA (section 3.4.1.). Here the monomer is styrene, the initiator is AIBN and the continuous phase is a water/methanol mixture. The overall process of the reaction is depicted simplistically (Fig. 101).

The AIBN acts to start the reaction by the generation of free radicals, as described previously (Fig. 83).

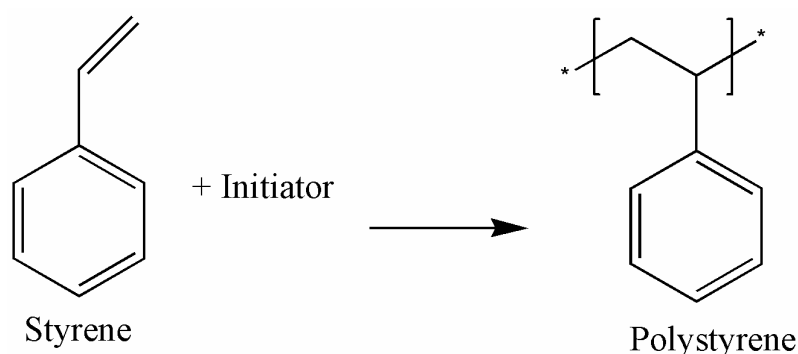


Figure 101 – Overall product of the free radical vinyl polymerisation of styrene to form polystyrene.

The first step in the polymerisation is the initiation step. The initiator-fragment radicals that are generated from the initiator go on to attack the styrene, which generates new radical species composed of monomer-initiator-fragment (Fig. 102). In the propagation step, this new radical species goes on to attack the double bond of another styrene, each time forming a new radical species and adding to the polymer chain (Fig. 103). The propagation will continue until a termination step occurs. Termination can occur by combination or disproportionation, as discussed in section 3.4.1.

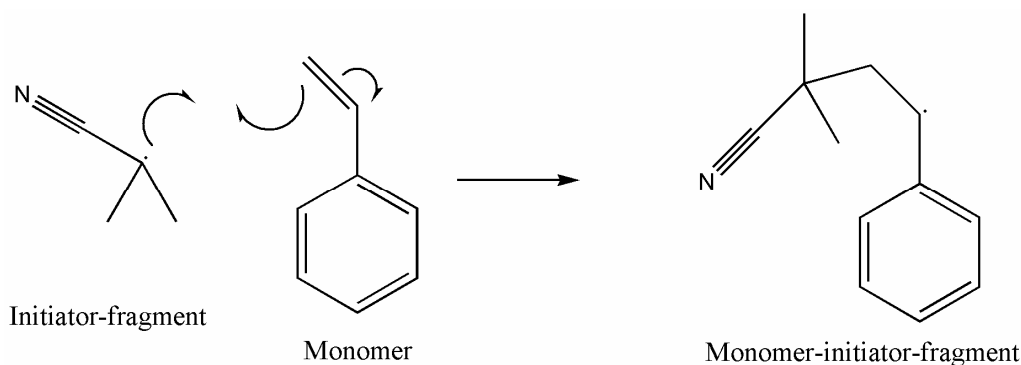


Figure 102 – *Initiation step* in the free radical vinyl polymerisation of styrene by AIBN.

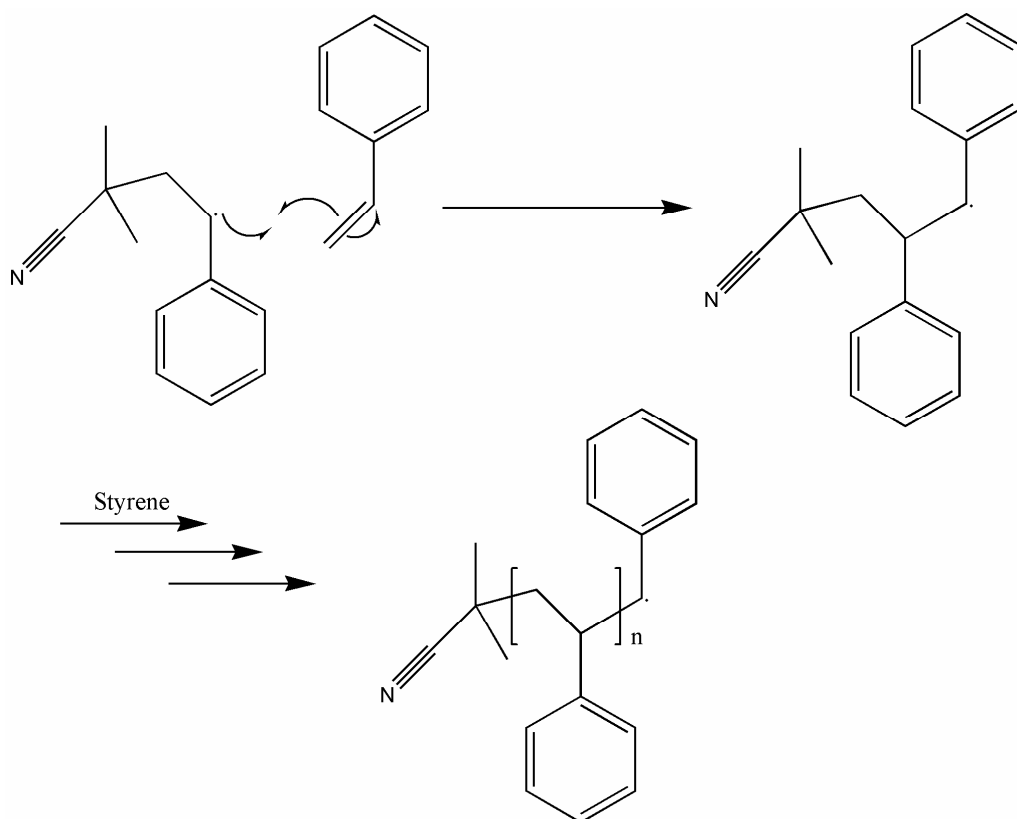


Figure 103 – *Propagation step* in the free radical vinyl polymerisation of styrene to form polystyrene. The new monomer-initiator-fragment radical then goes on to react with other monomers forming oligomer and eventually polymer radicals.

3.6.3 Reaction procedure

In a typical polymerisation experiment, aqueous magnetite nanoparticle solution is added to methanol to form the continuous phase. The resulting solution is then added to a mixture of AIBN and styrene. This homogeneous solution is stirred and heated up to the reaction temperature. The reaction is then maintained at constant temperature and stirring rate for the duration of the reaction before being cooled to room temperature, decanted into methanol, washed, filtered and dried. A detailed and technical description of this process is given in Chapter 5, section 5.3.4.

The reaction starts with a homogeneous solution of the monomer, initiator, and stable nanoparticle dispersion in the H₂O/MeOH co-solvent. Over the course of the reaction, as the initiator generates radicals to trigger polymerisation, the system becomes heterogeneous with the nucleation and growth of immiscible monomer-swollen polymer/oligomer phases (Fig. 104). At this stage, the magnetite nanoparticles assemble at the interface and cover the surface of the growing polymer particles since this reduces the high interfacial energy of the biphasic system. The nanoparticles provide a strong stabilising effect on the polymer/oligomer droplets during the polymerisation. This stabilising effect encourages the formation of discrete spherical beads in the continuous phase, as opposed to the agglomeration that would occur without stabilisation. Consequently, both the harvesting of magnetite nanoparticles from their aqueous solution and the stabilisation of the dispersion polymerisation are simultaneously achieved. There are neither by-products formed in the process nor unwanted contaminants remaining in the polymer.

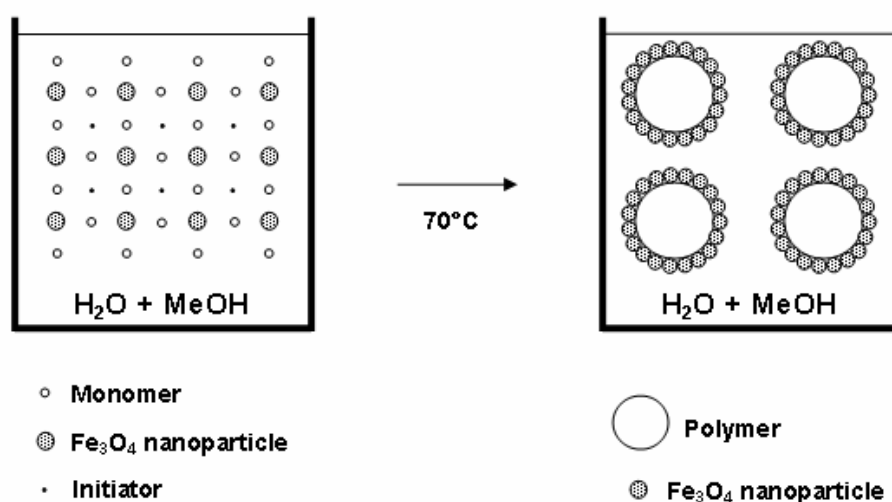


Figure 104 - The mechanism of magnetite nanoparticle stabilised free radical dispersion polymerisation reaction. The left side is the initial state of the reagents in a homogeneous phase. Upon the formation of polymer during the course of the reaction, the system becomes heterogeneous.

3.6.4 Results

Dispersion reactions were initially attempted using a nanoparticle concentration of 900 mgL^{-1} in water/methanol. This was prepared by concentrating 100 ml of the magnetite nanoparticle aqueous solution down to 20 ml and then adding it to 80 ml of methanol. This is the same concentration of nanoparticles that was found to be successful for the stabilisation of the suspension polymerisation of MMA. However, this concentration was not found to be able to stabilise the dispersion polymerisation to a suitable degree. The reactions commonly resulted in a coagulated mass of polymer. The nanoparticles could be seen to have transferred from the solution phase to the formed mass of polymer, as judged by the colouration of the two phases.

It is unsurprising that these reactions were not successful with the concentration of nanoparticles used. Although 900 mgL^{-1} was a sufficient concentration of nanoparticles to stabilise the suspension polymerisation, it must be noted that the dispersion polymerisation should theoretically be aiming to stabilise much smaller polymer particles. According to the mechanism of nanoparticle stabilisation proposed, the increase in surface/volume ratio that occurs for smaller particles should also require an increase in nanoparticle concentration. In order to test this principle, the concentration of nanoparticles was increased in two steps. The concentration of nanoparticles was first doubled from the original 900 mgL^{-1} to 1.8 gL^{-1} . At this concentration some degree of success was achieved, with some reactions successfully producing polymer powder as opposed to a single coagulated mass. Following this the concentration was then further and significantly increased to 40 gL^{-1} . At this

concentration it was possible to easily produce fine flowing polymer powder. The results for these two concentrations are discussed separately.

3.6.4.1 Results for 1.8 gL⁻¹ nanoparticle concentration

The polymer produced at this concentration takes the form of a darkly coloured powder, individual particles of which can be visibly identified. This indicates that the size range of the particles is above that expected for successful dispersion polymerisation. Optical microscopy of the polymer particles confirms this (Fig. 105 and Fig. 106). The general morphology can be seen to be poor. The polymer particles have a broad particle size distribution, and the particle shape is variable. Some of the polymer particles have definite spherical shape, others are irregular.

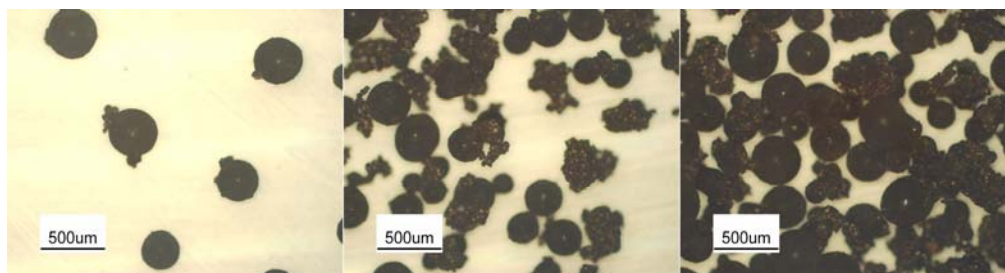


Figure 105 – Optical microscopy of polystyrene particles stabilized by magnetite nanoparticles. The scale bars show 500 μm.

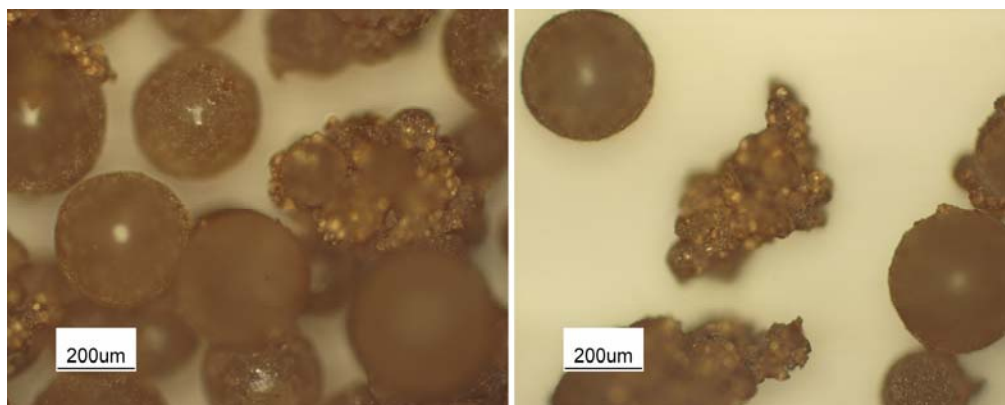


Figure 106 - Optical microscopy of polystyrene particles stabilized by magnetite nanoparticles. The scale bars show 200 μm .

At higher magnification it appears that the large spherical particles have a roughened surface, and that the irregularly shaped particles are formed by the aggregation of many smaller polymer particles (Fig. 107). This suggests that the nanoparticle concentration is still too low to successfully stabilise the dispersion, and because of this, smaller particles are coalescing to form larger beads. These larger beads presumably remain stable in the polymerisation system because of the effect of the nanoparticles on the surface and the agitation of the solution. The polymerisation environment may not be homogeneous in terms of nanoparticle to polymer concentration. This would explain how much smaller polymer beads could be formed in some areas and larger polymer particles in others, because the ratio of nanoparticles to polymer should dictate the size of stable particle that can be formed. Optical microscopy is of course limited in resolution and the smallest of the polymer particles would not be expected to be discernible by this technique. In order to better examine the polymer particles of a smaller size range, and to investigate the nature of the roughened surface of the larger polymer beads, SEM imaging was performed.

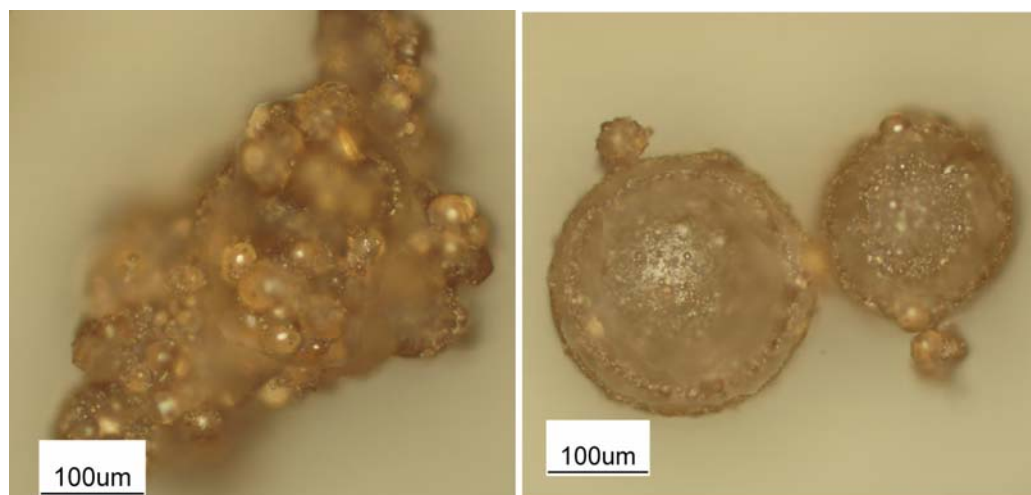


Figure 107 - Optical microscopy of polystyrene particles stabilized by magnetite nanoparticles. The scale bars show 100 μm .

3.6.4.2 SEM investigation

SEM imaging was performed to illustrate the morphology of the synthesized polymer powder. It can be seen that the polymer beads are spherical on low magnification (Fig. 108), but that the bead surface is very uneven under higher magnification (Fig. 109). In the later stages of the polymerisation, as the remaining growing oligomer chains partition out of the solution phase into the separate polymer phase, the high concentration of magnetite nanoparticles at the polymer surface may lead to the formation of this interesting morphology. The polymer at the surface layer appears to form much smaller semi-discrete micro-particles that are generally still attached to the larger polymer bead.

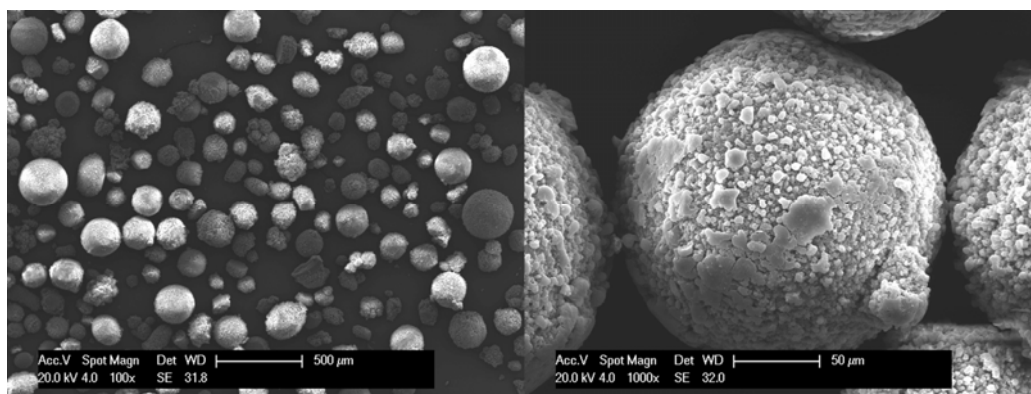


Figure 108 – Secondary electron mode SEM images of the polymer nanocomposite powder. Scale bars show 500 µm, left, and 50 µm, right.

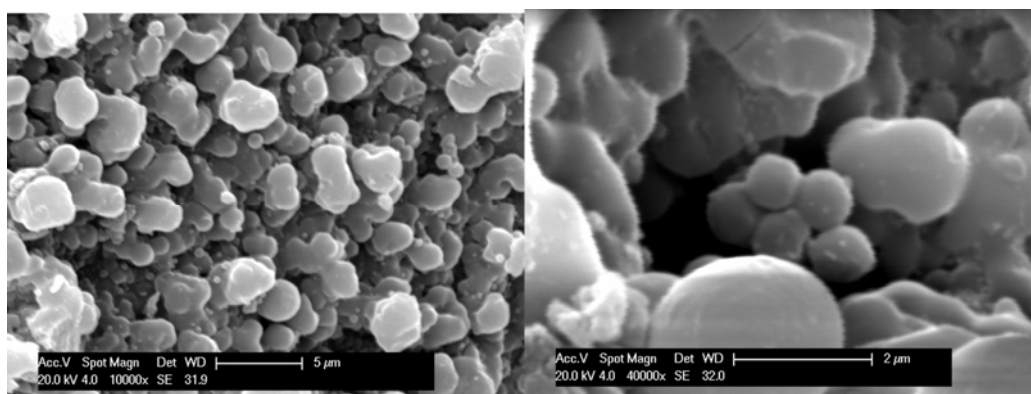


Figure 109 - Secondary electron mode SEM images of the polymer nanocomposite powder. Scale bars show 5 µm, left, and 2 µm, right.

EDX analysis was performed on the powder in the SEM (Fig. 110). Gold and palladium are detected from the coating deposited onto the polymer to prevent charging. Iron is also clearly detected, from the magnetite, but oxygen could not be resolved from the large carbon peak. However, this only indicates the presence of the magnetite nanoparticles. It was not possible from SEM to determine their location. This is of significant interest in order to confirm the mechanism by which the smaller polymer particles are stabilised around the surface of the larger polymer particles. In order to ascertain this information, TEM investigation was performed.

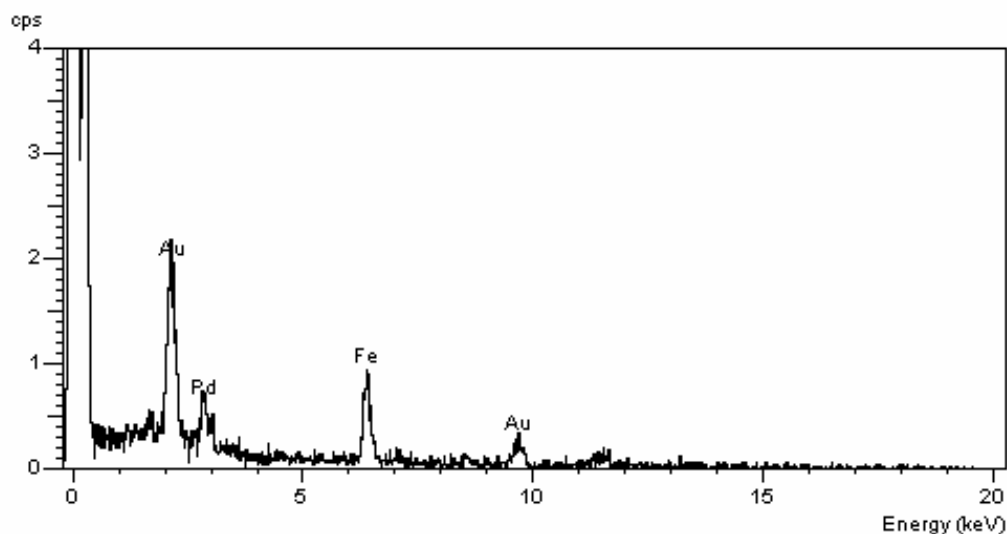


Figure 110 – EDX characterisation of the polymer nanocomposite, showing the presence of iron, and therefore indicating there is a significant level of magnetite close to the polymer surface.

3.6.4.3 TEM investigation

TEM observation of cross-sections of the polymer nanocomposite beads was performed. The polymer powder was prepared for TEM by embedding in resin, before being microtomed into thin sections that could be imaged. These sections were exposed to osmium tetroxide prior to imaging, in order to provide contrast. This is possible because the structure of the polystyrene has a high level of aromaticity, which allows the osmium complex to coordinate to it. The osmium deposits on the polystyrene areas of the cross section much more readily than the resin areas. In the TEM, the high atomic weight osmium then makes the styrene areas appear much darker.

The magnetite nanoparticles are located as a layer around the surface of the larger polymer beads (Fig. 111). The uneven surface morphology of the polymer observed in SEM can also be seen in the TEM images. The location of the nanoparticles clearly indicates that they perform a function to stabilise the larger bead formation as well as affecting the morphology of the surface. This result further proves that during the polymerisation process, the magnetite nanoparticles assemble at the interface between the methanol/water solution phase and the growing polymer/oligomer droplets as they become immiscible in the system. From the enlarged TEM images of the nanoparticles it can be seen that the size of magnetite nanoparticles is still very uniform between 10-20 nm and, despite occasional aggregations, there is no change in the nanoparticles compared to their initial size in aqueous solution.

The TEM and SEM imaging of the nanocomposite powder produced at this concentration suggest partial, but insufficient stabilisation. It appears the nanoparticles are collecting on the surface of large droplets of polymer/oligomer and providing enough stabilisation to prevent these from coalescing. However, these droplets are not the size that would be desired from dispersion polymerisation. The large size of the droplets indicates there is insufficient nanoparticle concentration to stabilise smaller and more stable droplets. However, at the surface of the large beads, where the local nanoparticle concentration is high, it can be noted that smaller, micrometer sized droplets of polymer become stable.

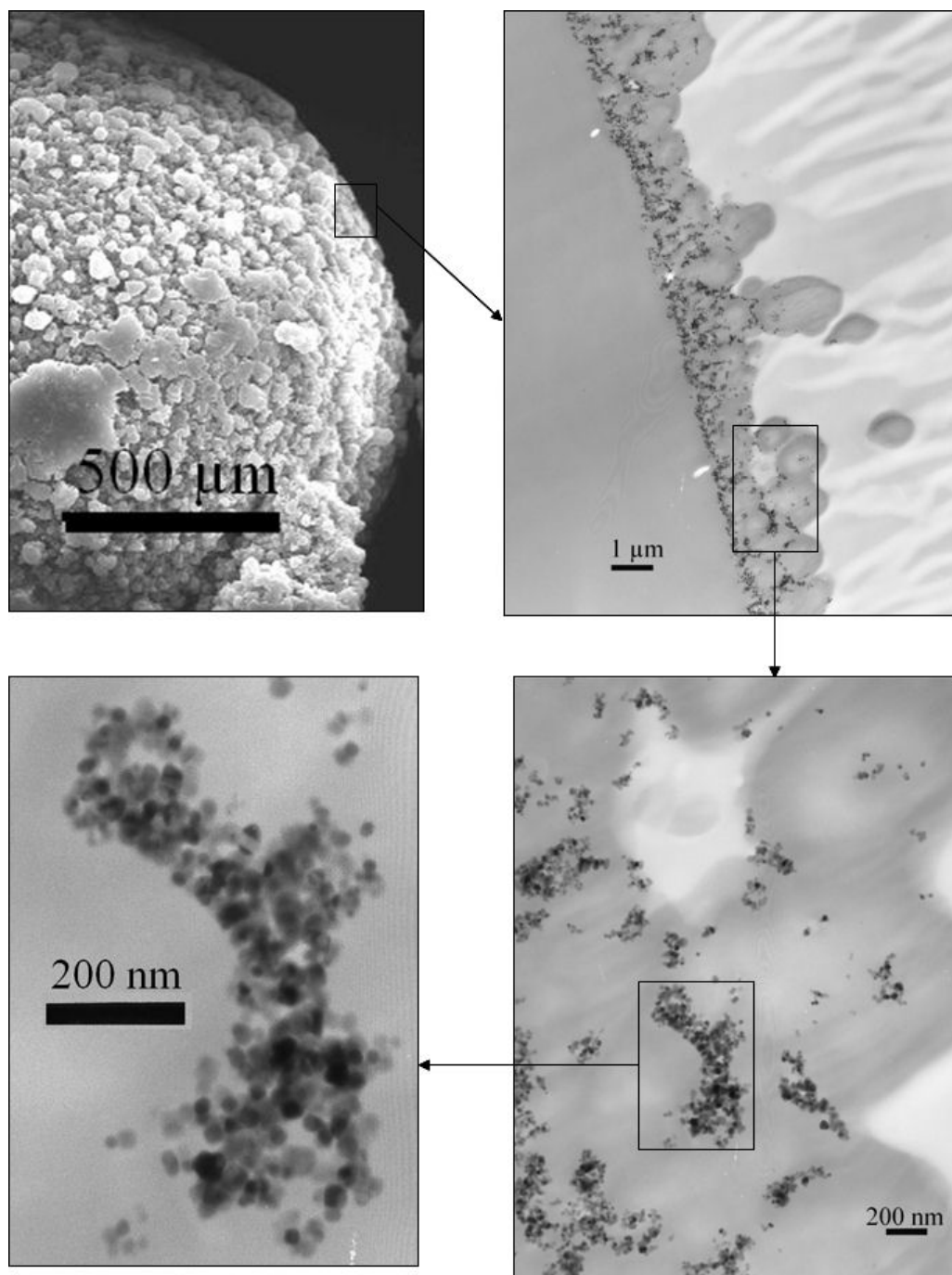


Figure 111 – Bright field TEM images of the polymer nanocomposite, shown with an SEM image, top left, for context. The arrows indicate the origin of each further enlargement. Scale bars, clockwise from top left, show 500 μm , 1 μm , 200 nm and 200 nm.

3.6.4.4 Results for 40 g L^{-1} nanoparticle concentration

The polymer produced at this concentration takes the form of a darkly coloured free flowing fine powder. Individual particles of this powder cannot be

discerned without magnification. This indicates that the size range of the particles is much smaller than that produced at the lower nanoparticle concentration of 1.8 gL^{-1} . Optical microscopy of the polymer powder confirms this (Fig. 112 and Fig. 113). All of the particles can be seen to be in the order of a few μm in size (Fig. 112). No larger polymer particles, like the $\sim 400 \mu\text{m}$ beads present at lower concentration, were detected. The magnetic properties of the nanoparticles have clearly been transferred to the polymer powder, as demonstrated by the strong attraction of the powder to a magnetic rod (Fig. 112, right). At higher magnification (Fig. 113) the shape of the polymer particles is shown to be roughly spherical. The particles also appear to be relatively uniform in size. SEM imaging was also performed to allow more detailed analysis of the morphology of the powder (described later).

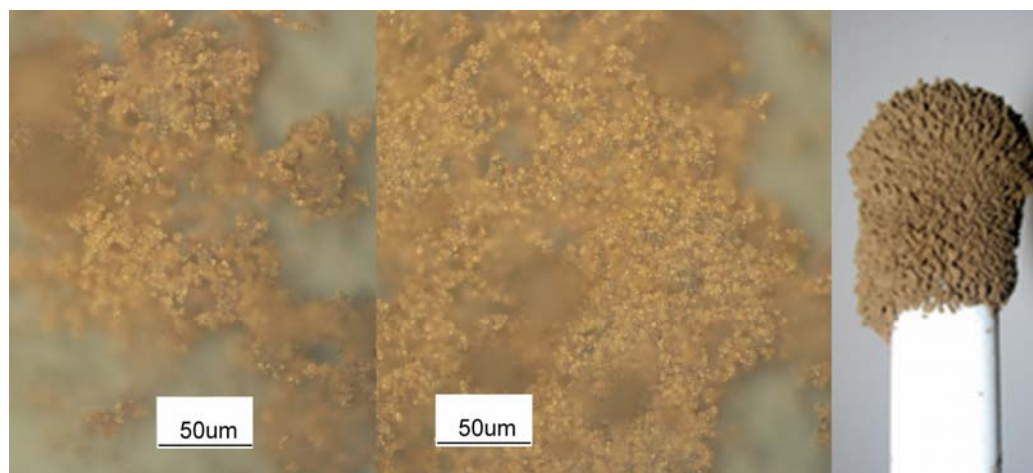


Figure 112 – Left and centre, optical microscopy of polymer powder nanocomposite material. Scale bars show $50 \mu\text{m}$. The right hand image is a conventional digital photograph of the polymer powder being attracted to a magnetic rod.

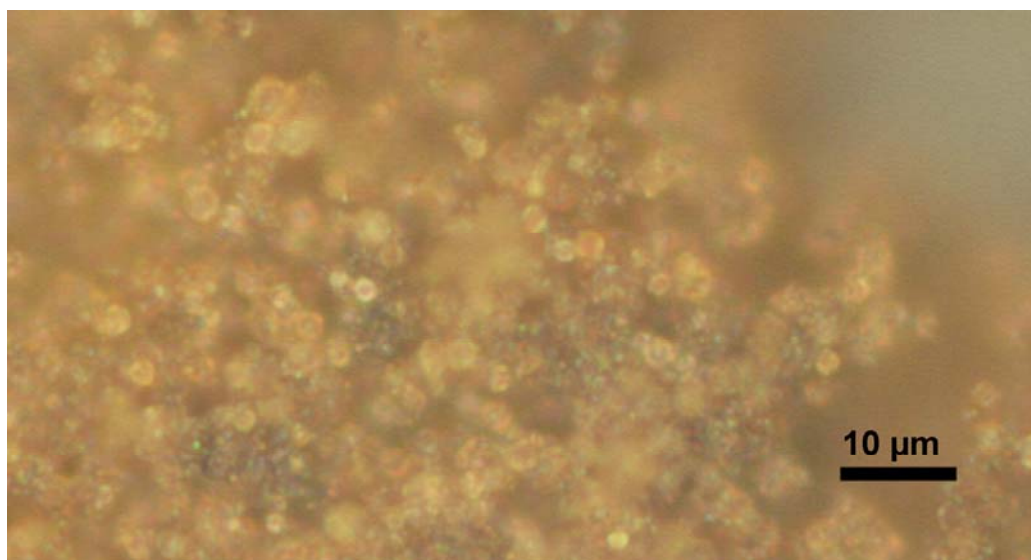


Figure 113 – Optical microscope image of magnetite-polystyrene nanocomposite powder. The scale bar represents 10 μm . Note that discrete particles, close to spherical in shape, can be discerned.

The high stabilisation efficiency from the nanoparticles enables successful dispersion polymerisation with reasonably high yield ($\sim 75\%$) and controlled morphology, results which are comparable to those synthesised with conventional stabilisers. The molecular weight of the polystyrene in the nanocomposite (M_n) is about 20,000 with polydispersity of 1.69. The slightly lower monomer conversion and molecular weight of our product compared with polystyrene synthesised from the conventional dispersion polymerisation method reveals that the magnetite nanoparticles may slightly inhibit the polymerisation. TGA analysis of the nanocomposite indicates that the total amount of magnetite uptake is $\sim 20\text{ wt}\%$ of the composite (Fig. 114). The theoretical maximum magnetite uptake in the nanocomposite is $17\text{ wt}\%$ provided the polymerisation conversion is 100% , *i.e.* if all the magnetite (4 g) was included into the polymer at full conversion ($\sim 20\text{ g}$). Considering the yield of polystyrene in this work, the experimental data suggest that the majority of

the nanoparticles in the solution have been harvested during the dispersion polymerisation. It is worth noting that a proportion of the magnetite nanoparticles may not have been directly involved in the polymerisation but magnetically attracted to the surface of the nanocomposite afterwards. Therefore, it is difficult to estimate the exact amount of nanoparticles functioning as stabiliser.

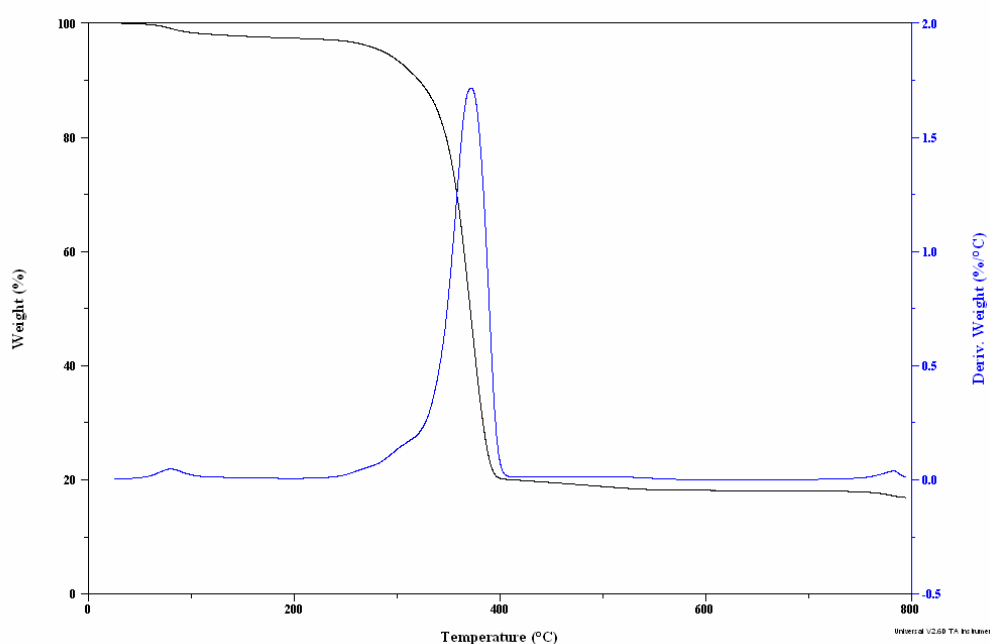


Figure 114 - TGA data of the magnetite-polystyrene nanocomposite. The measurement was taken under flowing nitrogen at a heating rate of $5\text{ }^{\circ}\text{Cmin}^{-1}$. The 20 wt% of material remaining consists of the magnetite material, as the polymer is fully degraded.

The magnetite-polystyrene nanocomposite powder was also analysed by IR spectroscopy (Fig. 115, and see Chapter 5.4.10). All the major characteristic bands are present and there is no difference from the infrared spectrum of polystyrene standard, as provided by the Spectral Database for Organic Compounds.³¹ The position of the same peaks as labelled in figure 36, for the polystyrene standard, are: 3026, 2924, 1601, 1493, 1453, 1028 and 906 cm^{-1} , all

within 3 wavenumbers of the observed values. This indicates that there is no or very weak chemical bonding between the magnetite nanoparticles and polymer, which would shift the vibrational frequencies of the polymer. This agrees with the theory that the stabilisation occurs through a physical-interfacial rather than chemical-bonding mechanism.

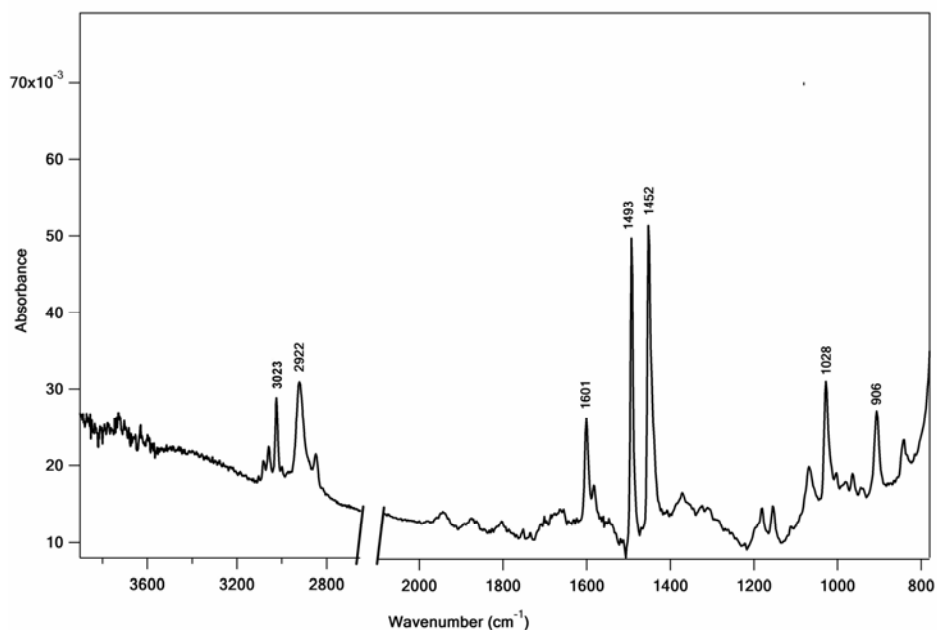


Figure 115 - IR spectrum of the magnetite-polystyrene nanocomposite powder. The major characteristic bands are labelled on the spectrum. The existence of Fe₃O₄ nanoparticles capped on polystyrene partly impairs its infrared signal.

3.6.4.5 SEM investigation

SEM investigations of the polymer powder support the observations from optical microscopy. The images (Fig. 116) show that most of the polymer beads are spherical, discrete and $\sim 1\text{-}3 \mu\text{m}$ in diameter. Some inhomogeneities are visible on the surface of some of the beads due to aggregated clusters of magnetite nanoparticles. The presence of the magnetite nanoparticles on the surface of the polymer is again confirmed by the use of EDX spectroscopy (Fig. 117). This detects both iron and oxygen, only present in the magnetite. It can be

noted that the EDX signal for iron is much stronger, relative to the gold signal, in this 40 gL⁻¹ sample than for the previous 1.8 gL⁻¹ sample (Fig. 110), presumably due to the higher relative concentration of nanoparticles to polymer. The individual nanoparticles cannot be resolved in SEM, so for higher resolution TEM was again utilised to investigate the material further.

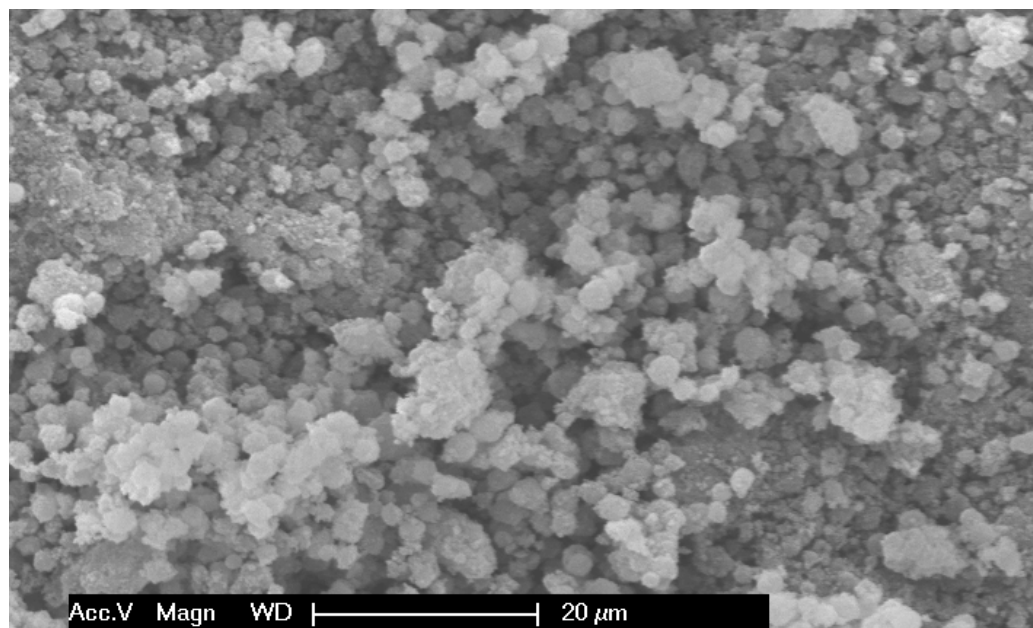


Figure 116 – Secondary electron mode SEM image of magnetite-polystyrene powder. The scale bar shows 20 μm.

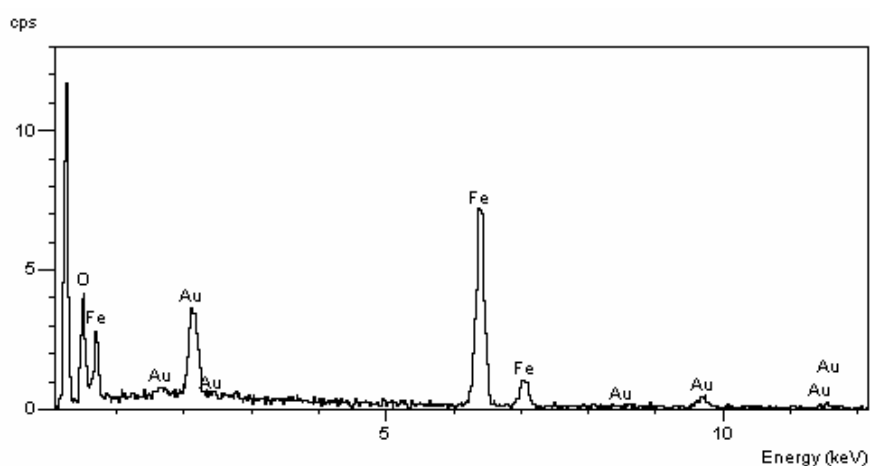


Figure 117 – EDX spectrum of magnetite-polymer powder, detecting iron and oxygen from magnetite.

3.6.4.6 TEM investigation

The small diameter of the polymer beads formed in this successful dispersion polymerisation meant that it was possible to perform some TEM imaging on the powder directly, without further preparation. Normally polymeric samples need to be microtomed to a thin enough width to allow the electron beam to pass through during imaging. However, the powder is fine enough that it allowed imaging without this step. To complement this imaging technique, another approach was also used to obtain cross section images. For this the powder was embedded in resin, microtomed and stained to provide contrast between the polystyrene and the resin.

Direct TEM characterisation of the polystyrene beads shows the polymer sphere is capped with magnetite nanoparticles (Fig. 118). Close observation (Fig. 119) shows that the nanoparticles are located on the surface, indicating they must have assembled at the polymer-liquid phase interface during polymerisation. Furthermore, the size of magnetite nanoparticles is still very uniform, falling between ~10-20 nm. Despite a few occasional aggregations, there is no significant change in the nanoparticle size from the original aqueous dispersion.

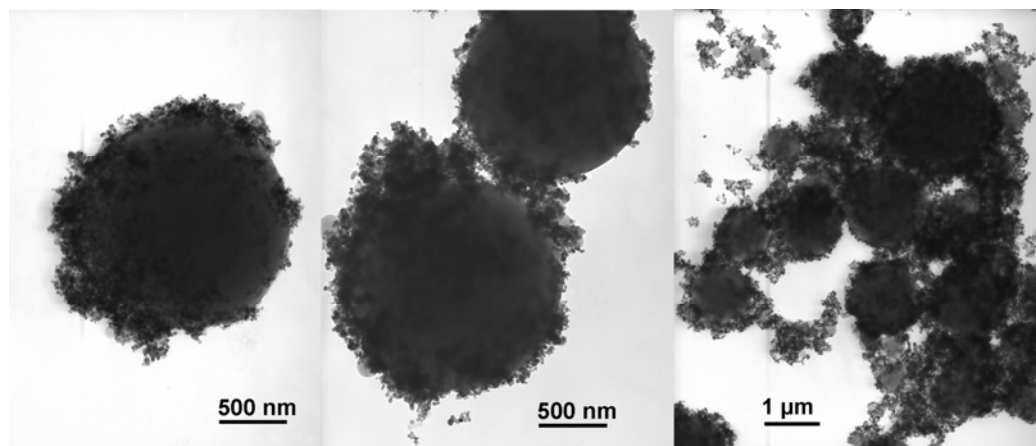


Figure 118 – Bright field TEM images taken directly of magnetite-polystyrene nanocomposite powder. The scale bars show 500 nm, 500 nm and 1 μm , from left to right.

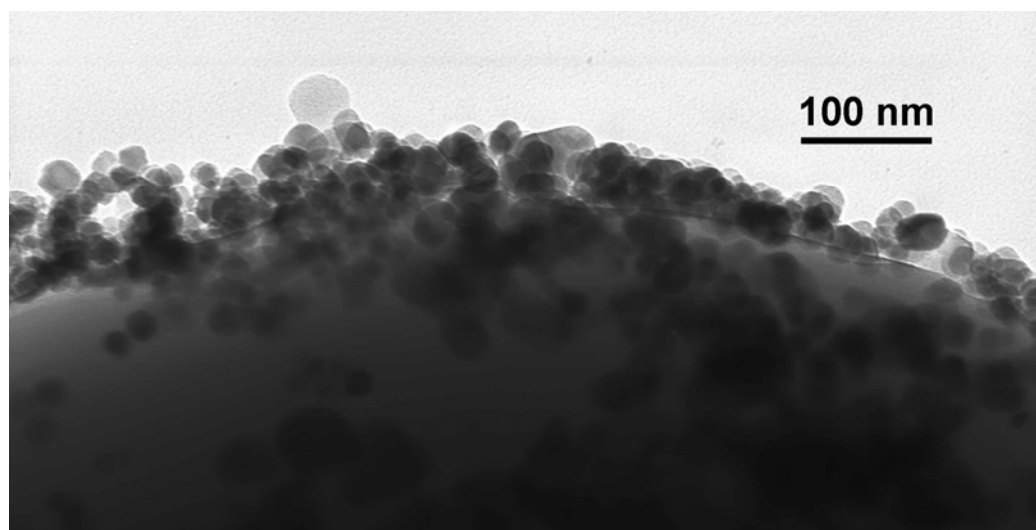


Figure 119 – Bright field TEM local magnification of polystyrene bead surface showing stabilization by magnetite nanoparticles. The scale bar shows 100 nm.

To further demonstrate the location of the nanoparticles, TEM observation of cross-sections of the embedded polymer beads was also carried out (Fig. 120 and Fig. 121). Osmium tetroxide staining clearly reveals darker shaded polystyrene and distinguishes from the embedding resin. All the polystyrene slices in view are surrounded by magnetite nanoparticles and these

nanoparticles can be seen to be located around the surface of the original polymer beads. Though a few loose nanoparticles/clusters can be observed, these were likely dislodged on the microtomed polymer surface during the sample preparation. No significant amount of magnetite is detected inside the polystyrene beads, as one would expect if the dispersion mechanism applies.

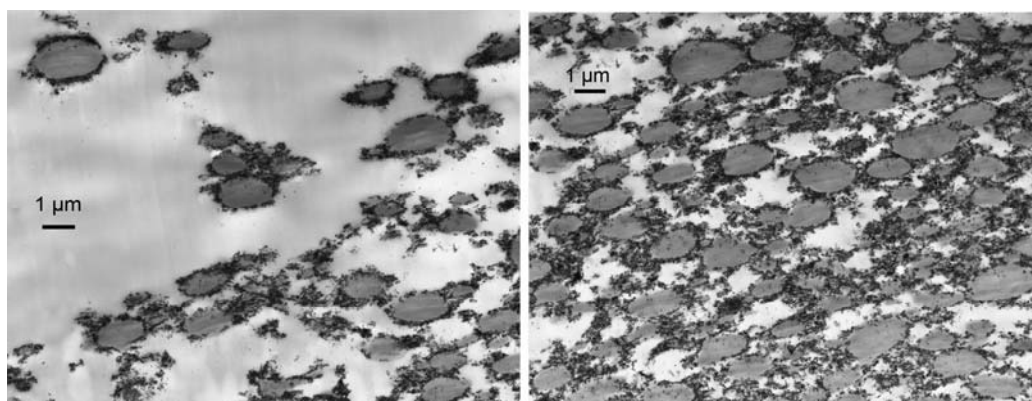


Figure 120 – Bright field TEM images of magnetite-polystyrene nanocomposite powder, showing general morphology. Images were obtained after the powder was resin embedded, microtomed and then stained with osmium tetroxide. The scale bars both show 1 μm .

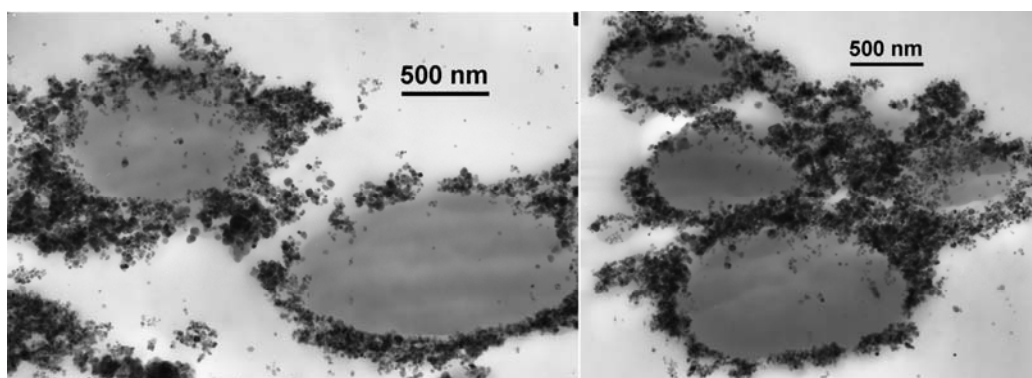


Figure 121 - Bright field TEM images of magnetite-polystyrene nanocomposite powder, showing higher magnification of the polymer bead surface. Images were obtained after the powder was resin embedded, microtomed and then stained with osmium tetroxide. The scale bars both show 500 nm.

All the characterisation results confirm the proposed mechanism of the nanoparticle stabilised dispersion polymerisation and show two complementary processes; harvesting of functional nanoparticles in the reaction system and stabilisation of the polymerisation. Surfactant concentration is well known to have a large effect on particle size, which has been observed to occur here with a change in the concentration of the magnetite nanoparticles. An increase in nanoparticle concentration reduces the size of polymer particles produced, as would be expected if they are functioning as a surfactant. The synthesized polymer nanocomposites are natural carriers for the nanoparticles and retain their characteristics to provide opportunities for practical applications.

3.6.5 Conclusions

A novel dispersion polymerisation based on stabilisation by magnetite nanoparticles has been successfully achieved in the absence of any other conventional stabiliser. Polystyrene microparticles decorated with magnetite nanoparticles on their surfaces were produced. Using this new polymerisation method, magnetite nanoparticles can be easily harvested from aqueous solution, which in the meantime act as stabiliser for the dispersion polymerisation of styrene. This in-situ polymerisation method stabilised by functional nanoparticles could open up a new route for preparing a wide range of polymer nanocomposites with different applications as diverse as antimicrobial paints, catalysts, photonic devices or water purification materials. As there are a wide range of polymer/nanoparticle combinations, we believe that many more functional hybrid nanocomposites could be prepared by this method.

3.7 Overall conclusions and future work

The original aims of this project can be summarised in the following bullet points:

- The successful recovery or harvesting of nanoparticles from aqueous solution.
- The incorporation of these nanoparticles into polymer powder.
- Specifically, the location of the nanoparticles to be targeted to the surface of the polymer.
- The furthering and expansion of the field of nanoparticles as a stabiliser for polymerisations, both in practical and theoretical terms.

All of these aims have been achieved. The two sections, on suspension and dispersion, have described polymerisations with metal oxide nanoparticles as the sole stabiliser present. The mechanism allowing this has been explored in terms of nanoparticle concentration, and by the extensive use of electron microscopy to characterise the nano-structure of the products. The two complementary polymerisation methods described allow a range of different polymers and powder sizes to be synthesised. It has been shown that not only magnetite, but also other metal oxide nanoparticles, can be used in this manner. This confirms the scope and versatility of this technique.

This field is still in very early stages and it can be noted that these suspension and dispersion reactions, with metal oxide nanoparticle stabilisers, represent the first of their type. For this reason this work only represents very

preliminary studies, which lay the foundation for much possible future research which should involve the following points:

- Clarification of mechanistic variables, such as detailed studies on the effect of the ratio of monomer to stabiliser, stirring speed, monomer to continuous phase ratio.
- Investigation of a wider range of nanoparticles, both to show versatility of technique and to determine if the nature of the material forming the nanoparticles influences the reaction.
- The formulation of the nanoparticle-polymer powder produced into a form suitable for applications testing.
- Collaborations with physical chemists should be sought to investigate the nature of the stabilisation mechanism in more detail, in terms of the reduction in interfacial energy. This should combine theoretical calculations, models and predictions with experimental data.

The initial, successful trials reported here have allowed for further research on this technique to be instigated at Nottingham University. Indeed, since this project finished, several new students have been funded in the Lester group to continue this work. Their current studies have begun testing other nanoparticles such as copper and silver, as well as further studies of magnetite and haematite in terms of mechanistic variables. It is intended to produce a polymer powder that can be tested for potential use as a water-filter. Steps have begun in setting up an official collaboration with Prof. Bernie Binks of the University of Hull, a physical chemist and a leading expert in the theory of nanoparticle stabilisation. This will involve an application for a larger funding grant.

3.8 References

1. E. Lester, P. Blood, J. Denyer, D. Giddings, B. Azzopardi and M. Poliakoff, *Journal of Supercritical Fluids*, 2006, **37**, 209-214.
2. E. H. Lester and B. J. Azzopardi, (The University of Nottingham, UK). 2005, pp. 2005-GB2483.
3. A. Cabañas, J. Li, P. Blood, T. Chudobac, W. Lojkowski, M. Poliakoff and E. Lester, *Journal of Supercritical Fluids*, 2007, **40**, 284.
4. M. H. Nilsen, C. Nordhei, A. L. Ramstad, D. G. Nicholson, M. Poliakoff and A. Cabanas, *Journal of Physical Chemistry C*, 2007, **111**, 6252-6262.
5. http://www.hero.ac.uk/uk/business/archives/2006/nano_spinout.cfm, 2008.
6. G. Carotenuto and L. Nicolais, *Composites Part B-Engineering*, 2004, **35**, 385-391.
7. M. K. Corbierre, N. S. Cameron, M. Sutton, S. G. J. Mochrie, L. B. Lurio, A. Ruhm and R. B. Lennox, *Journal of the American Chemical Society*, 2001, **123**, 10411-10412.
8. Y. Dirix, C. Darribere, W. Heffels, C. Bastiaansen, W. Caseri and P. Smith, *Applied Optics*, 1999, **38**, 6581-6586.
9. X. Q. Zou, H. F. Bao, H. W. Guo, L. Zhang, Q. Li, J. G. Jiang, L. Niu and S. J. Dong, *Journal Of Colloid And Interface Science*, 2006, **295**, 401-408.
10. C. J. Huang, F. S. Shieu, W. P. Hsieh and T. C. Chang, *Journal of Applied Polymer Science*, 2006, **100**, 1457-1464.
11. Y. Li, E. C. Y. Liu, N. Pickett, P. J. Skabara, S. S. Cummins, S. Ryley, A. J. Sutherland and P. O'Brien, *Journal of Materials Chemistry*, 2005, **15**, 1238-1243.
12. Y. Zhang, D. F. Kang, C. Saquing, M. Aindow and C. Erkey, *Industrial & Engineering Chemistry Research*, 2005, **44**, 4161-4164.
13. B. Jongsomjit, E. Chaichana and P. Praserttham, *Journal of Materials Science*, 2005, **40**, 2043-2045.
14. W. H. Binder, *Angewandte Chemie-International Edition*, 2005, **44**, 5172-5175.
15. Y. Lin, A. Boker, H. Skaff, D. Cookson, A. D. Dinsmore, T. Emrick and T. P. Russell, *Langmuir*, 2005, **21**, 191-194.
16. Y. Lin, H. Skaff, T. Emrick, A. D. Dinsmore and T. P. Russell, *Science*, 2003, **299**, 226-229.
17. S. U. Pickering, *Journal Of The Chemical Society*, 1907, **91**, 2001-2021.
18. B. P. Binks, J. Philip and J. A. Rodrigues, *Langmuir*, 2005, **21**, 3296-3302.
19. B. P. Binks and C. P. Whitby, *Colloids and Surfaces a-Physicochemical and Engineering Aspects*, 2005, **253**, 105-115.
20. Y. J. He, *Materials Letters*, 2005, **59**, 114-117.
21. Y. J. He, *Materials Letters*, 2005, **59**, 2133-2136.
22. Y. J. He, *Materials Chemistry And Physics*, 2005, **92**, 134-137.
23. Y. Y. Liu, X. Q. Chen, R. H. Wang and J. H. Xin, *Materials Letters*, 2006, **60**, 3731-3734.

24. D. J. Voorn, W. Ming and A. M. van Herk, *Macromolecules*, 2006, **39**, 2137-2143.
25. A. Schmid, S. Fujii and S. P. Armes, *Langmuir*, 2005, **21**, 8103-8105.
26. A. Schmid, S. Fujii and S. P. Armes, *Langmuir*, 2006, **22**, 4923-4927.
27. A. Schmid, S. Fujii, S. P. Armes, C. A. P. Leite, F. Galembeck, H. Minami, N. Saito and M. Okubo, *Chemistry of Materials*, 2007, **19**, 2435-2445.
28. R. W. Shaw, T. B. Brill, A. A. Clifford, C. A. Eckert and E. U. Franck, *Chemical & Engineering News*, 1991, **69**, 26-39.
29. B. Wong, in *Chemistry Thesis: The Preparation of Nanocomposite Materials using Supercritical Carbon Dioxide*, University of Nottingham, Nottingham, 2005.
30. M. P. Stevens, *Polymer Chemistry: An Introduction*, O.U.P., New York, 1990.
31. http://riodb01.ibase.aist.go.jp/sdbs/cgi-bin/cre_index.cgi, National Institute of Advanced Industrial Science and Technology (AIST), 2008.

Chapter 4: Novel synthetic routes to silver nanoparticle decorated polymer microspheres

4.1 Overview

Metal nanoparticles are very useful for a range of sensing and catalytic applications. These applications ideally require surface located nanoparticles supported on a suitable recoverable material. This chapter focuses on the production of polymer powders with silver nanoparticles located on the surface of polymer microspheres. This morphology is desirable because it is ideal for applications that require silver nanoparticles to be accessible but supported on a substrate to allow ease of use and recovery. Therefore, it was the target of this work to develop useful new routes to such composites. The chapter begins with a brief but general introduction to the potential applications of the materials as well as the objectives of the research. After this, two alternative synthesis routes, developed in this research, are reported. These routes, one aqueous and one supercritical, are quite different in approach, offering complementary choices, and are therefore discussed separately. Each route is tackled in turn with an introduction to the relevant theory and literature, a description of the method, and a discussion of the results. Conclusions as to the consequences of these routes and suggestions of future work are given at the end of each section, as well as a general conclusion and comparison of the two routes at the close of the chapter.

4.2 Contents

4.1	Overview	269
4.2	Contents	270
4.3	Introduction and aims	271
4.4	Aqueous route	273
4.4.1	Introduction	274
4.4.1.1	Crosslinking with DVB	277
4.4.1.2	Reaction procedure	278
4.4.2	Results	281
4.4.2.1	Silver nanoparticle solution	281
4.4.2.2	Sulfonated polystyrene synthesis and decoration with silver nanoparticles	288
4.4.3	Conclusions and future work	293
4.5	Supercritical Route	295
4.5.1	Introduction	295
4.5.1.1	Living Polymerisation	297
4.5.1.2	Reversible addition-fragmentation chain transfer – (RAFT).....	298
4.5.1.3	Silver nanoparticle reduction and stabilisation.....	303
4.5.1.4	Reaction procedure	305
4.5.2	Results	306
4.5.2.1	Nanoparticles synthesised independently	306
4.5.2.2	PMMA powder synthesised independently	307
4.5.2.3	Silver nanoparticle and PMMA combined synthesis.....	308
4.5.2.4	Concentration of Ag(hfac)COD	315
4.5.3	Conclusions and future work	320
4.6	Overall conclusions	321
4.7	References	322

4.3 Introduction and aims

The properties of silver nanoparticles, as well as some of their applications, have already been described in Chapters 1 and 2. This chapter reports the synthesis of polymer powders comprised of discrete spherical particles coated with silver nanoparticles. If such morphology could be synthesised simply and effectively, this would allow ease of use of the silver nanoparticles for many proposed applications. These applications are wide-ranging, and the material produced in this chapter is not tested or intended for any one specific role. However, in order to suggest how the material could be useful, some potential functions are described here.

Biosensing applications could take advantage of the SERS or MEF potential of surface located silver nanoparticles to detect analytes at low concentration. The silver nanoparticles could also be used to trigger drug release, by exciting the plasmon resonance, or to monitor the presence/interactions of a species by detecting changes in the plasmon resonance.

Surface located silver nanoparticles supported on a polymer powder could also find simple application in catalysis reactions. The solid polymer substrate would allow ease of recovery. Small polymer particles would be desirable to increase surface area for catalysis, and it would be necessary for the nanoparticles to be on the surface to be accessible. Such a powder could be formed into a

column that liquids or gases could be easily passed over, in order to take advantage of the catalytic potential reported from silver nanoparticles.¹⁻⁵

Furthermore, silver nanoparticles on the surface of a polymer powder would be useful to take advantage of the antimicrobial applications of silver.⁶⁻⁹ This could be for direct medical applications, such as wound dressings or implants. It could also be used indirectly such as in the production of a clean water filter.¹⁰⁻¹²

Potential for applications such as these has caused several groups to investigate pathways to silver nanoparticle surface decorated polymer microparticles.¹³⁻¹⁸ These synthesis methods are often overly complex and specific to certain systems. It is our aim here to develop two complementary synthesis routes for the general synthesis of silver nanoparticle decorated polymer microspheres. Ideally, these routes should be simple, low cost, scalable, free from contaminants, and widely transferable. These two alternative routes will be discussed individually. The first route reported is intended to be a general method of forming silver nanoparticles, and attaching them to the surface of polymer spheres, using standard ‘wet chemistry’ techniques. This second method reported uses a scCO_2 synthesis route to form silver nanoparticle coated polymer microspheres.

4.4 Aqueous route

Hypothesis

The synthesis of silver nanoparticle coated polystyrene microspheres was attempted. This synthesis comprised first a facile synthetic route to aqueous dispersions of silver nanoparticles, and secondly the attachment of these nanoparticles to separately synthesised polystyrene microspheres. Both the route in which the nanoparticles themselves are synthesised, and the route in which they are attached to the polymer powder, are novel and provide interesting new strategies for nanocomposite formation. Stable aqueous dispersions of silver nanoparticles were synthesised from an organometallic precursor dissolved in an organic phase. Hydrogen gas was used to reduce the precursor to form silver nanoparticles which spontaneously transferred into an immiscible aqueous phase where they were stabilised. The effectiveness of a variety of aqueous stabilizing agents was evaluated. All of the products were characterised by electron microscopy and UV-vis spectroscopy. A solution of these nanoparticles was then added to polystyrene microspheres with a sulfonated surface layer. An interaction between the sulfonated surface and the silver nanoparticles was intended to provide attachment of the metal nanoparticles to the polymer spheres. The final nanocomposite powder produced was again investigated by electron microscopy to determine if the process is successful.

4.4.1 Introduction

Many different routes to the production of silver nanoparticles have been investigated, each showing characteristic advantages and disadvantages. The majority of the more straightforward approaches are based on the reduction of silver nitrate by sodium borohydride¹⁹ or sodium citrate.²⁰ Some of the more diverse methods previously used include microwave plasma synthesis,²¹ electrolysis of Ag salts,²² rapid expansion of supercritical solvents,^{23, 24} microemulsion,²⁵ and photoreduction of Ag ions.^{26, 27} Hydrogen has been previously employed as a convenient and effective reducing agent for the production of noble metal nanoparticles.²⁸ Evanoff and Chumanov reported a synthetic pathway to aqueous silver nanoparticles by using hydrogen acting on dissolved Ag₂O.²⁹ In many nanoparticle synthetic routes organometallic precursors play an important role by allowing more control through tailored design,^{30, 31} *e.g.* by selecting appropriate ligands, the solubility and decomposition rate of the precursor can be modified.

It is essential to stabilize silver nanoparticles in the dispersing medium to prevent agglomeration. This can be achieved by either electrostatic or steric stabilization, as described in chapter 1.3.2.5. Many of the traditional routes to silver nanoparticle synthesis in an aqueous medium rely on electrostatic stabilization by the formation of an electrical double layer around the particles. This double layer is formed by the adsorption of negatively charged species,

usually inorganic ions, onto the silver nanoparticle surface. This results in a Coulombic repulsion between particles that prevents them from coagulating. Steric stabilization normally involves the adsorption of molecules such as polymers, surfactants or ligands onto the particle surface providing a protective layer. The protecting agent must have good affinity to the particle surface as well as being easily dispersible in the desired solvent. Various stabilizing agents such as gelatine, agar, cyclodextrins, poly(vinyl alcohol) (PVA), poly (vinyl pyrrolidone) (PVP), peptides and cellulose acetate among others have proved useful for protecting and dispersing nanoparticles in aqueous solutions. The polar side groups in PVP and PVA have been found especially effective in the stabilization of silver nanoparticles.

There is a common disadvantage for the majority of existing methods. These synthetic routes to aqueous silver nanoparticle dispersions lead to high levels of inorganic by-products in the resultant solution, either from the metal precursor or reducing agent, or as the intended stabilizer, *e.g.* boron compounds²⁵ or inorganic salt stabilizers.²⁸ The method used in this work is a synthesis of aqueous dispersions of silver nanoparticles passivated by polymeric stabilizers from a biphasic system. Organometallic silver complexes are dissolved in the organic phase, and then reduced to silver nanoparticles by hydrogen gas. These organic insoluble nanoparticles are forced into the aqueous phase by agitation where they are protected and dispersed by polymeric stabilizers, while the organic phase is removed simultaneously. The hydrogen reduction of organometallic precursors avoids the formation of unwanted inorganic products, leading to

stabilized aqueous dispersions of silver nanoparticles suitable for many potential applications.

This method of silver nanoparticle formation represents an interesting alternative pathway. The use of organic soluble precursor complexes should enable many different feedstocks to be used, providing an easily tailorable route to a wide range of metal nanoparticles, not just silver. In this work, the silver nanoparticles are attached to the surface of polystyrene beads that have been synthesised separately. These two steps are therefore independent. The route described for the attachment of the silver nanoparticles to the surface of the polymer should be equally applicable to silver nanoparticles produced in any other of the conventional routes. It should also be just as appropriate for use with gold nanoparticles. Therefore the attachment method also represents a transferable technique with wide ranging possible applications.

The polystyrene powder is synthesised by conventional dispersion polymerisation, as described in Chapter 3.5.1. However, unlike the dispersion polymerisation reported in Chapter 3, a conventional chemical stabilising agent is used, namely PVP, a water soluble stabiliser (Fig. 122). Divinylbenzene (DVB) was also used as a cross-linking agent, see below, to make it easier to produce small particles. A small size range of particle, $\sim 1 \mu\text{m}$, was desired to make TEM investigation more straightforward. The polystyrene powder produced could then be reacted with sulfuric acid to produce sulfonate groups on the surface of the polymer. These electron rich, soft, electron donating groups have a strong attraction to the surface of silver and gold nanoparticles.^{18, 32} This should allow

the polymer particles to be simply mixed with an aqueous solution of silver nanoparticles in order to decorate the surface of the powder. The simplicity and scalability of this technique makes it an advantageous route to the preparation of metal nanoparticle coated polymer powders.

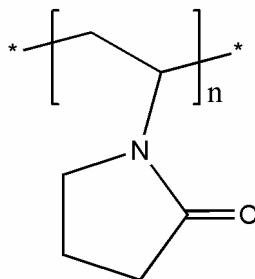


Figure 122 – The structure of the PVP stabiliser used in the dispersion polymerisation of Styrene.

4.4.1.1 Crosslinking with DVB

Cross-links are covalent bonds formed between polymer chains, linking one polymer chain to another. Crosslinking agents are chemical reagents used to form such bonds within a polymeric substance. This causes a dramatic change in the polymer properties. As the polymer chains become increasingly bound together, the material becomes a single, highly entangled, molecule. This means that the polymer cannot ‘melt’ as such, because the polymer chains cannot move freely with respect to each other. The polymer chains cannot flow past or around each other, they are effectively held in place. When two discrete, growing, polymer particles are crosslinked to a sufficient degree before coming in contact, then the particles are less likely to coalesce. This is because all the polymer chains in each

particle are bound together, so it is impossible for the two separate particles to merge together effectively.

Divinylbenzene is a crosslinking agent commonly used for the crosslinking of styrene. The structures of the monomer and crosslinking agent are very similar, making them easily compatible in reactions. The divinylbenzene structure differs significantly from styrene, however, in that it contains two vinyl groups that can be polymerised rather than one (Fig. 123). This means that if the divinylbenzene is linked into a forming polymer chain, there will be an additional vinyl group left exposed as a side group of the chain. This can then go on to react further to bind to another forming chain.

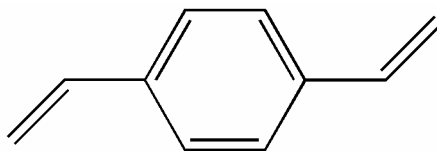


Figure 123 – The structure of para-divinylbenzene crosslinking agent. The two vinyl groups allow separate polymer chains to be linked together.

4.4.1.2 Reaction procedure

A brief outline of the reactions performed will be provided here, for a more technical description see Chapter 5.3.5 and 5.3.6. A schematic is shown (Fig. 124) to show how the two routes converge for the formation of silver nanoparticle coated polystyrene microspheres.

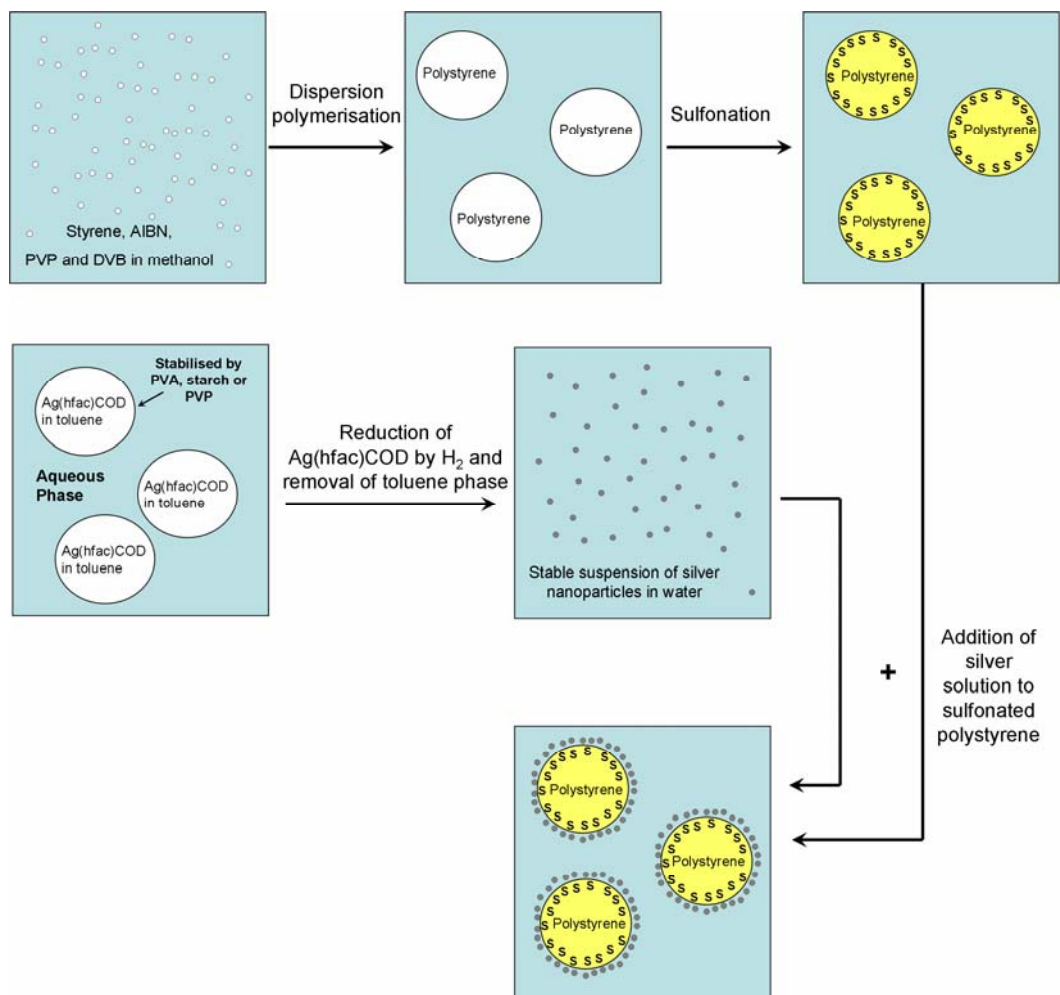


Figure 124 – Schematic showing the synthetic routes for the silver nanoparticle solution and the sulfonated polystyrene beads, and their combination to form the final nanocomposite material.

Aqueous silver nanoparticle solution:

First, a suitable aqueous soluble stabilizer for silver nanoparticles is dissolved in deionised water. Three such stabilisers were investigated, PVP, PVA and starch. An organic soluble precursor is simultaneously dissolved in an organic phase. These consisted of Ag(hfac)COD for the precursor, and toluene as the organic phase. Ag(hfac)COD was used because it was readily available in the laboratory, and toluene was chosen because it is a good solvent for the precursor.

Both solutions are then added together and the resulting biphasic solution is stirred with a continuous flow of hydrogen bubbling through. The reaction is then heated to temperature and the progress is monitored as the colour of the solution changes from white to brown over the course of the reaction. The reaction is stopped after a time by which it is judged to have reached completion as observed by the colour no longer darkening. The end product is a single aqueous phase containing the nanoparticulate dispersion.

Sulfonated Polystyrene:

A conventional dispersion polymerisation was performed in methanol to convert styrene monomer into polystyrene. AIBN was used as the initiator in the presence of PVP stabilizing agents and DVB crosslinking agents. The reaction was heated and stirred until completion before being decanted, washed and filtered. The resulting fine powder was then sulfonated by reaction with concentrated sulfuric acid under heating with 1,2-dichloroethane solvent.³³ The powder was then washed with deionised water, filtered, and re-washed for a further three cycles. The pH of an aqueous solution of the powder was then tested, and NaOH added until the pH was brought up to ~5. The powder was then filtered again and dried.

Combination of silver nanoparticles and sulfonated polystyrene:

The sulfonated polystyrene powder was added to deionised water and stirred to form a suspension. An aqueous solution of PVA stabilised silver

nanoparticles was then added slowly. After the addition was complete the stirring rate was increased for a further duration, in order to ensure complete mixing, before the suspension was filtered, washed, re-filtered and dried.

4.4.2 Results

4.4.2.1 Silver nanoparticle solution

All three solutions stabilized by starch, PVP and PVA, respectively, exhibited a brown colouration caused by the plasmon resonance absorption of the silver nanoparticles. However, there were some apparent differences between these solutions according to the stabilizer used. The PVP and PVA stabilized solutions were transparent and stable to dilution, with no precipitation or residue. The starch stabilized nanoparticles were slightly less stable, and led to a cloudy solution in comparison to the other two. Interestingly, the silver/PVP solution was light yellow/brown, as opposed to the deeper brown coloration of the silver/PVA and silver/starch solutions. This indicates a difference in the intensity or position of plasmon absorption in these solutions possibly due to differences in the size or concentration of the nanoparticles.

The reaction products obtained for each of the three stabilizers were investigated using TEM. It should be noted that some aggregation of the silver nanoparticles upon drying onto TEM grids occurred. However it was found that this effect could be minimized by careful sample preparation from dilute solution. A representative bright field TEM image of the general nanoparticle appearance

and distribution for the PVA stabilized sample is shown (Fig. 125a). Selected area electron diffraction patterns recorded from groups of nanoparticles confirm them to be crystalline in structure (Fig 125b). Such diffraction patterns were indexed to the crystal plane spacings of face-centred cubic silver. EDX analysis of the area containing the nanoparticles also confirms the presence of elemental silver (Fig. 125c). A histogram showing the general size distribution of the particles, averaged across many TEM images, demonstrates that most of the particles (> 95 %) have diameters within the 5–40 nm range with an average value of ~ 20 nm (Fig. 125d).

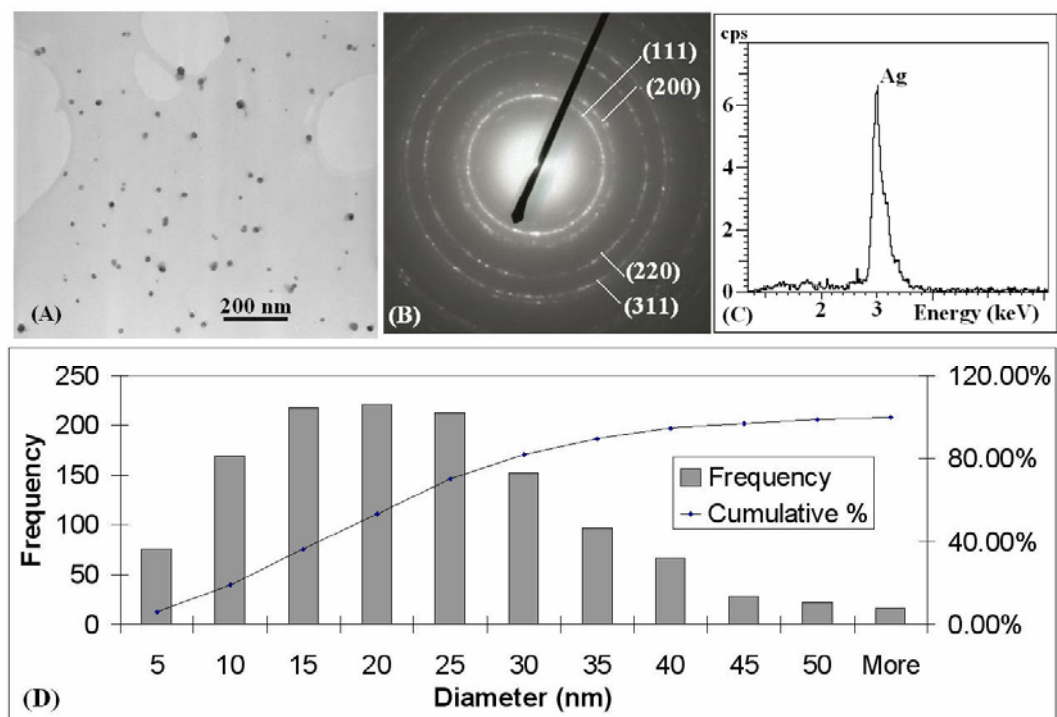


Figure 125 - PVA stabilized silver nanoparticles of average diameter ~20 nm. (A) Representative bright field TEM image. (B) SAED pattern of the nanoparticles shows crystalline structure. (C) EDX analysis of the nanoparticles verifies the presence of silver. (D) Size distribution histogram.

Representative TEM images and corresponding histograms for PVP and starch stabilized solutions are shown (Figs. 126 and 127, respectively). Both PVP and starch stabilized solutions show a smaller average nanoparticle size and slightly narrower size distribution than the PVA stabilized solution. The average nanoparticle diameters for the PVP and starch stabilized solutions were found to be ~ 14 nm and ~ 11 nm, respectively. All the silver objects observed are particulate in structure; no silver nanowires, nanorods, or nanoplatelets were found.

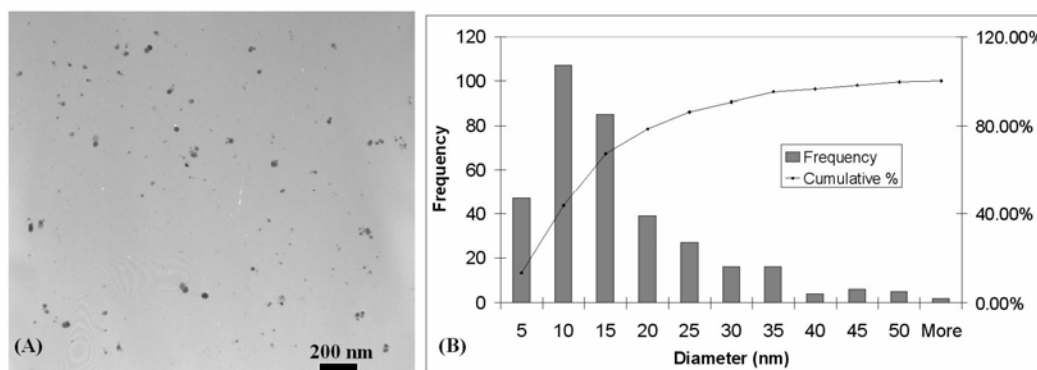


Figure 126 - PVP stabilized silver nanoparticles of average diameter ~14 nm. (A) Representative bright field TEM image. (B) Size distribution histogram.

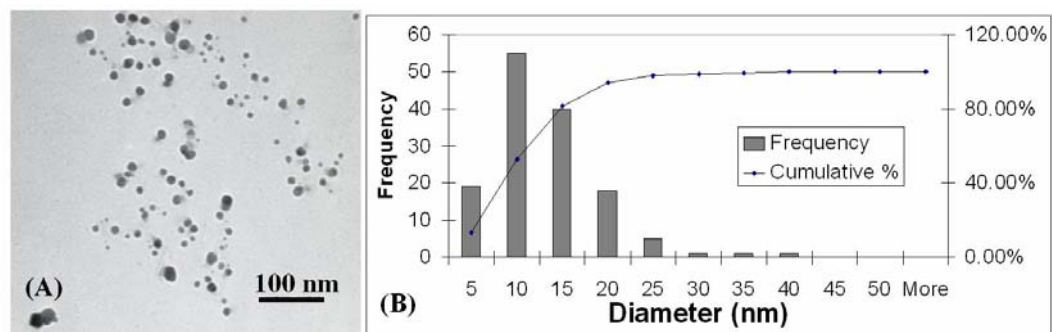


Figure 127 - Starch stabilized silver nanoparticles of average diameter ~ 11 nm. (A) Bright field TEM image of silver nanoparticles produced with starch stabilizers. (B) Size distribution histogram.

UV-visible spectra of the dispersions with the three different stabilizers were obtained to allow more detailed analysis of the plasmon resonance property (Fig. 128). All the spectra show a strong absorption in the wavelength range characteristic of silver nanoparticles, with only one observable peak in the plasmon region. This is consistent with the presence of only nanoscale particles, being significantly smaller than the wavelength of the incident light. For larger particles, the electric field becomes non-uniform and higher multipole resonances become important, leading to a splitting of the plasmon absorption into two or more peaks.^{34, 35} Since the quadrupole resonance becomes visible at ~ 70 nm particle size,³⁴ it is inferred that the size of the silver nanoparticles produced in this work is mostly below this value, being consistent with the TEM observations.

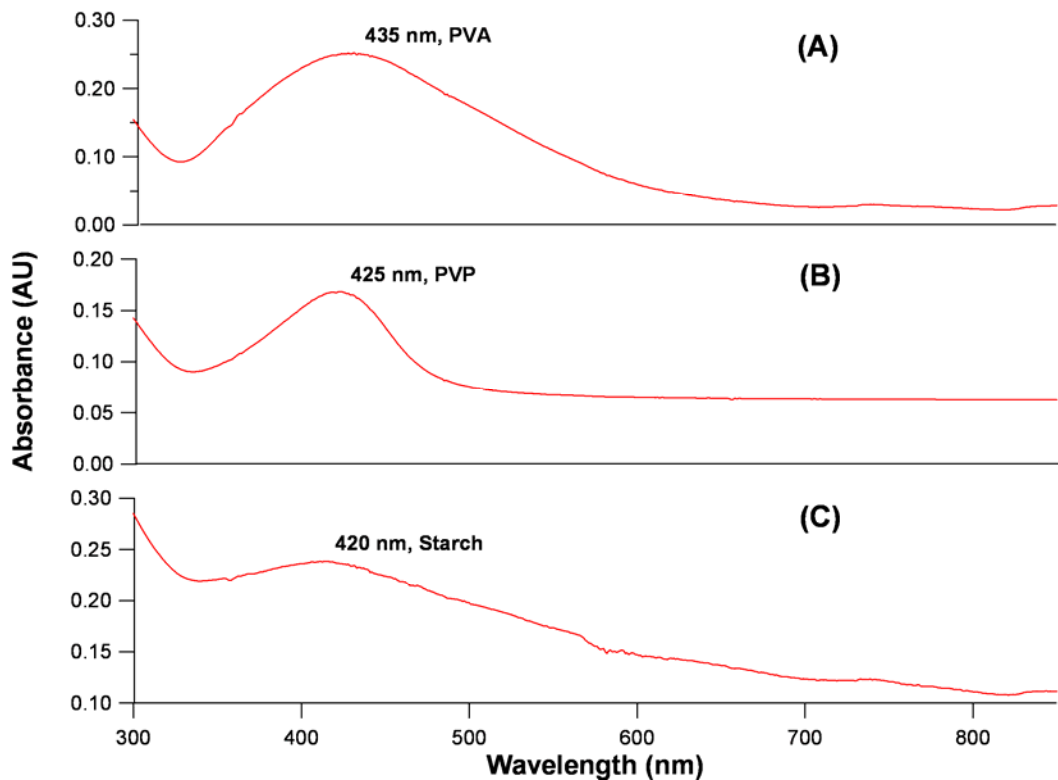


Figure 128 - UV-visible spectra of three silver nanoparticle solutions with different stabilizers. (A) PVA, (B) PVP, and (C) starch. Starch and PVA solutions were diluted to a quarter of their original concentration, for more accurate spectral acquisition.

The positions of the peak maxima attributed to the plasmon resonance of the silver nanoparticles differ with the stabilizer being used in the synthesis. Using PVA as the stabilizer produces the most red-shifted peak at ~ 435 nm (Fig. 128a). While PVP and starch stabilized solutions show shorter wavelength peak positions at ~ 425 nm and ~ 420 nm, respectively (Fig. 128b and 128c). It is recognized that an increase in the size of silver nanoparticles corresponds to a red-shift in the plasmon position^{36, 37} and it is tempting to draw conclusions as to the relative nanoparticle size in these solutions, *i.e.* the order of stabilized nanoparticle diameters PVA >PVP >starch, again consistent with TEM observations. On the

other hand, the effect of the dielectric strength of the stabilizer on the plasmon position must also be taken into account. If the dielectric constant of the medium surrounding the nanoparticle is reduced, the plasmon position is expected to blue-shift to shorter wavelengths.³⁴ This makes the comparison of particle size simply from plasmon positions less clear, as the dielectric strength and thickness of the stabilizer layers will vary between solutions. The strength of the stabilizer binding will also affect the growth of the nanoparticles. A stabilizer must bind strongly enough to stabilize the nanoparticles, however, an overly strong binding will act to inhibit further growth of the nanoparticles. These two competing factors will determine the final size of the nanoparticles formed.

Nevertheless, the size distribution of nanoparticles determined by TEM shows good agreement with the approximate size predicted from the UV-visible spectra. The order of average stabilized nanoparticle size, PVA>PVP>starch, observed in TEM concurs with the peak positions in the UV-visible spectra. The narrow nanoparticle size distribution of the PVP stabilized solution in the TEM results, in comparison to PVA, accounts for the narrower plasmon peak observed for the PVP solution compared to the PVA solution in the UV-visible spectra. The higher electron donating ability of the PVP leads to a stronger interaction with positively charged silver ions during the reduction and formation of the nanoparticles.³⁵ It is this effect that causes a narrow and more controlled nanoparticle size, and a lower nanoparticle concentration, as inferred from the lower plasmon intensity in comparison to the other two solutions. The starch stabilized solution would also be expected to show a similarly narrow plasmon

peak based on the TEM data. However, it is possible that slight nanoparticle aggregation or agglomeration due to the less stable nature of the starch solution leads to the broader plasmon peak observed.

The combination of high temperature, 80 °C, and a constant flow of hydrogen facilitates the reduction process and generation of silver nanoparticles and at the same time the gradual removal of the toluene phase from the reaction mixture by distillation. The aqueous-dispersed stabilizer then binds to the surface of the emerging nanoparticles thereby inhibiting agglomeration. It is considered that dissociated ligands are removed by co-evaporation with toluene, assisted by the flow of hydrogen through the reaction system and the elevated temperatures. Both ligands have a significant vapour pressure (6.8 mmHg for COD, 27 mmHg for hfac at 25 °C) which is likely to enable their gradual removal throughout the course of the reaction. A pure aqueous silver nanoparticle solution produced in this manner is therefore potentially suitable for medical or biological application, enabled by the use of non-toxic stabilizing agents demonstrated in this work. When the temperature is lowered to below 80 °C and the hydrogen flow reduced, it is found that a toluene phase is maintained in the reaction mixture. In these cases it is observed that a dark colour associated with the nanoparticles collects at the interface of the aqueous and toluene phases, leading to a lower intensity of plasmon absorption signal in the UV-visible spectra of the aqueous phase. This effect is caused by the preferential partitioning of nanoparticles to liquid-liquid interface, as has been previously documented.^{38, 39}

In summary, stable aqueous dispersions of silver nanoparticles have been produced by a novel method which allows silver to be converted from an organometallic precursor in an organic phase into nanoparticles in an aqueous phase, without the production of unwanted inorganic ions. Different stabilizers were found to subtly vary the size distribution of the nanoparticles. Control of reaction conditions, and modification of precursor and stabilizer design, may allow for improved control over size and size distribution of the nanoparticles. This method opens up a new pathway that allows organometallic precursor routes to be easily and simply applied to the production of aqueous dispersions of metal nanoparticles.

4.4.2.2 Sulfonated polystyrene synthesis and decoration with silver nanoparticles

The polymerisation reaction of styrene successfully resulted in a fine white powder. This was confirmed to be particulate by SEM (Fig. 129), which showed the powder to be microscopic polymer beads in a size range of ~ 0.5 to 3 μm . This small size range is ideal in that it allows TEM investigation to be easily performed without the need to microtome the particles (Fig. 130). EDX analysis performed as part of the TEM shows the presence of sulfur, confirming that the sulfonation reaction has been successful (Fig. 131).

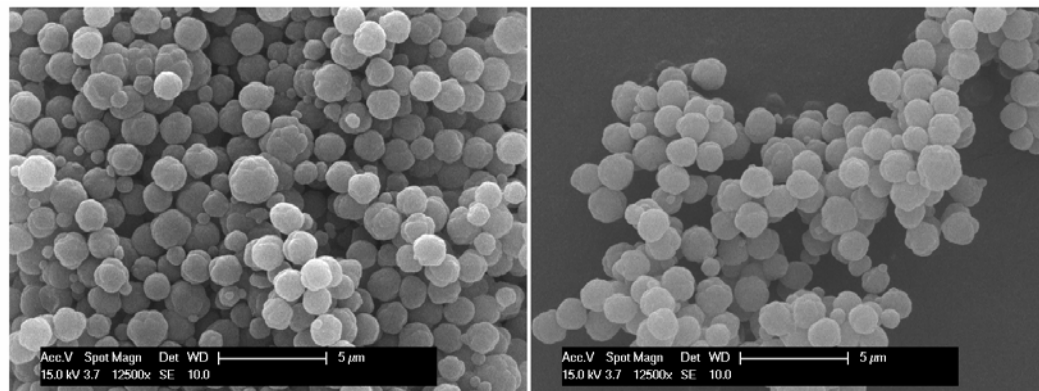


Figure 129 – Secondary electron SEM images of gold coated sulfonated polystyrene powder produced by emulsion polymerisation. Scale bars represent 5 µm.

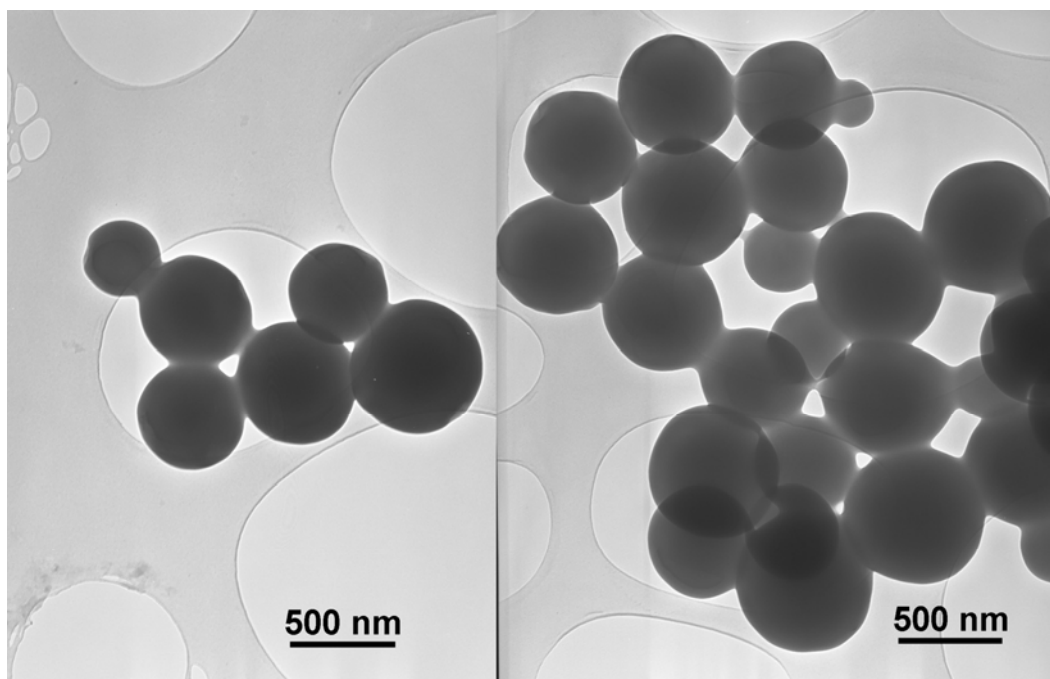


Figure 130 – Bright field TEM images of sulfonated polystyrene particles supported on holey carbon film. The scale bars represent 500 nm.

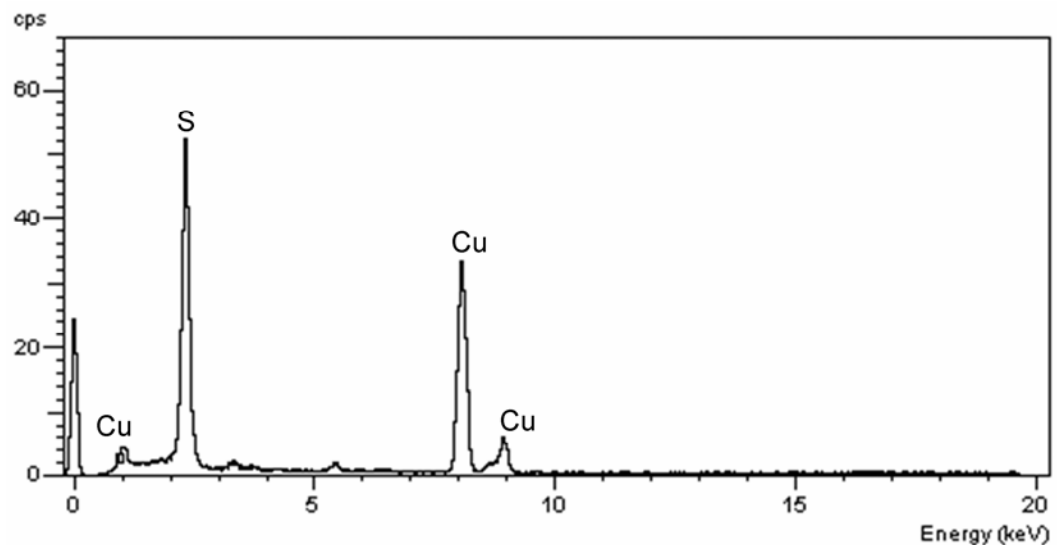


Figure 131 – EDX spectrum taken during TEM investigation of sulfonated polystyrene powder. Copper is present from the copper support grid used in the TEM.

After the sulfonated polystyrene was combined with aqueous silver nanoparticles, TEM was used to image the resulting powder. All of the polystyrene beads observed were coated in a dense and uniform layer of nanoparticles (Fig. 132). EDX of the beads detected the presence of silver, sulfur, and sodium (Fig. 133). Copper was detected as a result of the copper grids used to support the sample.

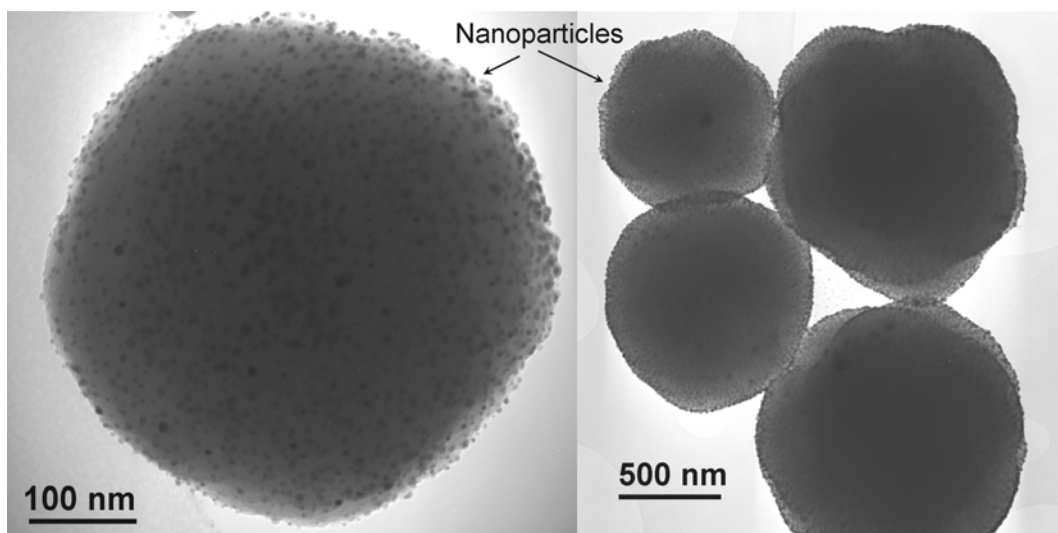


Figure 132 – Bright field TEM images of sulfonated polystyrene beads with a surface covering of silver nanoparticles. The scale bars represent 100 nm (left image) and 500 nm (right image).

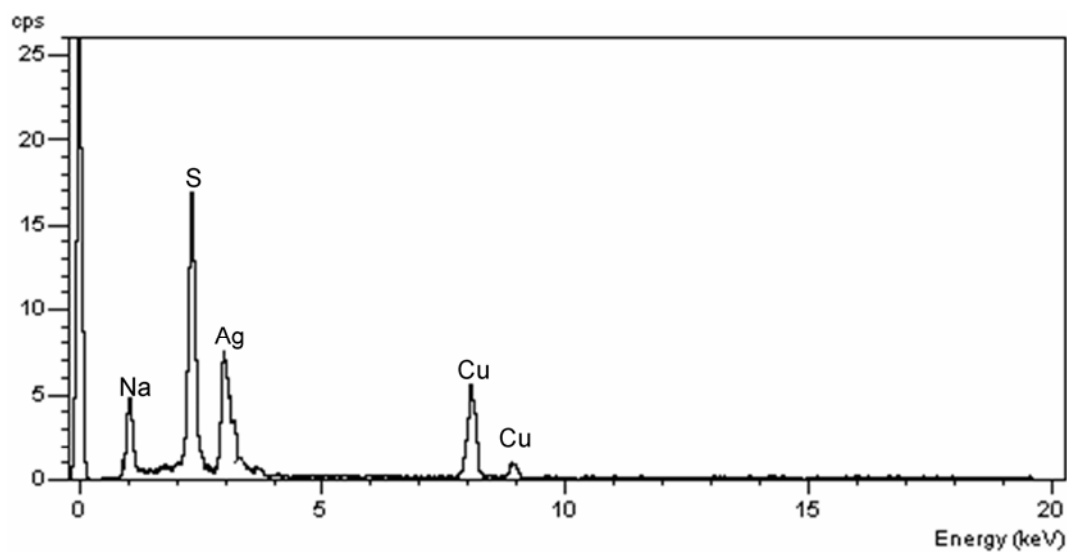


Figure 133 – Selected area EDX spectrum of a polystyrene bead with silver nanoparticle coating.

Interestingly, it was discovered during TEM analysis that the silver nanoparticles could be fused together by focusing the electron beam on a single

bead for a few minutes (Fig. 134). Though this phenomenon is not fully understood, it is likely that the ‘sintering’ of the silver is caused by a charging effect of the electron beam, either on the silver nanoparticles themselves or on the host polymer. This could potentially be used in a controlled manner to manipulate the plasmon response of the nanoparticles.

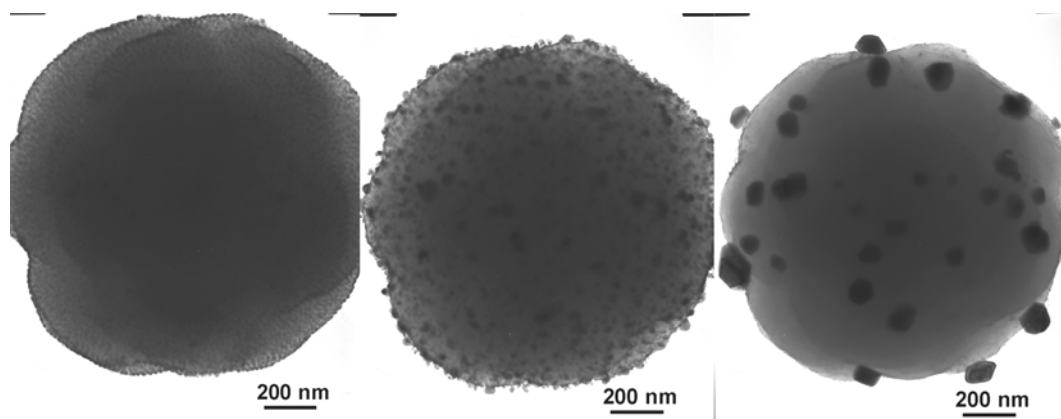


Figure 134 - Three bright field TEM images of the same polystyrene bead taken in succession from left to right. After the first picture was taken the electron beam was focussed at high current and positioned on the bead for 1 minute. After the second picture was taken the electron beam was again focussed similarly for 2 further minutes before the final picture was taken.

In summary, it has been shown sulfonation of conventionally synthesised polystyrene microspheres enables the simple attachment of silver nanoparticles. The morphology of the polymer powder has been fully investigated, and shown to be discrete spheres of the target size range. The sulfonation reaction has been confirmed by the EDX detection of sulfur, and the sulfonate groups appear to provide sufficient interaction with the silver nanoparticles to encourage their attachment to the surface.

4.4.3 Conclusions and future work

A novel route to stabilised silver nanoparticles in aqueous solution has been demonstrated. This provides an interesting alternative to existing routes as it introduces a large range of possible variations, by allowing organic soluble precursors to be used. The design of the ligands for the organic precursors can be easily changed, as can the choice of metal, and the choice of stabilising agent. The results of testing three different stabilising agents were investigated with respect to their effect on the nano-composition of the products. It was then shown that the silver nanoparticles produced by this method could be easily attached to the surface of a polystyrene powder by sulfonation. This is a simple and straightforward method that is easily scaleable and first reported here. The polymer-nanoparticle composite powder produced has been extensively investigated by electron microscopy, and the position of the silver nanoparticles has been confirmed to be at the surface. This surface-location of the silver makes this cheaply producible powder ideal for many applications, such as SERS, catalysis or antimicrobial functions.

The main advantages of both the silver synthesis method, and the method for its surface-attachment, are their versatility. Obviously this is an area that should be developed by future work. In terms of the aqueous nanoparticle route, it would be interesting to see what other metals or mixtures of metals could be produced. It would also be interesting to investigate a range of different ligand designs, reaction parameters, and stabilisers. As for the attachment of the particles to polystyrene by sulfonation, it would be significant to show that this same method

can be used for other solutions of nanoparticles. These could include silver nanoparticles produced by any of the other synthesis methods reported, even commercially available solutions, as well as gold nanoparticles. However, as well as demonstrating the transferability of these techniques, it is also important for future work to show the utility of the materials produced. There are of course a number of possible routes this could take, depending on the equipment and expertise available. For instance, the powder could easily be formed into a column to be tested for antimicrobial applications as water filter, or catalytic applications. Alternatively the polymer powder could be tested for potential effectiveness as a SERS enhancement material for the detection of low concentration analytes.

4.5 Supercritical Route

Hypothesis

Here is attempted a one-pot, one step synthesis of a silver-polymer nanocomposite in scCO₂. In this synthesis a scCO₂ soluble organometallic silver complex will be thermally decomposed in the presence of a reversible addition fragmentation chain transfer (RAFT) agent during a polymerisation reaction in which the RAFT agent should simultaneously stabilise the growing polymer microparticles and the formation of surface located silver nanoparticles. The products will be extensively characterised by electron microscopy. If successful, this novel route to the production of silver nanoparticle decorated polymer spheres is advantageous in that it is entirely free of conventional solvents.

4.5.1 Introduction

The nanocomposite material synthesised by this method should be similar in many ways to the one previously reported in this chapter. The target material still consists of polymer microspheres coated in silver nanoparticles. The surface location of the nanoparticles is important for their application, and the polymer functions as an effective support material. However, there are some important differences, and it is useful to compare these separate routes and consider them as complementary. The polymerisation reaction reported here is again a dispersion polymerisation, as was the one described in the previous section. Only instead of a styrene monomer and aqueous continuous phase, here we report the

polymerisation of MMA monomer in a scCO₂ continuous phase. The aqueous route reported is split into separate steps and uses conventional chemical techniques. The scCO₂ based route reported now consists of only one reaction step occurring in a single reaction vessel. The entire reaction also occurs in the absence of any conventional solvents. The absence of conventional organic solvents is preferential as it avoids the possibility of solvent residues, which would be disadvantageous for medical or bio-detection applications. In addition, scCO₂ is seen as a green alternative to conventional solvents because it is non-toxic and can be simply removed without leaving any residues in the material.⁴⁰⁻⁴²

RAFT polymerisation is a facile technique for the functionalisation of polymer chain ends that can produce narrow polydispersity products. RAFT polymerisation reactions have been recently performed in scCO₂⁴³⁻⁴⁵ and the technique has also been successfully applied to dispersion polymerisation.⁴⁶ Silver nanoparticles have also been synthesised in scCO₂ through the use of scCO₂ soluble precursors and stabilizing agents.^{47, 48} Here, we demonstrate that a scCO₂ soluble RAFT agent can be designed to fulfil two roles in a single reaction; polymerisation and stabilisation of polymer as well as stabilisation of silver nanoparticles. The RAFT agent is used as a non-migratory surfactant; it effectively grafts into the growing polymer particle by RAFT chemistry (see below), while a CO₂-philic segment acts as a polymeric stabiliser. Therefore, the RAFT moiety will always be located at the surface of the polymer particle. The RAFT agent also acts simultaneously to stabilise the formation of silver nanoparticles through favourable silver-sulfur interaction.^{18, 32} Because the silver nanoparticles are

attached to the RAFT agent, this directs the silver nanoparticles to the surface of the polymer where they are advantageously positioned for most applications. This will be explained in more detail later, but it is important to first explain RAFT polymerisation, and living polymerisations in general.

4.5.1.1 Living Polymerisation

RAFT is a specific form of what in general is known as ‘living’ polymerisation. Living polymerisation is a form of addition polymerisation where the ability of a growing polymer chain to terminate has been severely inhibited, which can be accomplished in a variety of ways. Termination step reactions are absent and the rate of the initiation is also much larger than the rate of propagation. The result is that the polymer chains grow at a more constant rate than seen in traditional polymerisation and their lengths remain very similar, i.e. they have a very low polydispersity index. This form of polymerisation is useful for the synthesis of block co-polymers, because a polymerisation can be carried out fully with one monomer, and then another monomer can be added afterwards to further add to the polymer chain. Additional advantages are controllable molar mass and control over end-groups.

Living polymerisation was first reported in 1956 by Szwarc, who described the anionic polymerisation of styrene with an alkali metal / naphthalene system in THF.^{49, 50} He found that after addition of monomer to the initiator system that the increase in viscosity would eventually cease but that after addition of a new amount of monomer after some time the viscosity would start to increase

again. However, most of the initial applications of living polymerisation were successful only in anionic systems. Whilst a large amount of ‘living’ character was observed, anionic systems have limited commercial uses due to stringent reaction conditions and limited choice of monomers.

However, late in the twentieth century several new methods were discovered which allowed the development of living polymerization using free radical chemistry.⁵¹⁻⁵⁵ Radical polymerisation is one of the most widely used processes for the commercial production of high molecular weight polymers. The emergence over the last ten years of techniques for implementing living radical polymerisation has provided a new set of tools for polymer chemists that allow very precise control over the polymerisation process while retaining much of the versatility of conventional radical polymerisation. The living radical polymerisation techniques that are receiving greatest attention are nitroxide-mediated polymerization, atom-transfer radical polymerisation, and RAFT.⁵⁶ Most of these methods are beyond the scope of this thesis to describe, except for RAFT,⁵⁷⁻⁶⁰ which is now briefly outlined.

4.5.1.2 Reversible addition-fragmentation chain transfer – (RAFT)

RAFT is a method for the synthesis of living radical polymers that uses thiocarbonylthio compounds ($ZC(=S)SR$), such as dithioesters, dithiocarbamates, trithiocarbonates, and xanthates in order to mediate the polymerisation via a reversible chain-transfer process. This allows access to polymers with low polydispersity and high functionality. RAFT also allows for the production of

complex architectures such as block, star, graft, comb, and brush co-polymers. RAFT is also known for its compatibility with a great variety of monomers. However, vital and universal for this process is the addition of a small amount of thiocarbonylthio compound (Fig. 135) to monomer and initiator during polymerisation.

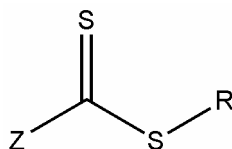


Figure 135 – General formula for thiocarbonylthio compounds used in RAFT systems. The R group has to be a better leaving group in comparison with the growing chain, whilst the Z component influences the stability of the thiocarbonyl-thio radical intermediate.

The RAFT agent is susceptible to attack from radical moieties, be they initiator fragments or growing polymer-radical chains. The growth of the polymer is then regulated by the equilibrium of chain transfer agent between dormant polymer chains at high concentration and growing radical chains at low concentration (Fig. 136). The mechanism is described as it is reported by Moad *et al.*⁵⁶, an expert in this field.

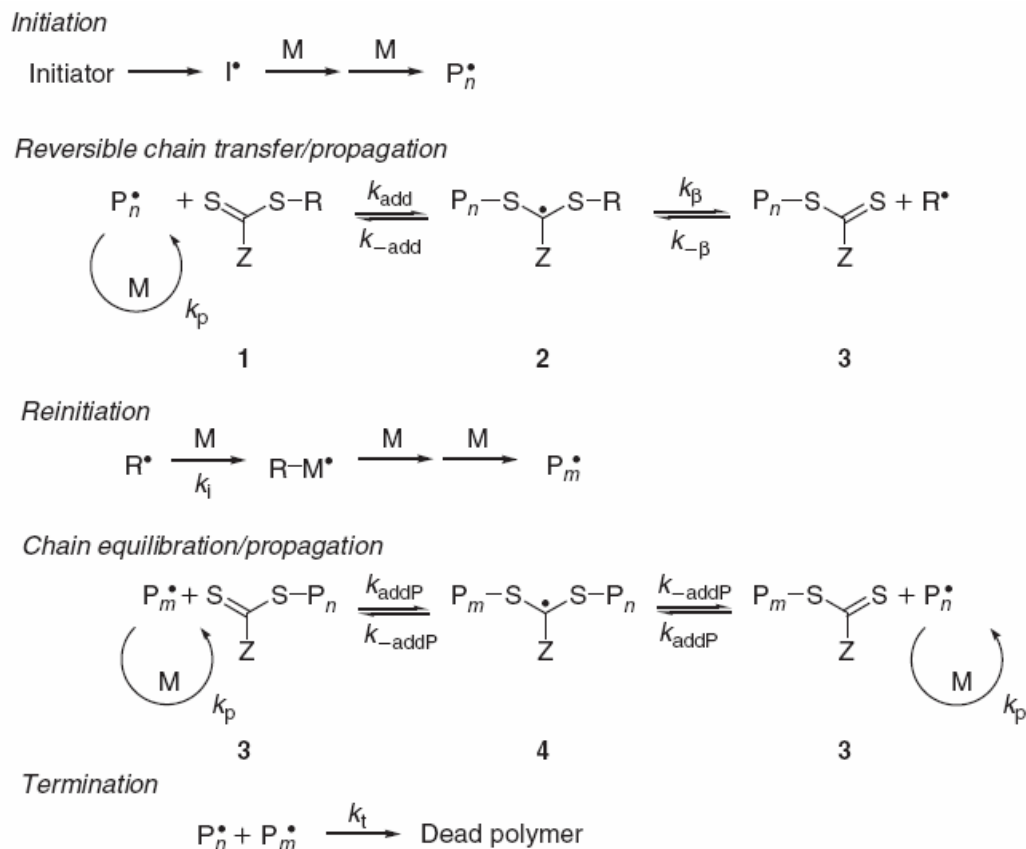


Figure 136 – Mechanism of RAFT polymerisation, see text for details.⁵⁶

Like all radical polymerisations, the reaction is started by the generation of a radical species (I^\bullet), liberated by the decomposition of the initiator (I), which then reacts with monomer units (M) to form a growing polymer chain (P_n^\bullet) (Fig. 136, *initiation*). The initiation and radical–radical termination occur as they would in conventional radical polymerisation. The propagating polymer radical (P_n^\bullet) can add to the $\text{C}=\text{S}$ bond of the RAFT chain transfer agent (1) (k_{add}) to form a radical intermediate (2). This intermediate is in equilibrium and may return to form the initial polymer growing chain (k_{-add}) or the macro chain-transfer agent (3) (k_β) and reinitiating group (R^\bullet) (Fig. 136, *Reversible chain transfer/propagation*). The R^\bullet

group can re-initiate the polymerisation process by reacting with monomer (k_i) to form another propagating radical species (P_m^{\bullet}) (Fig. 136, *Reinitiation*) or react back with the macro chain-transfer agent (k_{β}). After the initial amount of chain transfer agent has been exhausted, the reaction enters equilibrium (Fig. 136, *Chain equilibrium/propagation*). This equilibrium, between the active propagating radicals (P_n^{\bullet} and P_m^{\bullet}) and the dormant polymeric thiocarbonylthio compounds is regarded as the main RAFT polymerisation equilibrium and ensures a rapid exchange of active and dormant thiocarbonyl-thio capped chains. By this exchange method, equal probability is given for all chains to grow thus leading to the characteristic narrow chain polydispersity. Whilst living radical polymerisation seeks to limit termination, the inevitable combination and disproportionation termination reactions that occur in all free radical polymerisations still occur (Fig. 136, *Termination*). When the polymerisation is complete, or stopped, most chains retain the thiocarbonylthio end group and can be isolated as stable materials.

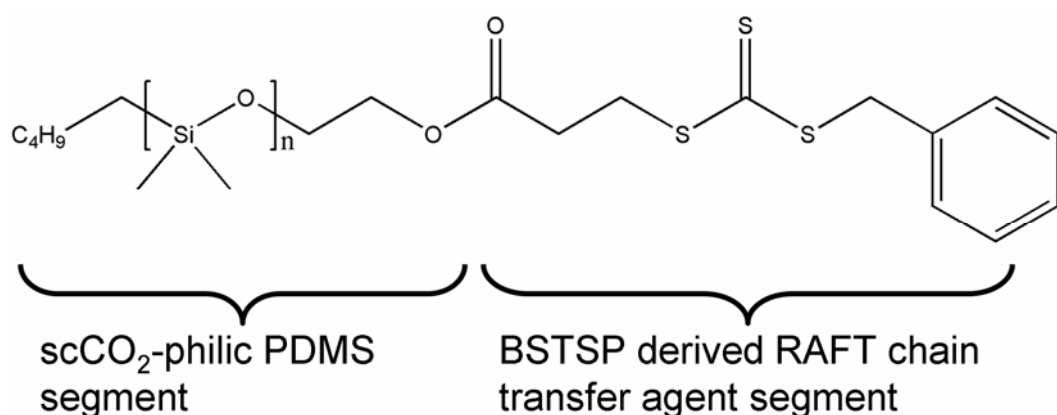


Figure 137 – The structure of the chemical agent used in this work, designed to act as both a stabilising agent and RAFT chain transfer agent simultaneously.

The RAFT agent utilised in this work (Fig. 137) is formed from the combination of polydimethylsiloxane (PDMS) and benzylsulfanylthiocarbonylsulfanylpropionic (BSTSP) acid to form a PDMS-RAFT agent (full synthesis details are given in Chapter 5.3.7). This RAFT agent has been chosen to function in two roles in the polymerisation, both as a chain transfer agent, and as the stabiliser for the polymerisation. The reaction to be performed with this RAFT agent is the polymerisation of MMA in scCO₂. This is a dispersion polymerisation, the MMA monomer is soluble in the scCO₂, but as would be expected, when the PMMA chains become too long they will become insoluble in the scCO₂ (see Chapter 1.5.2.1). Some form of stabilising agent is therefore required, in order to keep forming particles of polymer suspended in the scCO₂ to allow the reaction to continue, and more monomer to be transported to the growing polymer. PDMS is a good stabiliser for PMMA in scCO₂. This is because PDMS has a high affinity for scCO₂ because of the Si and O atoms in the polymer backbone. The affinity for CO₂ of the PDMS moiety will position the RAFT agent on the surface of the growing polymer, as well as ensuring effective stability of the growing polymer particle. The full RAFT mediated synthesis in scCO₂ should therefore lead to the synthesis of PMMA spheres, the PMMA chains of which are terminated with RAFT-PDMS agent. What is significant is that this positions the thiolated moiety at the surface of the polymer beads (Fig. 138). It should be noted that the RAFT is not intended to be used here as a radical control agent, but merely as a means to provide surface functionalisation of the polymer particle. Indeed, it is well known that trithiocarbonates of the form used in this

work, are poor mediating agents for MMA polymerisations. However, if this can be shown to be successful then future work can begin designing new macro-RAFT agents that will more accurately control the polymer molecular weight.

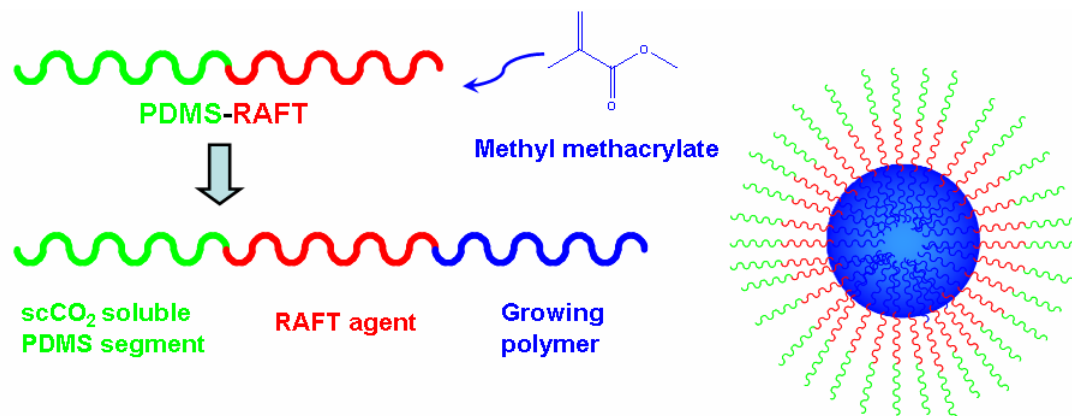


Figure 138 – Schematic representation of how the PDMS-RAFT agent incorporates into the forming polymer particle, with the RAFT-PDMS attached to the PMMA and at the surface of the polymer. The right image depicts a PMMA spherical particle (blue), with the PDMS surfactant extending out into the scCO₂ phase.

4.5.1.3 Silver nanoparticle reduction and stabilisation

The electron rich sulfur groups of the BSTSP acid moiety are attracted to the electron deficient surface of the growing silver nanoparticles, providing *in situ* stabilisation. However, the BSTSP moiety is itself attached to PDMS, which has good solubility for scCO₂. The BSTSP-PDMS can therefore be thought of as an ideally designed stabiliser for silver nanoparticles in scCO₂. When this is

combined with the silver feed-stock Ag(hfac)COD precursor, which we have already shown has good solubility in scCO₂, then this means the entire silver nanoparticle generation and stabilisation can occur in scCO₂. The synthesis of scCO₂ soluble silver nanoparticles is a relatively new field, with only two published papers.^{47, 61} These papers report early developments, intending to take advantage of the useful properties and environmentally benign nature of CO₂ for silver nanoparticle synthesis. The properties of scCO₂ such as solvent tune-ability, zero surface tension, and ease of solvent removal, make it ideal for use in many metal deposition processes for the fabrication of nanomaterials. The synthesis of silver nanoparticles reported here is relatively simple, the Ag(hfac)COD is decomposed by heat to form nanoparticles which are stabilised by the RAFT agent (Fig. 139). However, when this is combined with the polymerisation process simultaneously, it results in the direction of the nanoparticles to the surface of the polymer, according to the mechanism of the RAFT polymerisation.

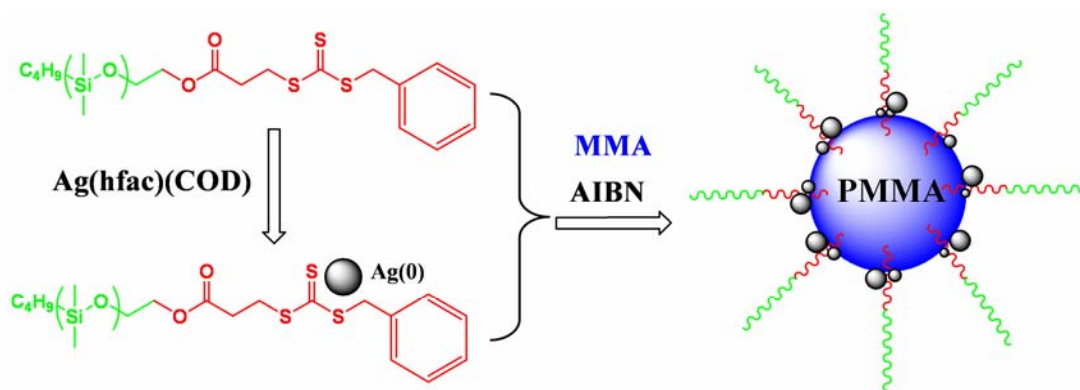


Figure 139 – Schematic showing how the presence of the RAFT agent during decomposition of Ag(hfac)COD can stabilise the formation of the silver nanoparticles, left. If monomer and initiator are also present then a polymerisation reaction will occur simultaneous to this, incorporating the RAFT and silver nanoparticles into the surface of the forming polymer spheres, right.

4.5.1.4 Reaction procedure

An overview of the procedures used for the reactions presented here is now given, for a more technical description see chapter 5.3.7. Silver nanoparticle and polymer synthesis reactions were first performed separately to ensure both worked successfully in the presence of RAFT stabiliser.

The synthesis of silver nanoparticles in the absence of polymer was performed as follows. The silver precursor and PDMS-RAFT agent were simply placed in the autoclave, which was then flushed with CO₂ before being heated and pressurised. The reaction was maintained at these conditions until completion being cooled to room temperature and depressurised. Chloroform was then added as solvent to disperse and remove PDMS-RAFT stabilised silver nanoparticles as a transparent brown solution. Chloroform was chosen as the dispersing medium because of the very high solubility of PDMS in this solvent. The Ag(hfac)(COD) and PDMS-RAFT used in the synthesis of these nanoparticles are both readily scCO₂ soluble. The Ag(hfac)(COD) acts as the silver feedstock as it is thermally decomposed during the reaction to yield elemental silver. As the silver nanoparticles are formed, they are stabilised by the PDMS-RAFT that is dissolved in the scCO₂.

Polymer microparticles were formed by dispersion polymerisation in scCO₂. The PDMS-RAFT agent and AIBN initiator were added to the autoclave and flushed with CO₂. Degassed MMA monomer was then added under a slightly positive flow of CO₂ in order to prevent the ingress of oxygen into the system. The

autoclave was then brought up to the required temperature and pressure, under agitation, and left for the remainder of the reaction. After this time the vessel was cooled to room temperature and the CO₂ vented.

The reactions to produce silver-polymer nanocomposites were performed in the same method as the separate reactions, except they were performed simultaneously in the same vessel. The reactions were performed under identical conditions to the polymer synthesis except that Ag(hfac)COD was added to the autoclave along with the other reactants.

4.5.2 Results

4.5.2.1 Nanoparticles synthesised independently

The product formed in the nanoparticle synthesis reaction is a transparent brown coloured stable solution. TEM investigation of this solution (Fig. 140) showed silver nanoparticles mostly of 5-20 nm in size. Brown colouration is characteristic of the plasmon resonance absorption of silver nanoparticles. As the TEM micrographs show little agglomeration of the nanoparticles, it can be assumed that stabilisation by PDMS-RAFT is very effective. EDX performed in the area of the nanoparticles detects silver from the nanoparticles, but also sulfur, suggesting that the RAFT agent is present.

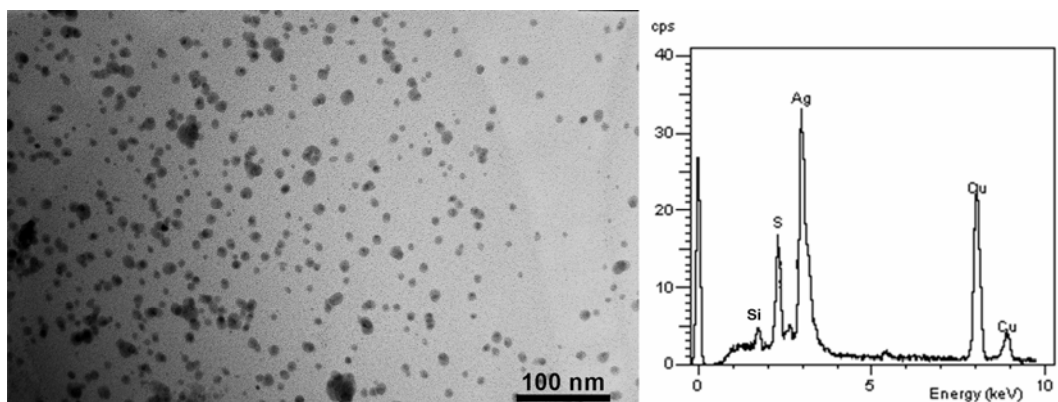


Figure 140 – Bright field TEM image of PDMS-RAFT stabilised silver nanoparticles, left, and EDX spectrum, right, showing the presence of silver and sulfur.

4.5.2.2 PMMA powder synthesised independently

The product of the polymerisation reaction was a free-flowing, off-white powder. SEM investigation of this powder (Fig. 141) shows discrete spherical particles of $\sim 1\text{-}4\ \mu\text{m}$. This polymer product in the morphology expected from the theory, suggesting that the stabilisation in scCO_2 is working effectively. After the polymer powder and silver nanoparticles had both been successfully synthesised in scCO_2 , these two separate processes were combined into a single reaction.

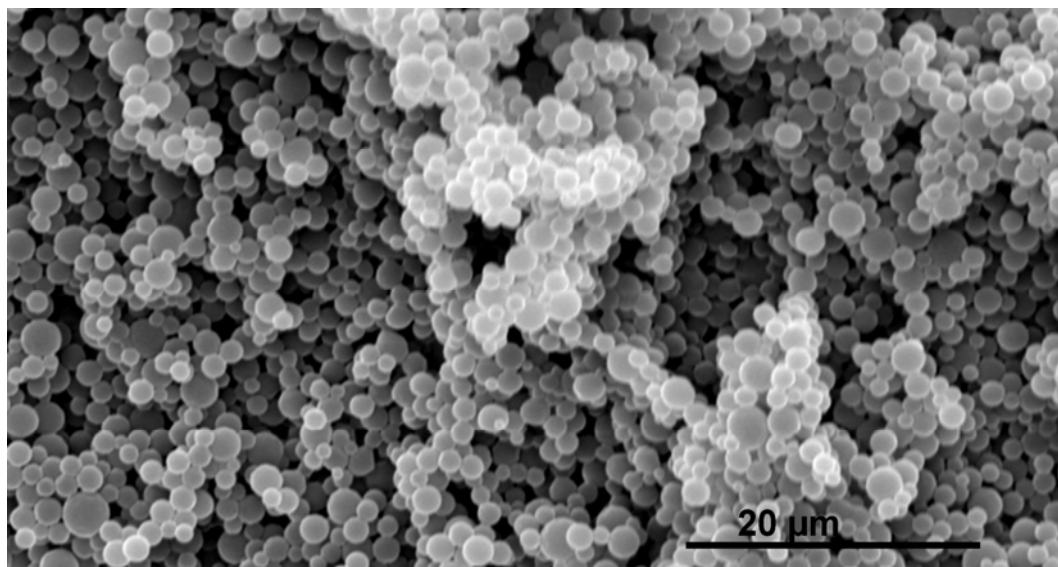


Figure 141 – Secondary electron mode SEM image of PDMS-RAFT stabilised PMMA particles.

4.5.2.3 Silver nanoparticle and PMMA combined synthesis

The combined reaction resulted in the production of a fine free-flowing brown powder. SEM investigation showed discrete sphere polymer morphology indicating that the inclusion of silver has no significant adverse effect on the polymerisation reaction (Fig. 142). Molecular weight analysis was performed by GPC using THF as eluent (Table 7). The molecular weight and polydispersity of the PMMA product formed both with and without silver precursor were similar.

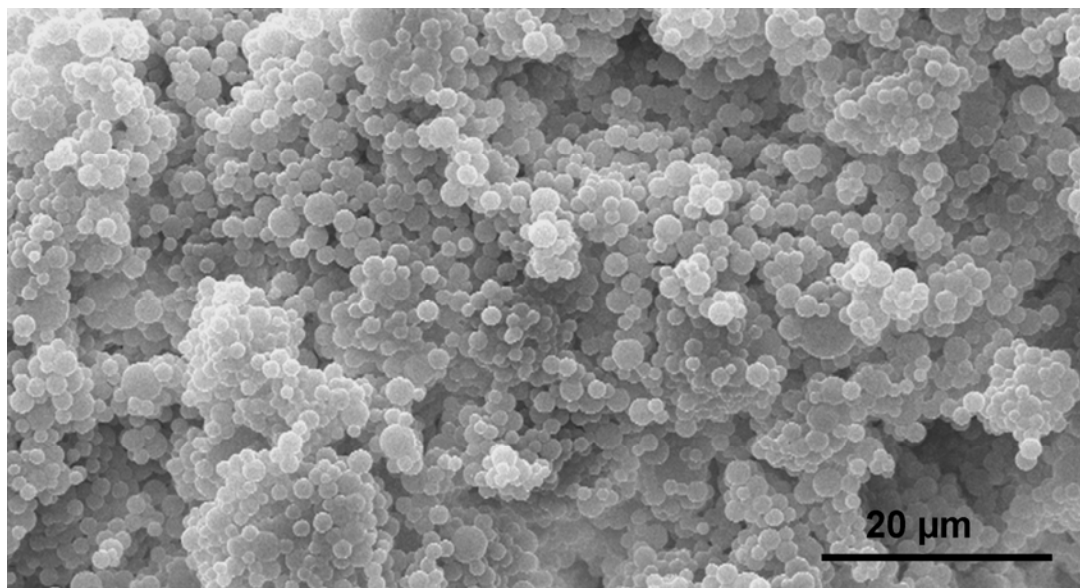


Figure 142 - Secondary electron mode SEM image of powder synthesised in a combined PMMA and silver nanoparticle synthesis.

Table 7 – GPC comparison of pure PMMA and PMMA synthesised with silver nanoparticles.

	M_n / kDa	M_w / kDa	PDI
Pure polymer	48	142	2.9
Silver-Polymer nanocomposite	41	130	3.1

Note that to obtain the GPC data of the polymer after processing to form silver nanoparticles, it was necessary to pass these down GPC columns. Even after dissolution in a very good solvent for both PDMS and PMMA (i.e. chloroform), intense sonication and then ultracentrifugation, we could not separate the silver from the polymer. This underscores the very strong interaction between the RAFT moiety and the silver nanoparticles.

TEM investigation revealed silver nanoparticles coating the surface of the polymer spheres (Fig. 143). This implies that the PDMS-RAFT surfactant was successful in simultaneously stabilising the growing polymer particle and the silver nanoparticles. The presence of silver in the polymer particles was confirmed by EDX analysis (Fig. 144).

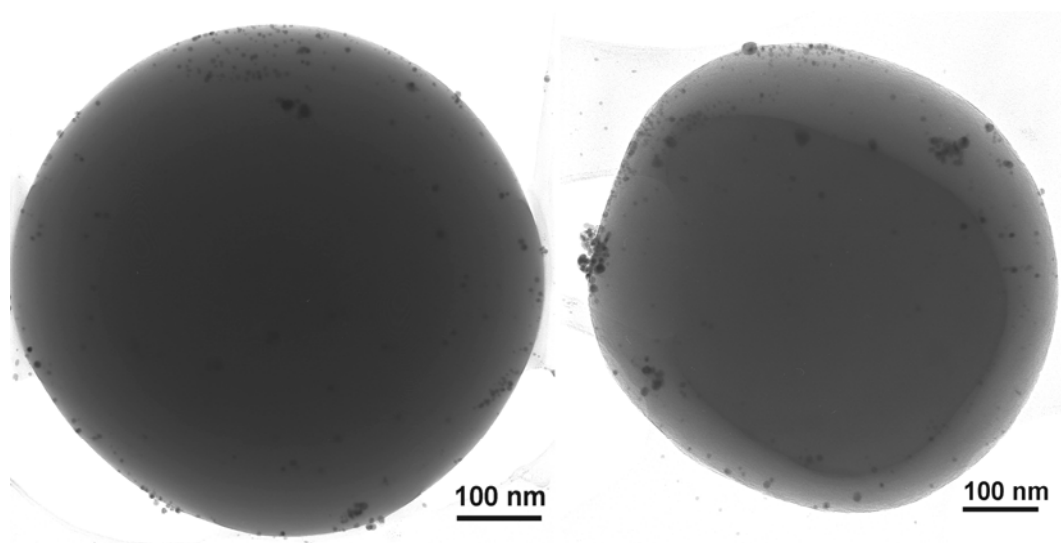


Figure 143 – Bright field TEM micrographs of PMMA beads coated in silver nanoparticles. The scale bars represent 100 nm.

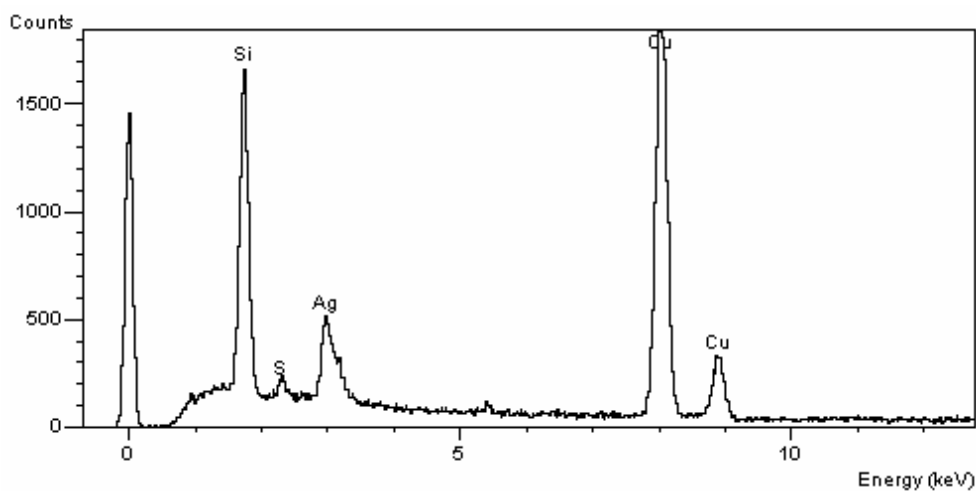


Figure 144 – EDX spectrum taken of a silver nanoparticle coated PMMA bead in TEM observation. Note the presence of sulfur and silica from the RAFT agent and silver from the nanoparticles.

Closer inspection of the particle surface reveals that the silver nanoparticles are tightly bound to the surface of the polymer particle (Fig. 145). Indeed, the TEM micrographs show that the nanoparticles generally appear to be partly embedded into the polymer surface (Fig. 146, right). This apparent strong attachment to the polymer particle surface is advantageous as it would imply minimal nanoparticle loss in applications where some friction of particles is required. All of the nanoparticles observed were within the appropriate size range for favourable applications. All lie within 3-30 nm in diameter with the majority occurring in the 5-20 nm range.

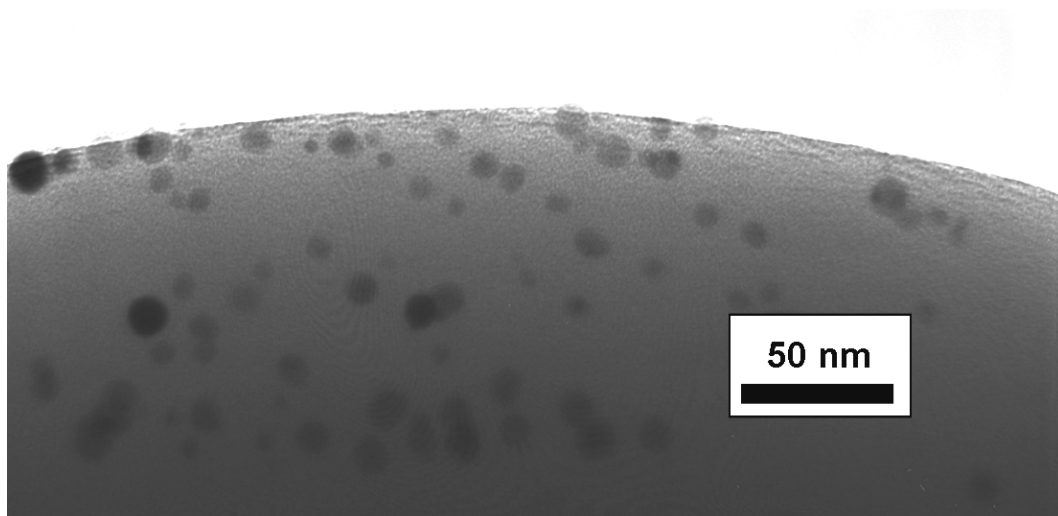


Figure 145 – Bright field TEM micrograph of the edge of a silver nanoparticle coated PMMA bead. Scale bar shows 50 nm.

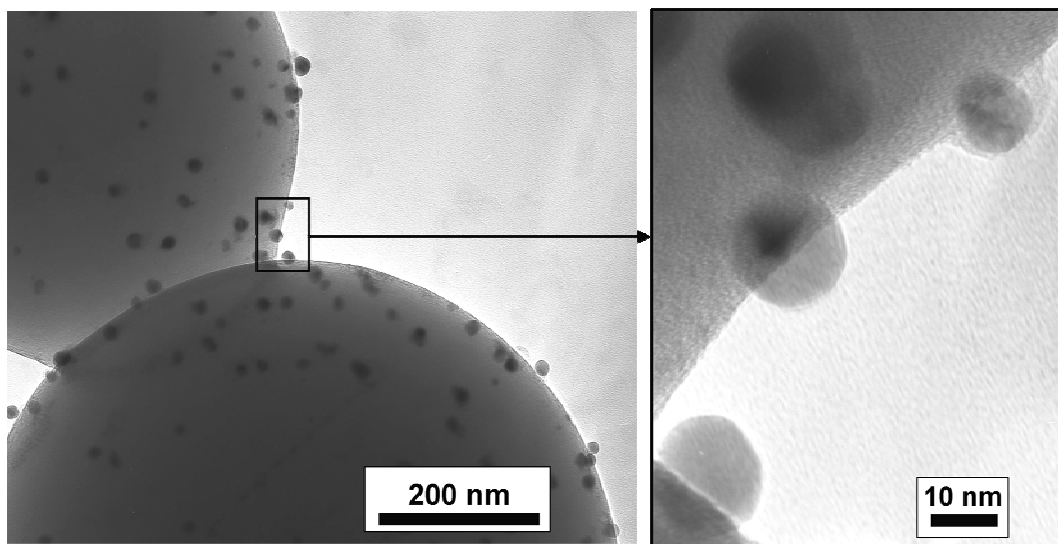


Figure 146 – Bright field TEM image demonstrating the surface location of the silver nanoparticles on the polymer beads. Scale bars show 200 nm, left, and 10 nm in the enlarged image, right.

We believe that the silver nanoparticles are located only on the surface of the polymer particles. This is especially evident during TEM microscope operation. However, it could be argued that from the TEM images, some nanoparticles are observed to be inside the beads. To refute this it must be noted that the samples for TEM characterisation were prepared by depositing complete polymer spheres on the TEM grids. In other words, these are not cross sections, so we see 2-D images of the 3-D spheres. Many nanoparticles can be seen on the ‘edges’ of the sphere, and are obviously surface located. The observer can also notice nanoparticles that appear to be further towards the centre of the polymer sphere, but this is merely because the image is produced by looking through the whole sphere, nanoparticles on the ‘top’ and ‘bottom’ of the sphere are being observed (Fig. 147). What is important to note is that the concentration of nanoparticles can be seen to remain roughly constant across the image of the sphere. This is consistent with

nanoparticles residing on the surfaces and the observer looking through two sphere surfaces. If the nanoparticles were located inside the polymer sphere then the concentration of nanoparticles that one observed would be significantly higher when viewed away from the edge further towards the centre of the sphere. This is because, if nanoparticles were located extensively throughout each polymer sphere, then the area of polymer being imaged through is very relevant. Under these circumstances, one would expect that near the ‘edge’ should have very few nanoparticles observed and the majority of the particles would be observed towards the centre and away from the edge. This is clearly not the case.

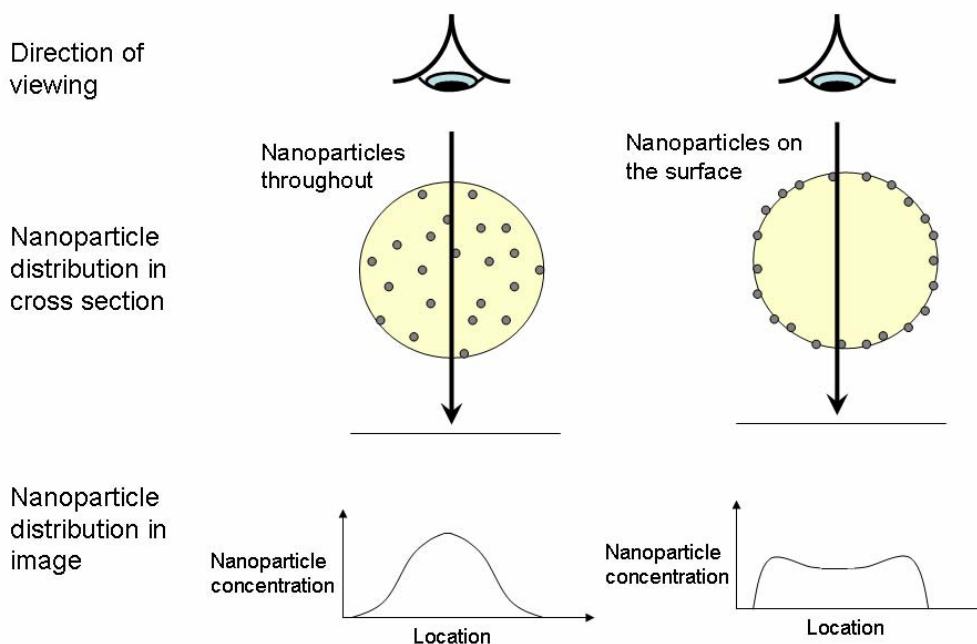


Figure 147 – Schematic representation of how the distribution of nanoparticles in a sphere affects the appearance of the nanoparticles in an image created by viewing through the sphere.

The electron microscopy effectively confirms the structure of the nanocomposite products to be in agreement with that expected from the reaction design. It can therefore be inferred that the RAFT-stabilising agent is functioning as expected, not only to stabilise the silver and PMMA, but also to graft into the PMMA itself. We ran ¹H NMR of both the PDMS-RAFT macroRAFT agent and the nanocomposite polymer. The NMR spectrum for the polymer-silver nanocomposite is shown with an expansion of the region between 4.2 ppm and 4.8 ppm (Fig. 148). The absence of the singlet signal at 4.63 ppm for the methylene protons of the benzyl group of the RAFT agent shows that the stabiliser has been grafted into the polymer through the RAFT agent. The singlet methylene protons adjacent to the benzyl group of the RAFT agent (4.63 ppm) were evident in the PDMS-RAFT agent. Upon reaction with MMA, this peak disappears from the NMR spectrum because it is no longer adjacent to the trithiocarbonate moiety of the RAFT. This analysis concisely shows that the PDMS-RAFT is grafting into the polymer particle.

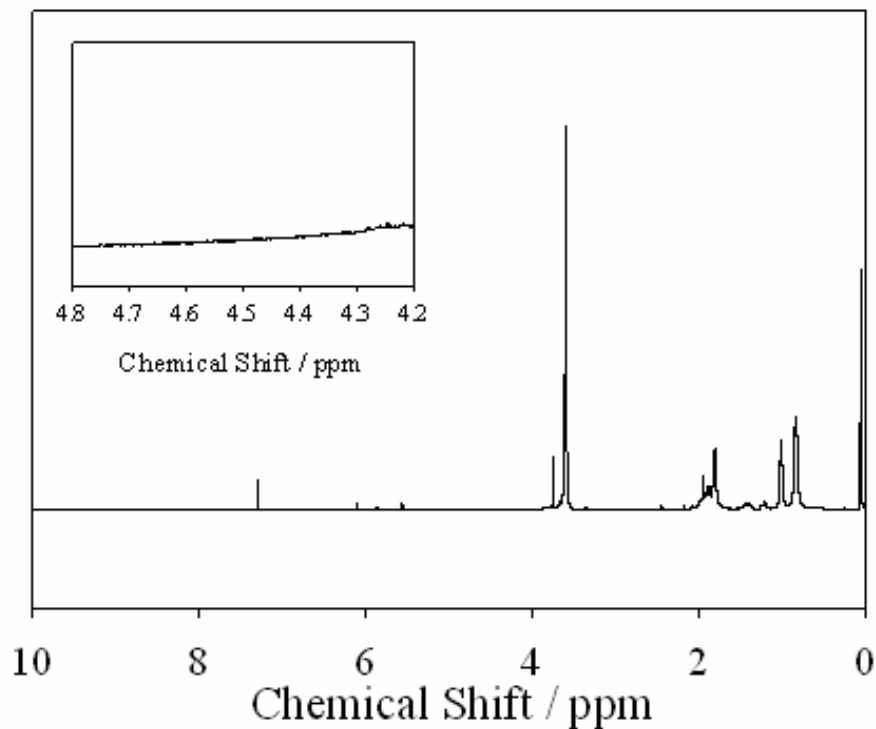


Figure 148 – ^1H NMR spectrum of the polymer product showing the absence of the singlet methylene signal at 4.63 ppm.

4.5.2.4 Concentration of $\text{Ag}(\text{hfac})\text{COD}$

The concentration of the silver precursor in the reaction was investigated to determine how this affected the silver loading of the products. This was achieved experimentally by increasing the amount of $\text{Ag}(\text{hfac})\text{COD}$ reagent from 100 mg, 200 mg, 400 mg and 800 mg, whilst keeping all other reagents and conditions constant. Immediately it was observed that an increase in the concentration of $\text{Ag}(\text{hfac})\text{COD}$ made the shade of brown in the nanocomposite polymer samples darker (Fig. 149).



Figure 149 – Photograph of silver nanocomposite samples containing (left to right) 100 mg, 200 mg, 400 mg and 800 mg Ag (hfac) COD.

The SEM and TEM images of samples reported above were for 200 mg silver precursor reactions. To allow comparison, similar electron microscopy images and discussion for the 100 mg, 400 mg and 800 mg samples are reported here:

100 mg Ag (hfac) COD:

The 100 mg Ag(hfac)COD sample showed a similar or slightly smaller amount of nanoparticles on the surface in comparison to 200 mg (Fig. 150, left). There was no observable difference in the polymer morphology (Fig. 150, right).

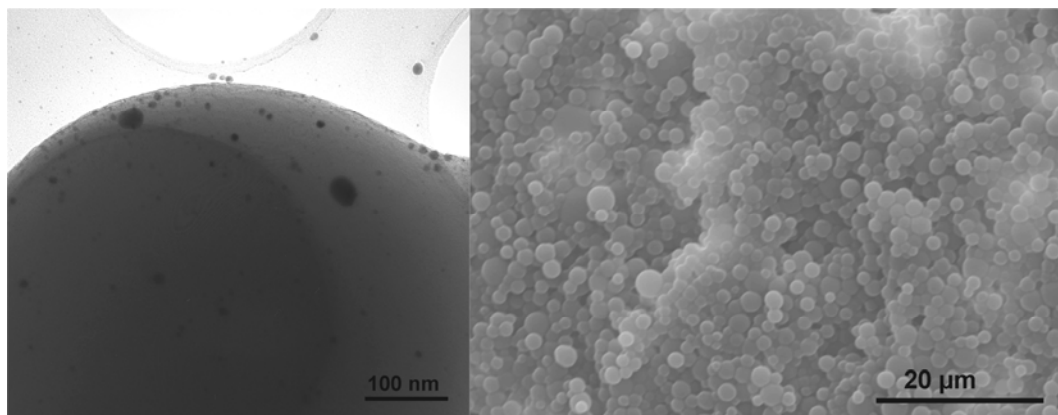


Figure 150 – Bright field TEM, left, and secondary electron mode SEM, right, observation of a sample produced with 100 mg of silver precursor. Scale bars show 100 nm, left, and 20 μm, right.

400 mg Ag(hfac)COD:

The sample produced with 400 mg of silver precursor showed a definite increase in the amount of nanoparticles on the surface, in comparison with the 100 mg and 200 mg samples (Fig. 151, left). However, signs of particle deformation in the morphology begin to appear (Fig. 151, right). The polymer beads have become sometimes distorted, enlarged or merged, although discrete spherical beads can still be discerned.

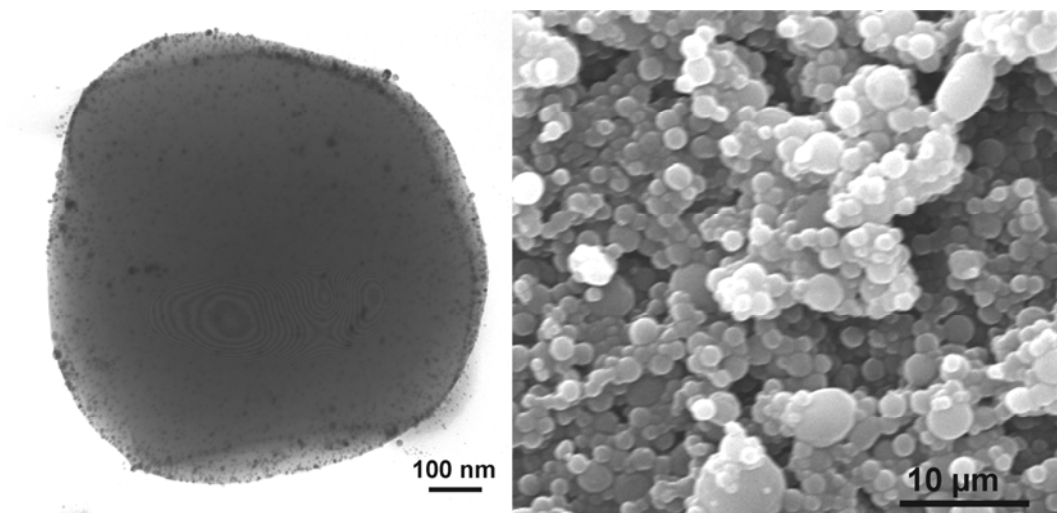


Figure 151 - Bright field TEM, left, and secondary electron mode SEM, right, observation of a sample produced with 400 mg of silver precursor. Scale bars show 100 nm, left, and 10 μm , right.

800 mg Ag(hfac)COD:

The sample produced with 800 mg silver precursor showed a further increase in the amount of nanoparticles on the surface in comparison to 400 mg (Fig. 152, left). However the polymer morphology is now completely deformed (Fig. 152, right). There are now very few discrete polymer spheres observed in SEM, only large coagulated masses of polymer. TEM was made possible by sonicating the polymer in methanol to disperse any smaller particles prior to deposition onto a carbon grid.

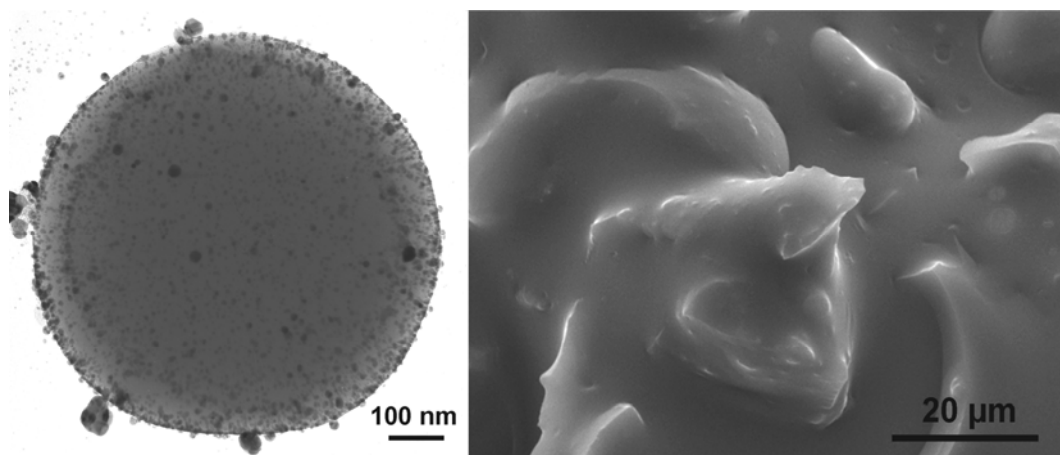


Figure 152 - Bright field TEM, left, and secondary electron mode SEM, right, observation of a sample produced with 800 mg of silver precursor. Scale bars show 100 nm, left, and 20 μm, right.

In summary, whilst 800 mg Ag(hfac)COD provides the largest amount of nanoparticles on the surface, it also results in the most deformed polymer formation. This may be due to the PDMS-RAFT failing to stabilise both nanoparticle and polymer. It is possible that when the attachment of silver nanoparticles to the RAFT agent may inhibit its function in the stabilisation of the polymer, therefore too high a loading of silver compared to the amount of RAFT is disadvantageous. However, at lower concentrations of silver the reaction appears to be successful, and therefore a compromise between silver loading and polymer stabilisation must be chosen.

4.5.3 Conclusions and future work

The use of an appropriately designed RAFT-stabilising agent allows simple and effective synthesis of polymer microspheres decorated with silver nanoparticles in CO₂. The surface location of the nanoparticles gives the polymer powder excellent potential for catalytic, antibacterial and biosensing applications. This synthetic route has the additional advantages of being a single step, one pot reaction that does not require conventional solvents at any stage during the process. The single step and single reaction vessel nature of the process make it appealing from an industrial point of view, in terms of cost of production and scalability. The absence of conventional solvents is highly desirable especially for medical or biosensing applications as there is no chance of contamination by trapped harmful solvents. Furthermore, the versatility of this technique suggests its applicability for a wide range of polymer nanoparticle composite materials.

In terms of future work, the most obvious next step is the redesign of the RAFT agent in order to obtain the narrow control of polydispersity associated with RAFT polymerisation. This could easily be completed by an analysis of the literature to select a range of RAFT agents known to be effective for an associated range of monomers. Following this the chosen RAFT agents should be grafted to suitable CO₂ soluble stabilising agents, such as PDMS. The effectiveness of such a range of RAFT agents could then be evaluated on a wider range of monomers, as well as for their potential to control polydispersity. Finally, the potential of the products of this synthesis for applications should be tested.

4.6 Overall conclusions

Two alternative and complementary synthesis routes to silver nanoparticle decorated polymer microspheres have been reported. The products of these reactions have been extensively characterised by electron microscopy. This has shown that the products have a nanocomposite structure ideal for many applications. Both of the routes could be seen as general synthesis strategies as they have the potential to be transferred to a wide range of polymer systems, and could be used not only with silver nanoparticles but also other noble metals. Neither route contains any problematically complex or expensive steps that would be a barrier to scale up or industrial use. The first route reported has the advantage that it can be easily used with conventional ‘bench-top’ equipment and would be applicable for many systems. However, for delicate systems such as medical or fine detection applications where it is especially important to avoid any contaminating solvents in the polymeric products, the scCO₂ route is preferable. Although this route requires high pressure equipment, it also has an industrial advantage of being ‘green’ and in avoiding the costs normally associated with the removal and disposal of waste solvents.

4.7 References

1. J. Z. Guo, H. Cui, W. Zhou and W. Wang, *Journal of Photochemistry and Photobiology a-Chemistry*, 2008, **193**, 89-96.
2. N. R. Jana, T. K. Sau and T. Pal, *Journal of Physical Chemistry B*, 1999, **103**, 115-121.
3. A. Murugadoss and A. Chattopadhyay, *Nanotechnology*, 2008, **19**.
4. H. Rashid and T. K. Mandal, *Journal of Physical Chemistry C*, 2007, **111**, 16750-16760.
5. N. Pradhan, A. Pal and T. Pal, *Colloids and Surfaces a-Physicochemical and Engineering Aspects*, 2002, **196**, 247-257.
6. J. R. Morones, J. L. Elechiguerra, A. Camacho, K. Holt, J. B. Kouri, J. T. Ramirez and M. J. Yacaman, *Nanotechnology*, 2005, **16**, 2346-2353.
7. H. Q. Jiang, S. Manolache, A. C. L. Wong and F. S. Denes, *Journal of Applied Polymer Science*, 2004, **93**, 1411-1422.
8. I. Sondi and B. Salopek-Sondi, *Journal Of Colloid And Interface Science*, 2004, **275**, 177-182.
9. F. Furno, K. S. Morley, B. Wong, B. L. Sharp, P. L. Arnold, S. M. Howdle, R. Bayston, P. D. Brown, P. D. Winship and H. J. Reid, *Journal Of Antimicrobial Chemotherapy*, 2004, **54**, 1019-1024.
10. P. Jain and T. Pradeep, *Biotechnology and Bioengineering*, 2005, **90**, 59-63.
11. V. A. Oyanedel-Craver and J. A. Smith, *Environmental Science & Technology*, 2008, **42**, 927-933.
12. A. S. Nair and T. Pradeep, *Journal of Nanoscience and Nanotechnology*, 2007, **7**, 1871-1877.
13. H. Y. Xia, Y. Zhang, S. Sun and Y. Fang, *Colloid and Polymer Science*, 2007, **285**, 1655-1663.
14. J. L. Ou, C. P. Chang, Y. Sung, K. L. Ou, C. C. Tseng, H. W. Ling and M. D. Ger, *Colloids and Surfaces a-Physicochemical and Engineering Aspects*, 2007, **305**, 36-41.
15. L. C. de Santa Maria, M. Aguiar, M. A. S. Costa, A. S. S. Valle, J. G. M. Soares, J. D. C. Souza and S. H. Wang, *Materials Letters*, 2007, **61**, 2993-2999.
16. Y. Lu, Y. Mei, M. Schrunner, M. Ballauff and M. W. Moller, *Journal of Physical Chemistry C*, 2007, **111**, 7676-7681.
17. L. M. Wang and D. J. Chen, *Colloid and Polymer Science*, 2006, **284**, 449-454.
18. J. M. Lee, D. W. Kim, Y. H. Lee and S. G. Oh, *Chemistry Letters*, 2005, **34**, 928-929.
19. J. A. Creighton, C. G. Blatchford and M. G. Albrecht, *Journal Of The Chemical Society-Faraday Transactions Ii*, 1979, **75**, 790-798.
20. P. C. Lee and D. Meisel, *Journal of Physical Chemistry*, 1982, **86**, 3391-3395.
21. J. L. H. Chau, M. K. Hsu, C. C. Hsieh and C. C. Kao, *Materials Letters*, 2005, **59**, 905-908.

22. B. S. Yin, H. Y. Ma, S. Y. Wang and S. H. Chen, *Journal of Physical Chemistry B*, 2003, **107**, 8898-8904.
23. M. J. Meziani, H. W. Rollins, L. F. Allard and Y. P. Sun, *Journal of Physical Chemistry B*, 2002, **106**, 11178-11182.
24. Y. P. Sun, P. Atorngitjawat and M. J. Meziani, *Langmuir*, 2001, **17**, 5707-5710.
25. M. Ji, X. Y. Chen, C. M. Wai and J. L. Fulton, *Journal of the American Chemical Society*, 1999, **121**, 2631-2632.
26. J. P. Abid, A. W. Wark, P. F. Brevet and H. H. Girault, *Chemical Communications*, 2002, 792-793.
27. H. H. Huang, X. P. Ni, G. L. Loy, C. H. Chew, K. L. Tan, F. C. Loh, J. F. Deng and G. Q. Xu, *Langmuir*, 1996, **12**, 909-912.
28. H. Bonnemann and R. M. Richards, *European Journal Of Inorganic Chemistry*, 2001, 2455-2480.
29. D. D. Evanoff and G. Chumanov, *Journal of Physical Chemistry B*, 2004, **108**, 13948-13956.
30. K. Philippot and B. Chaudret, *Comptes Rendus Chimie*, 2003, **6**, 1019-1034.
31. B. Chaudret, *Comptes Rendus Physique*, 2005, **6**, 117-131.
32. T. Linnert, P. Mulvaney and A. Henglein, *Journal of Physical Chemistry*, 1993, **97**, 679-682.
33. Y. Feng, A. Karim, R. A. Weiss, J. F. Douglas and C. C. Han, *Macromolecules*, 1998, **31**, 484-493.
34. D. D. Evanoff and G. Chumanov, *Chemphyschem*, 2005, **6**, 1221-1231.
35. J. H. Kim, B. R. Min, J. Won and Y. S. Kang, *Journal Of Polymer Science Part B-Polymer Physics*, 2006, **44**, 1168-1178.
36. K. L. Kelly, E. Coronado, L. L. Zhao and G. C. Schatz, *Journal of Physical Chemistry B*, 2003, **107**, 668-677.
37. P. N. Prasad, *Nanophotonics*, Wiley, Hoboken, New Jersey, 2004.
38. Y. Lin, A. Boker, H. Skaff, D. Cookson, A. D. Dinsmore, T. Emrick and T. P. Russell, *Langmuir*, 2005, **21**, 191-194.
39. Y. Lin, H. Skaff, T. Emrick, A. D. Dinsmore and T. P. Russell, *Science*, 2003, **299**, 226-229.
40. Y. Zhang and C. Erkey, *Journal of Supercritical Fluids*, 2006, **38**, 252-267.
41. J. A. Behles and J. M. DeSimone, *Pure and Applied Chemistry*, 2001, **73**, 1281-1285.
42. H. M. Woods, M. M. C. G. Silva, C. Nouvel, K. M. Shakesheff and S. M. Howdle, *Journal of Materials Chemistry*, 2004, **14**, 1663-1678.
43. T. Arita, S. Beuermann, M. Buback and P. Vana, *E-Polymers*, 2004.
44. T. Arita, S. Beuermann, M. Buback and P. Vana, *Macromolecular Materials And Engineering*, 2005, **290**, 283-293.
45. K. J. Thurecht, A. M. Gregory, S. Villarroja, J. X. Zhou, A. Heise and S. M. Howdle, *Chemical Communications*, 2006, 4383-4385.
46. A. M. Gregory, K. J. Thurecht, W. X. Wang and S. M. Howdle, *Macromolecules*, 2007, **40**, 2965-2967.

47. M. Anand, P. W. Bell, X. Fan, R. M. Enick and C. B. Roberts, *Journal of Physical Chemistry B*, 2006, **110**, 14693-14701.
48. X. Fan, M. C. McLeod, R. M. Enick and C. B. Roberts, *Industrial & Engineering Chemistry Research*, 2006, **45**, 3343-3347.
49. M. Szwarc, M. Levy and R. Milkovich, *Journal of the American Chemical Society*, 1956, **78**, 2656-2657.
50. M. Szwarc, *Nature*, 1956, **178**, 1168-1169.
51. C. J. Hawker, A. W. Bosman and E. Harth, *Chemical Reviews*, 2001, **101**, 3661-3688.
52. M. Kamigaito, T. Ando and M. Sawamoto, *Chemical Reviews*, 2001, **101**, 3689-3745.
53. J. S. Wang and K. Matyjaszewski, *Macromolecules*, 1995, **28**, 7901-7910.
54. J. S. Wang and K. Matyjaszewski, *Journal of the American Chemical Society*, 1995, **117**, 5614-5615.
55. M. Kato, M. Kamigaito, M. Sawamoto and T. Higashimura, *Macromolecules*, 1995, **28**, 1721-1723.
56. G. Moad, E. Rizzardo and S. H. Thang, *Australian Journal of Chemistry*, 2006, **59**, 669-692.
57. J. Chiefari, Y. K. Chong, F. Ercole, J. Krstina, J. Jeffery, T. P. T. Le, R. T. A. Mayadunne, G. F. Meijs, C. L. Moad, G. Moad, E. Rizzardo and S. H. Thang, *Macromolecules*, 1998, **31**, 5559-5562.
58. R. T. A. Mayadunne, E. Rizzardo, J. Chiefari, Y. K. Chong, G. Moad and S. H. Thang, *Macromolecules*, 1999, **32**, 6977-6980.
59. G. Moad, J. Chiefari, Y. K. Chong, J. Krstina, R. T. A. Mayadunne, A. Postma, E. Rizzardo and S. H. Thang, *Polymer International*, 2000, **49**, 993-1001.
60. G. Moad, E. Rizzardo and S. H. Thang, *Australian Journal of Chemistry*, 2005, **58**, 379-410.
61. M. C. McLeod, W. F. Gale and C. B. Roberts, *Langmuir*, 2004, **20**, 7078-7082.

Chapter 5: Methods and techniques

5.1 Overview

The first half of this chapter describes the synthesis methods and equipment used in this research. Details of the high pressure reaction vessels designed for use with scCO₂ are given, along with the changes made to them. The materials and reagents for all the reactions are listed, along with the specific synthesis of any chemicals produced in-house. The second half of the chapter covers the techniques that have been used to characterise the nanocomposite materials produced. For each technique, a short explanation of the general theory is given to explain how the process works. Also, any specific settings or methods used for the samples, especially preparation, are listed in detail along with the model and type of apparatus used.

5.2 Contents

5.1	Overview	325
5.2	Contents	326
5.3	Reaction methods and equipment.....	327
5.3.1	High Pressure Equipment	327
5.3.2	Reaction procedure for the impregnation of silver nanoparticles into polymer substrates in scCO ₂	333
5.3.3	Reaction procedure for suspension polymerisation with nanoparticles as stabiliser	336
5.3.4	Reaction procedure for dispersion polymerisation with nanoparticles as stabiliser	337
5.3.5	Reaction procedure for the synthesis of aqueous soluble stabilised silver nanoparticles	338
5.3.6	Reaction procedure for the dispersion polymerisation of polystyrene microparticles, their sulfonation and decoration with silver nanoparticles	340
5.3.7	Reaction procedure for the RAFT assisted synthesis of silver nanoparticle decorated PMMA microparticles in scCO ₂	342
5.4	Characterisation techniques and equipment	345
5.4.1	UV-Vis Spectrometry	345
5.4.2	Microtomy	346
5.4.3	Scanning electron microscopy (SEM).....	347
5.4.4	Transmission electron microscopy (TEM).....	349
5.4.5	Energy dispersive x-ray spectroscopy (EDX)	352
5.4.6	Supercritical fluid - high pressure liquid chromatography (sc- HPLC).....	354
5.4.7	Raman spectroscopy	358
5.4.8	Gel permeation chromatography (GPC).....	360
5.4.9	Thermo-gravimetric analysis (TGA).....	362
5.4.10	Attenuated total reflectance – Fourier transform infrared spectroscopy (ATR-FTIR).....	363
5.4.11	Inductively coupled plasma atomic emission spectroscopy (ICP-AES)	364
5.5	References	365

5.3 Reaction methods and equipment

5.3.1 High Pressure Equipment

The extreme conditions of scCO₂ processing; high pressure and temperature, require the use of specially designed reaction vessels. The reaction vessels and set-ups used in this research have been split up into categories which are described below. For all the autoclaves described, pressurised CO₂ was provided from compressed CO₂ cylinders via a liquid compressor (*NWA PM-101, Pickel Pump*). Both food grade and supercritical grade CO₂ were used CO₂ (~400 ppm and <20 ppm water respectively). Hydrogen was supplied directly from a high pressure cylinder.

MkI autoclave:

The first reaction vessels used in this work consisted of stainless steel autoclaves purchased from *Thar Technologies, Pittsburgh USA*. Each autoclave comprises of a 10 mL cylindrical body to which two identical end pieces are attached (Fig. 153). Each end piece consists of an autoclave sealing mechanism and a 10 µm inline filter to prevent pipe blockages. Each end of the autoclave was attached to an inlet and outlet valve using stainless steel tubing. A pressure transducer was positioned between the inlet valve and the autoclave. This pressure transducer consists of a piezoelectric crystal which is able to convert mechanical pressure into an electrical signal. When pressure is applied to the crystal, the resultant charge allows the digital monitoring of the pressure. Processing temperature was controlled by means of an externally situated

thermocouple, connected via a feedback loop to a set of heating cartridges located within an aluminium heating block placed around the autoclave. This autoclave type was only used for the early high pressure work reported in chapter 2, in which the polymer substrate is placed inside the autoclave along with the precursor complex, which was also placed inside a ceramic sinter to prevent contact.

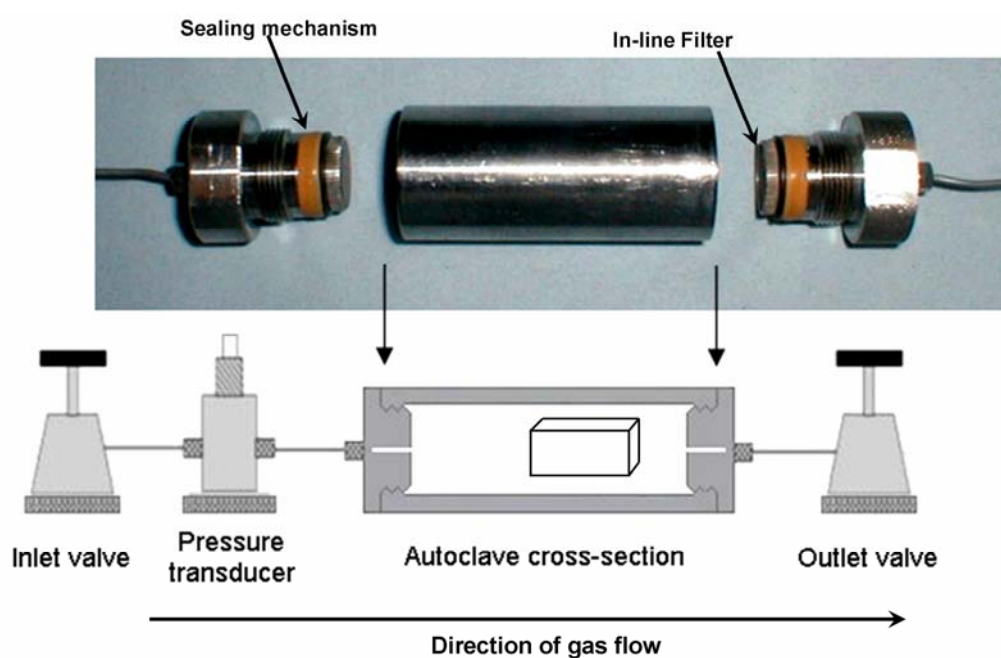


Figure 153 – Digital photograph and schematic of MkI autoclave. External heating block not shown. The white block shown inside the autoclave depicts the location of the substrate. Adapted from Wong.¹

MkII autoclave:

The second type of autoclave used in this work was a custom designed autoclave built in Nottingham University, intended for general scCO₂ use in our research group. The main body of the autoclave consists of a 60 ml volume stainless steel pot that splits into two halves, body and head (Fig. 154). These

two segments are held together by a clamp, which is tightened by a unique key. The lower 'body' half of the reactor contains no inlet or outlet pipes or moving parts and effectively just the 'high pressure beaker' that the reaction takes place in. The upper 'head' segment is where the functioning aspects of the apparatus are mounted. Inlet and outlet pipes are connected into the autoclave via the head segment, outside of the autoclave these pipes are connected up to inlet and outlet valves and a pressure transducer in the same manner as the MkI autoclave. The reaction is heated by a band heater placed around the autoclave body and itself covered in an insulating band, both for safety and efficiency. The temperature is controlled by a thermocouple mounted inside the reaction, directly through the autoclave head, and connected to the band heater. The reaction vessel is agitated by a paddle stirrer that projects vertically down into the vessel from the head segment. Because of the problems associated with high pressure reactions, it is difficult to directly couple the stirrer to a motor without the danger of pressure escaping. To avoid this problem the stirrer is instead driven by an external magnetic coupling which is itself rotated by a motor. Two safety systems are in place to prevent over-pressurising the vessel or opening the vessel while it is under pressure. An emergency pressure relief valve is connected into the autoclave head. This valve contains a disc designed to rupture if the pressure increases above a safe level (~35 MPa) so to safely release the pressure. The key required to open the clamp sealing the two halves of the autoclave together is located at the top of a needle that extends through the head into the interior of the vessel. Therefore in order to remove the key to open the clamp, the needle valve must be removed, this causes the safe and controlled venting of the internal pressure through a small hole near the top of

the needle. This configuration of autoclave was used for some of the high pressure work in chapter 2 and all of the work high pressure work reported in chapter 4. In the work reported in chapter 2, the polymer substrate was placed directly into the bottom of the autoclave along with the precursor complex. In the work reported in chapter 4, all of the reagents added initially were placed directly into the bottom segment of the autoclave. Reagents that were added later were inserted through the open needle valve under a small positive gas pressure so as not to allow the ingress of oxygen.

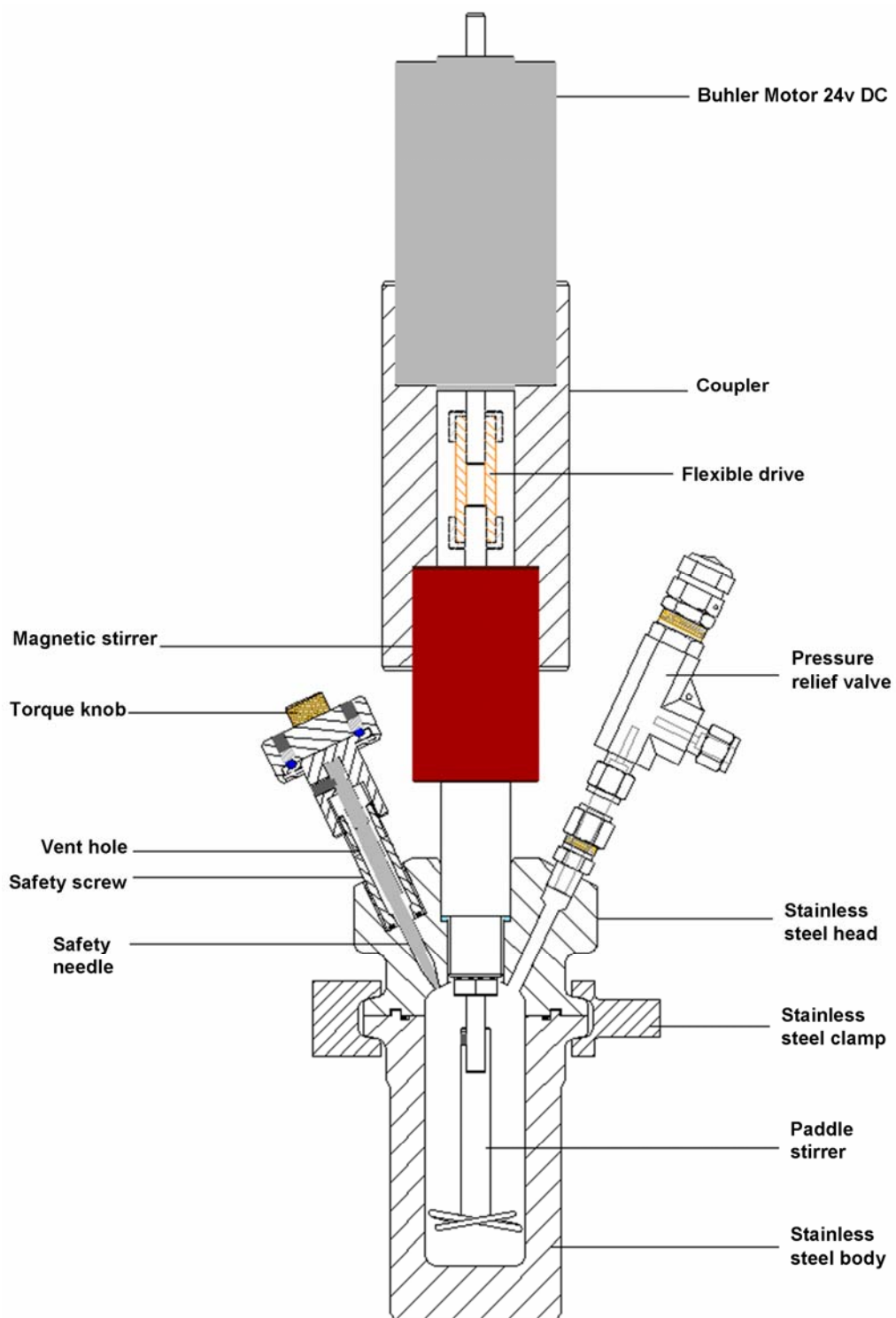


Figure 154 – Schematic depiction of MkII 60 ml autoclave custom made at Nottingham university. Inlet and outlet taps are situated on pipes fitted into the autoclave ‘head’, these are not shown, but penetrate the steel head in the same manner as the pressure relief valve and safety needle.

MkIII autoclave:

The MkIII autoclave configuration is a modification of the MkII version intended to overcome some problems encountered during the research described in chapter 2. The MkIII version is identical to the MkII except for the modification of the paddle stirrer and the location of the polymer substrate and precursor complex. The vertical drive bar of the stirrer, above the paddles, was fitted with a set of two slotted braces. Each brace forms a cross shape, enabling four polymer strips to be held in place between the two braces (Fig. 155). This ensures a symmetrical and dynamic environment for the polymer strips. The precursor was placed inside a small glass dish in the lower segment of the autoclave, below the paddles of the stirrer, to prevent interaction with the steel autoclave floor before solubility is achieved.

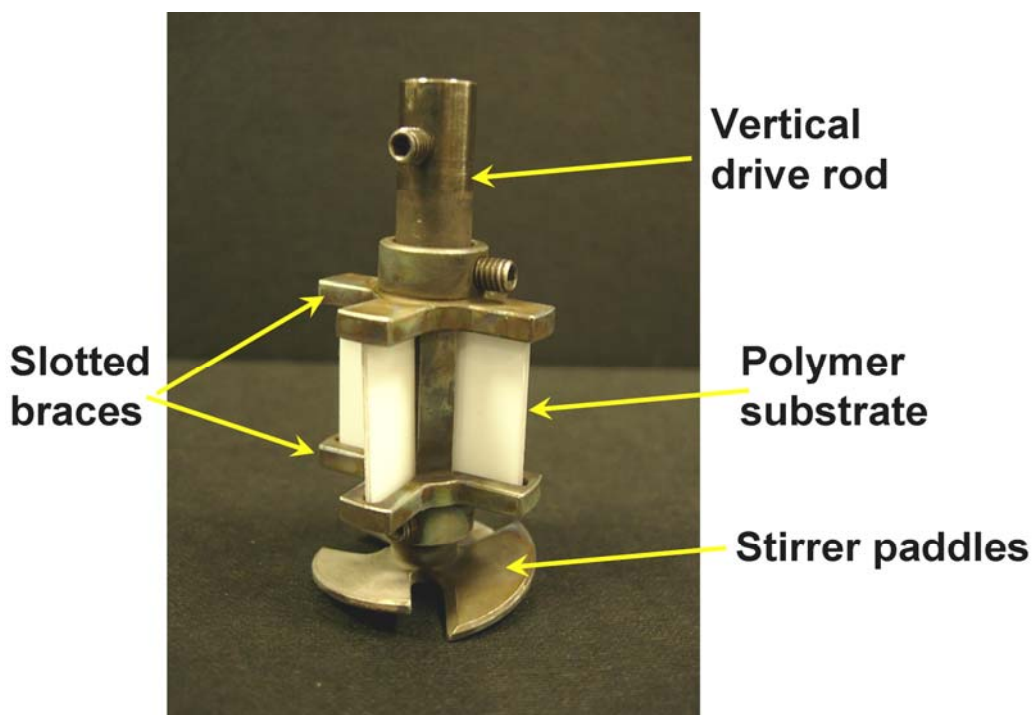


Figure 155 – Digital photograph showing the modifications to the paddle stirrer of the MkIII autoclave.

5.3.2 Reaction procedure for the impregnation of silver nanoparticles into polymer substrates in scCO₂

Materials:

The silver precursor complex 1,5-cyclooctadiene silver(I)-1,1,1,5,5,5-hexafluoroacetylacetonate (Ag(hfac)COD, *Aldrich*) was used as received. The CO₂ and H₂ gases were obtained as gas cylinders (*BOC*) and used as received. Teflon[®] AF 1600 (*DuPont*) was obtained in the form of a granulated powder, which was processed into 15 mm diameter, 1 mm thickness discs before use. This was done by pressing the granules, at 10 tonnes for 10 minutes, into a pellet. The pellets were then heated to 250 °C in a steel mold, under compression, to form the discs. Only a small amount of Teflon[®] AF 2400 was available (*DuPont*). This was in the form of hollow tubes of external diameter 1 mm and wall thickness 0.1 mm, used as received. poly(methyl methacrylate) (PMMA, *Nigel Smith Alloys Ltd*) was obtained in the form of 10 mm, and 6 mm sheets. This was processed in-house to form samples of 20x10x10 mm and 20x10x6 mm respectively. Polycarbonate (*Nigel Smith Alloys Ltd*) was obtained in the form of 0.8 mm and 0.5 mm sheets which were processed into strips of 20x10x0.8 mm and 20x10x0.5mm strips respectively.

Reaction process:

Variable conditions were used during this research as many reaction were performed, where values are given here they should be taken as representing those used most commonly. The reaction process used to prepare the nanocomposites consists of three steps: impregnation, decomposition and

purge, although the purge step was commonly omitted. A standard operating procedure flowchart is provided to show the optimised conditions used with the MkIII autoclave (Fig. 156).

Impregnation: The precursor (200 mg) and substrate (500 mg) are placed in the autoclave and the equipment is assembled. The inlet tap is opened to allow CO₂ to be pumped into the autoclave to a pressure of ~800 psi (~5.5 MPa). The autoclave is then heated to 40 °C before being topped up with further CO₂ to 1500 psi, (10.3 MPa). After 24 hr the outlet tap is opened slightly and the CO₂ is allowed to vent out over ~3 to 5 minutes.

Decomposition: The autoclave is connected to a hydrogen cylinder and the inlet tap is opened to allow the ingress of H₂. The autoclave is filled with H₂ to ~1000 psi (6.9 MPa) and heated to 80 °C to instigate the decomposition of the Ag(hfac)COD. These conditions are maintained for 3 hr before the outlet tap is opened fully to vent the H₂ and the autoclave is allowed to cool to room temperature.

Purge: The autoclave is reattached to the CO₂ line and the inlet tap is opened. The autoclave is repressurised with CO₂ to ~ 4000 psi (27.6 MPa), again at 40 °C, and the outlet tap is left slightly open. The scCO₂ is then allowed to flow slowly through the autoclave for 24 hr to ensure complete extraction of the dissociated ligands. The rate of CO₂ flow is monitored by bubbling the outlet CO₂ through water so the bubble rate could be maintained at a constant flow. The inlet tap is then closed and the outlet tap was left open to allow complete evacuation of the CO₂. The autoclave is then cooled to room temperature before it is disassembled and the samples are removed.

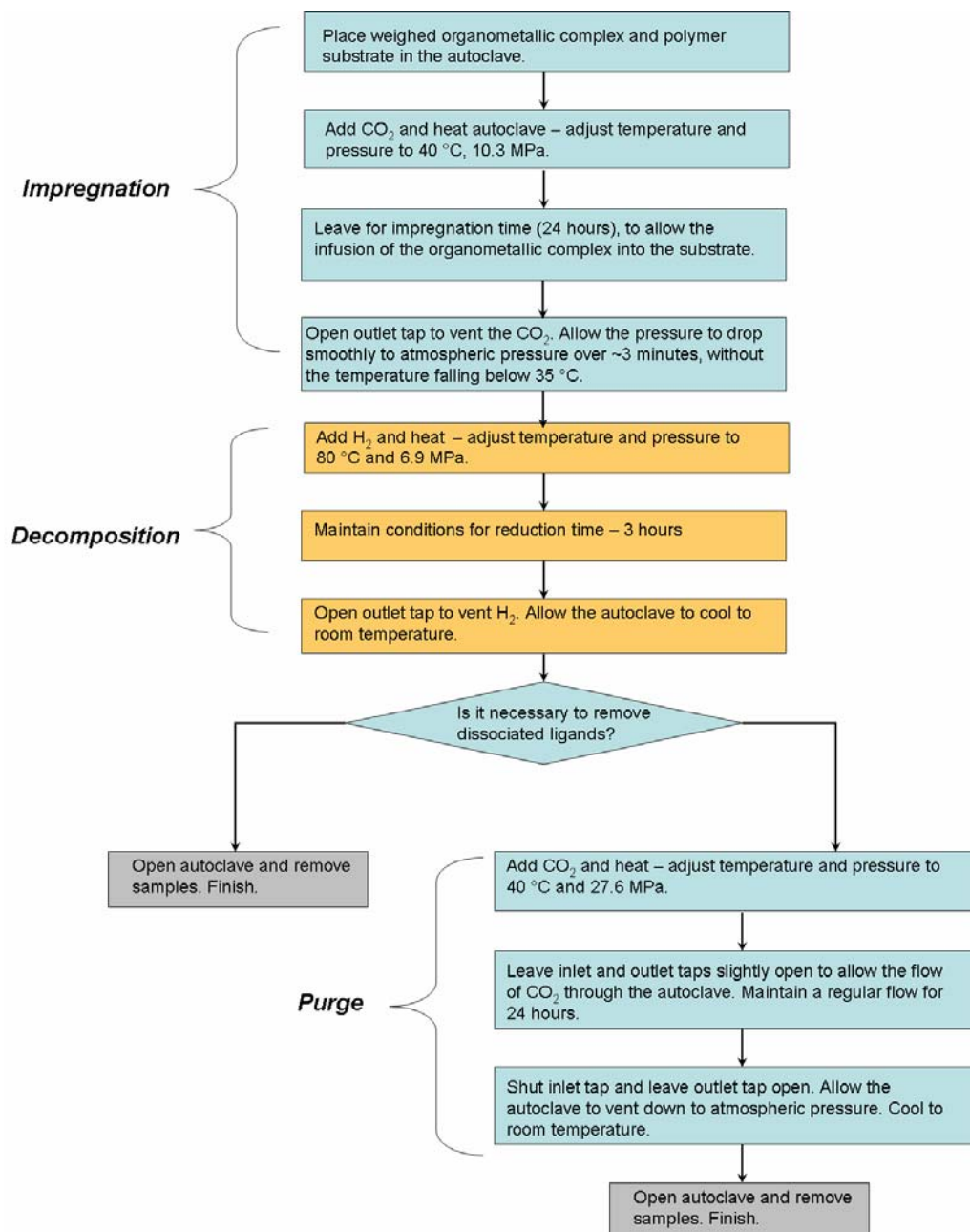


Figure 156 – Standard operating procedure flowchart outlining the most common processing conditions used to produce nanocomposite materials.

5.3.3 Reaction procedure for suspension polymerisation with nanoparticles as stabiliser

Materials:

Metal oxide nanoparticles of magnetite, haemetite cobalt oxide were used as produced by the preparation method described in chapter 3.3.1. Methyl methacrylate (MMA) and poly(vinyl alcohol) (PVA, 87-89 % hydrolyzed) were purchased from *Aldrich* and used as received. The initiator 2,2'-azobis(isobutyronitrile) (AIBN, Fisher Chemicals) was purified through recrystallization with THF.

Polymerisation reaction:

In a typical polymerisation experiment, 300 mg AIBN was dissolved in 20g MMA. Then, the monomer/initiator and an 80 ml aqueous nanoparticle solution (900 mgL^{-1}) were added to a 250 mL three neck flask and the resulting biphasic solution stirred at 400 rpm by a Eurostar digital driver. The reaction was then brought up to a temperature of $\sim 70 \text{ }^\circ\text{C}$ in a thermocouple controlled silicone oil bath for 8 hours.

5.3.4 Reaction procedure for dispersion polymerisation with nanoparticles as stabiliser

Materials:

Aqueous magnetite nanoparticles were produced according to the method described in chapter 3.3.1. Styrene (ReagentPlus >99%, *Aldrich*) and methanol (99.9%, *Fluka*) were used as received. The initiator AIBN (*Fisher Chemicals*) was purified through recrystallisation with THF.

Polymerisation reaction:

In a typical polymerisation experiment, 20 ml of Fe₃O₄ aqueous nanoparticle solution (ca. 200 gL⁻¹ Fe₃O₄) is added to 80 ml of methanol. The resulting solution is then added to a 250 ml three neck flask along with the mixture of 300 mg AIBN and 20 g styrene. This homogeneous solution is stirred at 300 rpm for 10 minutes at room temperature before being gradually heated up to 70 °C over 30 minutes. The reaction is then maintained at constant temperature and stirring rate for 8 hours before being cooled to room temperature, decanted into 800 ml of methanol, washed, filtered and dried. In order to ensure no magnets were present in the vicinity of the synthesis, an overhead stirrer was used (Eurostar IKA digital driver) and heating was performed by means of a magnet-free heating mantle.

5.3.5 Reaction procedure for the synthesis of aqueous soluble stabilised silver nanoparticles

Materials:

The stabilizers used were: 87-89 % hydrolyzed PVA (*Aldrich*), poly(vinyl pyrrolidone) (PVP, *Aldrich*) and soluble starch (*Aldrich*). The organometallic precursor was Ag(hfac)(1,5-COD), (*Aldrich*). The solvents in this work were standard deionized water and reagent grade toluene (*Aldrich*). All chemicals were used as received.

Nanoparticle synthesis reaction:

In a typical reaction, 500 mg of stabilizer is dissolved in 100 mL deionized water while 500 mg of Ag(hfac)(COD) is dissolved in 20 mL toluene. Both solutions are added to a 250 mL three neck flask and the resulting biphasic solution is stirred at 300 rpm with a continuous flow of hydrogen bubbling through (Fig. 157). The reaction is then brought up to a temperature of ~ 80 °C and the progress can be monitored as the colour of the solution changes from white to brown over the course of the reaction. The reaction is stopped after 4 hours by which time it is judged to have reached completion as observed by the colour no longer darkening. The end product is a single aqueous phase containing the nanoparticulate dispersion. A water cooled condenser is used to collect distilled organic vapour. This procedure was performed using starch, PVP and PVA as the stabilizer, respectively.

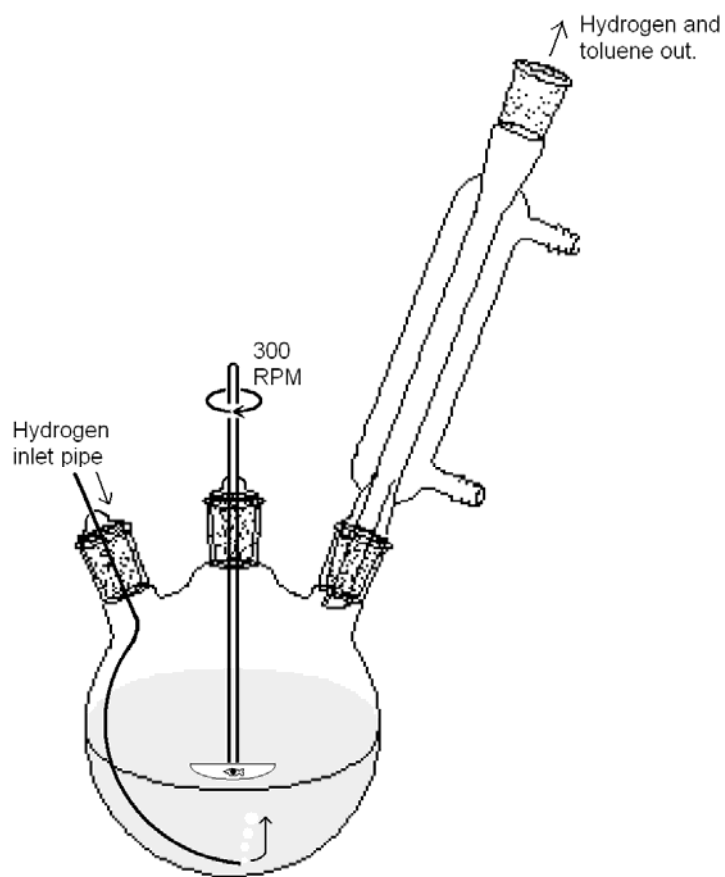


Figure 157 – Apparatus set up used for silver nanoparticle synthesis.

5.3.6 Reaction procedure for the dispersion polymerisation of polystyrene microparticles, their sulfonation and decoration with silver nanoparticles

Materials:

Aqueous silver nanoparticle solution was produced in house. Styrene (*Aldrich*) was used as received, as was PVP (M_w 40,000, *Aldrich*). The initiator, AIBN (*Aldrich*) was recrystallised before use. Sodium hydroxide, divinylbenzene (DVB), sulfuric acid (95 %) and 1,2-dichloroethane were all used as received (*Aldrich*).

Reaction procedure:

Dispersion polymerisation of styrene: DVB crosslinker (2 g) and AIBN initiator (300 mg) were dissolved in styrene monomer (18 g). PVP stabilising agent (2 g) was dissolved in methanol (100 ml). Both solutions were then added to a round bottomed 250 ml 3 neck flask fitted with a thermometer and overhead stirrer. The reaction was stirred at 300 rpm and heated to 65 °C for 12 hr. After cooling to room temperature the products were washed out into 800 ml of methanol and vacuum filtered with porosity-3 sinter. The resulting fine white powder was dried in a vacuum oven.

Sulfonation of polystyrene beads: Polystyrene powder (5 g) was placed in a round bottom flask with 1,2-dichloromethane (1.8 g), and stirring was started at 100 rpm. The reaction was heated up to 80 °C over 30 minutes while sulfuric acid (95%, 25 ml) was slowly added to the flask. The reaction temperature was maintained at 80 °C for 2 hr before being raised to 90 °C and left for a further 3

hr. The reaction was then cooled to room temperature and washed out into 800 ml of deionised water before the solid products were filtered out by porosity-3 sinter. The solid products were then washed and filtered a further 3 times with 800 ml portions of deionised water. The pH of the polystyrene suspension was tested in each wash step but remained at ~ pH 2. NaOH was added dropwise until the pH was raised to ~ pH 5. The powder was then filtered a final time before being dried in a vacuum oven.

Addition of silver nanoparticles to the surface of the beads: The sulfonated powder (500 mg) was added to deionised water (100 mL) and stirred at 600 rpm by a magnetic stirrer bar for 30 minutes. An aqueous solution of PVA stabilised silver nanoparticles (50 mL) was added by pipette over a further 30 minutes. The stirring rate was increased to 800 rpm for 3 hr before the suspension was filtered by suction with a porosity-3 sinter. The powder was vacuum-dried before being washed with deionised water (200 mL) for 1 hr and then filtered and dried overnight in a vacuum oven.

5.3.7 Reaction procedure for the RAFT assisted synthesis of silver nanoparticle decorated PMMA microparticles in scCO₂

Synthesis of RAFT agent:

Synthesis of 3-benzylsulfanylthiocarbonylsulfanylpropionic acid: 3-mercaptopropionic acid (20 mL, 0.23 mol) was added to potassium hydroxide solution (26 g in 250 mL H₂O, 0.46 mol). 30 mL of CS₂ was added dropwise. The orange solution was stirred for a further 5 hours. 39.6 g of benzyl bromide (0.23 mol) was added and the mixture was heated to 80 °C for 12 hours. Chloroform (300 mL) was added to the cooled mixture and then HCl was slowly added until the organic layer turned yellow. The water layer was extracted with chloroform (2 x 100 mL) and then the organic layers dried over MgSO₄. The acid functionalised RAFT agent was purified by chromatography (3:1 hexane – ethyl acetate). ¹H NMR: 11.1 ppm (bs – COOH), 7.2-7.3 ppm (m, aromatic), 4.63 ppm (s, S-CH₂), 3.64 ppm (t, S-CH₂), 2.87 (t, CH₂-COOH).

Synthesis of PDMS-RAFT: 30 g of mono-hydroxy terminated PDMS (3 mmol, M_n = 10 kDa) was mixed with dicyclohexyl carbodiimide (0.64 g, 3.1 mmol) and anhydrous chloroform in molecular sieves (40 mL). 3-benzylsulfanylthiocarbonylsulfanylpropionic acid (1.08 g, 4 mmol) was added to the solution and refluxed for 72 hours. The sieves were removed by filtration and the solution was extracted with H₂O until the water phase was colourless. The solvent was removed under vacuum and then the yellow PDMS-RAFT

product was washed with hexane. This solution was dried over MgSO₄, filtered and then the product recovered following evaporation of solvent.

Materials: The PDMS-RAFT was produced in-house by the method given above. MMA, chloroform, and Ag(hfac)COD (*Aldrich*) were all used as received. The AIBN initiator (*Aldrich*) was recrystallised before use. The CO₂ used in this work was supercritical fluid grade (*BOC*), which contains less water than food grade.

Reaction procedure for nanoparticle synthesis, polymer synthesis and combined synthesis:

These reactions were performed in 60 mL paddle stirred autoclaves of the type described as MkII – Nottingham type.

Nanoparticle synthesis: Ag(hfac)COD (100 mg) was loaded into an autoclave along with PDMS-RAFT (300 mg). The autoclave was then flushed with CO₂ for 15 min before being heated to 65 °C and pressurised to 275 bar scCO₂. The reaction was maintained at these conditions for 48 hr before being cooled to room temperature and depressurised. Chloroform (10 mL) was then added as solvent to disperse and remove PDMS-RAFT stabilised silver nanoparticles as a transparent brown solution.

Polymerisation in scCO₂: PDMS-RAFT (500 mg) and AIBN (0.6 wt %, 60 mg) were added to the autoclave and flushed with CO₂ for 15 minutes. Degassed MMA (10 mL) was then added under a slightly positive flow of CO₂, in order to prevent the ingress of oxygen into the system. The autoclave was pressurised to 55 bar, heated to 65 °C and then pressurised to 275 bar. After 48 hours, the

vessel was cooled to room temperature and the CO₂ vented. The resulting polymer was a free-flowing, off-white powder.

Combined polymer and silver nanoparticle synthesis: The one-pot, simultaneous reaction was performed under identical conditions to the polymer synthesis except that Ag(hfac)COD (200 mg) was added to the autoclave along with the other reactants. The reaction resulted in the production of a fine free-flowing brown powder.

5.4 Characterisation techniques and equipment

The equipment and techniques used for the characterisation of the products and materials of this research. Each section aims to briefly explain the general theory of how the technique works, before describing specifically how it was used here in terms of the equipment models and configuration, and the sample preparation methods.

5.4.1 UV-Vis Spectrometry

A UV/Vis spectrometer is used to obtain light absorption readings in the near UV and visible portions of the electromagnetic spectrum. Typically, a light source located inside a spectrometer is separated into its component wavelengths using a prism or diffraction grating. The spectrometer then scans across the UV/vis region and plots differences in absorption versus wavelength. Absorbance is a dimensionless quantity plotted on the y-axis commonly ranging from 0, no absorption to 2, 99% absorption. Normally UV-vis spectrometers are used with samples that can transmit light, usually liquids but also gases and solids, in which case the monochromatic beam is simply directed through the sample. However, in the case of opaque samples, commonly solids, reflectance mode must be used. This requires a special spectrometer that is capable of capturing the light reflected from the surface of the sample and redirecting it back into a detector.

In this work all light transmitting samples were measured using an *Agilent 8453* spectrometer. Liquid samples were placed in a 10 mm path length quartz cuvette. Transparent solid samples were placed in a specially constructed sample holder and scanned without modification. Reflectance

spectroscopy was performed on non-transmitting samples at Southampton, using a *Jasco V570 UV/VIS/NIR* spectrometer.

5.4.2 Microtomy

Microtomes are mechanical instruments used to cut samples into transparent thin sections for microscopic examination. Microtomes use steel, glass or diamond blades depending upon the specimen being sliced and the desired thickness of the sections being cut. The blade is normally held firmly in place at an adjustable angle, whilst the gripped sample moves towards it in carefully controlled arcing movements. When very thin slices are being cut, each section must be floated out onto the meniscus of a liquid located in a ‘boat’ behind the blade. This prevents the sections from rolling up or crumpling on the back of the blade and allows them to be transferred onto a TEM grid for imaging.

The samples microtomed for TEM imaging as part of this research were sectioned as follows. An appropriate area of the solid sample was cut out using a clean razor blade. This was mounted in a *Reichert Ultra-microtome* and trimmed down to a flat surface using a fresh glass blade. After this a diamond blade was inserted and positioned to a blade angle of 45°. Sections of the sample were then cut at an increment of 100 nm and a cutting speed of 1 mm/min. The sections were floated out onto the surface of deionised water before being transferred to TEM grids and dried.

5.4.3 Scanning electron microscopy (SEM)

The scanning electron microscope (SEM) is a type of electron microscope. It uses electrons rather than light to form an image of a sample. A stream of highly energetic, monochromatic electrons is focused on the sample. Electrons scattered or emitted from the sample can then be detected. The incident beam is rastered across the sample surface to produce an image. When the primary electron beam interacts with the sample, the electrons lose energy by repeated scattering and absorption within a teardrop-shaped volume of the specimen known as the interaction volume, which extends from less than 100 nm to around 5 μm into the surface. The size of the interaction volume depends on the electron landing energy, the atomic number of the sample atoms and the sample density. The energy exchange between the electron beam and the sample results in the emission of electrons and electromagnetic radiation, which can be detected. The type of signal gathered in an SEM varies and can include secondary electrons and back scattered electrons. These signals come not only from the primary beam impinging upon the sample, but from other interactions within the sample near the surface.

Secondary electron mode: Secondary electrons, originating from the first few \AA , give information on the topography of the surface. This imaging mode monitors low energy (<50 eV) electrons. Because of their low energy, these electrons originate within a few nanometers from the surface. The brightness of the signal depends on the number of secondary electrons reaching the detector. If the beam enters the sample perpendicular to the surface, then the activated region is uniform about the axis of the beam and a certain number of electrons "escape" from within the sample. As the angle of incidence increases, the

"escape" distance of one side of the beam will decrease, and more secondary electrons will be emitted. Thus steep surfaces and edges tend to be brighter than flat surfaces, which results in images with a well-defined, three-dimensional appearance.

Backscattered electron mode: Backscattered electrons are less sensitive to surface topography and more sensitive to differences between elements. Backscattered electrons consist of high-energy electrons originating in the electron beam. These are reflected out of the specimen interaction volume. Nuclei with high atomic numbers backscatter more electrons than lower atomic numbered nuclei, thus creating differences in image contrast. Backscattered electrons may therefore be used to detect contrast between areas with different chemical compositions, especially when the average atomic number of the various regions is different, since the brightness of the image tends to increase with the atomic number.

All the samples that were investigated by SEM in this study were prepared as follows: The specimen was mounted on a 12 mm diameter carbon tab attached to the surface of an aluminium pin stub (*Agar Scientific*). The specimen was then plasma coated in a conductive material, usually gold, for 3 minutes. This deposits a thin layer of the conductive material over the surface of the sample, too thin to adversely affect the imaging, but preventing problems of excessive charging of the material under the electron beam, which would cause polymeric material to melt or become damaged. All SEM images were acquired using a *Philips XL-30* SEM operating at 20 kV.

5.4.4 Transmission electron microscopy (TEM)

In TEM an electron beam of uniform current density is directed at a thin sample. Electrons that travel through the sample are detected. Electrons have a shorter wavelength than photons, and can therefore provide a higher resolution than conventional light microscopes. TEM also has a higher resolution than SEM, because the resolution of SEM is limited to the minimum beam width of the SEM. TEM provides the cornerstone of the analysis of the nanostructure of the composite materials produced in this work because it has sufficient resolution to directly image the nanoparticles. TEM can provide two separate kinds of information about a specimen – a magnified image and a diffraction pattern. Electrons that are transmitted through the bulk material generate a form of contrast that enables observation of the internal structure. Electrons pass more easily through thinner, lower density, or lower atomic mass material. This means that because fewer electrons pass through the thicker, denser or higher atomic mass regions of the sample, these regions appear darker. Electrons that are diffracted produce a diffraction pattern which gives information on the crystallinity of the sample and enables identification of the specimen by comparison to corresponding d spacings of known phases. In this work, TEM has enabled visualisation of the trapped nanoparticles throughout the different impregnated matrices. The dispersion and homogeneity of the nanocomposites has been assessed and quantitative particle size analysis achieved.

The contrast in a TEM image is not like the contrast in a light microscope image. A crystalline material interacts with the electron beam mostly by diffraction rather than absorption, although the intensity of the

transmitted beam is still affected by the volume and density of the material through which it passes. A high-contrast image can therefore be formed by blocking electrons deflected away from the optical axis of the microscope by placing the aperture to allow only unscattered electrons through. This produces a variation in the electron intensity that reveals information on the crystal structure. This technique (known as Bright Field) is extensively used in the TEM images reported in this work. The aperture is positioned so that the electrons diffracted by the crystalline nanoparticles are excluded from the image. This increased the contrast in the images by making the nanoparticles appear even darker. It is also possible to produce an image from electrons deflected by a particular crystal plane. By either moving the aperture to the position of the deflected electrons, or tilting the electron beam so that the deflected electrons pass through the centred aperture, an image can be formed of only deflected electrons, known as a Dark Field image, although this is not used in this work.

The two most important parameters in electron diffraction are the angular distribution of the scattered electrons and the intensity of scattering. If an electron beam is incident with the sample, it will be elastically scattered by some of the atoms. The diffraction of electrons and their relationship with wavelength is defined by the Bragg law and since only certain planes can diffract, there is only a finite number of possible d-spacings. If the beam is parallel to the planes of the crystal, then it will diffract and lead to a diffraction spot pattern consisting of a regular array of spots. If the sample contains many crystals in different orientations then the pattern will be a sum of the individual planes. If the sample contains many randomly orientated crystals then the

diffraction pattern will be a sum of the individual planes, hence diffraction spots will occur in a circular manner (Fig. 158).

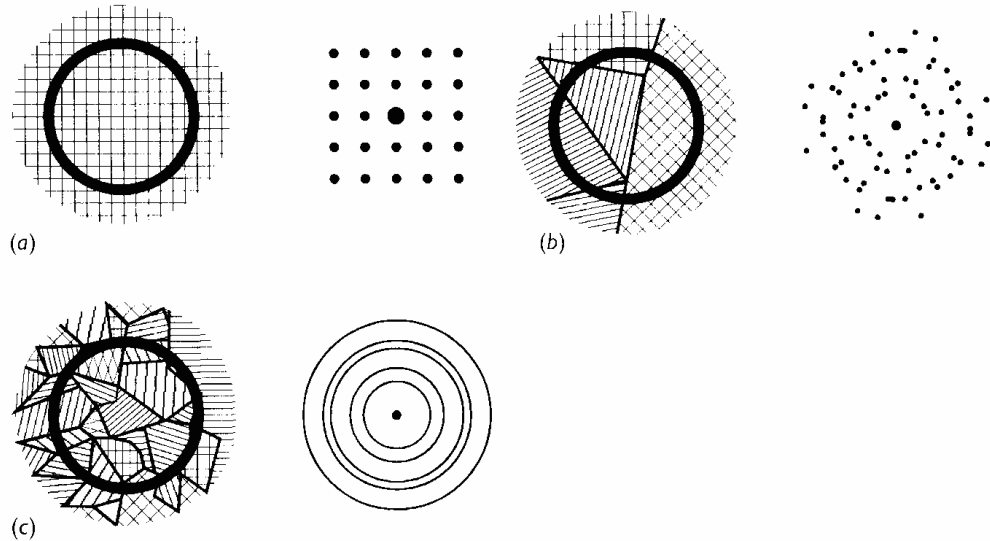


Figure 158 - A schematic of the types of diffraction pattern that arise from different microstructures. (a) A single perfect crystal, (b) A small number of grains or crystals, (c) A large number of randomly ordered grains or crystals.²

A modern TEM microscope is a complex piece of equipment and a comprehensive description of the instrument is beyond the scope of this thesis. For further information regarding TEM the reader is directed to “*Electron Microscopy and Analysis*” by Goodhew, Humphreys and Beanland.²

TEM image acquisition and sample preparation:

TEM images were collected using a *JEOL JEM-2000FX II* electron microscope operating at 200 keV. The samples were prepared in a variety of methods depending on their nature. Solid, bulk polymer samples were prepared by directly microtoming the sample into 100 nm cross sections. The sections were supported on 3.05 mm diameter holey carbon coated copper grid (300

lines per inch mesh, *Agar Scientific*). Samples that were too large to be imaged unmodified in TEM, but too small to be microtomed directly, were first embedded in resin. Embedding was performed as follows: (Chemicals from *Agar Scientific*) Dodecenyl succinic anhydride (8 ml), methyl nadic anhydride (4 ml), and Agar 100 epoxy resin (10 mL) were warmed to 60 °C and mixed by shaking for one minute, before the addition of N-benzyl dimethylamine (0.75 g) followed by a further minute of shaking. Polymer samples were then added to moulds along with the resin and baked at 55 °C for 48 hr. The resin blocks were then microtomed to a thickness of ~ 100 nm and supported on a copper grid (300 mesh). Samples that were small enough to allow direct TEM imaging, i.e. polymer powder of ~1 µm diameter or metal nanoparticles in solution, were prepared as follows. Dry powders were dispersed in a suitable liquid medium to create a suspension, normally methanol. Sonication of such powders in solution was undertaken for a few seconds where it was necessary to aid in the dispersion of the material. The resultant solution, or the unmodified solution, in the case of originally solution samples, was then deposited dropwise onto holey-carbon coated copper grids (300 mesh, *Agar Scientific*). The suspensions were either added as one drop and allowed to dry slowly, or added a few drops in succession each sucked through the grid onto filter paper.

5.4.5 Energy dispersive x-ray spectroscopy (EDX)

EDX is an analytical technique used for elemental analysis of a specimen. Being a type of spectroscopy, it relies on the investigation of a

sample through interactions between electromagnetic radiation and matter, analyzing X-rays emitted by the matter in this particular case. In this research it has been used in conjunction with SEM and TEM as both of them can trigger x-ray emission by interaction of the electron beam with the sample. EDX characterisation capabilities arise because each element of the periodic table has a unique atomic structure. This allows x-rays that are characteristic of each element's atomic structure to be distinguished from each other.

When the incident e^- beam in SEM or TEM interacts with the sample it can excite an electron in an inner shell of one of the sample's atoms, prompting the ejection of that electron and the formation of an electron 'hole' within the atom's electronic structure. An electron from an outer, higher-energy shell then 'drops down' in energy to fill the hole. The difference in energy between the higher-energy shell and the lower-energy shell must therefore be released. This occurs in the form of emitted radiation, as an x-ray (Fig. 159). The detector in an EDX analyser consists of a semiconductor that is positioned so that a high number of X-rays emitted from the specimen fall onto it. Each incoming X-ray excites a number of electrons into the conduction band of the silicon leaving a number of positively charged holes in the outer electron shells. This converts the X-ray energy into voltage signals. The information is then sent to a pulse processor, which measures the signals and passes them onto an analyser for data display and analysis. The resultant spectrum is organised horizontally in terms of energy and can be used to determine the presence of elements as well as approximate relative concentrations.

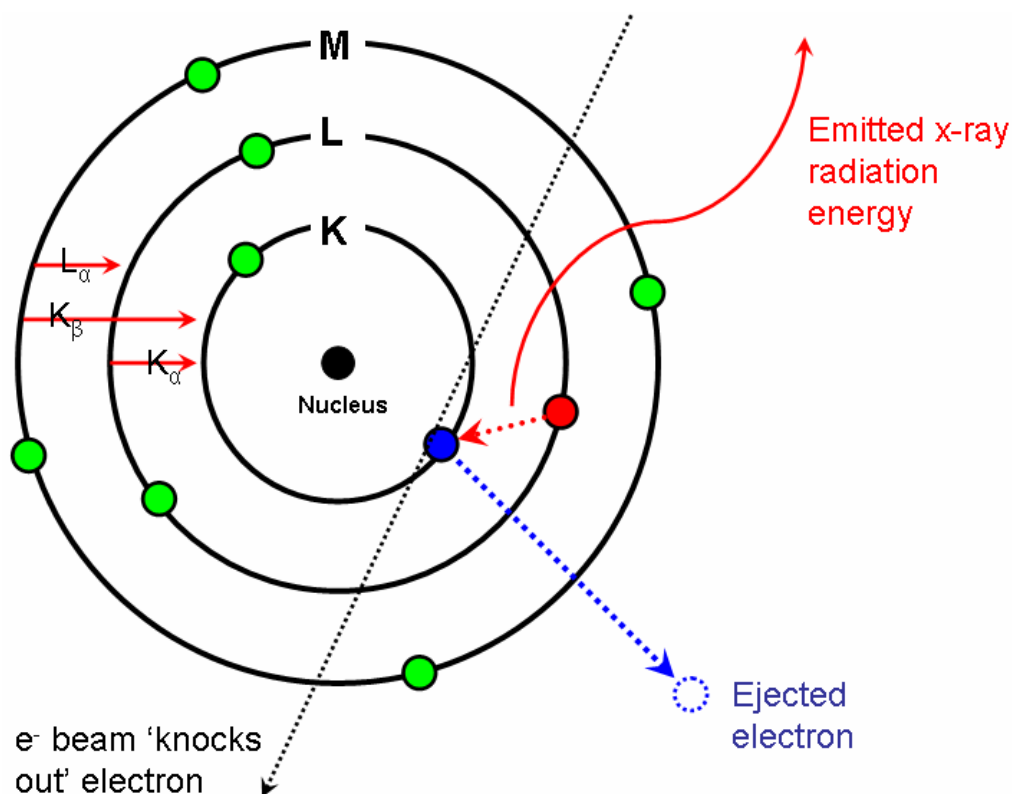


Figure 159 – Bohr model of the electronic structure of an atom. An incident electron removes an inner shell electron causing a higher energy-shell electron to drop into a lower orbital, releasing an x-ray. The nomenclature for possible energy transitions is shown.

In this work EDX spectra were obtained using either a *Philips XL-30* SEM with embedded *INCA x-sight* EDX analyser, or alternatively, using a *JEOL JEM-2000FX II* TEM coupled with a *Noram Series II* EDX analyser.

5.4.6 Supercritical fluid - high pressure liquid chromatography (sc-HPLC)

This section describes how solubility measurements were performed using a prototype supercritical-HPLC system with the assistance of Dr. Satoshi

Yoda in Tsukuba, Japan. Dr. Yoda is part of the Nanofluidic Process Group which is based in the Nanotechnology Research Institute of the National Institute of Advanced Industrial Science and Technology (AIST).

HPLC is a form of column chromatography used to separate components of a mixture by using a variety of chemical interactions between the analyte and the chromatography column. The sample to be analyzed is introduced in small volume to a mobile phase stream and is retarded by specific chemical or physical interactions with the stationary phase as it traverses the length of the column. The degree of retardation depends on the nature of the analyte, stationary phase and mobile phase composition. High pressure increases the speed of elution giving the components less time to diffuse within the column, leading to improved resolution in the resulting chromatogram. As the analytes pass out of the end of the column they give a signal in the detector, which can give further information on the analyte, e.g. detectors can include UV-vis or IR spectrometers.

sc-HPLC is a useful method for measuring the solubility of analytes in supercritical fluids by using HPLC. This method involves direct injection of a scCO₂ solution into a HPLC eluent. In this method, the substances employed should have a higher solubility in the HPLC eluent than in scCO₂, a condition that is fulfilled for most substances. All of the injected scCO₂ can be dissolved into the HPLC eluent before detection; thus, the scCO₂ density and pressure do not affect the analysis.³

The high-pressure flow system for this work (Fig. 160) was designed with reference to Ashraf-Khorassani's et al.⁴ The metal complex was placed in the small sample column along with 1 mm glass beads. Then, scCO₂ was

loaded at the prescribed pressure (8–30MPa) and temperature (313 K) by means of a high-pressure pump and back pressure regulator. At this stage the valves 6V1 and 6V2 were positioned such that the scCO₂ was able to flow through the red section of piping, without going through the sample vessel, and then out through the back pressure regulator (BPR on diagram). Next, valve 6V2 was switched to allow the scCO₂ to flow into the sample vessel. The equilibrium solubility was checked by periodical analyses until the measured values were constant for three successive analyses. A small amount of the sample/scCO₂ solution was directly injected into the HPLC eluent through the inner-volume sampler valve 4V1 (2 μL, *Valco*). This injects 2 μL of scCO₂ into the sample loop (pink in the diagram). In normal use the sample loop is filled with the liquid eluent that is flowing through the HPLC, so this injects the CO₂-solute into the HPLC eluent flow. The injected sample/scCO₂ solution is dissolved into the HPLC eluent, and is then detected at the detector after passing through the analytical column. After equilibrium solubility at each condition was reached, recordings for solute concentration were taken, before changing to the next pressure. After each injection, valves 6V1 and 6V3 were positioned to allow scCO₂ to flow through the sample loop so as to remove any trace solute and to clean the lines. Valve V2 could then be opened to bleed the trapped CO₂ out of the sample loop before allowing HPLC solvent to begin flowing through it again prior to the next measurement.

The system was heated with a silicone rubber heater and a temperature controller (*Chino DB-1000*). The temperature was measured around the sample loop with a probe and a digital thermometer (*Advantest TR2114*). The pressure was measured with a pressure transducer (*Kyowa Electric Instruments, PG-*

5.4.7 Raman spectroscopy

The use of Raman spectroscopy was introduced in chapter 1.3.1.2. That introduction is now extended here to show the underlying theory. When light interacts with matter, the photons may be absorbed or scattered, or may not interact with the material and pass straight through. If the energy of an incident photon corresponds to the energy gap between the ground state of a molecule and an excited state, the photon may be absorbed and the molecule promoted to a higher energy excited state. It is this change that is measured in absorption spectroscopy, such as conventional UV-vis or IR spectroscopy. These methods measure the frequencies of light missing from the transmitted beam of light in order to determine the energies of the transitions excited in the molecule. However, it is also possible for the photon to interact with the molecule and scatter from it. In this case there is no need for the photon to have an energy which matches the difference between the two energy levels of the molecule. In Raman spectroscopy it is these scattered photons that are observed by collecting light at an angle to the incident beam.

In infrared spectroscopy, infrared energy covering a range of frequencies must be directed onto the sample. In Raman spectroscopy, because there is no need for the incident light frequency to match the frequency of the energy transition being measured, only a single frequency of light is required. However, it is important that the energy of the incident light is higher than the transitions measured. Also, the scattering measured in Raman spectroscopy is an inherently weak process, and therefore very high intensities of incident light are required to get sufficient signals. For these reasons laser light, normally in the visible range, is used for the incident light beam in Raman spectroscopy.

The scattering of the incident light occurs by the following mechanism. The light interacts with a molecule of the sample and distorts the cloud of electrons around the nuclei to form a short lived excited state. This state is not stable and the photon is quickly re-radiated (Fig. 161). If only the electron cloud distortion is involved in scattering, the photons will be scattered with very small frequency changes, as the electrons are comparatively light. This is Rayleigh scattering. However, if nuclear motion is induced during the scattering process, energy will be transferred either from the incident photon to the molecule (Stokes) or from the molecule to the scattered photon (anti-Stokes). In these cases the process is inelastic and the energy of the scattered photon is different from that of the incident photon by one vibrational unit. This is Raman scattering, and it can be used to identify the chemical bonds in molecules.⁵

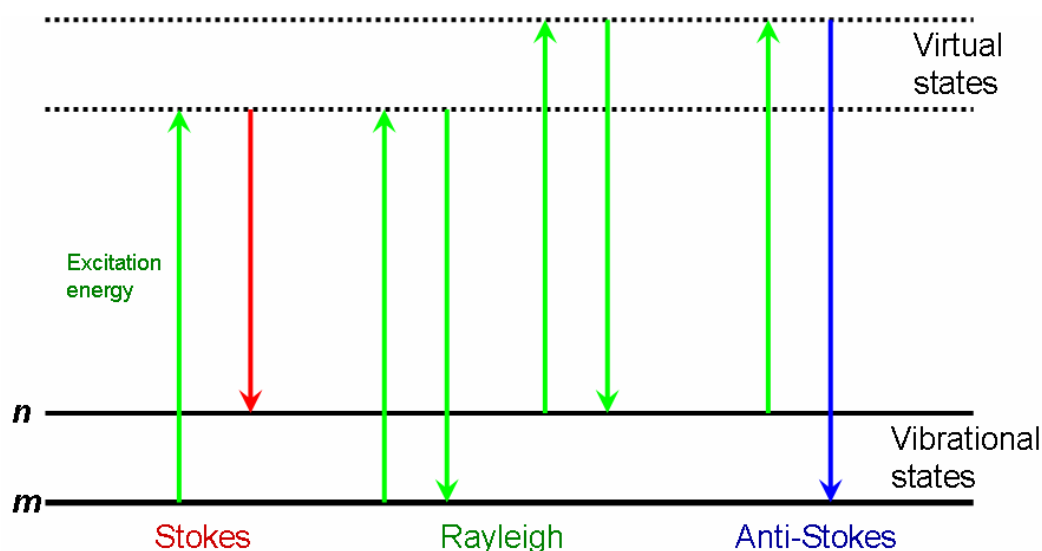


Figure 161 – Diagram of the Rayleigh and Raman scattering processes. The lowest energy vibrational state m is shown with states of increasing energy above it. Note that the energy of the incident radiation (upward arrows) and scattered radiation (downward arrows) is higher than the energy of a vibration (m to n).⁵

The Raman spectroscopy performed as part of chapter 2 was conducted using a conventional Renishaw Raman spectrometer with a 633 nm He-Ne excitation source launched via a 50× microscope objective to produce a spot size of ~ 2 μm in diameter with ~ 3mW of optical power. Light from the illuminated spot was collected with a lens and sent through a monochromator. Wavelengths close to the laser line, due to elastic Rayleigh scattering, were filtered out while the rest of the collected light was dispersed onto a charge-coupled-device detector.

5.4.8 Gel permeation chromatography (GPC)

GPC is a method of determining the average molecular weight (M_n , M_w) and polydispersity (PDI) of polymer samples. M_n and M_w are different methods of defining the average molecular weight of polymers (equations 7 and 8, below). M_n is the *number average molecular weight*, and is the ordinary arithmetic mean of the molecular weights of the individual macromolecules. It is determined by measuring the molecular weight of n polymer molecules, summing the weights, and dividing by n . However, this can reflect too much significance of short chain polymers or unreacted monomer, as this averaging method does not give more significance to longer chains to take into account that they contain more monomer units. M_w gives the *weight average molecular weight* which gives more significance to longer chains. This can give more relevant results because it means that given a M_w of w , if a monomer unit is chosen at random, then the polymer it belongs to will have a weight of w on average. M_w is determined by summing the squared molecular weights of n

polymer molecules, and dividing by the sum of the molecular weights. The PDI is determined by M_w/M_n and is a measure of the distribution of molecular mass in a polymer sample. It indicates the distribution of individual molecular masses in a batch of polymers. The PDI has a value always greater than 1, but as the polymer chains approach uniform chain length, the PDI approaches unity.

$$\overline{M}_n = \frac{\sum N_x M_x}{\sum N_x} \quad (7)$$

Equation 7 – The number average molecular weight, where N_x is the number of moles whose weight is M_x .

$$\overline{M}_w = \frac{\sum N_x M_x^2}{\sum N_x M_x} \quad (8)$$

Equation 8 – The weight average molecular weight, where N_x is the number of moles whose weight is M_x .

In the operation of GPC, the polymer is dissolved in a solvent and passed through a column of highly porous material. Larger molecules are less able to fit into the pores and so pass through the columns more quickly than smaller molecules, which spend more time trapped in the pores. A detector connected to a computer at the end of the column is able to plot detector signal versus retention time. By comparing the retention time to that of a narrow molecular weight distribution standard, it is possible to obtain molecular weight data for the sample.

The GPC measurements presented in chapter 3 were taken after using a LC 1120 HPLC pump (Polymer Laboratories) with two PLgel 5 μ m Mixed-D

columns (*Polymer Laboratories*), and an evaporative light scattering detector (*Polymer Laboratories PL-ELS 1000*). Calibration was established using polystyrene standards (*Polymer Laboratories*). The polymer samples were dissolved in an appropriate solvent and filtered to remove nanoparticles prior to analysis. The eluent used for PMMA was chloroform, and THF was used for polystyrene. The GPC measurements presented in chapter 4 were performed using a *PL-120* GPC instrument (*Polymer Laboratories*) fitted with two *PLgel 5 μ m Mixed-D* columns (*Polymer Laboratories*), and a refractive index (RI) detector. The instrument was calibrated with polystyrene standards using THF as eluent.

5.4.9 Thermo-gravimetric analysis (TGA)

TGA is a method of determining the thermal stability of polymers and other materials. A small sample (usually a few μ g) is weighed continuously on a sensitive balance inside a furnace. The temperature is increased at a specific rate and a thermogram of weight versus temperature is recorded. The loss of volatile materials, such as evaporation of moisture or residual solvent, or polymer decomposition, leads to a decrease in sample mass at an identifiable temperature. The temperature ranges at which mass is lost, and the magnitude of the loss, can be used as an aid to characterise the composition and nature of materials.

This technique was used to measure the relative amount of magnetite contained in the magnetite-polymer nanocomposites described in chapter 3. At

the temperature range to which the TGA was heated only the polymer is decomposed, so the remaining mass can be attributed to the magnetite nanoparticles. All TGA measurements of sample decomposition and weight loss taken in this work were made using a *Perkin-Elmer Pyris 1* TGA. The measurements were taken under a nitrogen flow at a heating rate of 5 °Cmin⁻¹.

5.4.10 Attenuated total reflectance – Fourier transform infrared spectroscopy (ATR-FTIR)

ATR-FTIR is a method of performing spectroscopy on a solid sample to detect the frequencies of IR radiation absorbed by the material. The sample to be analysed is pressed firmly against a solid crystal. ATR uses a property of total internal reflection called the evanescent wave. A beam of infrared light is passed through the crystal in such a way that it reflects at least once off the internal surface in contact with the sample. This reflection forms the evanescent wave which extends into the sample, typically by a few micrometres. The beam is then collected by a detector as it exits the crystal. The infrared spectrum obtained then gives information on the molecular structure of the sample according to which energies of IR radiation were absorbed. The ATR-FTIR spectrum presented in chapter 3 was recorded using a *380 FT-IR (Thermo electron corporation)*.

5.4.11 Inductively coupled plasma atomic emission spectroscopy (ICP-AES)

ICP-AES is used for detecting and quantifying low concentrations of unknown elements. It is a type of emission spectroscopy that uses a plasma (e.g. inductively coupled plasma) to produce excited atoms and ions that emit electromagnetic radiation at wavelengths characteristic of a particular element. An inductively coupled plasma (ICP) is a type of plasma source in which the energy is supplied by electrical currents which are produced by electromagnetic induction, that is, by time-varying magnetic fields. Typically an aqueous solution is sprayed as an aerosol into flowing argon and passed into the inductively coupled flame. The colours and intensity of the light emitted from the flame is then recorded by a detector connected to a computer. The ICP-AES reported in chapter 3 was performed using a *Perkin-Elmer optima 3300 DV*.

5.5 References

1. B. Wong, in *Chemistry Thesis: The Preparation of Nanocomposite Materials using Supercritical Carbon Dioxide*, University of Nottingham, Nottingham, 2005.
2. P. J. Goodhew, J. Humphreys and R. Beanland, *Electron Microscopy and Analysis*, Taylor and Francis, London, 2001.
3. S. Yoda, Y. Mizuno, T. Furuya, Y. Takebayashi, K. Otake, T. Tsuji and T. Hiaki, *Journal of Supercritical Fluids*, 2008, **44**, 139-147.
4. M. Ashraf-Khorassani, M. T. Combs and L. T. Taylor, *Talanta*, 1997, **44**, 755-763.
5. E. Smith and G. Dent, *Modern Raman Spectroscopy - A Practical Approach*, Wiley, Chichester, 2005.

Chapter 6: Conclusions

The introductory chapter outlined the importance of the emergent field of nanocomposite functional materials, and showed that the development of new routes to novel metal-polymer nanocomposites is a relevant and necessary area of study. Supercritical fluid technology was described to be a useful and interesting technique with many advantages over conventional solvents.

The main aim of chapter 2 was to demonstrate the possibility of using scCO_2 techniques for the formation of an optical quality polymer-metal nanocomposite. This was successfully achieved, and scCO_2 was demonstrated to be a viable technique to produce uniform and transparent plasmonic nanocomposites. The impregnation process shows good potential for control of both depth and size/concentration of the nanoparticles, by modification of time and pressure variables. The process itself has been significantly improved by the development of the high pressure equipment and system. As a result of this development, the method is ideally suited for the production of optical and photonic materials as it does not require surface modification of the nanoparticles and avoids aggregation of the nanoparticles in the polymer. The products have been demonstrated as excellent SERS enhancement materials, which could find application in many optical devices and systems. Future work, capable of further improving the system, was suggested, and there is scope for as yet untested applications, such as MEF and optical limitation.

The original aims of chapter 3 are summarised in the following points:

- The successful recovery or harvesting of nanoparticles from aqueous solution.
- The incorporation of these nanoparticles into polymer powder.

- The location of the nanoparticles to be targeted to the surface of the polymer.
- The furthering and expansion of the field of nanoparticles as a stabiliser for polymerisations, both in practical and theoretical terms.

All of these aims were achieved. The two main sections, on suspension and dispersion, described polymerisations with metal oxide nanoparticles as the sole stabiliser present. The two complementary polymerisation methods allow a range of different polymers and powder sizes to be synthesised, and it was shown that not only magnetite, but also other metal oxide nanoparticles, can be used in this manner. We have demonstrated both the harvesting, and the capturing upon the surface of polymer beads, of nanoparticles from aqueous dispersion. This *in-situ* polymerisation method, using functional nanoparticles as stabilisers, opens up new routes to the preparation of a wide range of polymer nanocomposites, and these successful trials have allowed for further research to be instigated at Nottingham University.

Chapter 4 reported two alternative and complementary synthetic routes to silver nanoparticle decorated polymer microspheres, with extensive characterisation by electron microscopy. This showed that the products have a nanocomposite structure ideal for many applications. Both of the routes can be seen as general synthesis strategies as they have the potential to be transferred to a wide range of polymer systems, and neither route contains any problematically complex or expensive steps that would be a barrier to scale up or industrial use.

In the first route, a novel route to stabilised silver nanoparticles in aqueous solution was demonstrated, which provides an interesting alternative to existing routes as it introduces a large range of possible variations, by allowing organic soluble precursors to

be used. It was then shown that the silver nanoparticles produced by this method could be easily attached to the surface of a polystyrene powder by sulfonation. This is a simple and straightforward method that is easily scaleable and first reported here. This surface-location of the silver makes this cheaply producible powder ideal for many applications, such as SERS, catalysis or antimicrobial functions.

In the second route, the use of an appropriately designed RAFT-stabilising agent, which allows simple and effective $scCO_2$ synthesis of polymer microspheres, decorated with silver nanoparticles, was reported. The surface location of the nanoparticles again gives the polymer powder excellent potential for catalytic, antibacterial and biosensing applications. This synthetic route has the additional advantages of being a single step, one pot reaction that does not require conventional solvents at any stage during the process.

In summation, this thesis has described new synthetic pathways for the inclusion of metal and metal oxide nanoparticles into polymeric materials. These new materials, and synthetic routes, enable the exciting properties of nano-structures to be exploited for future applications.